CHALMERS

On Modeling the Dynamics of Fixed Biofilm Reactors

with focus on nitrifying trickling filters

Torsten Wik

Control Engineering Laboratory
Department of Signals and Systems
CHALMERS UNIVERSITY OF TECHNOLOGY
Göteborg, Sweden

THESIS FOR THE DEGREE OF DOCTOR OF PHILOSOPHY

On Modeling the Dynamics of Fixed Biofilm Reactors

WITH FOCUS ON NITRIFYING TRICKLING FILTERS

Torsten Wik

Control Engineering Laboratory
Department of Signals and Systems
Chalmers University of Technology
Göteborg, Sweden 1999

On Modeling Dynamics of Fixed Biofilm Reactors
with focus on nitrifying trickling filters
Torsten E. I. Wik
ISBN 91-7197-797-X

Doktorsavhandlingar vid Chalmers Tekniska Högskola
Ny serie nr 1500
ISSN 0346-718X

Technical Report No 365
Control Engineering Laboratory
Department of Signals and Systems
School of Electrical and Computer Engineering
Chalmers University of Technology
SE-412 96 Göteborg, Sweden

Cover: Water being distributed over a nitrifying trickling filter at the Rya wastewater treatment plant in Göteborg, Sweden.

Printed by Chalmers Reproservice
Chalmers University of Technology
Göteborg, Sweden 1999

Abstract

Fixed biofilms, which are matrix-enclosed populations of organisms attached to solid surfaces, are increasingly used in environmental biotechnology processes, such as the treatment of potable water and wastewater. This thesis aims to give some insight into the dynamic modeling of biofilms and fixed biofilm reactors, with a focus on nitrifying trickling filters (NTFs) for the treatment of wastewater. However, most of the presented methods are applicable to fixed biofilm reactors in general. Some of them are also applicable to mathematically related areas, such as the modeling of porous catalytic reactors and immobilized cells.

Various models are derived for different purposes and time-scales using a physically based multi-species model of biofilms, which takes into consideration the transportation phenomena inside the biofilm as well as the bacterial processes causing the population dynamics. Different operating modes of a biofilm reactor can be deduced from the origin of the dynamics. The slow dynamics are mainly caused by changes in biology, which can take days or weeks to change, and the fast dynamics are mainly caused by reactor hydraulics and transients of the dissolved components in the biofilm. The fast transients typically settle in less than a few hours after a change in operating conditions. Based on this division, simplified models and numerical solution methods are presented for (i) a steady state, (ii) a quasi-steady state, where the fast and slow modes are in steady states corresponding to two different operating conditions, (iii) fast dynamics, where the biofilm composition is constant and (iv) slow dynamics, where only the fast modes are in a steady state.

A wide range of biofilm reactors can conveniently be modeled by units called continuously stirred biofilm reactors (CSBR), which are tanks with a homogeneous gas phase and bulk liquid, and a biofilm that varies with the distance from the substratum. Specifically, it is shown that the dynamics of NTFs can be modeled by cascaded CSBRs. A method to determine physically based rational transfer functions of low order, describing the fast dynamics of CSBRs, is derived. With these transfer functions an appropriate number of CSBRs, as well as other biofilm and reactor parameters, can be determined from residence time distributions.

From comparisons between simulations and experiments carried out on different pilot scale NTFs, physical phenomena, such as adsorption and desorption of ammonium, denitrification, oxygen mass transfer, changes in bulk volume, are observed and quantified. Simulations of operating strategies indicate that the nitrifying capacity can be improved by regularly inversing the order of cascaded NTFs and by varying the individual flow through NTFs operating in parallel.

Keywords: Adsorption, biofilm reactors, dormancy, dynamics, modeling, nitrification, operation, transfer functions

Preface

The work presented in this thesis originated as a part of a large research program called STAMP, which was administrated and financed by NUTEK (The Swedish National Board for Industrial and Technical Development). The program, initiated in 1991 and now ended, consisted of several consortia with researchers from various university departments and employees at some of the larger wastewater treatment plants in Sweden. The main issues in the program concerned the control and operation of wastewater treatment plants, development and investigations of new processes and new technology as well as human factor issues.

My work was a part of the Göteborg Consortium and has been carried out in cooperation and after discussions with people at the Rya Wastewater Treatment Plant (WWTP) in Göteborg, the Sjölunda WWTP at Malmö, the Department of General and Marine Microbiology at Göteborg University (GU), the Department of Sanitary Engineering at Chalmers University of Technology (CTH), the Department of Chemical Reaction Engineering at CTH, and the Control Engineering Laboratory at CTH. Because of the extensions of the Rya WWTP and the Sjölunda WWTP for extended nitrogen removal by nitrifying trickling filters, the focus of the work has been on such biofilm reactors. However, most of the methods and theories presented apply to biofilms and biofilm reactors more in general.

Researchers and others working in the area of wastewater treatment can have very different backgrounds, which is evident from the constellations of the consortia. This makes it difficult to write in a way that everyone understands. It has been my wish though that as many as possible should be able to read as much as possible of this thesis. Thus, as a reader you may find some parts over-explicit while other parts may seem incomprehensible. I hope you will be able to overlook this.

Acknowledgments

I would like to thank everyone that has been involved in my work, including all those who have made my time as a PhD student at the department so joyful and interesting. The list of people could be made almost infinite. Without leaving anyone out on purpose, I particularly wish to express my gratitude towards:

My supervisor Dr Claes Breitholtz and Dr Claës Lindeborg, project manager of the Control Engineering Group of the Göteborg Consortium in the STAMP-program, for all kinds of valuable discussions, our cooperation and their enthusiastic support in my work.

My friend and room mate Stefan Pettersson, who has put up with my constant interruptions of his work and who has also been of great help in discussions although the subject of this thesis is far from his specialty.

Dr Ann Mattsson at the Rya WWTP, who has been an invaluable contact at the plant and who always looks at things from new and interesting angles.

Dr Henrik Aspegren at Malmö Water and Sewage Works for his enthusiasm, our discussions and for making the experiments at Sjölunda possible to carry out.

Ingemar Söderlind at the Sjölunda WWTP for his assistance during my time at the plant.

Ann Mari Thorner and Lennart Johansson at the Water Laboratory, Malmö Water and Sewage Works, for helping me with the analyses of water samples.

Lucica Enhanch, Annette Svensson and Monica Karlsson at the laboratory of the Rya WWTP, who helped me with chemical analyses and took great responsibility for the maintenance of the experimental equipment I used at the Rya WWTP.

Dr Claes Nicklasson at the Department of Chemical Reaction Engineering (CTH) for our cooperation and his assistance in the pulse response experiments at the Rya WWTP.

Dr Bengt Carlsson at the Department of Materials Science, Systems and Control Group, Uppsala University, who examined my thesis for the degree of Licentiate of Engineering in 1996 and then gave me some good ideas about further work.

Lars Jansson, system administrator at the department, for all the extra efforts he put into helping me carry out my final simulations.

Prof Markus Boller at the Department of Environmental Engineering, Swiss Federal Institute for Environmental Science and Technology, for providing data and background material that I have used for comparisons with simulations.

Dr Sverker Molander at the Department of Sanitary Engineering (CTH), for discussions about the biological processes in microbial populations.

Prof Bengt Andersson, at the Department of Chemical Reaction Engineering (CTH), for discussions about catalytic reactors.

Dr Per Nielsen at the Environmental Engineering Laboratory, Aalborg University, for rewarding discussions about adsorption of ammonium to organic matter.

My father, Prof. Ingemar Wik at the Department of Mathematics, Umeå University, for discussions about Bessel functions and for correcting some of my language and equations.

Finally, I dearly thank my mother Dr Berit Wik, who has carefully read this thesis, as well as many of my articles, and corrected my English in a way that no one else

would have done.

Many thanks to you also, Ia, for all the joy and support you have given me!

The work presented in this thesis was first financed by NUTEK (The Swedish National Board for Industrial and Technical Development) and since 1997 by the School of Environmental Sciences (GU/CTH). The assistance and equipment used in the experiments were mainly paid by the Sjölunda WWTP and the Rya WWTP, which is gratefully acknowledged.

Göteborg, November 27, 2003

TORSTEN WIK

Publications

To a large extent this thesis is based on the following publications:

Wik, T. and C. Lindeborg (1994). Modelling the dynamics of a trickling filter for waste water treatment. In: *3rd IEEE Conf. on Control Appl.*. Glasgow, UK. pp. 1035–1040.

Wik, T., A. Mattsson, E. Hansson and C. Niklasson (1995). Nitrification in a tertiary trickling filter at high hydraulic loads. *Wat. Sci. Tech.* **32**(8), 185–192.

Wik, T. and C. Breitholtz (1996). Steady-state solution of a two-species biofilm problem. *Biotechnol. Bioeng.* **50**(6), 675–686.

Wik, T. (1997). Modelling dynamics of nitrifying trickling filters and ammonium meters. *Med. Fac. Landbouww. Univ. Gent* **62**(4b), 1641–1647.

Wik, T. and C. Breitholtz (1998). Rational transfer function models for biofilm reactors. *AIChE J.* **44**(12), 2647–2657.

Wik, T. (1999*a*). Adsorption and denitrification in nitrifying trickling filters. *Wat. Res.* **33**(6), 1500–1508.

Wik, T. (1999*b*). Rational transfer function models for nitrifying trickling filters. *Wat. Sci. Tech.* **39**(4), 121–128.

The thesis also contains results from several technical reports which are referred to in the text and listed in the Bibliography.

CONTENTS

Chapter 1

INTRODUCTION

Biofilms can be defined as matrix-enclosed bacterial populations adherent to each other and/or to surfaces or interfaces (Costerton *et al.* 1995). This definition includes microbial aggregates and floccules, but also adherent populations within pore spaces of porous media. The majority of microorganisms in nature are associated with solid surfaces, such as microscopic particles in aquatic environments, clay or sand particles in soils, or on the surfaces of animal or plant tissues (Bradshaw 1995). By attaching to surfaces, the organisms create small ecosystems that make them more resistant to environmental changes. Thus, *fixed biofilms*, which are biofilms that are attached to impermeable solid surfaces, are the most common form of microbial life. The definition of fixed biofilms includes mono-layers of microbial cells, but typically the expression *fixed biofilms* refers to thicker complex communities of bacteria, algae, fungi and protozoa embedded in organic polymers.

Though most people never talk, or even think of biofilms, we all carry around biofilms, for example as dental plaques (Wimpenny 1995). Biofilms are, in fact, a very costly problem in our modern society. Pipes and heat exchangers in factories and houses cease to function due to biofilm fouling, which has to be controlled by large quantities of anti-fouling agents. Corrosion by iron oxidizing organisms in biofilms is another large problem, as is also the corrosion on buildings and culturally valuable artifacts by acids being withheld and produced by biofilms covering surfaces exposed to rain.

The use of invasive medical products is a major risk factor for infection due to microbial colonization in and around the device. The resulting biofilms become extremely resistant to antibiotics. According to Bacterin Inc., Bozeman, Montana, these infections are responsible for nearly 10 percent of all patients admitted to hospitals in the United States and are the sixth leading cause of death. Hospitals in the U. S. spend 6.5 billion dollars per year on device related nosocomial (hospital acquired) infections.

However, biofilms are also industrially used for useful causes, particularly in environmental biotechnology processes, such as the treatment of potable water and wastewater. As our knowledge of the consequences of wastewater treatment plant (WWTP) effluents on the environment has increased, the plants have been succes-

sively extended from treating the water from aesthetical and odor points of view to reducing harmful bacteria, organics, heavy metals and phosphates. Nitrogen let into the sea from various sources, such as agricultural and forest farming, industrial and municipal wastewater, and car emissions, is seen as a likely cause of some of the environmental damage in the sea today, where most attention has perhaps been paid to the blooming of blue-green algae and oxygen depletion at the sea bottom. As a consequence, legislation and guidelines by the European Community and individual governments have set severe limits on wastewater discharges, which requires that many existing WWTPs have to be upgraded.

Growing urbanization has led to sewage treatment plants located within densely populated areas and makes the extension of plants economically and physically difficult. To avoid the expense of pumping stations and transfer of wastewater, which can amount to 80% of the total investment, high rate processes with compact footprints can provide the most cost-efficient solutions (Lacampe *et al.* 1993). Compared with reactors with suspended bacteria, such as the activated sludge process, biofilm reactors can be operated at high biomass concentrations in the reactor, without the need to separate the biomass and the treated effluent. This implies that biofilm units often require less land area than conventional basins with suspended bacteria.

Today, many WWTPs are being extended with biological nitrification/denitrification processes for increased nitrogen removal. Such units have a tendency to become very large, due to slow growth of the bacteria involved in the nitrification process. Thus, nitrifying biofilm reactors, which have been found to be more efficient per unit land area than conventional systems with suspended bacteria (Rittmann 1989), have become a common alternative for upgrading. For example, several Swedish WWTPs are planned to be upgraded, or have already been upgraded, with nitrifying trickling filters. The most common types of biofilm reactors used in wastewater treatment are briefly described in the next section.

1.1 Biofilm Reactors

When water flows over a solid surface, bacteria in the water attach to the surface and slowly increase in number so that eventually a biofilm is established. In the biofilm, the bacteria live on the energy they acquire from carrying out transformations of substrates, available carbon sources and necessary trace substances in the water.

The substrates involved in the reactions are transported, mainly by diffusion, into and out of the biofilm, where the reactions take place (see Figure 1.1). In aerobic processes the oxygen required for the reactions enters the bulk water mainly at the water/air interface, where also gaseous products, such as carbon dioxide, leave the water. The biofilm thickness is governed by the growth and decay of the bacteria, as well as the erosion of the biofilm and the adsorption of material in the water (Arvin and Harremoës 1990).

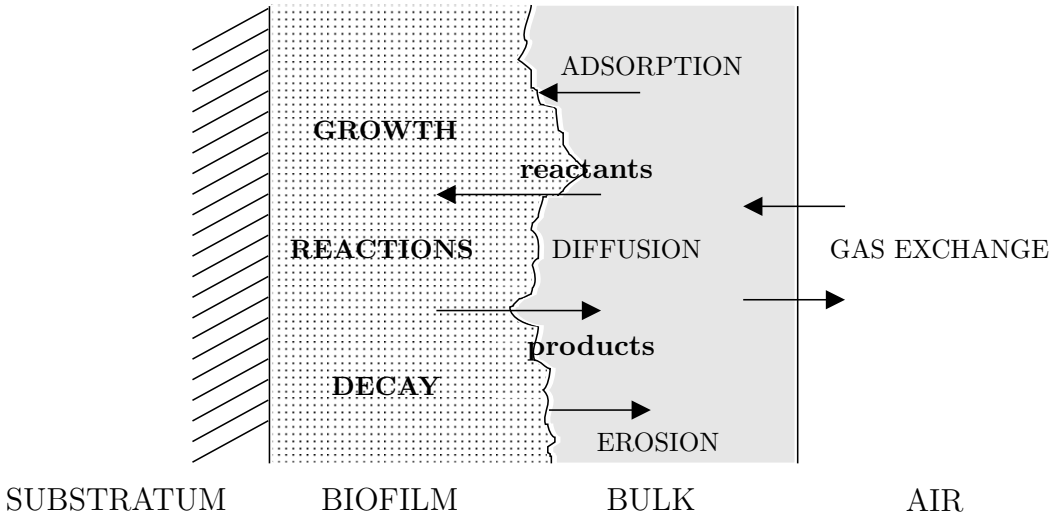

Figure 1.1 *Illustration of the basic phenomena in the biofilm.*

Most biofilm reactors use fixed biofilms on impermeable substrata, though there are other reactors, where the biofilm is attached to a membrane, for example (Debus *et al.* 1994, Wobus *et al.* 1996). Such reactors are not described here since they are not as common (yet) in municipal wastewater treatment. Nitrifying biofilm reactors of the types mentioned below have been investigated and compared by Boller *et al.* (1994).

Trickling Filters (TFs)

The first biofilm reactors for wastewater treatment were probably trickling filters, which were introduced more than hundred years ago. However, it was soon realized that the organic content in the wastewater was reduced by biological degradation rather than by simple screening. The filters were towers filled with rocks over which the water was distributed. On the rocks heterotrophic bacteria grew as biofilms and oxidized the organics in the water. The use of stones as packing media made the constructions heavy and the area of biofilm per reactor volume (specific surface area) low. Modern TFs are generally filled with cross-flow plastic media that give high specific surface areas and light constructions. Nowadays, TFs are also used for nitrification. However, the general idea is the same: water is sprinkled over the top of the filter (see front cover) and trickles down on the media where the biofilm is attached. The necessary oxygen flows through the filter, either by natural draft or by forced ventilation. At the bottom of the tower the water is collected and let into a denitrifying process stage where the nitrate is reduced to nitrogen gas (see Figure 1.2).

The advantages of trickling filters are the relatively low costs for construction and

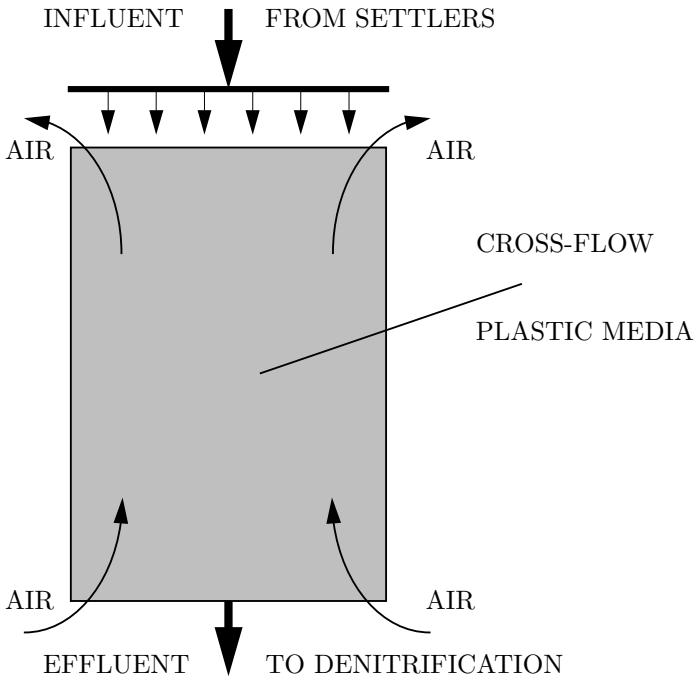

Figure 1.2 *Illustration of a nitrifying trickling filter.*

operation, as well as their being simple and robust. The disadvantages are high costs for pumping the water to the top of the reactor, if necessary, and short residence times. Short residence times imply that peak loads cause peak effluent levels, which may cause problems in the subsequent denitrifying process. Particularly, in treatment of industrial wastewater, where peak loads are more common than in municipal wastewater treatment, the trickling filters are sometimes equipped with recirculation to increase the retention time.

Rotating Biological Contactors (RBCs)

Usually it is the concentration of oxygen that limits the reaction rates in the biofilm. Rotating biological contactors are supposed to give better aeration of the biofilm by periodically exposing the biofilm directly to the air. RBCs are constructed of several parallel discs or drums, partly submerged into the wastewater, and distributed on a rotating axis. Often RBCs are divided into a number of compartments containing several discs (see Figure 1.3).

The nitrification rates found in RBCs are comparable to those of NTFs (Gönenç and Harremoës 1985, Lyngå and Årebäck 1991). However, the rates are dependent on the speed of rotation (Boller *et al.* 1994). Generally, higher rates are achieved when the rotation speed is increased, but this also increases the energy consumption.

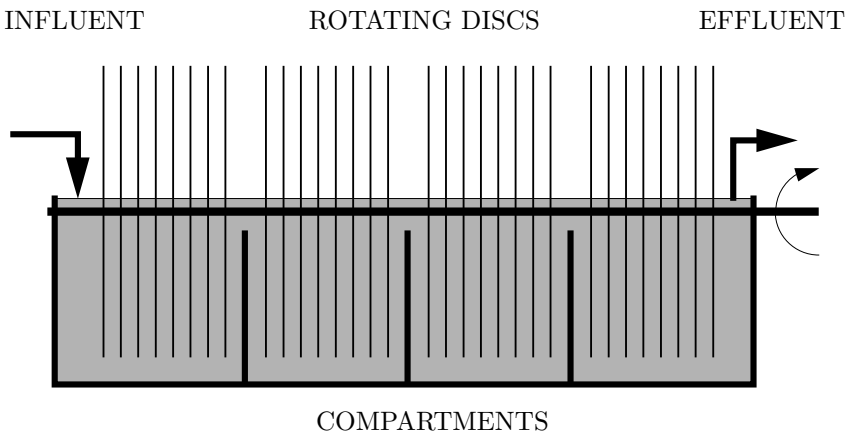

Figure 1.3 *Illustration of a rotating biological contactor.*

Aerated Biofilters (BF)

Aerated biofilters are becoming common in wastewater treatment. They are more complicated than the reactors previously described, more expensive to operate but generally give higher rates per cubic meter of reactor (Boller *et al.* 1994, Rittmann 1989, Tschui *et al.* 1994). BFs are reactors working in up-flow or down-flow mode and filled with granulated media or corrugated sheets on which the biofilm is attached. Compressed air is either introduced internally or at the bottom if the filter works in an up-flow mode (see Figure 1.4). The air bubbles ensure good mixing, but the hydraulics are difficult to define. Generally, the rates increase with increasing air velocity, but this also increases the costs of operation significantly.

There are numerous different types of biofilm reactors not described here, such as non-aerated biofilters for anaerobic processes, fluidized biofilters and moving beds, to mention a few.

1.2 A Simple Steady-State Biofilm Model

To illustrate the basics in biofilm modeling, we derive a simple stationary model that describes the substrate concentrations inside the biofilm and the substrate flux into the biofilm. Essentially all biofilm models are based on these mass balance equations. More sophisticated models, such as the ones presented in Chapter 3, combine the mass balances for dissolved components with equations describing the microbial processes in the biofilm.

Let the reaction in the biofilm be the complete nitrification of ammonium (NH_4^+) into nitrate (NO_3^-) in a bicarbonate (HCO_3^-) buffered environment:

$$NH_4^+ + 2HCO_3^- + 2O_2 \rightarrow NO_3^- + 3H_2O + 2CO_2. \tag{1.1}$$

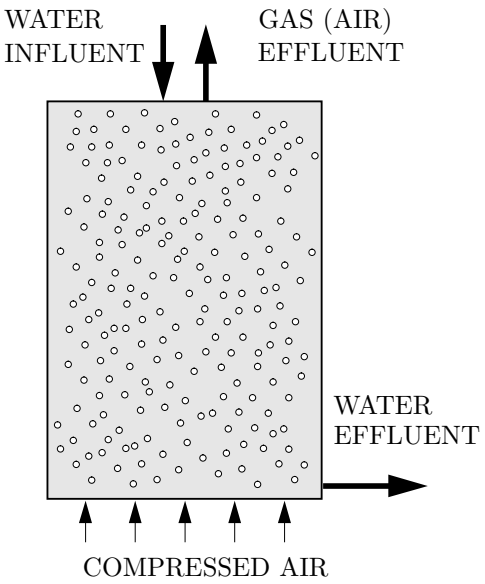

Figure 1.4 *Illustration of a down-flow, counter-current, aerated biofilter.*

Although this reaction represents ideal stoichiometric relations, it can be seen that ammonium, oxygen (O_2) and bicarbonate (or an equivalent base) are required for the nitrification to occur.

The substrate gradients in a biofilm are in general far larger perpendicular to the biofilm surface than parallel to the surface. Hence, only one space dimension is usually considered in biofilm modeling. Now, assume that the biofilm is planar, completely homogeneous and of thickness L. The substrate concentrations in the biofilm, $c(x)$, are then continuous functions of the distance x from the biofilm substratum.

Fick's first law of diffusion in one dimension is assumed to describe the transport of substrates within the biofilm, i.e.,

$$J_i = -D_i \frac{d}{dx} c_i, \quad 0 < x < L, \quad i = \mathrm{NH}_4^+,\ \mathrm{O}_2,\ \mathrm{HCO}_3^-,\ \mathrm{NO}_3^-,\ \mathrm{CO}_2,$$

where J_i is the outward flux of substrate i, and D_i is the molecular diffusion coefficient in the biofilm.

A mass balance for each substrate over an infinitesimal film segment dx gives

$$\frac{d}{dx} J_i = r_{v,i},$$

where $r_{v,i}$ is the volumetric production rate (see Figure 1.5). Hence,

$$D_i \frac{d^2}{dx^2} c_i = -r_{v,i}. \tag{1.2}$$

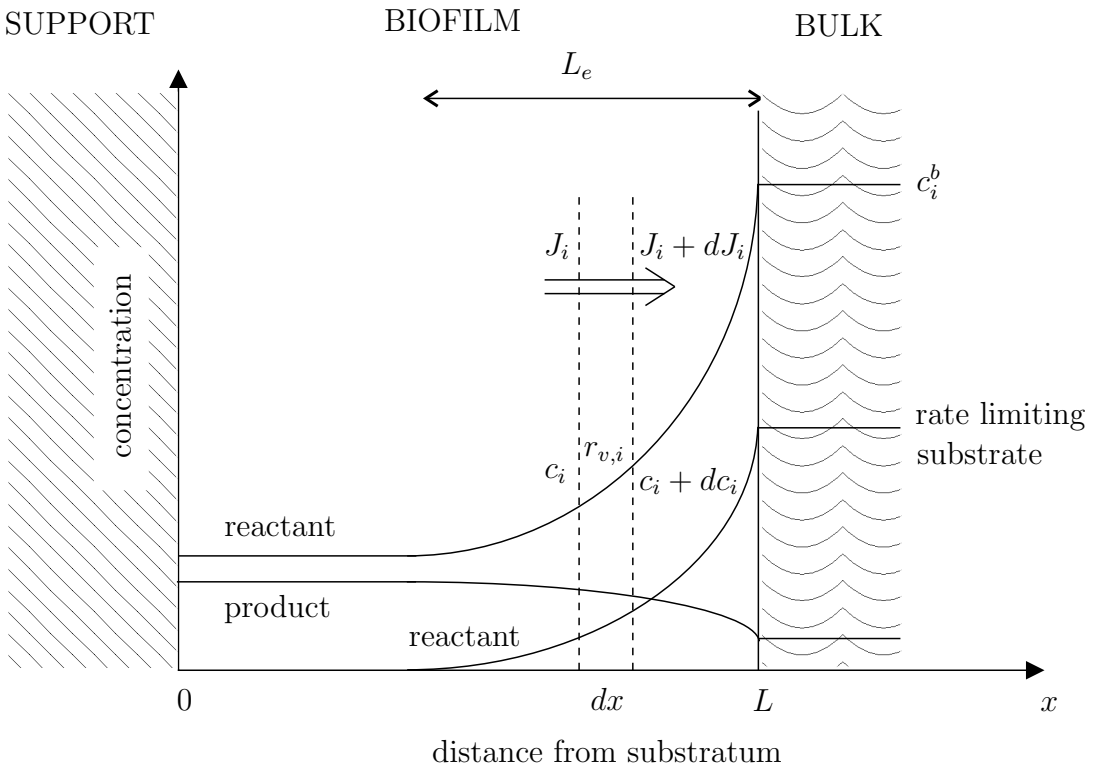

Figure 1.5 *Illustration of the mass balance, the definition of rate limiting substrate and the definition of penetration depth L_e.*

To solve this equation we need two boundary conditions for each substrate. Since no substrate can diffuse through the substratum, we have the boundary condition

$$\left[\frac{d}{dx}c_i\right]_{x=0} = 0.$$

If we assume that there is no transfer resistance between the biofilm and the bulk, we get the second boundary condition

$$c_i(L) = c_i^b,$$

where c_i^b is the substrate concentration in the bulk.

A common form of rate expression used in bacterial systems are Monod-expressions, such as

$$r_{v,i}(c_j) = \nu_i X \frac{\mu_m}{Y} \frac{c_j}{K + c_j}, \tag{1.3}$$

where ν_i is the stoichiometric coefficient for substrate i in (1.1), μ_m is the maximum growth rate of the bacteria, X is the concentration of the bacteria, Y is the yield coefficient that determines how much mass the bacteria gain from the reaction, c_j is the substrate concentration that determines the rate, and K is a Monod saturation

coefficient. The saturation coefficient determines the transition from a first order reaction

$$r_{v,i} = \nu_i r_1 c_j, \quad \text{where} \quad r_1 = X\frac{\mu_m}{YK},$$

to a zero order reaction

$$r_{v,i} = \nu_i r_0, \quad \text{where} \quad r_0 = X\frac{\mu_m}{Y},$$

as the concentration c_j increases from $c_j \ll K$ to $c_j \gg K$.

Sometimes several Monod-expressions are combined to form double or triple Monod-expressions to model the rate dependence on several substrates. For example, the volumetric production rate of ammonium in reaction (1.1) may be expressed as ($\nu_{NH_4} = -1$):

$$r_{v,NH_4} = -X\frac{\mu_m}{Y}\frac{S_{O_2}}{K_{O_2}+S_{O_2}}\frac{S_{NH_4}}{K_{NH_4}+S_{NH_4}}\frac{S_{HCO_3}}{K_{HCO_3}+S_{HCO_3}}. \tag{1.4}$$

Some relations do not depend on the kinetics. For example, integration of Eq. (1.2) for all substrates twice gives

$$\frac{D_i}{\nu_i}(c_i^b - c_i(0)) = \frac{D_j}{\nu_j}(c_j^b - c_j(0)), \quad \text{for all } i \text{ and } j, \tag{1.5}$$

independent of the kinetics used.

For simple rate expressions, Eq. (1.2) can be solved analytically to determine the flux J_f at the biofilm surface. The substrate concentrations of the reactants decrease with increasing depth of the biofilm. Two cases may occur if the reaction is of zero order. Either the biofilm is so thin that none of the concentrations become zero, or the biofilm is so thick that one of the concentrations reaches zero and no reaction occurs inside that point. The substrate that is depleted in the biofilm is commonly called the *rate limiting substrate* (see Figure 1.5), and the depth L_e where the concentration of that substrate reaches zero is called the *penetration depth* (Szwerinski *et al.* 1986). The penetration depth is

$$L_e = \min_i \sqrt{\frac{2c_i^b D_i}{-\nu_i r_0}}. \tag{1.6}$$

The substrate i that gives the minimum is the rate limiting substrate. If $L_e < L$, the substrate concentrations are

$$c_i(x) = \begin{cases} c_i(0) & , \quad 0 < x < L - L_e \\ c_i^b - \dfrac{\nu_i r_0}{D_i}\left(\dfrac{(L-x)^2}{2} - L_e(L-x)\right) & , \quad L - L_e < x < L \end{cases}$$

and the fluxes *out of* the biofilm are

$$J_{f,i} = \nu_i r_0 L_e, \tag{1.7}$$

where $c_i(0)$ is zero for the rate limiting substrate. The other concentrations at the substratum may then be determined with Eq. (1.5). If $L_e > L$, no concentration reaches zero in the biofilm and the solution to Eq. (1.2) is

$$\begin{aligned} c_i(x) &= c_i^b + \frac{\nu_i r_0}{2D_i}(L^2 - x^2), \qquad 0 < x < L, \\ J_{f,i} &= \nu_i r_0 L. \end{aligned}$$

If the reaction is of first order in the concentration c_j, the concentration of that substrate (reactant) is

$$c_j(x) = c_j^b \frac{\cosh(x\sqrt{-\nu_j r_1/D_j})}{\cosh(L\sqrt{-\nu_j r_1/D_j})},$$

where ν_j is negative. The flux out of the biofilm is

$$J_{f,j} = -c_j^b \sqrt{-\nu_j r_1 D_j}\,\tanh(L\sqrt{-\nu_j r_1/D_j}).$$

The biofilm surface flux of the other substrates follows from the stoichiometry:

$$J_{f,i} = \frac{\nu_i}{\nu_j} J_{f,j}. \tag{1.8}$$

Generally, it is difficult to solve Eq. (1.5) for nonlinear rate expressions. However, for the simple Monod expression (1.3) the biofilm surface flux can be derived by elimination of dx and separation of variables (Gujer and Boller 1986):

$$J_{f,j} = -\sqrt{-\frac{2\nu_j D_j X \mu_m}{Y}\left(c_j^b - c_j(0) - K\ln\left(\frac{K + c_j^b}{K + c_j(0)}\right)\right)}, \tag{1.9}$$

where $\ln(\cdot)$ denotes the natural logarithm. Thus, the fluxes of substrates at the biofilm surface are approximately proportional to the square root of the bulk concentration of the rate limiting substrate.

1.3 Modeling Analogies

From a mathematical point of view there are at least a few analogies to biofilm modeling. An obviously closely related field is modeling of artificially immobilized cells, e.g. alginated beads. In alginated beads, the bacteria cells are initially homogeneously dispersed in a gel matrix. The substrates diffuse through pores into the matrix, where the bacteria carry out the transformations of the substrates and form micro-colonies. Due to the growth of the bacteria, there will be a continuous leakage of single bacteria and/or eruptions of expanded colonies that break through the gel surface. A group of researchers in the Netherlands have extensively studied such systems with nitrifying bacteria by experiments and by simulation [de Gooijer *et al.* (1991), Hunik *et al.* (1993), (1994), dos Santos *et al.* (1996), Wijffels *et al.*

(1994), (1995*a*), (1995*b*), Wijffels and Tramper (1989), (1995)]. The models they have used are almost identical to models of biofilm systems, but their later and more sophisticated models include diffusion limitations caused by the expansion of the micro-colonies within the gel pores. This phenomenon, however, has no direct correspondence in biofilm systems.

There are also several modeling analogies between biofilm reactors and catalytic reactors with porous catalysts, which has been pointed out by Atkinson and Daoud (1968), for example. In such catalytic reactors the reactants (unfortunately in this context sometimes referred to as species) diffuse through the pores into the catalyst, where the reactions take place on the active sites of the catalyst. Due to saturation on the active sites, kinetic expressions like (1.3) are often used, but are then referred to as Michaelis-Menten kinetics instead of Monod kinetics. The growth of bacteria has no direct correspondence in catalytic systems, but the aging of the active sites can be modeled in a way similar to how the decay of bacteria can be modeled.

1.4 Scientific Contribution and Thesis Outline

The purpose of this thesis is to give some insight into dynamic modeling of biofilms and biofilm reactors. Due to the origin of the project underlying the experiments and simulation studies made, the focus is on nitrifying trickling filters (NTFs) for treatment of tertiary wastewater. Scientifically, the main contributions are:

- Applications of quite an established multispecies biofilm model to nitrifying biofilms and nitrifying biofilm reactors, as well as discussions about numerical techniques to solve the equations (Chapter 3, 4, 7, 8 and Appendix F).
- An investigation of stationary biofilms, as predicted by the multispecies biofilm model. The investigation shows, among other things, how coexistence of different bacteria in a biofilm can be predicted and how it depends on the biofilm thickness (Chapter 4).
- Discussions about how biofilm models can be used in reactor modeling using the concept of continuously stirred tank reactors (Chapter 5).
- Estimations of oxygen transfer coefficients from profile measurements in an NTF and estimations of how incorrectly estimated coefficients affects simulation results (Chapter 5).
- A method to derive physically based low order rational transfer functions that can be used for rapid simulation and controller design of systems with biofilm reactors. This method may also be applied to reactors with gel beads as well as catalytic reactors with porous catalysts (Chapter 6 and Appendix C).
- Comparisons between simulations using the transfer functions and experiments carried out on NTFs (Chapter 6).

- Methods to simulate residence time distributions rapidly and studies of how residence time distributions depend on biofilm and reactor parameters (Chapter 6 and Appendices D and E).
- Estimation of biofilm and reactor parameters from trace substance pulse response experiments carried out on pilot-scale NTFs (Chapter 6).
- Simulations and experiments carried out on nitrifying trickling filters that show that denitrification and adsorption/desorption of ammonium may occur in the biofilm and how this affects the rapid transients after changes in operating conditions (Chapter 6).
- A quasi-steady state analysis of a factorial design experiment carried out on an NTF. The analysis shows that an increased flow improves the substrate transport into the biofilm, which can be modeled by an increase of the oxygen mass transfer from the air to the bulk with the flow (Chapter 7).
- Comparisons between simulated and measured behavior of a pilot-scale NTF that during more than two months had been alternatingly fed wastewater with ammonium and wastewater without ammonium (Chapter 8).
- An extension of the multi-species biofilm model to consider *exogenous dormancy* and a dependence of the specific death rate on the history of the growth conditions (Chapter 8).
- Simulations of operational strategies that improve the nitrifying capacity of NTFs: alternating the order of two NTFs operating in series and periodically varying the individual flow through NTFs operating in parallel (Chapter 8).

The notation used is listed in Chapter 2. The subsequent chapters, i.e. Chapters 3 to 8, are organized as individual articles with cross references that the reader should be able to follow without recapitulating entire chapters. These chapters begin with a summary and end with discussions and conclusions. The purpose is to give the reader the possibility to skip chapters that are not of interest. Chapter 9 summarizes the conclusions made in all chapters.

Chapter 2

NOTATION

The notation below is used throughout the thesis. Sometimes, however, the meaning may differ from the definitions below, which is then specifically pointed out. The meaning of variables and parameters that are not listed here should be apparent from the context.

Abbreviations

BFC	biofilm compartment
BOD	biological oxygen demand
COD	chemical oxygen demand
CST	continuously stirred tank
CSTR	continuously stirred tank reactor
CSBR	continuously stirred biofilm reactor
FEM	finite element method
GPC	gas phase compartment
NTF	nitrifying trickling filter
ODE	ordinary differential equation
PDE	partial differential equation
PFD	partial fraction decomposition
RBC	rotating biological contactor
RTD	residence time distribution
TF	trickling filter
WWTP	wastewater treatment plant

Capital Letters

A	area (m^2), biofilm area (m^2)
D	diffusion coefficient ($m^2 d^{-1}$)
G	transfer function, transfer function matrix
J	substrate flux ($gm^{-2}d^{-1}$, mole $m^{-2}d^{-1}$)
J_s	flux of solids (gCOD $m^{-2}d^{-1}$)
K	saturation coefficient (gm^{-3}, mole m^{-3})

K_L gas-bulk mass transfer coefficient (md^{-1})
L biofilm thickness (m)
L_w liquid film thickness (m)
N number of tank reactors
Q volumetric flow rate (m^3d^{-1})
R microbial transformation rate (gCOD $m^{-3}d^{-1}$ or d^{-1}), radius (m)
T temperature (°C), mean residence time (d)
V bulk water volume (m^3)
X bacterial concentration (gCOD m^{-3})
Y yield coefficient (gCOD g^{-1})

Small Letters

a specific surface area (m^2m^{-3})
b endogenous respiration rate coefficient (d^{-1})
c concentration of dissolved component (gm^{-3}, mole m^{-3})
d time delay in ammonium meter (d)
g impulse response
h reactor height or reactor length (m)
k_0 zero order rate coefficient ($gm^{-3}d^{-1}$)
k_1 first order rate coefficient(d^{-1})
k_a adsorption coefficient ($gm^{-3}[gm^{-3}]^{-1}$)
k_c convection coefficient (md^{-1})
k_I inactivation rate coefficient (d^{-1})
m number of singularities, transfer function order
n_l number of dissolved components
n_s number of species
q hydraulic load (md^{-1})
r radial distance (m)
r_v specific substrate production rate ($gm^{-3}d^{-1}$, mole $m^{-3}d^{-1}$)
r_{vs} specific production rate of solids (gCOD $m^{-3}d^{-1}$)
s Laplace transform variable
t time (d)
u velocity of biofilm matrix (md^{-1})
v specific bulk volume (m^3m^{-3})
x distance from substratum (m)

Greek Letters

α transfer function singularity
γ non-dimensional coefficient for substrate flux into biofilm
δ non-dimensional biofilm thickness $(1 - \rho)$
ϵ volume fraction of solid component (m^3m^{-3})

ϵ_l	biofilm porosity (m^3m^{-3})
η	correction factor for denitrification
ϑ	stoichiometric coefficient
κ	non-dimensional first order rate coefficient
λ	time-scaling coefficient (d^{-1})
μ	non-dimensional zero order rate coefficient, moment specific growth rate (d^{-1})
μ_m	maximum growth rate (d^{-1})
μ_o	observed specific growth rate (d^{-1})
ν	net stoichiometric coefficient
ξ	scaled distance from origin (x/L or r/L)
ρ	density of solid component (gCOD m^{-3}), non-dimensional radius R/L
τ	time constant (non-dimensional or d)
σ^2	variance (d^2)
ς^3	skewness (d^3)
φ	scaled production rate of inert material (d^{-1})
ω	frequency (rad/time)

Subscripts

A	activation
D	death
E	endogenous respiration
I	inactivation
L	lysis
a	active
ao	ammonium oxidizers
b	beaker
d	dormant
f	film
e	electrolyte
g	gas
h	heterotrophs
no	nitrite oxidizers
r	reactor

Superscripts

b	bulk
r	reactant
p	product
sat	saturation

Diacritical marks

- $\tilde{}$ scaled
- $\hat{}$ approximation or estimate
- $\bar{}$ steady-state or infinite sum

Chapter 3

BIOFILM MODELING

A fairly complex, and quite general, fixed biofilm model is presented in this chapter. The model, which is based on mass balances, describes in mathematical terms the transportation phenomena inside the biofilm as well as the microbial processes causing the population dynamics. It is exemplified by the processes involved in nitrifying biofilms. Since the biofilm model covers the entire time-scale of the dynamic processes in the biofilm, it is an appropriate basis for development of further simplified models.

If we choose to ignore the *black box* approach, some kind of biofilm model is required for modeling a fixed biofilm reactor. The first biofilm models were very simple, not based on physical principles, and strictly used for reactor design purposes. From the sixties physical aspects have been used in biofilm modeling. Early such models were stationary and concentrated on the phenomena of substrate transport to and within a biofilm of fixed thickness, combined with a rate expression of one single reaction in the biofilm (Atkinson and Davies 1974, Harremoës 1976, Williamson and McCarty 1976). Only one bacterial species was considered in the biofilm, and the bacterial concentration was assumed constant in the entire biofilm. Rittmann and McCarty introduced biofilm growth and loss in their single-substrate steady-state model (Rittmann and McCarty 1980). This model was extended to describe the dynamic behavior of the biofilm itself by allowing the biofilm thickness to vary in time depending on the balance between growth and a combination of decay and shear losses (Rittmann 1982, Rittmann and Brunner 1984). However, the concentration of the bacterial species considered in the biofilm was still assumed constant, and only one substrate was included in the model.

A major step in biofilm modeling was taken when Kissel *et al.* (1984) and Wanner and Gujer (1984, 1986) presented their one-dimensional multi-species models. Conceptually, their models are the same, but it is the work of the latter group that has been continued and resulted in the commercially available software AQUASIM (Reichert 1994).

The idea behind the models is a division of the biofilm into separate continuous volume fractions; one for each active bacterial species considered, one for inert (non-active) material, and one for the water content. For each bacterial species, three transformations are typically considered: (i) Growth of the bacteria due to the reactions they carry out, (ii) endogenous respiration that is an oxygen consuming mineralization of the bacteria, and (iii) inactivation, i.e. when active bacteria turn into being non-active (inert). Rate expressions, like Monod-kinetics, are assigned to each of these transformations for all bacterial species considered as in models of the activated sludge process (e.g. the IAWPRC model no. 1 by Henze *et al.* (1987)).

The bacteria in the biofilm will move due to the net growth or net decay. For example, a net growth at a certain distance from the substratum will push the biofilm outside this point further away from the substratum. This transport phenomenon, mass balances inside the biofilm for the solid fractions and for the substrates, together with the rate expressions and Fickian diffusion of the substrates yield a system of non-linear partial differential equations (PDEs) of Diffusion-Reaction type combined with a set of first order PDEs. Since the biofilm thickness may vary with time, the system equations become a moving boundary problem. Gujer and Wanner (1990) describe this general biofilm model in detail.

Although several of the parameters used in the modeling are temperature dependent, none of the models commented here include energy balances. This is basically due to the formulation of the models from a wastewater perspective. The net energy in the reactions carried out are then ignorable compared to the capacity of the water in the bulk. This is illustrated by a numerical example in Appendix A. Also when the bulk is not water, energy balances can often be ignored since the energy gained in the transformation of substrates is used by the bacteria for their growth and, hence, is only released as secondary heat caused by the metabolic activity of the bacteria (Yantarasri *et al.* 1992). With knowledge of the net specific heat produced by the bacteria, though, energy balances may be incorporated in biofilm models as an additional heat equation.

The model presented here is essentially the same as the models formulated by Kissel *et al.* (1984) and Wanner and Gujer (1984, 1986). For illustration, and for later use, the processes involved are exemplified with a nitrifying biofilm, where ammonium oxidizing bacteria are coexisting and competing with nitrite oxidizers.

3.1 Assumptions

In order to formulate a feasible mathematical model of multi-species biofilm systems several assumptions have to be made. Wanner (1995) discusses the typical kinds of assumptions used in biofilm modeling in detail. As a basis for further assumptions later on, the following ones are used [adapted from Gujer and Wanner (1990)]:

A1 The biofilm is treated as a continuum: Variables are described by averaging quantities such as concentrations and volume fractions.

A2 Gradients of system properties are orders of magnitude greater perpendicular to the substratum than in other directions: Only one space-dimension is required.

A3 The biofilm consists of one liquid (water) phase and one or more solid phases, where each solid phase consists of the mass of one particulate component.

A4 The constituent particulate components are bound to each other and form a continuous solid matrix.

A5 The void spaces between the constituent particulate components are interconnected and occupied by the liquid phase.

A6 The liquid phase contains only dissolved components.

A7 Transport of the dissolved components in the liquid phase is by molecular diffusion, and can be described by Fick's first law of diffusion.

A8 The densities of the solid components, as well as the volume fraction of the liquid phase, are constant in time but may depend on the distance from the substratum.

A9 Stoichiometry and kinetics of transformation processes are invariant in the biofilm.

The first assumption is an aggregation of the states and is basically the basis for the subsequent assumptions. Lately, its validity has been questioned in a number of Confocal Scanning Laser Microscopy (CLSM) studies, which show that biofilms may consist of partly or fully disconnected colonies of organisms (de Beer *et al.* 1994*b*, Lewandowski *et al.* 1994, Costerton *et al.* 1995). In agreement with these observations fluorescent latex micro-beads have been observed to move parallel to the substratum in channels in the biofilm (Stoodley *et al.* 1994, de Beer *et al.* 1994*a*).

Due to a limited penetration depth of around 200 μm for the laser light, the investigations have been carried out on thin and relatively young biofilms. In more or less all studies the biofilms were also grown under laboratory conditions and consisted of either a mono-culture or a consortium of only two or three laboratory species (Bishop 1997).

Like most biological systems, biofilms adapt to the surrounding conditions. Based on experiments carried out in a Biofilm Airlift Suspension (BAS) reactor, and work of others, van Loosdrecht *et al.* (1995) suggest a conceptual model of how the biofilm structure depends on interactions between hydraulics and substrate surface load. At low substrate loads and high shear the biofilm becomes patchy due to biofilm detachment and erosion. At high substrate loads and low shear forces the biofilm becomes porous, heterogeneous and may easily slough. Smooth, stable, dense and relatively homogeneous biofilms occur when the substrate loads are moderate and

the growth of the biofilm is balanced by erosion caused by shear stress. This general description is in accordance with the observations made by Kugaprasatham *et al.* (1992) of nitrifying biofilms exposed to increasing turbulence.

To date, we have found no direct experimental findings reported which violates the continuum assumption for mature biofilms. It appears as if many biofilms begin with the formation of separate micro-colonies, which later may grow together, be overlapped and become a continuous biofilm. Predictions in a wide range of applications, using models based on biofilm continuity, have been found to be in accordance with experimental data (Gujer and Boller 1990, Fruhen *et al.* 1991, Arcangeli and Arvin 1995, Okabe *et al.* 1995, Horn and Hempel 1997*b*, Horn and Hempel 1997*a*). Many experimental findings on the microbial composition of multi-species biofilms can also qualitatively be explained by such models (Zhang *et al.* 1994, Ohashi *et al.* 1995, Schramm *et al.* 1996, Schramm *et al.* 1997). In conclusion, the presented biofilm model is not applicable to all biofilm systems, but may apply to mature, dense biofilms exposed to moderate ratios of surface load to shear stress.

Accepting assumption **A1**, assumption **A2** holds for most types of biofilm reactors. Generally, quite a large biofilm surface has to be passed by a substrate containing liquid to obtain any changes in the concentrations, while the concentrations change significantly over the depth of the biofilm, which is only around 10^{-3} m thick. This is illustrated in Figure 3.1 for a nitrifying trickling filter. The filter is 10 meters high and the influent ammonium concentration is 10 gN m^{-3}. The effluent ammonium concentration is close to zero and, thus, the concentration gradient along the reactor is about $\partial c/\partial z \approx 1$ gm^{-4}. At the biofilm substratum the concentration has also decreased to almost zero, but at a length of about 1 mm, i.e. $\partial c/\partial x \approx 10^4$ gm^{-4}. Hence, we may approximate the z space coordinate by a far sparser discretization than is needed for the x coordinate.

Assumptions **A4**, **A7** and **A8** are further discussed in Section 3.3 and Section 3.4.

3.2 Model Equations

The biofilm process is described as follows:

A biofilm has been developed on a planar impermeable substratum ($x = 0$), e.g., on a plastic material, a metal or stones. The biofilm consists of water (subscript l) and $n_s + 1$ different solid phases (subscript j); n_s different types of bacteria, and inert material (subscript $n_s + 1$). These are expressed as volume fractions $\epsilon_j(x, t)$, which are continuous functions in time and space. On the surface of the biofilm ($x = L$) a bulk liquid is streaming. Substrates, i.e., the dissolved components, are diffusing from the bulk phase and into the biofilm and vice versa. In the biofilm some of the substrates (*reactants*) will be transformed into new substrates (*products*) by the bacteria in the biofilm. If the number of substrates is n_l, the stoichiometry of the

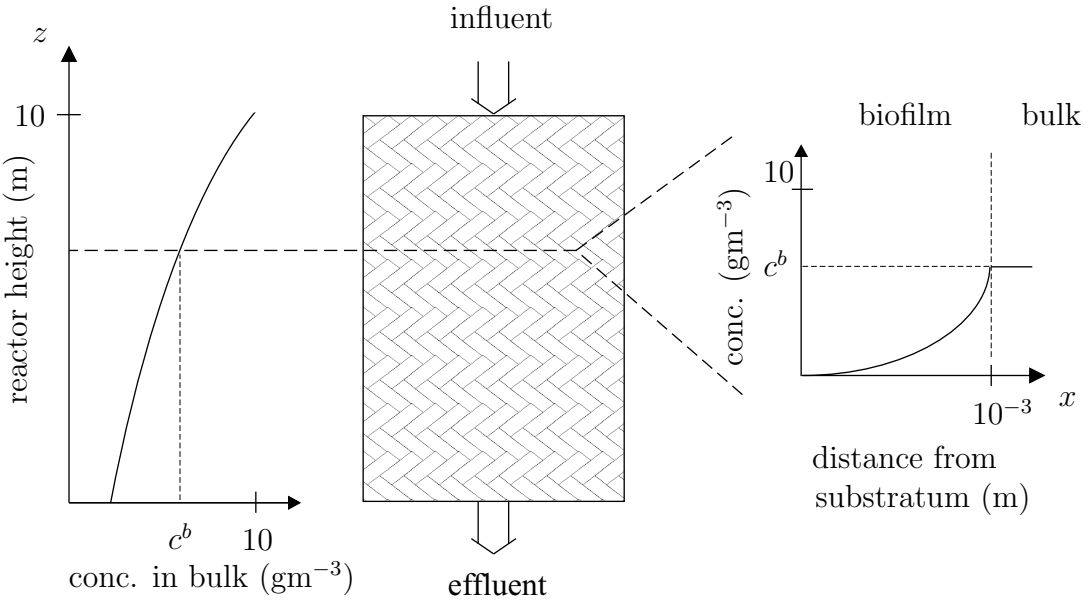

Figure 3.1 *Illustration of the concentration gradients in a trickling filter.*

transformations can be written

$$\begin{array}{ccc} \vartheta^r_{11}S_1 + \cdots + \vartheta^r_{1n_l}S_{n_l} & \longrightarrow & \vartheta^p_{11}S_1 + \cdots + \vartheta^p_{1n_1}S_{n_l} \\ \vdots & \vdots & \vdots \\ \vartheta^r_{n_s1}S_1 + \cdots + \vartheta^r_{n_sn_l}S_{n_l} & \longrightarrow & \vartheta^p_{n_s1}S_1 + \cdots + \vartheta^p_{n_sn_l}S_{n_l}, \end{array} \tag{3.1}$$

where S_i represents the substrates and ϑ^r_{ji} and ϑ^p_{ji} are stoichiometric coefficients.

The substrate transformations due to (3.1) cause a growth of the bacteria at a rate that can be expressed as

$$\rho_j(x)\epsilon_j(x,t)R_{j,1}(\mathbf{c}(x,t)), \quad 0 < x < L(t), \quad j = 1, \ldots n_s,$$

where $\mathbf{c}$ denotes a vector of all the substrate concentrations, $R_{j,1}$ is a positive rate expression, usually of the Monod type, L is the biofilm thickness, and $\rho_j\epsilon_j$ is the bacterial concentration. It is common to denote each bacterial concentration by X_j, but for easier interpretation it is expressed as a product of the bacterial density ρ_j and the volume fraction it is occupying, ϵ_j.

The bacteria undergo two more processes except growth, namely endogenous respiration and inactivation. Endogenous respiration is a mineralization of the bacteria that requires oxygen (Characklis 1990). The rate of the endogenous respiration is expressed as

$$\rho_j(x)\epsilon_j(x,t)R_{j,2}(\mathbf{c}(x,t)), \quad 0 < x < L(t), \quad j = 1, \ldots n_s,$$

where $R_{j,2}$ is a positive rate expression, e.g. a Monod expression with respect to the oxygen concentration.

The inactivation process describes the transformation process of the bacteria as they are transformed from active into inactive (*inert*) organic material. The rate of this transformation is expressed as

$$\rho_j(x)\epsilon_j(x,t)R_{j,3}(\mathbf{c}(x,t)), \quad 0 < x < L(t), \quad j = 1, \dots n_s,$$

where $R_{j,3}$ is usually equal to a positive inactivation rate coefficient for the bacteria, but the inactivation may also depend on toxic substances, for example.

The *observed specific growth rate* for the bacteria is

$$\mu_{o,j} = R_{j,1} - R_{j,2} - R_{j,3}, \quad j = 1, \dots n_s. \tag{3.2}$$

Since all the transformations are proportional to the amount of each species, the net growth rates of the solid materials can be expressed as

$$r_{vs,j} = \rho_j \epsilon_j \mu_{o,j}. \tag{3.3}$$

The net growth rate of the inert phase is only caused by inactivation:

$$r_{vs,n_s+1} = \sum_{j=1}^{n_s} \rho_j \epsilon_j R_{j,3}. \tag{3.4}$$

The production rates for the substrates are directly related to the bacterial growth and the stoichiometric relations given by (3.1) and can be expressed as

$$r_{v,i} = \sum_{j=1}^{n_s} \rho_j \epsilon_j \nu_{ji} \frac{R_{j,1}}{Y_j}, \quad 0 < x < L, \quad i = 1, \dots n_l, \tag{3.5}$$

where $\nu_{ji} = \vartheta^p_{ji} - \vartheta^r_{ji}$, and Y_j is a yield coefficient that relates the bacterial growth to the amounts transformed in the reaction (3.1). For oxygen, the rate of the consumptions in the endogenous respirations, i.e. $\sum_{j=1}^{n_s} \rho_j \epsilon_j R_{j,2}$, should be subtracted from the production rate (3.5).

Dissolved Components

The entire biofilm process model can be thought of as two integrated subsystems, one describing the concentrations of the n_l dissolved components in the biofilm, and another describing the distribution of the n_s solid phases in the biofilm. The subsystem describing the concentrations of the substrates is a diffusion-reaction problem given by Eqs. (3.6) to (3.11) below.

Fick's first law of diffusion in one dimension is assumed to describe the transport of substrates within the biofilm, i.e.,

$$J_i = -D_i \frac{\partial c_i}{\partial x}, \quad 0 < x < L, \quad i = 1, \dots n_l, \tag{3.6}$$

where J_i is the outward flux of substrate i, and D_i is the molecular diffusion coefficient for substrate i in the biofilm.

A mass balance for each substrate over an infinitesimal film segment dx gives (see Figure 1.5)

$$\epsilon_l \frac{\partial c_i}{\partial t} = -\frac{\partial}{\partial x} J_i + r_{v,i}, \tag{3.7}$$

which combined with Eq. (3.6) gives

$$\epsilon_l \frac{\partial c_i}{\partial t} = \frac{\partial}{\partial x}\left(D_i \frac{\partial c_i}{\partial x}\right) + r_{v,i}. \tag{3.8}$$

Except for initial conditions, two boundary conditions are needed for each substrate concentration in order to solve Eq. (3.8). The first arises from the fact that no substrates diffuse into the substratum, i.e.,

$$\frac{\partial}{\partial x} c_i(0,t) = 0. \tag{3.9}$$

If a boundary layer of depth L_w has developed on the surface of the biofilm, the second boundary condition can be written

$$J_i(L,t) = -\frac{D_i^b}{L_w}(c_i^b(t) - c_i(L,t)), \tag{3.10}$$

where D_i^b is the diffusion coefficient in the bulk and c_i^b is the bulk concentration. Horn and Hempel (1995) have compared the thickness of the boundary layer for different biofilms and different liquid flow velocities over the biofilm. Increased flow velocities decrease the boundary layer and improve the mass transfer into the biofilm (Kugaprasatham *et al.* 1992). Hence, it is advantageous to design and operate biofilm reactors such that the effects of the boundary layer can be ignored. The boundary condition is then

$$c_i(L,t) = c_i^b(t). \tag{3.11}$$

Solid Components

The second subsystem describing the distribution of solid material in the biofilm is given by Eqs. (3.12) to (3.15) below.

A mass balance analogous to (3.7) results in

$$\rho_j \frac{\partial \epsilon_j}{\partial t} = -\frac{\partial}{\partial x} J_{s,j} + r_{vs,j}, \qquad j = 1, \ldots n_s, \tag{3.12}$$

where $J_{s,j}$ is the flux of solid material from the substratum towards the biofilm surface. The flux is given by

$$J_{s,j} = u\rho_j\epsilon_j, \tag{3.13}$$

where u is the velocity (positive or negative) at which the solid material moves towards the biofilm surface. The velocity is equal to the sum of the expansions of the volume-fractions integrated from the substratum, i.e.,

$$u(x,t) = \int_0^x \frac{1}{1-\epsilon_l(x')} \sum_{j=1}^{n_s+1} \frac{r_{vs,j}(x',t)}{\rho_j(x')} dx'. \tag{3.14}$$

The entire biofilm problem is an example of a moving boundary problem since the thickness of the film varies with time according to

$$\frac{dL(t)}{dt} = u(L(t),t) - f(L(t),Q(t),t), \tag{3.15}$$

where Q is the flow of bulk liquid over the biofilm surface. The function f describes, in general terms, the erosion minus the adsorption of solid material at the biofilm surface (see Figure 1.1). In most applications the erosion is larger than the adsorption and hence the function f can be considered as a net erosion function. Generally, the erosion tends to increase with increasing film thickness and also with increasing bulk flow due to increased shear. It has also been observed that higher fluid velocities during a longer period make the biofilm less inclined to erode (Debus *et al.* 1994). Incorporated in the time argument is the dependence on various factors, e.g., biofilm density, age of the biofilm and sloughing. As long as the erosion exceeds the adsorption no boundary condition at $x = L$ is necessary. However, if that is not the case, an additional boundary condition at the biofilm surface is required (Gujer and Wanner 1990).

Due to the no flux condition at the substratum and a non-negative flux of solids out of the biofilm, only the initial condition on the biofilm thickness and the initial distribution of solid materials in the biofilm remain for the solution of the second subsystem. Combining the two subsystems defines the general dynamic biofilm model.

Spherical and Cylindrical Substrata

In packed beds, for example, pellet beads are often used as biofilm support. If the radius of the pellets is large relative to the biofilm thickness the substratum can be assumed planar and the presented biofilm model can be used. However, if this is not the case we have to account for the dependence of the biofilm volume on the radius in the derivation of the mass balances.

Assuming the biofilm is of thickness L and is attached to a sphere of radius R (see Figure 3.2), the mass balance (3.8) should be replaced by

$$\epsilon_l \frac{\partial c_i}{\partial t} = \frac{2}{r} D_i \frac{\partial c_i}{\partial r} + \frac{\partial}{\partial r}\left(D_i \frac{\partial c_i}{\partial r} \right) + r_{v,i}, \qquad R < r < L, \tag{3.16}$$

where r is the radial distance from the center of the sphere. The boundary conditions at $x = 0$ and $x = L$ for Eq. (3.8) should now be applied to $r = R$ and $r = L$. All

the rate expressions are the same as for planar coordinates, though the independent variable x should be replaced by r.

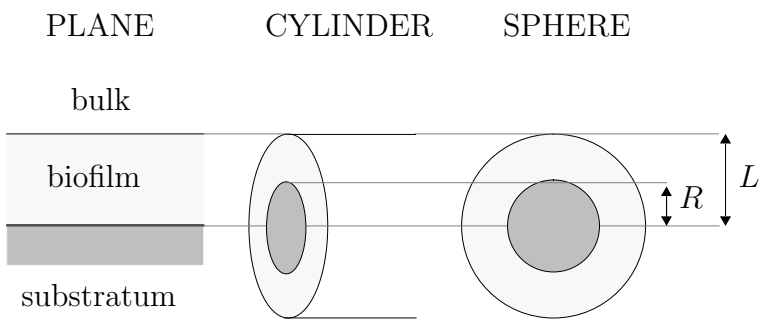

Figure 3.2 *Illustration of biofilm and biofilm substrata.*

Similarly, the mass balance for the solid components (3.12) become

$$\rho_j \frac{\partial \epsilon_j}{\partial t} = -\frac{2}{r} J_{s,j} - \frac{\partial}{\partial r} J_{s,j} + r_{vs,j}, \qquad R < r < L. \tag{3.17}$$

Since the volume expansions depend on the radial distance, also the expression (3.14) for u is changed:

$$u(r,t) = \frac{1}{r^2} \int_R^r \frac{(r')^2}{1-\epsilon_l(r')} \sum_{j=1}^{n_s+1} \frac{r_{vs,j}(r',t)}{\rho_j(r')} dr'. \tag{3.18}$$

If the substratum is assumed to be an infinite cylinder Eqs. (3.16), (3.17) and (3.18) should be replaced by

$$\epsilon_l \frac{\partial c_i}{\partial t} = \frac{1}{r} D_i \frac{\partial c_i}{\partial r} + \frac{\partial}{\partial r}\left(D_i \frac{\partial c_i}{\partial r} \right) + r_{v,i}, \qquad R < r < L, \tag{3.19}$$

$$\rho_j \frac{\partial \epsilon_j}{\partial t} = -\frac{1}{r} J_{s,j} - \frac{\partial}{\partial r} J_{s,j} + r_{vs,j}, \qquad R < r < L, \tag{3.20}$$

$$u(r,t) = \frac{1}{r} \int_R^r \frac{r'}{1-\epsilon_l(r')} \sum_{j=1}^{n_s+1} \frac{r_{vs,j}(r',t)}{\rho_j(r')} dr' \qquad R < r < L. \tag{3.21}$$

3.3 Extensions

There is no end to how complex models of biological systems can be made. The complexity must be chosen with respect to the application, the computational effort, and the actual system knowledge. As mentioned on page 19, it is crucial in the derivation of the presented model to consider averaging quantities, such as concentrations

and volume fractions. To avoid some of the aggregation, and actually model biofilm inhomogeneities directly, the model has to be made three-dimensional in space, or at least two-dimensional. At present, the knowledge of two- or three-dimensional structures of biofilms is too limited to be formalized. The necessary computational effort also makes such extensions infeasible today. There are, however, some experimental findings concerning biofilm heterogeneity that can be incorporated in the biofilm model without considerably increasing the numerical complexity. The number of model parameters increases, though.

Particulate Motion

As presented, the model predicts movements of particulate matter only in the direction of the velocity u. Generally, this velocity is positive in the entire biofilm, which implies that particulate matter is forced outwards. Drury *et al.* (1993) and van Benthum *et al.* (1995) found that fluorescent micro-beads added to a biofilm reactor may penetrate the biofilm, which contradicts the solid movements predicted by the model. It appears likely that the same movements apply to microbial cells as well (de Beer and Stoodley 1995). Wanner and Reichert (1996) suggest that the observed phenomena can be modeled by simultaneous attachment and detachment of particulates in combination with diffusion of solid components. Due to the diffusion the solid flux (3.13) then becomes

$$J_{s,j} = u\rho_j\epsilon_j - D_{s,j}\frac{\partial}{\partial x}\rho_j\epsilon_j,$$

where $D_{s,j}$ is an effective diffusion coefficient that is much smaller than the coefficient of molecular diffusion of cells and particles in water.

Since the diffusion causes a mixing, with respect to the independent variable, of particulate matter, this implies that adsorbed matter on the biofilm surface is partly diffusing into the biofilm. Hence, a boundary condition for each solid phase is needed at the biofilm surface. Though probably negligible, the advective flux of dissolved components in the intra-cellular water of the moving solid phases has to be considered in Eq. (3.8) to achieve formally correct mass balances.

Convection of Dissolved Components

Existence of large pores in the biofilm will cause the dissolved components to reach deeper inside the biofilm in surroundings of the pores than Fickian diffusion may explain (de Beer and Stoodley 1995). Recalling that we only consider averaging properties parallel to the substratum, we may sometimes approximate this heterogeneity by adding a convective term to the mass balance for dissolved components. The flux of dissolved components then becomes

$$J_i = k_c c_i - D_i\frac{\partial c_i}{\partial x},$$

where k_c determines the convective flux. This results in a model for the dissolved components in principal equal to those used for large-pore catalytic particles (Rodrigues *et al.* 1991).

Varying Biofilm Density

During biofilm formation an initial transient decrease in biofilm density has been observed (Zhang and Bishop 1994*b*). The reasons may be changes in biofilm composition, i.e. changes in species and amount of inactive material, and changes in biofilm porosity. In a longer perspective the density may increase again as the biofilm matures. As mentioned earlier, the density also tends to increase with increasing shear forces. Partly, such changes can be explained by changes in biofilm composition. However, Wanner and Reichert (1996) conclude that the changes are related to variable porosity, a phenomenon observed by Zhang and Bishop (1994*a*). The extended biofilm model in the software AQUASIM offers the user to define ϵ_l as a state variable and to specify a space and time dependent expression for its time derivative.

All the extensions discussed here concern the physics in the biofilm model. In Section 8.5 it is discussed how the model can be extended to describe other microbial transformations than growth, endogenous respiration and inactivation.

3.4 Simplifications

The presented model may naturally be significantly simplified, though only the most common simplifying assumptions are commented on here. They are believed not to alter qualitative results and are "motivated" by lack of better understanding, and to reduce the number of uncertain parameters. The numerics also become slightly simpler.

Instead of assumptions **A7** and **A8** on page 19 the following assumptions are commonly used:

A7 The transport of dissolved components is by Fickian diffusion and the diffusion coefficients are proportional to the corresponding values in the bulk, i.e.,

$$D_i = f D_i^b, \quad i = 1, \ldots n_l,$$

where f is a constant.

A8a The volume fraction of the liquid phase is constant.

A8b The densities of the solid phases are constant.

In a number of studies, it has been evident that there is no universal constant f (Wanner 1995). Typical values range from 0.3 to 0.9, and there is also evidence that f may vary with depth in the biofilm (Fu *et al.* 1994).

The porosity probably varies with distance from the substratum as well, depending on the composition and the operating conditions. Zhang and Bishop (1994*a*) and (1994*b*), have found significant variations in porosity and total density over the depth of biofilms. However, the biofilms investigated were heterotrophic biofilms that had been rapidly grown and may not be covered by the continuum assumption **A1**. In simulations of a heterotrophic-autotrophic biofilm Wanner and Reichert (1996) found that spatial gradients in the porosity did not significantly change the fluxes of dissolved components into the biofilm.

Densities of bacterial species should be specific for each species and, therefore, should not vary much with time and distance from the the substratum.

Time-Scale Separation

Often, there is a natural time-scale separation in biofilm systems (Kissel *et al.* 1984). Writing the model equations in non-dimensional form we can deduce that the characteristic times of the mass balance for dissolved components in the biofilm is typically in the order of a few minutes while the characteristic times for the solid phase mass balances are in the order of days. In other words; it takes a few minutes for substrate concentrations to reach nearly steady-state profiles after changes in bulk concentrations, while it takes days for changes in the bacterial concentrations to settle.

The reactor hydraulics often have residence times in the order of minutes, tenths of minutes, or possibly hours. This means that when we are interested only in short term behavior we may assume constant bacterial concentrations. Conversely, we may solve the mass balance equation (3.8) and the mass balance equations for dissolved components in the reactor in steady state when we are only interested in the long term behavior of the plant. These simplifications are exploited in the next few chapters.

3.5 A Nitrifying Biofilm Model

Nitrification of ammonium refers to the oxidization of ammonium (NH_4^+) into nitrate (NO_3^-). In biological systems the nitrification is carried out in two steps. First ammonium is oxidized into nitrite (NO_2^-) by bacteria commonly generalized as the species *Nitrosomonas*:

$$NH_4^+ + \frac{3}{2}O_2 \rightarrow NO_2^- + H_2O + 2H^+. \tag{3.22}$$

The acid produced is neutralized by a reduction of the alkalinity, which is measured as bicarbonate (HCO_3^-) equivalents:

$$2H^+ + 2HCO_3^- \rightarrow 2CO_2 + 2H_2O. \tag{3.23}$$

Bacteria that have been generalized as the species *Nitrobacter*, further oxidize the nitrite into nitrate according to:

$$NO_2^- + \frac{1}{2}O_2 \rightarrow NO_3^-. \tag{3.24}$$

Recent research by Burrell *et al.* (1998) shows that the nitrite oxidization may be carried out by *Nitrospira*, and not *Nitrobacter*. Nevalainen *et al.* (1993) concluded from electron micro-graphs that the morphologies of the ammonium oxidizers in their nitrifying biofilms were similar to the species *Nitrosomonas, Nitrosospira* and *Nitrosolobus*. However, from our modeling point of view it is only the aggregated behavior of the bacteria that is important. In wastewater systems the division of the nitrifying species into *Nitrosomonas* and *Nitrobacter* is well established with numerous experiments showing fairly consistent behavior of the bacteria. Variables and parameters referring to ammonium oxidizers will be denoted by subscript *ao*, and for the nitrite oxidizers the subscript *no* will be used. Literature values are those of the species *Nitrosomonas* and *Nitrobacter* (see Appendix B).

The growth rate of the ammonium oxidizers depends on the concentrations of ammonium and oxygen. It also depends significantly on the pH with a flat optimum around 8-9 (Henze *et al.* 1990). Approximations of the pH can be calculated from the alkalinity, concentrations of carbon dioxide and equilibrium relations (Flora *et al.* 1993, Motta 1995, Flora *et al.* 1995). In many systems, though, the alkalinity and pH are strongly correlated. We therefore choose to consider only the alkalinity and assign the following triple Monod expression for the growth rate:

$$R_{1,1} = \mu_{m,ao} \frac{c_{O_2}}{K_{O_2,ao} + c_{O_2}} \frac{c_{NH_4}}{K_{NH_4} + c_{NH_4}} \frac{c_{HCO_3}}{K_{HCO_3} + c_{HCO_3}}.$$

With this expression the rate will increase with increasing alkalinity, which corresponds to an increase of the pH. This is typically observed in municipal wastewater systems, where the pH is less than the optimum.

According to Balmelle *et al.* (1992) the maximum growth rate for the nitrite oxidizers is fairly independent of pH between 6.5 and 9. At pH less than 6, they found a significant inhibition in the oxidization, which agrees with data from a pilot plant nitrifying trickling filter at Rya WWTP (Wik 1993). However, we assume the interval pH 6.5 to pH 9 covers the operating range and assign the following double Monod expression for the growth of nitrite oxidizers:

$$R_{2,1} = \mu_{m,no} \frac{c_{O_2}}{K_{O_2,no} + c_{O_2}} \frac{c_{NO_2}}{K_{NO_2} + c_{NO_2}}.$$

To account for the dependency of the rates of the endogenous respirations on the oxygen concentration, the rates are expressed as

$$R_{1,2} = b_{ao} \frac{c_{O_2}}{K_{O_2} + c_{O_2}} \qquad \text{and} \qquad R_{2,2} = b_{no} \frac{c_{O_2}}{K_{O_2} + c_{O_2}}.$$

The inactivation rates are set equal to the inactivation rate coefficients, i.e.

$$R_{1,3} = k_{I,ao} \qquad \text{and} \qquad R_{2,3} = k_{I,no}. \tag{3.25}$$

The above rate expressions and Eq. (3.2) to Eq. (3.5) can be summarized in a matrix form similar to those used in modeling of suspended-culture systems (see Table 3.1). Note that the stoichiometric coefficients ν_{ki} are not equal to those in Eq. (3.5) and that the units are gO_2m^{-3} for oxygen, gN m^{-3} for ammonium and nitrite, and mole $HCO_3^- m^{-3}$ for the alkalinity. All parameter values are summarized in Appendix B. With the chosen values of Y_{ao} and Y_{no}, the stoichiometry of the nitrification equals that found by Wezernak and Gannon (1967).

3.6 Conclusions and Discussion

A general dynamic model of fixed biofilms has been formulated. The model, which is based on mass balances, describes in mathematical terms the transportation phenomena inside the biofilm as well as bacterial processes that cause the population dynamics.

The main assumption in the derivation is an aggregation of the states parallel to the substratum. Its validity relies on the biofilm being fairly smooth and continuous. In the last few years experimental findings of biofilm heterogeneity show that in many cases this assumption is obsolete. However, it seems as if the assumption is relevant for mature biofilms exposed to moderate substrate loads and shear forces if the biofilm growth is approximately balanced by the erosion. Since this is often the case in many biofilm reactors, the modeling problems associated with biofilm heterogeneity may not be as severe as sometimes claimed.

The presented model has been illustrated by applying it to an autotrophic nitrifying biofilm.

Table 3.1 *Stoichiometric coefficients and process rates for nitrifiers*

Process (k)	Solids (j) (ν_{kj})			Substrates (i) (ν_{ki})				Rate
	ao	no	$inert$	O_2	NH_4^+	HCO_3^-	NO_2^-	R_k
Growth (ao)	1			$\frac{Y_{ao}-3.43}{Y_{ao}}$	$\frac{-1}{Y_{ao}}$	$\frac{-1}{7Y_{ao}}$	$\frac{1}{Y_{ao}}$	$\rho_1\epsilon_1\mu_{m,ao}\frac{c_{O_2}}{K_{O_2,ao}+c_{O_2}}\frac{c_{NH_4}}{K_{NH_4}+c_{NH_4}}\frac{c_{HCO_3}}{K_{HCO_3}+c_{HCO_3}}$
Growth (no)		1		$\frac{Y_{no}-1.14}{Y_{no}}$			$\frac{-1}{Y_{no}}$	$\rho_2\epsilon_2\mu_{m,no}\frac{c_{O_2}}{K_{O_2,no}+c_{O_2}}\frac{c_{NO_2}}{K_{NO_2}+c_{NO_2}}$
Respiration (ao)	-1			-1				$\rho_1\epsilon_1 b_{ao}\frac{c_{O_2}}{K_{O_2}+c_{O_2}}$
Respiration (no)		-1		-1				$\rho_2\epsilon_2 b_{no}\frac{c_{O_2}}{K_{O_2}+c_{O_2}}$
Inactivation (ao)	-1		1					$\rho_1\epsilon_1 k_{I,ao}$
Inactivation (no)		-1	1					$\rho_2\epsilon_2 k_{I,no}$

Solid net growth rate: $r_{vs,j}=\sum_{k=1}^{6}\nu_{kj}R_k, \quad j=1,2,3$ (ao, no, $inert$)

Substrate production rate: $r_{v,i}=\sum_{k=1}^{6}\nu_{ki}R_k, \quad i=$ O_2, NH_4, HCO_3, NO_2

Chapter 4

STEADY-STATE BIOFILMS

Solving the general multi-species biofilm model in a true steady state requires that the boundary conditions for the solid phases at the substratum are known. In the dynamic model no such boundary conditions are explicitly formulated. By analyzing the equations at the substratum it is shown that the boundary conditions can be divided into groups where the steady-state solutions either allow bacterial coexistence or result in complete depletion of some bacterial species. A rapid solution method using an ordinary differential and algebraic equation solver is presented. By simulations it is shown that not only the substrate bulk concentrations, but also the biofilm thickness, determine if different bacteria may coexist or not.

There are several advantages in looking at the steady-state biofilm problem. Dynamic simulations will generally tend towards the steady-state solution and it is only in the steady state that the results can be unique for a given set of conditions for the biofilm. With the steady-state solution available, the time required for initializing dynamic simulations will in most cases be considerably shortened as well.

In many applications of multi-species biofilm models there is a competition between different types of bacteria within the biofilm. The situation that is by far the most studied is a biofilm in which autotrophic nitrifying bacteria are competing for space and oxygen with heterotrophic bacteria living on biodegradable organic materials (Fruhen *et al.* 1991, Gadani *et al.* 1993, Kissel *et al.* 1984, Rittmann and Manem 1992, Wanner 1989, Wanner and Gujer 1986).

The material in this chapter is mainly based on the investigations by Wik and Breitholtz (1996). Prior to these investigations, the case of a multi-species biofilm model in the steady state had not yet been thoroughly investigated. The case of competition between heterotrophic and autotrophic bacteria had been solved by relaxation using a dynamic model by Gadani *et al.* (1993), and with a simplified steady state model by Rittmann and Manem (1992). A few solutions with a method similar to shooting and matching were reported early for fixed film thickness, no endogenous respiration and the same case of competition (Wanner and Gujer 1984). Wik

and Breitholtz (1996) attacked the problem of finding a more general and efficient method for solving the biofilm problem with endogenous respiration and varying biofilm thickness, which had not yet been fully addressed. This was, probably, due to the fact that the boundary conditions for the distribution of the bacterial concentrations at the biofilm substratum depend on the prevailing conditions in the entire biofilm. Hence, ordinary integration methods cannot be used for solving the problem from the substratum to the biofilm surface. However, the problem, being based on physical phenomena, has a solution that can be found by means of boundary value solvers combined with algebraic equation solvers if the boundary conditions are correctly formulated.

4.1 Model Equations

The dynamic biofilm model presented in the previous chapter generally results in a stiff system of equations. This is due to the large difference in characteristic time for the two subsystems (Kissel *et al.* 1984). The substrate concentration profiles inside the biofilm are usually established within minutes, while the bacterial concentrations typically require days or weeks to stabilize. Depending on which characteristic time is of interest, either the first subsystem that describes the substrate concentrations is assumed to be in the steady state, or the second subsystem that describes the bacterial distribution is assumed to be constant. For a biofilm in a true steady state, both subsystems have to be in a steady state.

The solution to the first subsystem is then given by setting the time derivative in Eq. (3.8) to zero, i.e.,

$$D_i \frac{d^2 c_i}{dx^2} + \frac{dD_i}{dx}\frac{dc_i}{dx} = -r_{v,i}, \qquad 0 \le x \le L, \quad i = 1, \dots n_l, \tag{4.1}$$

and by solving this equation with boundary conditions (3.9) and (3.10), or (3.9) and (3.11).

Differentiating Eq. (3.14) and inserting Eq. (3.4) give us

$$\frac{d}{dx}u = \frac{1}{1-\epsilon_l}\left(\sum_{j=1}^{n_s}\frac{r_{vs,j}}{\rho_j} + \frac{\rho_j \epsilon_j R_{j,3}}{\rho_{n_s+1}}\right) \tag{4.2}$$

$$u(0) = 0. \tag{4.3}$$

Let

$$\varphi_j = \frac{\rho_j}{\rho_{n_s+1}} R_{j,3}, \qquad j = 1, \dots n_s.$$

Using Assumption **A8b** in Section 3.4, setting the time derivative to zero and applying the chain rule to Eq. (3.12), after insertion of Eqs. (3.13) and (4.2), give

$$\frac{d\epsilon_j}{dx} = \frac{\epsilon_j}{u(1-\epsilon_l)}\left(\mu_{o,j}(1-\epsilon_l) - \sum_{k=1}^{n_s}\epsilon_k(\mu_{o,k} + \varphi_k)\right), \quad j = 1, \dots n_s. \tag{4.4}$$

Eqs. (4.2), and (3.15) in the steady state give the biofilm thickness from:

$$f = u(L). \tag{4.5}$$

The second subsystem in the steady state is given by Eqs. (4.2) to (4.5) above. However, for the existence of a unique solution the n_s degrees of freedom in Eq. (4.4) have to be fixed.

From the assumption of continuity at the boundary $x = 0$, and the fact that $u(0,t) = 0$, the equations describing the proportions of the bacteria at the substratum can be derived as follows: Insert (3.13) and (3.14) in (3.12) and apply the chain rule. This gives the following ordinary differential equation at the substratum:

$$\left[\frac{\partial \epsilon_j}{\partial t}\right]_{x=0} = \epsilon_j(0,t)\left(\mu_{o,j} - \frac{1}{1-\epsilon_l}\sum_{k=1}^{n_s}\epsilon_k(\mu_{o,k}+\varphi_k)\right). \tag{4.6}$$

Hence, the required steady-state boundary conditions for Eq. (4.4) at the biofilm substratum are given by

$$\epsilon_j(0,t)\left(\mu_{o,j} - \frac{1}{1-\epsilon_l}\sum_{k=1}^{n_s}\epsilon_k(\mu_{o,k}+\varphi_k)\right) = 0, \quad j = 1,\dots n_s, \tag{4.7}$$

which shows that either ϵ_j is zero or $\mu_{o,j}$ is independent of j. In other words, all species existing at the substratum in a steady state biofilm have equal observed specific growth rates. This fixates all remaining degrees of freedom in the system.

A Two-Species Biofilm in a Steady State

From here on, two-species biofilm models are used to illustrate biofilms in the steady state. For a two-species biofilm we have $n_s = 2$ and three different solid phases; two different types of bacteria (subscript 1 and 2), and inert material (subscript 3). Writing Eq. (4.4) for all indices gives

$$\frac{d\epsilon_1}{dx} = \frac{\epsilon_1}{u(1-\epsilon_l)}\left[\mu_{o,1}(1-\epsilon_l) - \epsilon_1(\mu_{o,1}+\varphi_1) - \epsilon_2(\mu_{o,2}+\varphi_2)\right] \tag{4.8}$$

$$\frac{d\epsilon_2}{dx} = \frac{\epsilon_2}{u(1-\epsilon_l)}\left[(\mu_{o,2}(1-\epsilon_l) - \epsilon_1(\mu_{o,1}+\varphi_1) - \epsilon_2(\mu_{o,2}+\varphi_2)\right]. \tag{4.9}$$

Equation (4.7) gives two different categories of boundary conditions, namely solutions corresponding to a coexistence of the two different types of bacteria (A), and

solutions where either one or both types of bacteria are spaced out (B):

$$(A) \qquad \begin{cases} \epsilon_1(\mu_{o,1}+\varphi_1)+\epsilon_2(\mu_{o,2}+\varphi_2)=\mu_{o,1}(1-\epsilon_l) \\ \mu_{o,1}=\mu_{o,2} \end{cases}$$

$$(B1) \qquad \epsilon_1=0, \qquad \epsilon_2=(1-\epsilon_l)\frac{\mu_{o,2}}{\mu_{o,2}+\varphi_2}$$

$$(B2) \qquad \epsilon_2=0, \qquad \epsilon_1=(1-\epsilon_l)\frac{\mu_{o,1}}{\mu_{o,1}+\varphi_1}$$

$$(B3) \qquad \epsilon_1=0, \qquad \epsilon_2=0.$$

Note that (A) only gives a linear dependence between ϵ_1 and ϵ_2 beside the rather natural condition that the observed specific growth rate for the two types of bacteria should be equal. The linear dependence leaves 1 degree of freedom for the second subsystem. However, the condition $\mu_{o,1}=\mu_{o,2}$ decreases the degree of freedom for the first subsystem by one, i.e., a relation between at least two substrate concentrations at the substratum holds.

Quite an efficient way of determining the steady-state solution of the first subsystem is to use a shooting and matching routine (Kissel *et al.* 1984, Wik and Lindeborg 1994). In such routines the substrate concentrations at the substratum are initially guessed and Eq. (3.8) is integrated to the biofilm surface where the solution is compared to the boundary conditions there. A Newton method is then used to find better guesses for the substrate concentrations at the substratum. This method can be extended to solve the case when the volume fractions in the biofilm are also in the steady state, and case (A) holds. A guess is then made of one of the bacterial volume fractions at the substratum and one of the substrate concentrations is eliminated from the condition $\mu_{o,1}=\mu_{o,2}$. Simultaneous integration of Eqs. (3.8), (4.2), (4.8) and (4.9) and a comparison of the solution at the biofilm surface with the boundary conditions on the substrate concentrations and Eq. (3.15) will, together with the matching process described above, yield the solution. This is exemplified in a later section.

4.2 Stability

We now have four possible sets of boundary conditions: (A), $(B1)$, $(B2)$ and $(B3)$. By investigating the stability of these equilibrium points we may conclude if they have any physical meaning or not, and also if all of them are valid as steady state solutions. To find the possible criteria for the stability of each equilibrium point we chose to study Eq. (4.6) solely, i.e., what happens in the rest of the biofilm is not

considered. Throughout this section the following notation is used:

$$\begin{aligned} \epsilon_{10} &= \epsilon_1(0,0), & \epsilon_1 &= \epsilon_1(0,t) \\ \epsilon_{20} &= \epsilon_2(0,0), & \epsilon_2 &= \epsilon_2(0,t) \\ \epsilon_{30} &= \epsilon_3(0,0), & \epsilon_3 &= \epsilon_3(0,t). \end{aligned}$$

Writing Eq. (4.6) for each subscript, we get

$$\dot{\epsilon}_1 = -\frac{\epsilon_1}{1-\epsilon_l}[\epsilon_1(\mu_{o,1}+\varphi_1)+\epsilon_2(\mu_{o,2}+\varphi_2)]+\epsilon_1\mu_{o,1} \tag{4.10}$$

$$\dot{\epsilon}_2 = -\frac{\epsilon_2}{1-\epsilon_l}[\epsilon_1(\mu_{o,1}+\varphi_1)+\epsilon_2(\mu_{o,2}+\varphi_2)]+\epsilon_2\mu_{o,2}. \tag{4.11}$$

Further, we have

$$\begin{aligned} \dot{\epsilon}_3 &= -\dot{\epsilon}_1-\dot{\epsilon}_2 \\ &= -\frac{\epsilon_3}{1-\epsilon_l}[\epsilon_1(\mu_{o,1}+\varphi_1)+\epsilon_2(\mu_{o,2}+\varphi_2)]+\epsilon_1\varphi_1+\epsilon_2\varphi_2, \end{aligned} \tag{4.12}$$

since $\epsilon_1+\epsilon_2+\epsilon_3+\epsilon_l=1$ and ϵ_l is assumed time invariant.

When the stability of these equations is analyzed the obstacle is that $\mu_{o,1}$ and $\mu_{o,2}$ may vary with time. However, with some physical insight it seems natural that if the observed specific growth rate is negative, then the bacteria should diminish, i.e., (B) should hold in the steady state. Therefore, we begin by assuming $\mu_{o,1}\le 0$ and $\mu_{o,2}\le 0$. Noting that φ_1 and φ_2 are always positive, we get from (4.12)

$$\begin{aligned} (1-\epsilon_l)\dot{\epsilon}_3 &= (\epsilon_1\varphi_1+\epsilon_2\varphi_2)(1-\epsilon_l)-\epsilon_3[\epsilon_1(\mu_{o,1}+\varphi_1)+\epsilon_2(\mu_{o,2}+\varphi_2)] \\ &= \epsilon_1\varphi_1(1-\epsilon_l-\epsilon_3)+\epsilon_2\varphi_2(1-\epsilon_l-\epsilon_3)-\epsilon_3(\epsilon_1\mu_{o,1}+\epsilon_2\mu_{o,2}) \\ &= (\epsilon_1\varphi_1+\epsilon_2\varphi_2)(\epsilon_1+\epsilon_2)-\epsilon_3(\epsilon_1\mu_{o,1}+\epsilon_2\mu_{o,2})\ge 0, \end{aligned}$$

where equality holds if and only if $\epsilon_1=0$ and $\epsilon_2=0$, i.e., $(B3)$ is an asymptotically stable equilibrium point provided that $\mu_{o,1}\le 0$ and $\mu_{o,2}\le 0$.

Next, assume $\mu_{o,2}\le 0$ and $\mu_{o,1}>0$. From (4.11) we get

$$\begin{aligned} (1-\epsilon_l)\dot{\epsilon}_2 &= \epsilon_2[\mu_{o,2}(1-\epsilon_l)-\epsilon_1(\mu_{o,1}+\varphi_1)-\epsilon_2(\mu_{o,2}+\varphi_2)] \\ &\le \epsilon_2(\mu_{o,2}(1-\epsilon_l-\epsilon_2)-\epsilon_1\mu_{o,1}) \\ &= \epsilon_2(\mu_{o,2}(\epsilon_1+\epsilon_3)-\epsilon_1\mu_{o,1}) \\ &= \epsilon_2(\epsilon_1(\mu_{o,2}-\mu_{o,1})+\mu_{o,2}\epsilon_3)\le 0, \end{aligned}$$

where equality holds if and only if $\epsilon_2=0$. Hence $\epsilon_2\to 0$ as $t\to\infty$.

From (4.10) it follows that

$$(1-\epsilon_l)\dot{\epsilon}_1 > 0 \quad \text{if} \quad \epsilon_1 < \frac{(1-\epsilon_l)\mu_{o,1}}{\mu_{o,1}+\varphi_1}-\epsilon_2\frac{\mu_{o,2}+\varphi_2}{\mu_{o,1}+\varphi_1} \qquad \text{and}$$

$$(1-\epsilon_l)\dot{\epsilon}_1 < 0 \quad \text{if} \quad \epsilon_1 > \frac{(1-\epsilon_l)\mu_{o,1}}{\mu_{o,1}+\varphi_1}-\epsilon_2\frac{\mu_{o,2}+\varphi_2}{\mu_{o,1}+\varphi_1}.$$

Thus, as long as $\mu_{o,1} > 0$ and $\mu_{o,2} \leq 0$, $(B2)$ is an asymptotically stable equilibrium point. In exactly the same manner, it is readily deduced that if $\mu_{o,1} \leq 0$ and $\mu_{o,2} > 0$, then $(B1)$ is an asymptotically stable equilibrium point.

It still remains to derive which equilibrium point is valid if both the observed specific growth rates are positive. Let us study the solutions to (4.10) and (4.11) in the (ϵ_1, ϵ_2) plane. If we set $\epsilon_2 = 0$, it follows from (4.10) that

$$\begin{aligned} \dot{\epsilon}_1 < 0 \quad \text{if} \quad \epsilon_1 > \frac{\mu_{o,1}(1-\epsilon_l)}{\mu_{o,1}+\varphi_1}, \\ \dot{\epsilon}_1 > 0 \quad \text{if} \quad \epsilon_1 < \frac{\mu_{o,1}(1-\epsilon_l)}{\mu_{o,1}+\varphi_1}, \end{aligned}$$

and $\dot{\epsilon}_1 = 0$ if and only if either

$$\epsilon_1 = 0 \quad \text{or} \quad \epsilon_1 = \mu_{o,1}\frac{1-\epsilon_l}{\mu_{o,1}+\varphi_1}.$$

Hence, all solutions will tend toward $(B2)$ on the axis $\epsilon_2 = 0$ if $\epsilon_{10} > 0$. By studying (4.11) we can, in the same manner, deduce that all solutions on the axis $\epsilon_1 = 0$ converge toward $(B1)$ if $\epsilon_{20} > 0$. Incidentally, there exist analytical solutions on the axes if $\mu_{o,1}$ and $\mu_{o,2}$ are time invariant:

$$\epsilon_1 = \frac{\mu_{o,1}\epsilon_{10}}{\epsilon_{10}\frac{\mu_{o,1}+\varphi_1}{1-\epsilon_l}[1-\exp(-\mu_{o,1}t)] + \mu_{o,1}\exp(-\mu_{o,1}t)} \tag{4.13}$$

$$\epsilon_2 = \frac{\mu_{o,2}\epsilon_{20}}{\epsilon_{20}\frac{\mu_{o,2}+\varphi_2}{1-\epsilon_l}[1-\exp(-\mu_{o,2}t)] + \mu_{o,2}\exp(-\mu_{o,2}t)}. \tag{4.14}$$

These solutions give us an idea of the settling times. They may also be used directly for thin mono-cultural biofilms because $\mu_{o,1}$ and $\mu_{o,2}$ are then more or less equal over the depth of the biofilm.

Now, assume $\mu_{o,1} > \mu_{o,2} > 0$ and define line l_1 by setting $\dot{\epsilon}_1 = 0$ in (4.10), i.e.,

$$\mu_{o,1} - \frac{\mu_{o,2}+\varphi_2}{1-\epsilon_l}\epsilon_2 - \frac{\mu_{o,1}+\varphi_1}{1-\epsilon_l}\epsilon_1 = 0, \tag{4.15}$$

and line l_2 by setting $\dot{\epsilon}_2 = 0$ in (4.11), i.e.,

$$\mu_{o,2} - \frac{\mu_{o,1}+\varphi_1}{1-\epsilon_l}\epsilon_1 - \frac{\mu_{o,2}+\varphi_2}{1-\epsilon_l}\epsilon_2 = 0. \tag{4.16}$$

The positive quadrant of the (ϵ_1, ϵ_2) plane is divided into the three areas Ω_1, Ω_2, and Ω_3 by lines l_1 and l_2 (see Figure 4.1). By studying the tangential directions in these areas we get a picture of the general behavior of the solutions. On line l_1 we have $\dot{\epsilon}_1 = 0$ and by inserting (4.15) into (4.11) we get

$$\dot{\epsilon}_2 = \epsilon_2(\mu_{o,2} - \mu_{o,1}) < 0.$$

Similarly, on line l_2 we have $\dot{\epsilon}_2 = 0$ and by inserting (4.16) into (4.10) we get

$$\dot{\epsilon}_1 = \epsilon_1(\mu_{o,1} - \mu_{o,2}) > 0.$$

A study of (4.10) and (4.11) readily verifies that

$$\begin{array}{llll} \dot{\epsilon}_1 > 0 & \text{and} & \dot{\epsilon}_2 > 0 & \text{if} \quad (\epsilon_1, \epsilon_2) \in \Omega_1 \\ \dot{\epsilon}_1 > 0 & \text{and} & \dot{\epsilon}_2 < 0 & \text{if} \quad (\epsilon_1, \epsilon_2) \in \Omega_2 \\ \dot{\epsilon}_1 < 0 & \text{and} & \dot{\epsilon}_2 < 0 & \text{if} \quad (\epsilon_1, \epsilon_2) \in \Omega_3. \end{array}$$

From the phase portrait (frozen time) in Figure 4.1, we see that all the solutions converge toward $(B2)$ as long as $\epsilon_{10} > 0$. Thus, if $\mu_{o,1} > 0$ and $\mu_{o,1} > \mu_{o,2}$, the steady-state solution for the boundary conditions is $(B2)$.

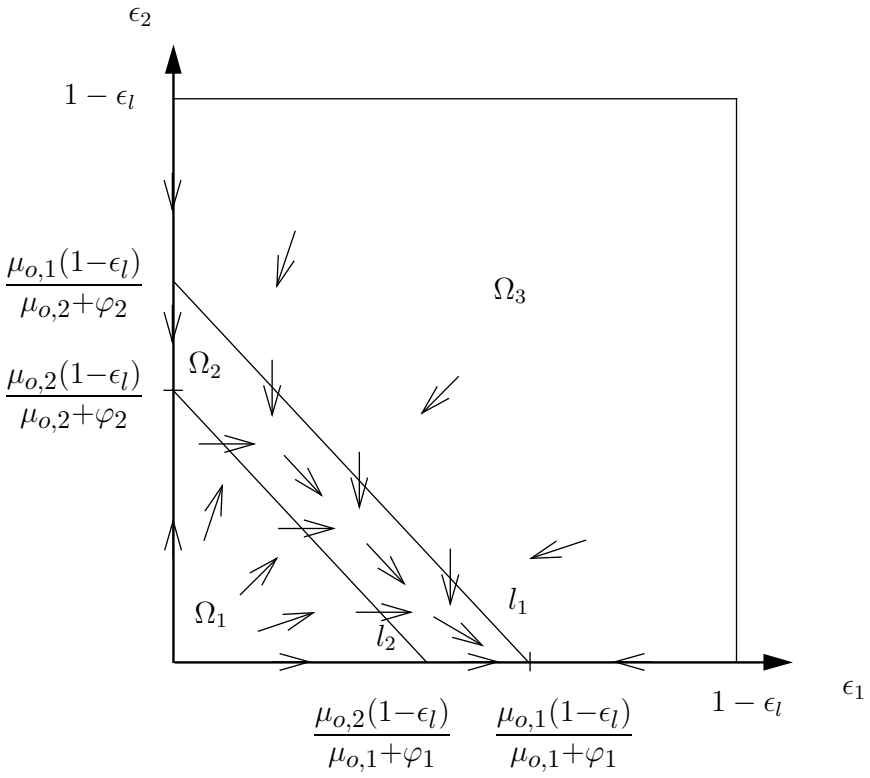

Figure 4.1 *Phase portrait when* $0 < \mu_{o,2} < \mu_{o,1}$ *(case* $(B2)$*).*

If we assume $\mu_{o,2} > \mu_{o,1} > 0$ and define lines l_1 and l_2 in the same way as before, the lines will swap places in the plane. The tangential directions on the lines will also change signs. Deriving the tangential directions in the plane in the same manner as before, we get the phase portrait (frozen time) in Figure 4.2, where we see that all the solutions converge toward $(B1)$ as long as $\epsilon_{20} > 0$. Thus, if $\mu_{o,2} > 0$ and $\mu_{o,2} > \mu_{o,1}$, the steady-state solution for the boundary conditions is $(B1)$.

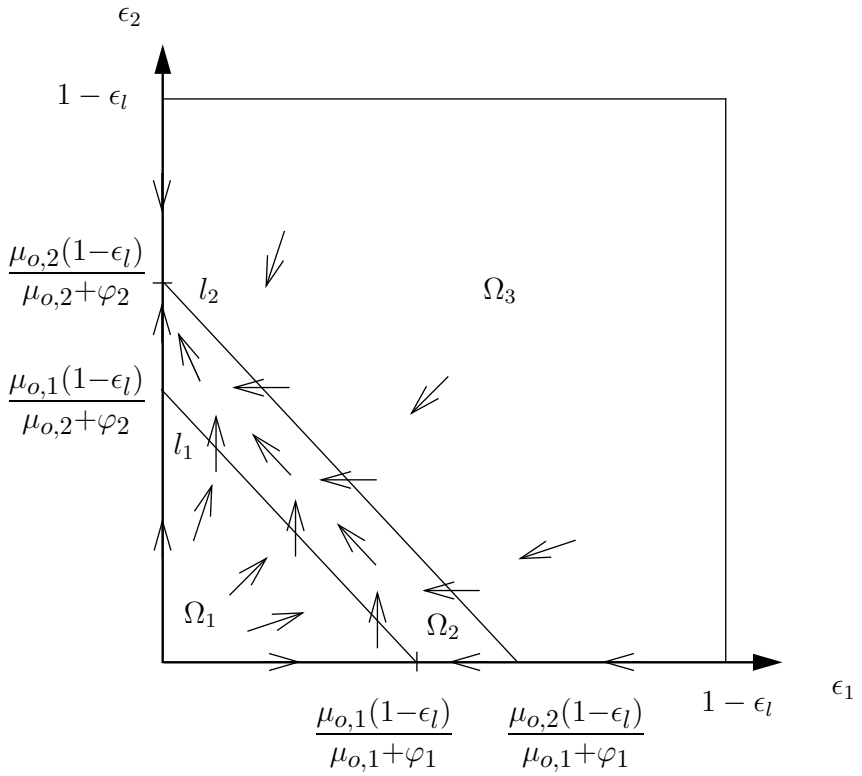

Figure 4.2 *Phase portrait when* $0 < \mu_{o,1} < \mu_{o,2}$ *(case* $(B1)$*).*

Finally, assume $\mu_{o,1} = \mu_{o,2} > 0$, i.e. the condition for (A) to hold in the steady state. It turns out that this is a special case of $(B1)$ and $(B2)$. The only difference is that lines l_1 and l_2 coincide because $\mu_{o,1} = \mu_{o,2}$. The positive quadrant of the plane will now be divided into only the two areas Ω_1 and Ω_3 (see Figure 4.3), with tangential directions

$$\begin{array}{llll} \dot{\epsilon}_1 > 0 & \text{and} & \dot{\epsilon}_2 > 0 & \text{if} \quad (\epsilon_1, \epsilon_2) \in \Omega_1 \\ \dot{\epsilon}_1 < 0 & \text{and} & \dot{\epsilon}_2 < 0 & \text{if} \quad (\epsilon_1, \epsilon_2) \in \Omega_3. \end{array}$$

If we divide (4.10) by (4.11) we find that all solutions must satisfy

$$\frac{d\epsilon_1}{\epsilon_1} = \frac{d\epsilon_2}{\epsilon_2},$$

from which we deduce that

$$\epsilon_2 = \frac{\epsilon_{20}}{\epsilon_{10}}\epsilon_1. \tag{4.17}$$

From Figure 4.3, where the tangential directions are illustrated, we see that the solutions converge towards stationary solutions on the line $l_1 = l_2$. By inserting (4.17) into the equation for the line, we get the steady-state solution in case (A) as

$$\epsilon_1 = \frac{\mu_{o,1}(1-\epsilon_l)\epsilon_{10}}{\epsilon_{10}(\mu_{o,1}+\varphi_1) + \epsilon_{20}(\mu_{o,2}+\varphi_2)}$$

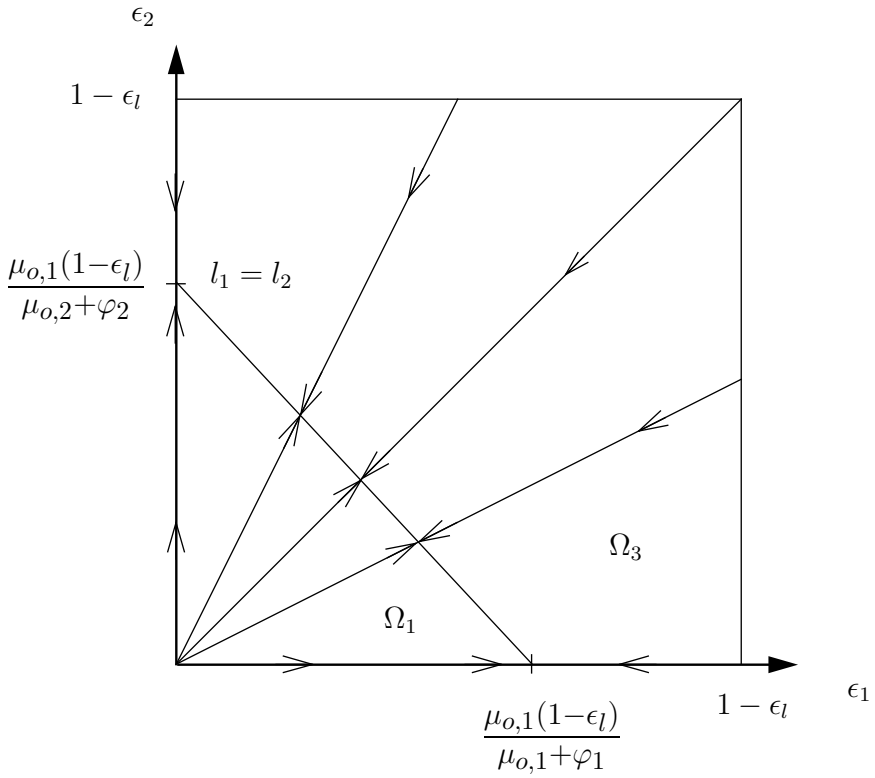

Figure 4.3 *Phase portrait when $\mu_{o,1} = \mu_{o,2} > 0$ (case (A)).*

$$\epsilon_2 = \frac{\mu_{o,1}(1-\epsilon_l)\epsilon_{20}}{\epsilon_{10}(\mu_{o,1}+\varphi_1)+\epsilon_{20}(\mu_{o,2}+\varphi_2)}.$$

Incidentally, there exists an analytical solution for this case also if the observed specific growth rates are assumed time invariant. If (4.17) is inserted into (4.10) and the result is divided by ϵ_1, after some rearrangement and integration from 0 to t, we get:

$$\int_{\epsilon_{10}}^{\epsilon_1} \frac{d\epsilon_1'}{\epsilon_1'[\epsilon_1'(\mu_{o,1}+\varphi_1+(\epsilon_{20}/\epsilon_{10})(\mu_{o,2}+\varphi_2))+\mu_{o,1}(1-\epsilon_l)]} = \frac{-t}{1-\epsilon_l}.$$

Solving the integral for ϵ_1 gives the solution

$$\epsilon_1 = \frac{\mu_{o,1}(1-\epsilon_l)\epsilon_{10}}{[\mu_{o,1}(1-\epsilon_l)-\Psi_0]\exp(-\mu_{o,1}t)+\Psi_0}, \tag{4.18}$$

where

$$\Psi_0 = (\mu_{o,1}+\varphi_1)\epsilon_{10}+(\mu_{o,2}+\varphi_2)\epsilon_{20}.$$

It should be noted that the probability of $\mu_{o,1}$ being exactly equal to $\mu_{o,2}$ for all times is small. This means that even if the solution is asymptotically stable, the solution

will wander along lines l_1 and l_2 as soon as $\mu_{o,1}$ is not equal to $\mu_{o,2}$ (see Figures 4.1 and 4.2). However, for thicker biofilms the case when $\mu_{o,1} = \mu_{o,2}$ is not at all uncommon, but is rather the usual case due to a stabilizing effect on the condition $\mu_{o,1} = \mu_{o,2}$, which is discussed in the next section.

4.3 Simulations

To illustrate the use of the results in the previous sections, a simulation of a thick biofilm in the steady state and simulations illustrating the dynamics of thin biofilms will be presented. Two common applications for the multi-species biofilm model are the case of autotrophic/heterotrophic bacteria and the case when only autotrophic nitrifying bacteria (ammonium oxidizers and nitrite oxidizers) are considered. In the former model the autotrophic bacteria are considered as one type of bacteria with no intermediate nitrite production. The heterotrophic bacteria, which are denoted by subscript h, consume biodegradable organic material (measured as biological oxygen demand, BOD) and oxygen. The rate expressions for the autotrophic/heterotrophic biofilm model are summarized in Table 4.1. The latter model was described at the end of Chapter 3.

Table 4.1 *Rates and stoichiometry for the autotrophic/heterotrophic biofilm*

$R_{1,1}$	$=$	$\mu_{m,ao}\dfrac{c_{O_2}}{K_{O_2,ao}+c_{O_2}}\dfrac{c_{NH_4}}{K_{NH_4}+c_{NH_4}}\dfrac{c_{HCO_3}}{K_{HCO_3}+c_{HCO_3}}$
$R_{1,2}$	$=$	$b_{ao}\dfrac{c_{O_2}}{K_{O_2}+c_{O_2}}$
$R_{1,3}$	$=$	$k_{I,ao}$
$R_{2,1}$	$=$	$\mu_{m,h}\dfrac{c_{O_2}}{K_{O_2,h}+c_{O_2}}\dfrac{c_{BOD}}{K_{BOD}+c_{BOD}}$
$R_{2,2}$	$=$	$b_h\dfrac{c_{O_2}}{K_{O_2}+c_{O_2}}$
$R_{2,3}$	$=$	$k_{I,h}$

r_{v,O_2}	$=$	$-\rho_1\epsilon_1(4.33R_{1,1}/Y_a + R_{1,2}) - \rho_2\epsilon_2((1-Y_h)R_{2,1}/Y_h + R_{2,2})$
r_{v,NH_4}	$=$	$-\rho_1\epsilon_1 R_{1,1}/Y_a$
r_{v,HCO_3}	$=$	$-\rho_1\epsilon_1 2R_{1,1}/14Y_a$
$r_{v,BOD}$	$=$	$-\rho_2\epsilon_2 R_{2,1}/Y_h$

Both cases are discussed and used for illustration. All numerical results were achieved with the aid of the ordinary differential and algebraic equation solver D02SAF from the NAG Fortran routine library (NAG n.d.). The solver is a shooting and matching routine in which algebraic equations can be included in the parameter

optimization process (matching). A singularity at $x = 0$ occurs in Eqs. (4.8) and (4.9), due to (4.3), in the integration from the substratum to the biofilm surface. However, the singularity may easily be avoided by setting the velocity $u(0)$ to a sufficiently small number. This is eligible because $[d\epsilon_j/dx]_{x=0} = 0$, which can be shown by applying l'Hospital's rule (Edwards and Penney 1982) on $(1/\epsilon_j)[d\epsilon_j/dx]_{x=0}$ for each set of boundary conditions.

The methods that are used in the discussions and simulations that follow can be applied to any two-species biofilm model, including anoxic biofilm models, that fits into the general model structure described in Chapter 3. However, complete knowledge of the kinetics and insight into the equations and biofilm behavior are required.

The terms very thin, thin, and thick biofilms will be used. These are relative quantities that depend on the application of the biofilm model. In the two examples of biofilms that are used, very thin biofilms have a thickness up to a few tenths of microns, thin biofilms are in the order of several tenths of microns, and thick biofilms have a thickness of hundreds of microns or more.

4.3.1 Criteria for Bacterial Coexistence

To avoid trial and error when solving the steady-state biofilm problem, we need to know which set of boundary conditions that should be used. Also, because the solutions tend toward the steady state, we may conclude important results of the biofilm behavior from criteria on the bulk concentrations for the different boundary conditions.

Assume that we have a very thin biofilm and that $\mu_{o,1} \gg \mu_{o,2}$ at the biofilm surface. Because the film is very thin, the substrate concentrations inside the biofilm will not differ much from those at the surface. Also, because $\mu_{o,1}$ and $\mu_{o,2}$ only depend on the substrate concentrations, $\mu_{o,1}$ will be larger than $\mu_{o,2}$ in the entire biofilm and only bacteria 1 can exist ($B2$).

For most rate expressions for the growth of the bacteria, i.e. $R_{1,1}$ and $R_{2,1}$, used in biofilm modeling, the growth rates decrease with decreasing substrate concentrations of the reactants. Hence, the observed specific growth rates, $\mu_{o,1}$ and $\mu_{o,2}$, will also decrease. In the two examples of competition chosen for illustration, $\mu_{o,1}$ and $\mu_{o,2}$ only depend on the concentrations of the reactants. Thus, $\mu_{o,1}$ will decrease with increasing depth of the biofilm for the mono-cultural biofilm in case ($B2$). On the other hand $\mu_{o,2}$ will increase if one of the reactants for bacteria 2 is a product of bacteria 1 (e.g., nitrite in the *ao/no* biofilm model), or remain more or less the same if not (e.g., the aut/het biofilm model). At some specific film thickness, $\mu_{o,1}$ will reach the value of $\mu_{o,2}$ at the substratum. Boundary conditions (A) and ($B2$) hold for a biofilm of that thickness. For the given bulk concentrations this is the *critical film thickness for bacterial coexistence*, which is denoted L_{crit}.

The same reasoning naturally applies when $\mu_{o,2} \gg \mu_{o,1}$ at the biofilm surface. In that case boundary conditions (A) and $(B1)$ will hold at the substratum when the biofilm has reached the thickness L_{crit}. If the film is thicker than L_{crit} then (A) will hold at the substratum due to the correlation between an increase in bacteria concentration and a decrease in the corresponding concentrations of reactants and observed specific growth rate, which creates a stabilization on the condition $\mu_{o,1} = \mu_{o,2}$.

For the two example models L_{crit} may be estimated, if the oxygen consumption by the endogenous respiration is neglected, using ordinary integration methods such as the Runge-Kutta methods. The necessary boundary conditions will either be (A) and $(B2)$ or (A) and $(B1)$ for the two possible cases. All substrate concentrations except one can be eliminated as variables because only one type of bacteria exists and the oxygen consumption by endogenous respiration is neglected. For example, the alkalinity is eliminated as follows: Insert the rate expressions r_{v,NH_4} and r_{v,HCO_3} in Table 4.1 in Eq. (3.8) in the steady state, integrate from 0 to an arbitrary x, and integrate once more from x to L. We then get

$$c_{HCO_3}(x) = c^b_{HCO_3} - \frac{2D^b_{NH_4}}{14D^b_{HCO_3}}(c^b_{NH_4} - c_{NH_4}(x)), \tag{4.19}$$

where it has been assumed that the diffusion coefficients D_{NH_4} and D_{HCO_3} can be written as products of the values in the bulk, i.e. $D^b_{NH_4}$ and $D^b_{HCO_3}$, and a function $f(x)$. This way of reducing the number of variables can often be used in dynamic simulations as well, where the first subsystem is assumed to be in a steady state. The substrate concentrations for substrates consumed only by the bacteria that do not exist in the film will remain the same in the entire biofilm if it is not produced by the other bacteria. If a substrate is produced, the concentration can be calculated in the same manner as the alkalinity. The condition $\mu_{o,1} = \mu_{o,2}$ will, together with the method used for achieving Eq. (4.19), give all the substrate concentrations at the substratum for each set of bulk concentrations. Integration of Eq. (3.8) in the steady state, Eqs. (4.2) and (4.8) or Eq. (4.9) until the substrate concentrations reach the prescribed bulk concentrations, will yield L_{crit}.

In many cases we are more interested in determining, for each L_{crit}, the corresponding set of bulk concentrations. We begin by considering the autotrophic biofilm. For each set of $c^b_{NO_2}$, $c^b_{O_2}$, $c^b_{HCO_3}$ and L_{crit} we want to determine the value of the corresponding $c^b_{NH_4}$ for the two cases $(B1/A)$ and $(B2/A)$. Note that the oxygen consumption by endogenous respiration from now on is included in the model.

The ordinary differential equations to be solved are (3.8) in the steady state and (4.2) combined with (4.8) for solving $(B2/A)$, or (4.9) for solving $(B1/A)$. Boundary conditions are (3.9), (4.3), and those given by $(B1)$ and (A), or $(B2)$ and (A). We may use shooting and matching to solve these equations as well. The unknown parameters at the substratum are the oxygen concentration and the ammonium concentration for $(B2/A)$. The ammonium concentration can be determined from the condition $\mu_{o,1} = \mu_{o,2}$, but is more conveniently found by including the algebraic equation in the search routine. For the case $(B1/A)$ it suffices to use the oxygen concentration as the unknown parameter at the substratum. The previously described

method for finding L_{crit} when the endogenous respiration was ignored can be used for finding initial approximations of the unknown oxygen concentration.

The results for

$$\begin{aligned} c^b_{HCO_3} &= 3 \text{ mole m}^{-3} \\ c^b_{O_2} &= c^{sat}_{O_2} \\ L_{crit} &= 100\ \mu\text{m} \end{aligned}$$

at 20°C, and with the parameter values in Appendix B, are presented in Figure 4.4. From the plot it is possible to determine, for each set of bulk concentrations, if the biofilm will tend toward coexistence or not. Dynamic simulations show that in the sets of bulk concentrations yielding $(B1)$ and $(B2)$, the rate of convergence toward a mono-cultural biofilm increases with distance from lines $(B1/A)$ and $(B2/A)$. The area in the lower left corner represents the conditions for no bacteria in the biofilm $(B3)$. The corresponding solutions for $L_{crit} = 50$, 75, 100, 125, 150, 175, and 200 μm are shown in Figure 4.5. The solutions for $(A/B1)$ are omitted for $L_{crit} = 125$, 150, and 175 μm for easier reading. The area between the lines having equal L_{crit} are the ammonium and nitrite concentrations that allow a steady state coexistence. Note that for thick biofilms $(B1)$ and $(B2)$ are unlikely to occur and that even though $\mu_{o,2} < 0$ at the bulk, the nitrite oxidizers may coexist with the ammonium oxidizers because of the nitrite produced inside the biofilm.

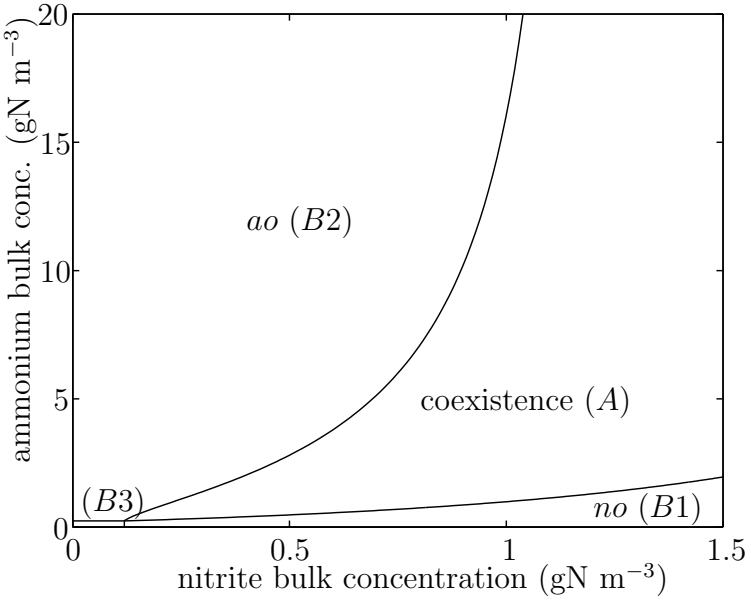

Figure 4.4 *Critical bulk concentrations for coexistence in a 100μm thick nitrifying biofilm at 20°C and $c_{HCO_3} = 3$ mole m^{-3}.*

In the biofilm model in which autotrophic and heterotrophic bacteria are competing, none of the bacteria are using a product from the other. Hence, if $\mu_{o,1} \leq 0$ in the bulk, autotrophs cannot exist, and if $\mu_{o,2} \leq 0$ in the bulk, heterotrophs cannot exist

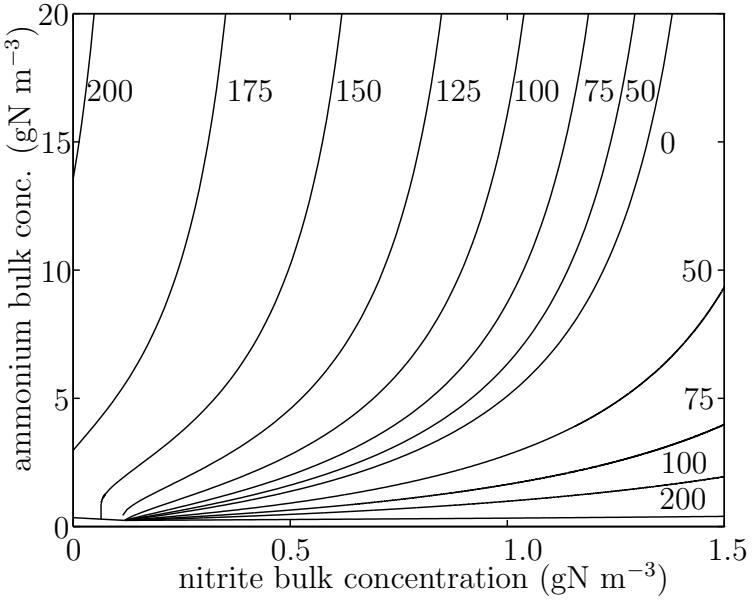

Figure 4.5 *Critical bulk concentrations for coexistence in autotrophic nitrifying biofilms of various biofilm thickness.*

in the biofilm. However, if the production of soluble microbial products (SMP) by the nitrifiers is included in the model, this may possibly be enough to guarantee the existence of small amounts of heterotrophs, no matter how low the bulk concentration of biological oxygen demand (BOD) is (Rittmann *et al.* 1994). Solving the same problem as for the autotrophic biofilm but for the autotrophic/heterotrophic biofilm under the following conditions:

$$\begin{aligned} c^b_{HCO_3} &= 3 \text{ mole m}^{-3} \\ c^b_{O_2} &= c^{sat}_{O_2} \\ L_{crit} &= 400, 600, \text{ and } 800\,\mu\text{m}, \end{aligned}$$

at 20°C yields the solutions presented in Figure 4.6. The area between the lines for each L_{crit} are the bulk concentrations that allow steady-state coexistence of autotrophs and heterotrophs (A). From the figure we can see that the thicker the biofilm, the easier it is for the nitrifiers to exist in the biofilm. The heterotrophs dominate the outer parts of the biofilm while the nitrifiers dominate closer to the substratum, where the BOD concentration is too low for the heterotrophs.

Note here that the exact location of the solution curves in Figure 4.5 and especially Figure 4.6 are quite dependent on the parameter values used. The way in which the regions of coexistence depend on the nitrite concentration in Figure 4.5 and on the BOD concentration in Figure 4.6 is particularly sensitive to the value of $\mu_{m,ao}\rho_1$ relative to $\mu_{m,no}\rho_2$, or relative to $\mu_{m,h}\rho_2$. In Figure 4.6 the solutions for ($B2/A$) behave differently than those in Figure 4.5, which is a result of the parameter values used. In

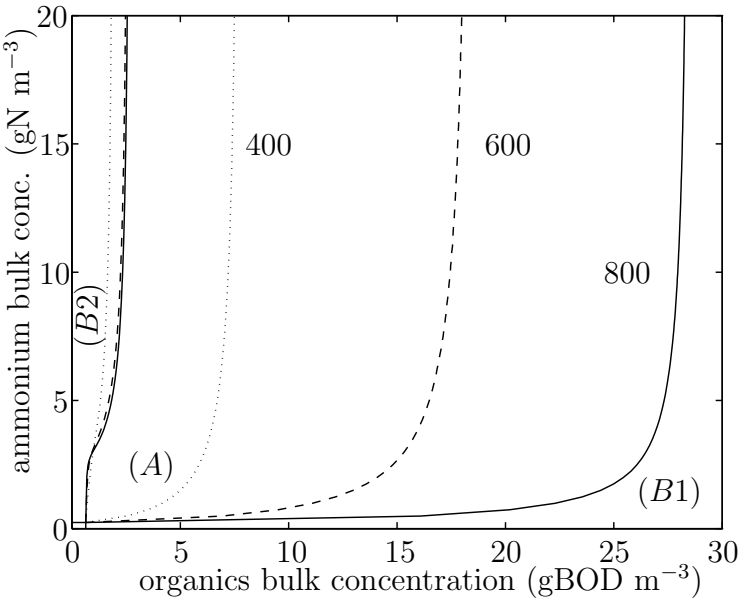

Figure 4.6 *Critical bulk concentrations for coexistence in the autotrophic/heterotrophic biofilm for* $L_{crit} = 400$*,* 600 *and* 800 μm *at* $20°C$ *and* $c_{HCO_3} = 3$ *mole* m^{-3}*.*

the autotrophic/heterotrophic biofilm the biofilm is thicker and oxygen is rate limiting, i.e., the oxygen concentration is very low at the substratum. Hence, the relation $\mu_{o,1}$ relative to $\mu_{o,2}$ is very dependent on the values of b_{ao} and b_h (and also on $k_{I,ao}$ and $k_{I,h}$), which are not chosen to be equal in the autotrophic/heterotrophic model. If they had been equal, the thicker the biofilm, the lower the BOD concentrations would have to be for the existence of heterotrophs in the biofilm.

From Figures 4.5 and 4.6 we see that the conditions for coexistence in thin biofilms are very narrow. This may be a consequence of the model assumptions and not of reality. The aggregation of the states ϵ_j, following the assumption of continuity, **A1** on page 19, may not be adequate for very thin biofilms. How well the different bacteria attach to the substratum should also be important for very thin biofilms. However, for medium thick biofilms the results should be relevant. From Figures 4.5 and 4.6 we can also see that it may be favorable in some situations to keep the biofilm thin (or possibly thick) by means of controlled erosion, because competition by unwanted bacteria may then be minimized. Even though the exact results presented in the figures depend on the parameter values used, the general behavior of the solution curves remain the same if the parameter values are changed.

Note that the conditions for coexistence are not as restrictive as they may appear. In many cases the balance between the bulk and the biofilm will ensure coexistence. For example, if the influent water to a continuous flow biofilm reactor contains too

little ammonium relative to organic matter for the autotrophs to survive, the organic content will decrease while the ammonium content will remain the same. At some point, if the reactor is large enough, the organic content will reach a concentration that allows for coexistence. The same reasoning applies to batch reactors, but then the residence time and the size will be critical for the coexistence of the bacteria.

Case $(B3)$ has to be considered separately and is not focused on here. The fact is that $(B3)$ does not give unique steady-state solutions as the model is formulated. This is due to the fact that if $\mu_{o,1} \leq 0$ and $\mu_{o,2} \leq 0$ at the substratum, and in the regions close to the substratum, then the steady-state film must consist of entirely inert material in those regions. At some point x^* either one or both of $\mu_{o,1}$ and $\mu_{o,2}$ will be larger than zero, because no active bacteria would exist otherwise. No substrates will be consumed in the interval $[0, x^*]$. Hence, there will be no flux at $x = x^*$ and Eq. (3.9) must hold there. The solution is then given by the steady state solution on the interval $[x^*, L]$ with boundary conditions $(B1)$, $(B2)$, or (A) at $x = x^*$. The interval occupied solely by inert material may never again be reoccupied by any active bacteria according to the model. However, for example, sloughing of the biofilm at discrete events will cause a renewal of the biofilm from $x = 0$ with active bacteria adsorbed from the bulk onto the substratum. A diffusive movement of solids, as discussed on page 25, would also theoretically provide the means for a biofilm renewal in the deepest parts of the biofilm.

4.3.2 Thick Biofilms

As an illustration for thick biofilms we choose the autotrophic biofilm consisting of ammonium oxidizers and nitrite oxidizers. When solving the equations with a shooting and matching routine, we may choose $c_{O_2}(0)$, $c_{NH_4}(0)$ and $\epsilon_1(0)$, which is the volume fraction of ammonium oxidizers, as unknown parameters. The value of $c_{NO_2}(0)$ is then given by the condition $\mu_{o,1} = \mu_{o,2}$. The value of $c_{HCO_3}(0)$ is given by Eq. (4.19), and the value of $\epsilon_2(0)$ follows from the first condition for case (A) on page 36. The erosion function f in Eq. (3.15) has to be specified. In this simulation the function used by Wanner and Gujer (1986) was assumed, i.e.,

$$f = \lambda L^2, \tag{4.20}$$

where $\lambda = 500\ \mathrm{m^{-1}d^{-1}}$.

Numerically, the steady-state solution is achieved iteratively as follows: First, an initial assumption of the film thickness (L_0) is made. Then the three unknown parameters are guessed and Eqs. (3.8), (4.2), (4.8) and (4.9) are integrated from the substratum to the biofilm surface where the values of the substrate concentrations are compared to the boundary condition (3.11). From this comparison a better guess of the unknown parameters is calculated using a modified Newton method (Deuflhard 1974). This matching procedure is repeated until the requested tolerance

is met. An iteration is then initiated, where the film thickness is determined by

$$L_{k+1} = \sqrt{\frac{u_k(L_k)}{\lambda}}, \quad k = 0, 1, \ldots \tag{4.21}$$

and the entire matching procedure is repeated with initial guesses chosen as the solution for the previous film thickness.

A typical steady-state solution is presented in Figures 4.7 and 4.8. The conditions were

$$\begin{aligned} T &= 20°\text{C} \\ c^b_{O_2} &= c^{sat}_{O_2} \\ c^b_{NH_4} &= 10 \text{ gN m}^{-3} \\ c^b_{HCO_3} &= 2 \text{ mole m}^{-3} \\ c^b_{NO_2} &= 1 \text{ gN m}^{-3}. \end{aligned}$$

These inputs are representative of wastewater treatment in a tertiary nitrifying bioreactor.

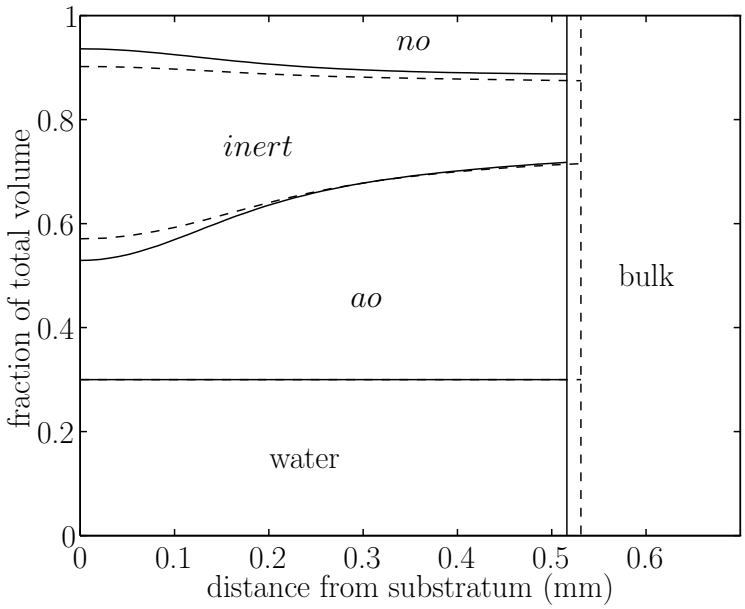

Figure 4.7 *Steady-state distribution (solid) of the volume-fractions and the solution after a 5-day simulation (dashed) with the dynamic model.*

The convergence for finding the correct steady-state film thickness using the simple iteration method, Eq. (4.21), is very fast because almost all of the contribution to $u(L)$ comes from the outer regions of the film, i.e., $u(L)$ is quite independent of the film thickness. For example, in this simulation the initial guess of the film thickness was 0.7 mm. After only one iteration the error in L was less than 2 μm and after two

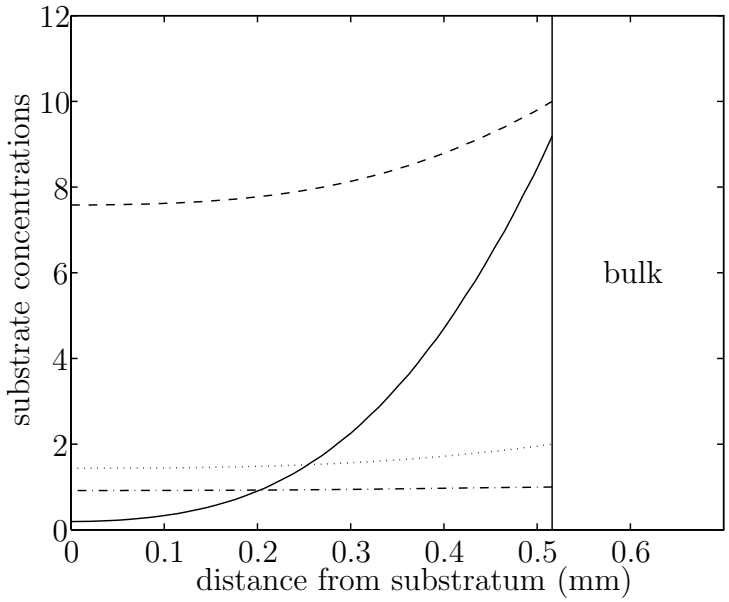

Figure 4.8 *Steady-state substrate concentrations in the thick autotrophic biofilm in the steady state; oxygen (solid), ammonia (dashed), alkalinity (dotted) and nitrite (dash-dotted).*

iterations less than 0.06 μm. Finding the steady-state solution for the biofilm with the method described here requires approximately 0.2 s of system time on a DEC station 5000/125 (comparable to a standard 486 PC). For comparison a simulation of the dynamic model for five days and fifty days under the same conditions and with initial conditions

$$\begin{aligned} \epsilon_1(x,0) &= 0.4 \quad 0 \leq x \leq L \\ \epsilon_2(x,0) &= 0.15 \quad 0 \leq x \leq L \\ L(0) &= 0.7\,\text{mm} \end{aligned}$$

was carried out. A shooting and matching routine was used for the first subsystem (assumed in the steady state) and the second subsystem was solved by a dynamic updating of the volume fractions with an Adams-Bashforth method (Lambert 1991), after a division of the film into control volumes (see Section 8.2). The results of the simulations are included in Figure 4.7, where only the 5-day simulation can be seen because the 50-day simulation is visually inseparable from the steady state solution. The system time required for these simulations was more than threefold and 25-fold, respectively, the time required for the exact steady-state solution. It should be noted that other boundary value differential equation solvers may be even more efficient for solving the steady-state problem. The major drawback of the shooting and matching routine is the possibility of non-convergence in the Newton method. In this case numerical problems may be encountered when the net nitrite production is very close to zero in the biofilm. Then the concentrations at the biofilm surface

are rather insensitive to the chosen nitrite concentration at the biofilm substratum. At the same time the concentrations are very sensitive to the value of the oxygen concentration at the substratum, if oxygen is rate limiting (c.f. Figures 4.8 and 1.5). This results in a stiffness of the problem, which causes convergence problems due to numerical limitations.

4.3.3 Thin Biofilms

In cases when the biofilm is thin, the normal case for the boundary conditions will be different. Thin biofilms exist in freshwater treatment processes, lower regions of TFs, the last reactor compartments in RBCs and in some biofilters, for example (Boller *et al.* 1994). As can be seen in Figures 4.5 and 4.6, the biofilm model predicts very narrow conditions on the bulk concentrations for coexistence of the bacteria in the film; i.e., in most cases no more than one type of bacteria can exist in a steady state. This is illustrated by a dynamic simulation of a 40-μm thick nitrifying film (*ao* and *no*) having the same bulk concentrations as in the simulation of a thick biofilm. The numerical methods were the same as in the previous dynamic simulation. Initial conditions were

$$\epsilon_1(x,0) = 0.3 \quad \text{and} \quad \epsilon_2(x,0) = 0.1 \qquad 0 \le x \le L.$$

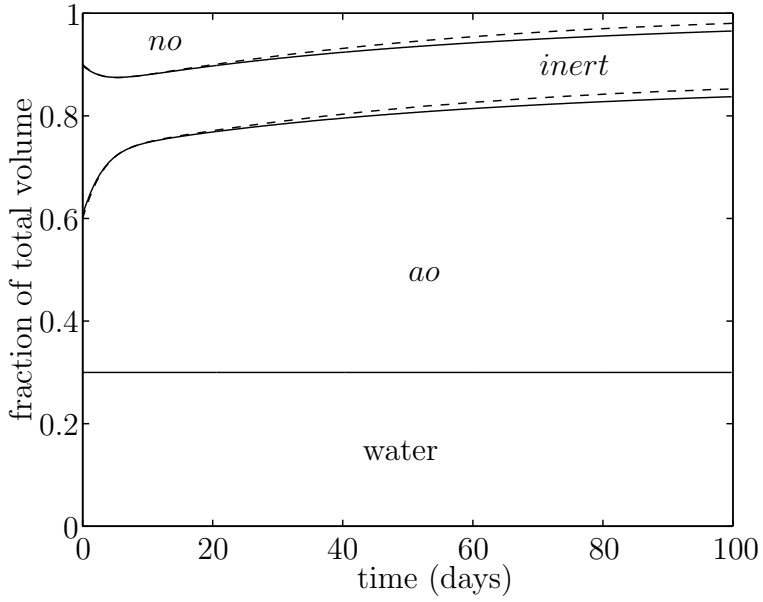

Figure 4.9 *Dynamic behavior of the volume-fractions at the substratum for the 40 μm autotrophic biofilm; the dynamic model (solid), solution by ODE45 (dashed).*

The results are shown in Figure 4.9 for the volume fractions at the substratum, $\epsilon_j(0,t)$. The values of the volume fractions at the biofilm surface are very close to those at the substratum and they cannot be visually separated. Included in the Figure is also a numerical solution by ODE45 (Runge-Kutta) in MATLAB to Eq. (4.6) with initial conditions $\epsilon_1 = 0.3$ and $\epsilon_2 = 0.1$. From the small difference between the solutions we conclude that for very thin and thin biofilms we may assume that the biofilm is uniform and that Eq. (4.6) may be used directly for calculations of the bacterial concentrations. As can also be seen in Figure 4.9, the nitrite oxidizers will be out-spaced even though the observed specific growth rate is positive in the entire film. However, the time required is evidently very long and during this period of time the conditions may very well have altered for the bacteria. From the earlier reasoning about stability of the equilibrium points, we deduce that if our modeling situation is that $\mu_{o,1} > \mu_{o,2}$ or vice versa for all possible situations, then there is no point in considering more than one type of the bacteria. Note that the curves for the volume fractions in Figure 4.9 follow the phase portrait in Figure 4.1. The solution enters the space between lines l_1 and l_2 quite quickly after which the volume occupied by *inert* material is almost constant because the slope of the lines are close to -1.

4.4 Conclusions and Discussion

A method for solving the two-species biofilm problem in the steady state has been presented. It is simple and requires little computational effort. The method was derived through a thorough investigation of the boundary conditions and may be extended to biofilm models considering more than two species. Four different sets of boundary conditions are possible, each having a physical interpretation. Criteria for each set of boundary conditions were deduced both at the substratum and at the biofilm surface.

By introducing the parameter L_{crit}, critical film thickness for bacterial coexistence, it is possible to determine the conditions in the bulk for which the bacteria will coexist in the steady state. However, the determination of L_{crit} requires complete knowledge of the stoichiometry and the kinetics. For typical rate expressions it is concluded that the thicker the biofilm is, the less restrictive the conditions for coexistence are. As a consequence, it may in some situations be favorable to keep the biofilm thin, or possibly thick, to minimize the population of an unwanted species. Furthermore, the spatial distribution of the bacteria in very thin biofilms can be assumed to be homogeneous. Depending on the prevailing conditions in the bulk, there will in many situations be no point in considering more than one species in the biofilm model.

Chapter 5

REACTOR MODELING

Combining a biofilm model with the continuously stirred tank concept results in a description of a continuously stirred biofilm reactor (CSBR). It is discussed how such modeling units can be used to build models of different biofilm reactors. Specifically, the CSBR-approach is applied to aerobic trickling filters. An expression, proportional to a mass transfer coefficient and to the difference between bulk concentration and saturation concentration, is assigned for the oxygen flux from the air to the bulk. From measured bulk concentrations of ammonium and oxygen inside a pilot-scale nitrifying trickling filter the mass transfer coefficients are determined. The average values increase from 1.5 md^{-1}, at a hydraulic load of 50 md^{-1}, to 3.3 md^{-1}, at a hydraulic load of 200 md^{-1}. However, the flux of substrates into the biofilm is fairly insensitive to the value of this coefficient.

The use of continuously stirred tank reactors (CSTRs) as modeling units is well established in chemical reaction engineering and design. A simple illustration of a CSTR is a reactor tank of volume V through which there is a flow, Q, with an influent concentration $c_{A,in}$ of a substance A. In the reactor, the substance A reacts irreversibly to the substance B at a rate r. Due to a perfect mixing, the effluent concentration equals that in the entire reactor, i.e. c_A (see Figure 5.1).

A mass balance for the substance A over the CSTR gives

$$V\frac{d}{dt}c_A = Q(c_{A,in} - c_A) - r,$$

where the reaction rate r usually depends on the concentration c_A.

5.1 A CSBR Model

In biofilm reactors the reactions take place in the biofilm, which means that, mathematically, the flux of substances into the biofilm has the same function as the

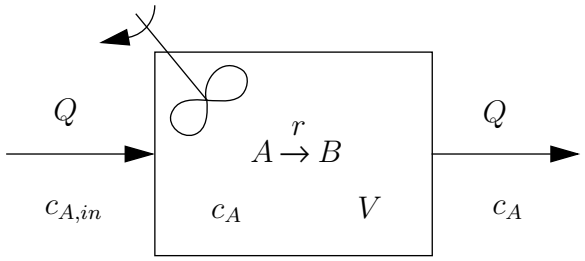

Figure 5.1 *Illustration of a CSTR where A reacts to B.*

reaction rate r in the CSTR-model. Aerobic biological systems require oxygen, which is usually supplied either by oxygenation of the bulk liquid, as in air lift biofilters, or by having a large contact area between the bulk and the air, as in trickling filters and rotating biological contactors. Sometimes there are also gaseous reaction products (dissolved in the liquid), such as the carbon dioxide produced in the nitrification (1.1).

A continuously stirred biofilm reactor (CSBR), i.e., a biofilm reactor where the bulk is completely mixed, can be seen as a combination of three compartments: a gas phase compartment (GPC), a continuously stirred tank (CST) with bulk liquid, and a biofilm compartment (BFC). The interactions between the three compartments are illustrated in Figure 5.2.

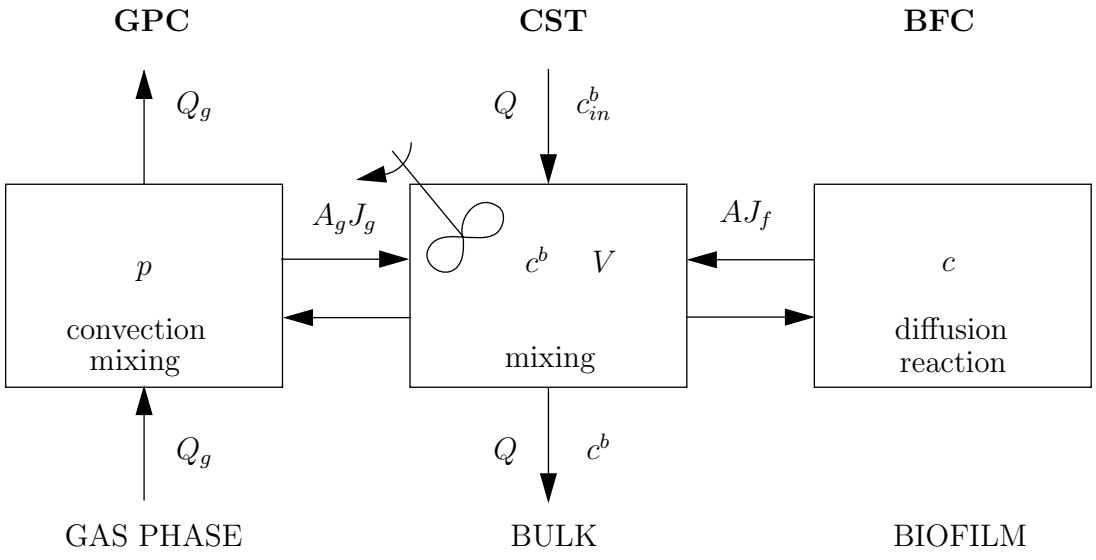

Figure 5.2 *Illustration of a CSBR.*

Using the variables in the figure, mass balances over the bulk give

$$V\frac{d}{dt}c_i^b = Q(c_{in,i}^b - c_i^b) + AJ_{f,i} + A_gJ_{g,i}, \qquad i = 1, \ldots n_l, \tag{5.1}$$

where the flux out of the biofilm is equal to the flux at the biofilm surface, i.e.,

$$J_{f,i} = -D_i\left[\frac{\partial c_i}{\partial x}\right]_{x=L} \tag{5.2}$$

if a planar biofilm is assumed. For cylindrical and spherical biofilms x should be replaced by the radius r (see page 24).

The total flux of a gaseous substance, $A_gJ_{g,i}$, depends on the contact area A_g between the bulk and the gas phase, the partial pressure p_i, the solubility, the bulk concentration, the mixing in the gas phase, etc. However, if the gaseous components are not of specific interest, and the situation is one of the following:

- the gaseous components do not affect the reaction rates,
- the corresponding bulk concentrations are known,
- the flux is empirically determined,

then there is no need for a general expression for the flux J_g. The first kind of situation occurs in many anaerobic biofilm systems. In aerobic biofilm systems, however, the reaction rates usually depend on the oxygen concentration. Systems with suspended carrier materials often have limited aeration due to the cost of pressurizing air. It is, therefore, common to continuously measure the oxygen concentrations with electrodes to ensure sufficiently high bulk concentrations. In some reactors, such as well aerated trickling filters with moderate oxygen consumptions, the bulk may be assumed saturated with oxygen. At higher respiration rates empirical approximations of the oxygen flux can be made, which is discussed in the next section.

5.2 Reactor Models

By combining CSBR units in parallel and in series, different hydraulic behavior can be modeled in the same way as CSTRs are combined in traditional chemical reactor engineering and design (Froment and Bischoff 1979).

Sometimes the exact way to structure the CSBRs is obvious. In rotating biological contactors (RBCs) the bulk is well mixed, which means that only one CSBR is needed if the RBC is not sectioned (Watanabe *et al.* 1982). If it is sectioned, like the RBC studied by Wanner and Gujer (1984), one should be used for each separate stage. Another example of natural CSBRs is aerated moving bed reactors of the kind used by Rusten *et al.* (1995*a*, 1995*b*).

In other reactors, though, the mixing cannot be idealized and combinations of CSBRs in parallel and in series may better approximate the hydraulics.

Ideally, there are reactors with a plug flow of bulk liquid. Mass balances over a reactor segment dz in such a reactor give

$$v\frac{\partial}{\partial t}c_i^b = -q\frac{\partial}{\partial z}c_i^b + aJ_{f,i} + a_gJ_{g,i}, \qquad i = 1, \ldots n_l, \tag{5.3}$$

where z is the distance from the inlet. If the reactor is uniform, the specific bulk volume v, the hydraulic load q, the specific biofilm surface area a, and the specific surface area of the gas-liquid interface a_g are defined as

$$\begin{aligned} v &= V/(A_r h) \\ q &= Q/A_r \\ a &= A/(A_r h) \\ a_g &= A_g/(A_r h), \end{aligned}$$

where A_r is the cross sectional area of the reactor and h is the reactor length or the reactor height.

Eq. (5.3) corresponds to an infinite number of CSBRs in series. Instead of solving this partial differential equation, the plug flow reactor may therefore be approximated by a large number of CSBRs in series.

5.2.1 Trickling Filters

Since the liquid pours down through a trickling filter due to gravity, the flow can be expected to be close to plug flow. Hence, it is natural to model trickling filters by N CSBRs in series, where N can be seen as a model design parameter: the higher N is, the closer to plug flow. In Section 6.3 it is shown how N can be determined from residence time distributions.

The Rya Pilot Plant NTF

Due to increased demands on nitrogen removal, the Rya WWTP in Göteborg, Sweden, had a large pilot-scale nitrifying trickling filter (NTF) operating from December 1990 to December 1995 to investigate different methods of removal. The plant, shown in Figure 5.3, was circular with an inner diameter of 2.7 m and filled with cross-flow plastic media to a bed height of 7.2 m. Influent water to the plant was the effluent water of the the Rya WWTP. A dual arm distributor, rotating at 0.3-0.7 rpm, was used for sprinkling the water over the bed. In Table 5.1 the average influent conditions during the first two years are listed (Mattsson and Rane 1993). The plant was, generally, back-washed weekly to control development of biofilm predators. Air was supplied by natural ventilation through four vents, having inner diameters of 15 cm, at the bottom of the plant.

For determination of concentrations inside the trickling filter five holes had been horizontally drilled into the center of the plant at 1.05, 1.65, 2.85, 4.5 and 5.7 m below the top of the packing media. By insertion of semi-open pipes, samples of the bulk water could be taken at these depths in the filter. Wik (1996) has described the plant and the pipe system more in detail.

Figure 5.3 *The pilot plant nitrifying trickling filter at the Rya WWTP in Göteborg.*

During the years the trickling filter was in operation, a few changes were made of the plant. The most important ones were:

Aug. -91: The uppermost 1.2 m of media was changed from the original cross-flow media, having a specific surface area of 157 m^2m^{-3}, to a denser material with a specific surface area of 243 m^2m^{-3}.

Nov. -92: All media was replaced by cross-flow PVC-media with a specific surface area of 226 m^2m^{-3} and 60° angle of inclination.

Dec. -93: The plant was equipped with pipes, pumps and controllers that made it possible to computer control a recirculation from the effluent to the influent to the filter.

Table 5.1 *Influent conditions December 90 - August 92*

		Min.	Average	Max.
Flow	(m^3d^{-1})	130	679	1236
Temperature	(°C)	7	14	20
Ammonium	(gN m^{-3})	6	19	31
Alkalinity	(mole $HCO_3^- m^{-3}$)	1.7	3.2	4.3
Nitrate	(gN m^{-3})	0.01	0.9	9.7
Total nitrogen	(gN m^{-3})	10	21	47
Total phosphor	(gP m^{-3})	0.17	0.3	0.41
Phosphate	(gP m^{-3})	0.02	0.10	0.66
COD	(gO_2m^{-3})	12	39	71
Suspended solids	(gSS m^{-3})	3.6	18.5	43.4

Oxygen Mass Transfer

In trickling filters oxygen is supplied as air, either by draft or by forced ventilation. If forced ventilation is used, the air is by convention introduced at the bottom of the reactor. Since the causality of the bulk flow is from top to bottom, this implies that if the oxygen supply is correctly modeled, all CSBRs have to be solved simultaneously. It is, therefore, numerically advantageous if the oxygen flux from the gas phase to the liquid, or the oxygen bulk concentration, can be approximated such that the causality of the bulk flow can be used. A schematic description of such a trickling filter model is shown in Figure 5.4.

At low respiration rates and proper ventilation it is natural to assume that the bulk is saturated with oxygen. At high respiration rates, though, the oxygen has to dissolve in the bulk liquid at a higher rate. The driving force has to be higher then, which implies reduced oxygen bulk concentrations.

From December 1990 to August 1992 quite an extensive sampling campaign was carried out on the pilot plant at the Rya WWTP. The alkalinity and the concentrations of nitrate, nitrite, ammonium and oxygen were measured on samples from the inlet, the outlet and the sampling holes (Mattsson and Rane 1993).

As a part of the measuring campaign there are 46 complete profiles (influent, effluent and all five sampling holes) of ammonium and oxygen concentrations when no encountered problems were reported. Three of the profiles were excluded in this investigation. In two of those, the reported ammonium concentration increased by several gN m^{-3} between two consecutive sampling holes, and in the third profile the reported oxygen concentration was higher than the saturation concentration in several of the sampling holes.

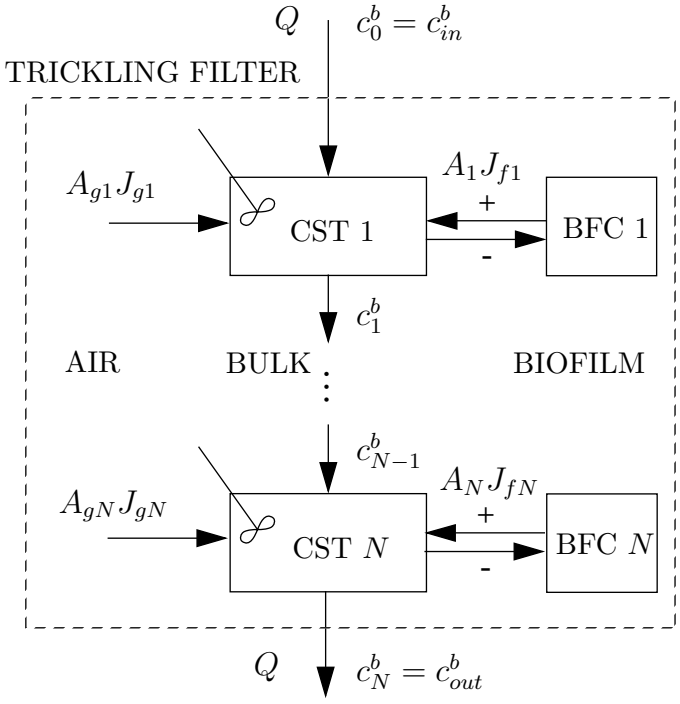

Figure 5.4 *Structure of a causal trickling filter model.*

The influent oxygen concentration was measured in the water leaving the distributor and was, generally, lower than in any of the sampling holes. Due to the large contact area, the mixing, and the drop when the water was sprayed over the bed (see front cover), the water at the top of the packing media should be close to saturated with oxygen. In accordance, the measured oxygen concentration in the first sampling hole soon after changing the media in the uppermost 1.2 m was only five percent less than the saturation concentration. In the presented data the measured influent oxygen concentration has, therefore, been replaced by the saturation concentration.

In Figure 5.5 the deviation from the saturation concentrations $c_{O_2}^{sat}(T)$ are shown. In the middle of the trickling filter the average oxygen concentrations were approximately 20% less than the saturation concentration. Near the outlet the average concentrations were closer to $c_{O_2}^{sat}$. Three reasons for this are:

- The effluent concentration was measured at the bottom of the reactor in a collecting volume below the packing media. Likely, significant mixing occurred due to a few decimeters' drop from the packing media.
- Fresh air was coming through the vents at the bottom.
- No, or very little, oxygen was consumed in the lower regions of the filter due to low nitrification rates.

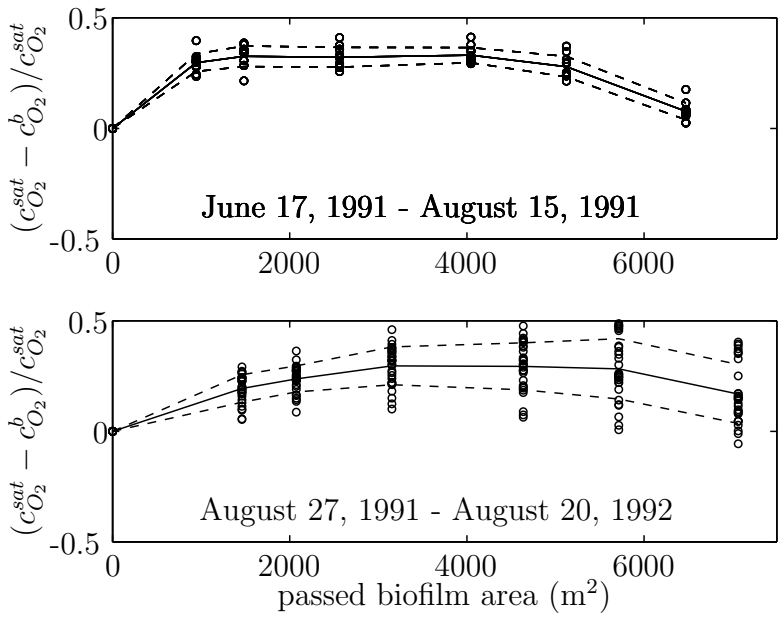

Figure 5.5 *Measured deviations from the oxygen saturation concentration (normalized). Solid lines are averages, and the dashed lines mark averages ± standard deviations.*

Boller and Gujer (1986) have modeled the oxygen flux from the gas phase in a nitrifying trickling filter by

$$J_{g,O_2}(z) = K_{L,O_2}(c^{sat}_{O_2} - c^{b}_{O_2}(z)). \tag{5.4}$$

Based on stationary measurements of the respiration rate and oxygen gradients along the reactor, they determined the oxygen transfer coefficient K_{L,O_2} using Eq. (5.3) in the steady state with $a = a_g$.

Using the concentration profiles from the pilot plant, values of K_{L,O_2} were determined in a similar way. First, the oxygen, temperature and ammonium profiles were replaced by least square fitted third degree polynomials as functions of passed biofilm area, A. Using the stoichiometry that 4.33 gO_2 is needed to nitrify 1 gN of ammonium and inserting Eq. (5.4) in Eq. (5.3) in the steady state, give

$$K_{L,O_2} = \frac{Q}{c^{sat}_{O_2}(T) - c^{b}_{O_2}} \left(\frac{d}{dA} c^{b}_{O_2} - 4.33 \frac{d}{dA} c^{b}_{NH_4} \right). \tag{5.5}$$

By using the polynomial approximations to determine the derivatives and the oxygen bulk concentration, K_{L,O_2} can be estimated with this equation. A typical illustration of the polynomial fitting and the resulting K_{L,O_2} are shown in Figure 5.6. Setting the oxygen concentration equal to the saturation concentration results in infinite values of K_{L,O_2} at the influent. The high values of the measured oxygen concentrations at

the effluent also cause very high values of the mass transfer coefficient. Since the data for the oxygen concentrations at the inlet and the outlet may be unreliable, polynomial fitting for the oxygen concentration and evaluation of K_{L,O_2} were made only for the parts between the first and the last sampling holes. The resulting mass transfer coefficients turned out to be almost the same for the time before changing the first 1.2 m of packing media as for the time after changing to the denser media. In Figure 5.7 the averages and standard deviations are presented for the passed biofilm area that was common before and after the change of media. Although the data for the oxygen concentration at the inlet was ignored, the mass transfer coefficients are still higher in the upper parts of the plant than in the lower parts.

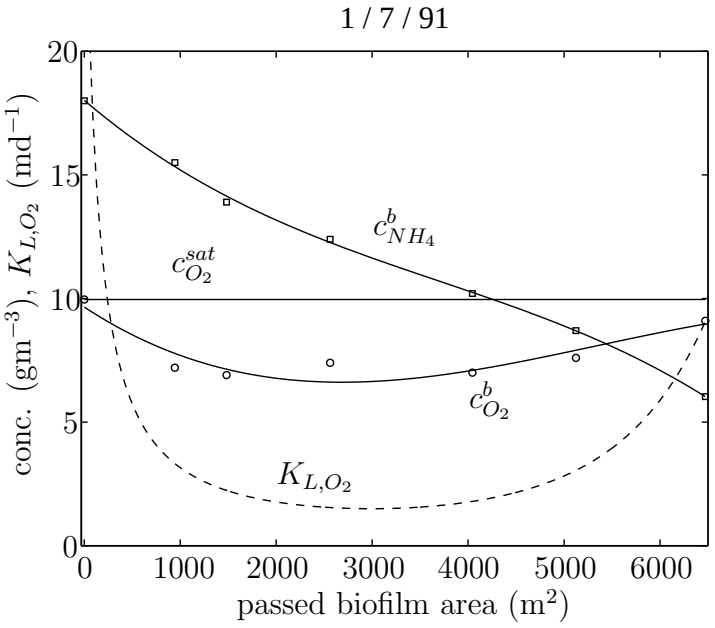

Figure 5.6 *Typical example of the polynomial fitting to measured profiles and the resulting oxygen mass transfer coefficient.*

Boller and Gujer (1986) suggested that the transfer coefficient should be compensated for the temperature according to

$$K_{L,O_2}(T) = K_{L,O_2}(10^\circ\mathrm{C}) \left(\frac{D^b_{O_2}(T)}{D^b_{O_2}(10^\circ\mathrm{C})} \right)^{0.5}, \tag{5.6}$$

where T is the temperature of the bulk water, and D^b is the diffusion coefficient in the bulk (water). For the values of K_{L,O_2} determined here, no dependency on the temperature was detected. However, for comparison with their results, the values were scaled to 10°C with Eq. (5.6) using the diffusion coefficients in Appendix B. The resulting values, after averaging over the area between the first and the last sampling holes, are shown in Figure 5.8. The least square fitted line is

$$\hat{K}_{L,O_2} = 0.0120q + 0.8541 \qquad (\mathrm{md}^{-1}). \tag{5.7}$$

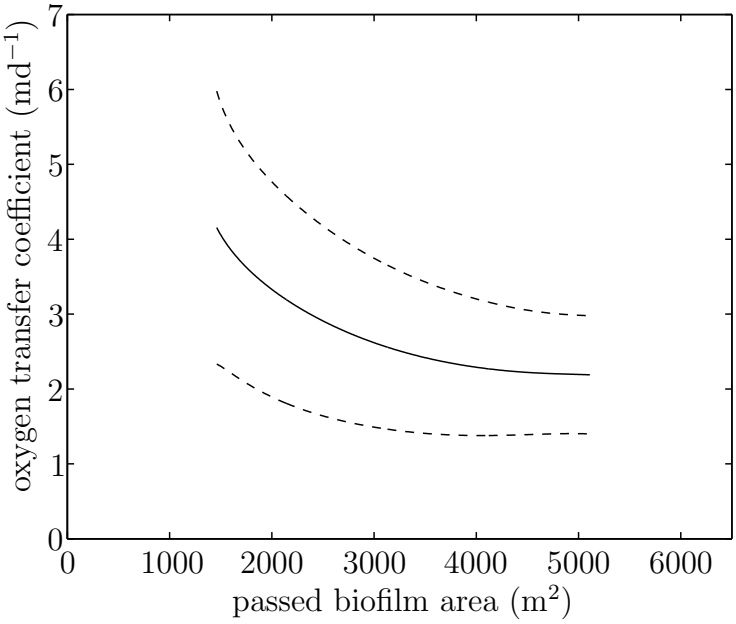

Figure 5.7 *Average (solid) ± standard deviation (dashed) oxygen mass transfer coefficient as function of passed biofilm area.*

As can be seen from the figure, the mass transfer coefficients agree fairly well with the values of Boller and Gujer (1986). However, the dependency on the flow appears to be weaker than what they found.

Although using Eq. (5.7) gives a very rough approximation of the mass transfer, the errors in the reactor efficiency caused by such an approximation will be quite small. The maximum errors can be estimated as follows:

An incorrect flux between the gas phase and the bulk gives incorrect oxygen bulk concentrations. This affects the substrate fluxes into the biofilm mainly in the upper and middle parts of the trickling filter, where oxygen is rate limiting. According to Figure 5.5 the largest deviations from the saturation concentrations are in the middle of the trickling filter. Hence, an incorrect value of K_{L,O_2} has the largest effect there.

Since oxygen is rate limiting, we may use Eq. (1.9) to conclude that the stationary ammonium gradient at the biofilm surface is approximately proportional to the square root of the oxygen bulk concentration, which gives

$$Q\frac{d}{dA}c^b_{NH_4} = J_{f,NH_4} \approx \text{constant} \cdot \sqrt{c^b_{O_2}}.$$

Further, the oxygen gradients along the reactor can be assumed to be zero in the middle of the reactor (see Figure 5.5).

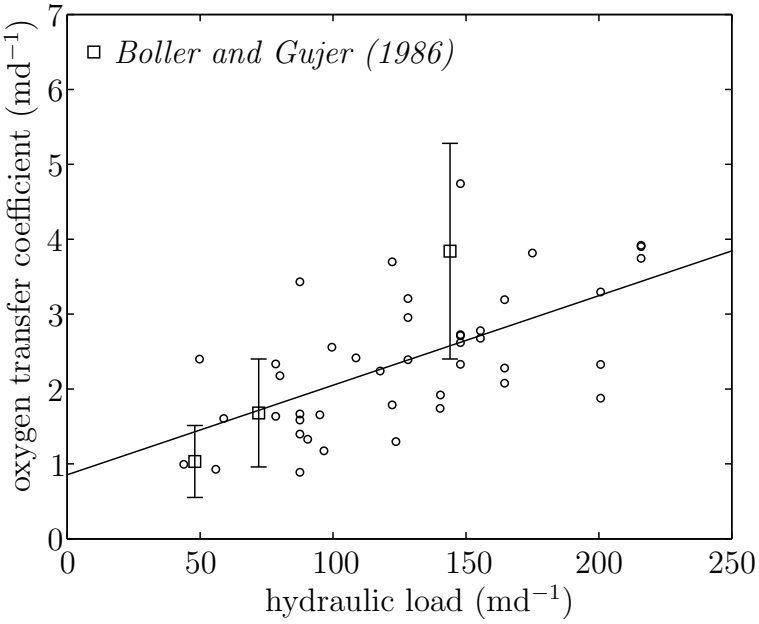

Figure 5.8 *Average values of K_{L,O_2} scaled to $10^\circ C$, and the values found by Boller and Gujer (1986) for an NTF with cross-flow plastic media having a specific surface area of 230 m^2m^{-3}.*

With these approximations Eq. (5.5) gives

$$\frac{\hat{K}_{L,O_2}}{K_{L,O_2}} = \frac{(c^{sat}_{O_2} - c^b_{O_2})\sqrt{\hat{c}^b_{O_2}}}{(c^{sat}_{O_2} - \hat{c}^b_{O_2})\sqrt{c^b_{O_2}}},$$

where $\hat{c}^b_{O_2}$ is the (incorrect) oxygen bulk concentration we get if we use Eq. (5.7).

The saturation concentration is approximately 10 gO_2m^{-3}, and the actual bulk concentration is about 8 gO_2m^{-3} in the middle of the filter. Then

$$\frac{\hat{K}_{L,O_2}}{K_{L,O_2}} = \frac{\sqrt{0.5\hat{c}^b_{O_2}}}{10 - \hat{c}^b_{O_2}},$$

which enables us to determine the errors in the substrate flux as a function of the quotient $\hat{K}_{L,O_2}/K_{L,O_2}$. In Figure 5.9 the quotient of the estimated substrate flux into the biofilm and the "correct" substrate flux, which is equal to the quotient $(\hat{c}^b_{O_2}/c^b_{O_2})^{0.5}$, is plotted as a function of $\hat{K}_{L,O_2}/K_{L,O_2}$.

From Figure 5.8 we conclude that, generally,

$$0.5\hat{K}_{L,O_2} < K_{L,O_2} < 1.5\hat{K}_{L,O_2}.$$

The maximum errors in substrate flux, corresponding to the dashed lines in Figure 5.9, may then be estimated to be less than approximately five percent. If the

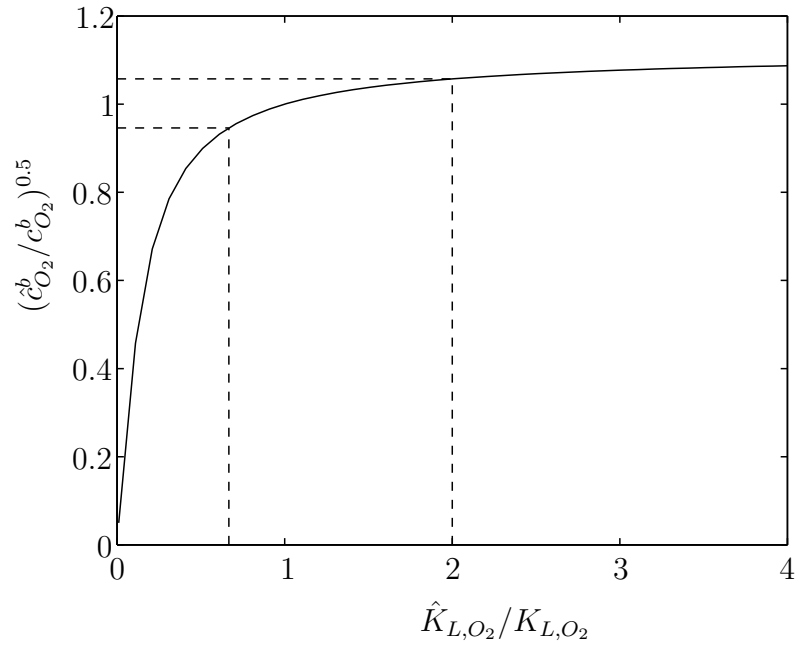

Figure 5.9 *Quotient of estimated substrate flux into biofilm and "correct" substrate flux as a function of the quotient of the approximate transfer coefficient and the exact transfer coefficient.*

bulk is assumed saturated with oxygen, which corresponds to an infinite $\hat{K}_{L,O_2}$, the maximum errors are estimated to be around ten percent.

5.3 Conclusions and Discussion

A continuously stirred biofilm reactor (CSBR) has been defined as a unit consisting of three compartments: a gas phase compartment, a continuously stirred tank with bulk liquid, and a biofilm compartment. The CSBR-units can be used to build models of different biofilm reactors in the same way as continuously stirred tank reactors are used in chemical reaction engineering and design.

The CSBR approach has been applied to a nitrifying trickling filter (NTF), by modeling the filter by cascaded CSBRs. To avoid having to solve the equations for all the CSBRs simultaneously, a simple model of the oxygen flux from the air to the bulk water is used. The flux is set to be proportional to a mass transfer coefficient and the difference between the oxygen bulk concentration and the saturation concentration in water. From measured bulk concentrations of ammonium and oxygen inside a pilot-scale nitrifying trickling filter with cross-flow plastic media, having a specific surface area of 157 m^2m^{-3}, the mass transfer coefficients were determined at different depths of the filter. It was found that the values decreased with depth and increased

with increasing flow. No dependency on the temperature was detected. The average values in the middle parts of the NTF increased from 1.5 md^{-1}, at a hydraulic load of 50 md^{-1}, to 3.3 md^{-1}, at a hydraulic load of 200 md^{-1}. The influent water could be assumed saturated with oxygen.

By using simplified expressions of the nitrification rate, it was shown that the flux of substrates into the biofilm is fairly insensitive to the value of the oxygen mass transfer coefficient. As a rough approximation, the bulk may be assumed saturated with oxygen in the entire NTF.

Chapter 6

FAST DYNAMICS

Using standard simplifying assumptions, models describing the fast dynamics of CSBRs are formulated. From these models non-rational first principle transfer functions are derived for cases when the reaction rate inside the biofilm is of zero or first order. By an investigation of the singularities of these transfer functions, a method to find low order rational transfer functions that approximate the non-rational ones is derived. It is shown how model parameters can be determined from residence time distributions using the transfer functions. Comparisons between model simulations and experiments carried out on nitrifying trickling filters show good agreement. From the comparisons it is concluded that ammonium may adsorb to the biofilm and that denitrification may occur in the inner parts of the biofilm. These phenomena affect the fast transients and imply that grab-sample measurements for determination of nitrification rates, for example, may have to be carried out several mean residence times after changes in operating conditions.

Most of the reported dynamic modeling and work on biofilm reactors have been focused on the slow biofilm dynamics, which have effects on the operation of the plants over longer periods of time (Andersson *et al.* 1994, Boller *et al.* 1997). However, there are several reasons to investigate, model and analyze the fast dynamics also. First of all, in the daily operation of a plant using biofilm reactors the fast dynamics often have to be taken into consideration to optimize the operation, and to guarantee stable control systems. The fast dynamics also play an important role for the reactor efficiency when the substrate load varies quickly (Rittmann 1985). Further, since physically based models of the fast dynamics are in many ways simplifications of more complex models of the slow dynamics, important model parameters are the same [c.f. Kissel *et al.* (1984), Gujer and Wanner (1990), Wik and Breitholtz (1996)]. Hence, parameter identification from experimental data, using models of the fast dynamics, can be a way of acquiring information about the slow dynamics as well.

The first sections of this chapter, where simplified models, based on physical principles and standard assumptions, are presented for the fast dynamics of CSBRs, are

mainly based on the investigations by Wik and Breitholtz (1998) and Wik (1999*b*). When the reaction rate inside the biofilm is of zero or first order, we can derive non-rational first principle transfer functions for the CSBR-models that describe the dynamics caused by changes in influent concentration. By showing that the singularities of these transfer functions are located on the negative real axis, with a distance between them that increases with the distance from zero, a method was developed to derive low order rational transfer functions that approximate the non-rational ones. The approximations have several appealing properties:

- Efficient routines for simulations, using the rational transfer function models, are available in most types of numerical software.
- Many standard methods of controller design require rational transfer functions.
- The derivation only requires Newton-Raphson searches for the values of the singularities and evaluations of a few expressions.
- Changes in physical parameters, in particular the first order rate coefficient that may depend significantly on temperature, can easily be related to changes in the transfer function.
- The approximations are based on a truncation of a sum of first order transfer functions with decreasing time constants and decreasing gain. Thus, the order of an approximate transfer function can be chosen for a specific application in a natural way and without any recalculations.

In the investigations by Wik and Breitholtz (1998) only one dissolved component, or several components that do not depend on each other, were considered. Wik (1999*b*) extended the results to the case of several dependent substrates when applying it to a nitrifying trickling filter.

Fixed biofilm reactors and catalytic reactors with porous catalysts have an attractive analogy, pointed out by Atkinson and Daoud (1968), which follows from the physics of the diffusion and the reaction in biofilms and in catalysts. Under the assumptions used in the development of the models, the mass balances are the same for the CSBRs and continuously stirred catalytic reactors with porous catalyst particles (Aris 1975). Hence, the methods developed for the biofilm reactors also apply to such catalytic reactors if the reaction in the catalyst can be assumed to be of zero or first order.

In the last sections of this chapter comparisons are presented between simulations of the fast dynamics and experiments carried out on pilot plant NTFs at the Rya WWTP in Göteborg and the Sjölunda WWTP in Malmö. The comparisons with the experiments at the Rya WWTP are based on the work by Wik (1997*a*) and Wik (1999*b*), and the comparisons with the experiments at the Sjölunda WWTP are based on the investigations by Wik (1999*a*).

6.1 Modeling

As mentioned in Section 3.4 the dynamics of biofilm systems can be divided into fast and slow modes, where the slow modes are due to biological changes in the biofilm. In this chapter we are only concerned with the fast dynamics, i.e., we assume that the biofilm matrix is unchanged during the periods of time considered here.

The purpose of the models presented in this section is to get simplified models of CSBRs that can be rapidly simulated, used for controller design, predictions and optimization, for example. In addition to the assumptions on pages 19 and 27 we, therefore, make the following assumptions:

A10 Each reaction in the biofilm is linearly dependent on only one substrate concentration in the biofilm.

A11 The mass transfer between the gas phase and the bulk can be ignored.

A12 There is no mass transfer resistance between the bulk and the biofilm.

Typically, the rate at which the bacteria carry out the transformations of substrates follows a nonlinear saturation function in one of the involved substrates. If the concentration is above the saturation level, or if we are interested in modeling other substrates than the rate limiting one, the reaction rate will be of zero order. At low concentrations the rate can be assumed to be of first order with respect to the limiting substrate. In an intermediate region, the rate may sometimes be linearized around an operating point. Assumption **A11** was discussed on page 55. For reactors with thin liquid film flow and reactors with turbulent flow, the boundary layer on the biofilm may be ignored, which is equivalent to assumption **A12**.

If we consider only one dissolved component, the mass balance (5.1) over the bulk in a CSBR combined with Eq. (5.2), can be written in a non-dimensional form as

$$\tau \frac{d}{d\tilde{t}} c^b = c^b_{in} - c^b - \gamma \left. \frac{\partial c}{\partial \xi} \right|_{\xi=1}, \tag{6.1}$$

where

$$\tau = \frac{V}{Q}\lambda, \quad \gamma = \frac{AD}{QL} \quad \text{and} \quad \lambda = \frac{D}{L^2 \epsilon_l},$$

time is scaled as $\tilde{t} = \lambda t$, and space is scaled as $\xi = x/L$ for planar substrata and $\xi = r/L$ for spheres and cylinders. Here, A is the total area of biofilm in the CSBR, and L denotes the value of x and r at the biofilm surface (see Figure 3.2).

Denoting the non-dimensional zero order rate coefficient by μ, which may depend on ξ, and denoting the first order rate coefficient by κ, the boundary conditions and the mass balances in the biofilm, i.e. Eqs. (3.8), (3.16) and (3.19), give the following equations:

Planes

Mass balance:

$$\frac{\partial c}{\partial \tilde{t}} = \frac{\partial^2 c}{\partial \xi^2} - \kappa c - \mu, \quad 0 < \xi < 1. \tag{6.2}$$

Boundary conditions:

$$\frac{\partial c}{\partial \xi} = 0 \ , \ \xi = 0 \quad \text{and} \quad c = c^b \ , \ \xi = 1.$$

Spheres and cylinders

Mass balance:

$$\frac{\partial c}{\partial \tilde{t}} = \frac{p}{\xi}\frac{\partial c}{\partial \xi} + \frac{\partial^2 c}{\partial \xi^2} - \kappa c - \mu, \quad \rho < \xi < 1. \tag{6.3}$$

Boundary conditions:

$$\frac{\partial c}{\partial \xi} = 0 \ , \ \xi = \rho \quad \text{and} \quad c = c^b \ , \ \xi = 1,$$

where $p = 2$ for spheres, $p = 1$ for cylinders, and $\rho = R/L$ (see Figure 3.2). When $\rho = 0$, the inner boundary condition should be replaced by c being bounded at $\rho = 0$.

6.2 Transfer Functions

After subtraction of the stationary solutions ($\bar{c}$ and $\bar{c}^b$) and Laplace transformation of Eqs. (6.2), (6.3) and the boundary conditions, the solutions $\Delta C(s) = \mathcal{L}\{c(\tilde{t}) - \bar{c}(\tilde{t})\}$ for each shape follow from the solutions of the corresponding stationary problems (Aris 1975):

$$\Delta C(\xi, s) = \begin{cases} \Delta C^b(s)\dfrac{\cosh \xi z}{\cosh z} & (plane) \\ \Delta C^b(s)\dfrac{I_0(\xi z)K_1(\rho z) + K_0(\xi z)I_1(\rho z)}{I_0(z)K_1(\rho z) + K_0(z)I_1(\rho z)} & (cylinder) \\ \Delta C^b(s)\dfrac{1}{\xi}\dfrac{z\rho\cosh z(\xi-\rho) + \sinh z(\xi-\rho)}{z\rho\cosh z(1-\rho) + \sinh z(1-\rho)} & (sphere), \end{cases}$$

where $z = \sqrt{s+\kappa}$, I_0 and I_1 are modified Bessel functions of the first kind, of zero and first order, and K_0 and K_1 are modified Bessel functions of the second kind, of zero and first order.

Subtraction of the stationary solution $\bar{c}^b$ to Eq. (6.1), Laplace transformation and insertion of the derivatives of the above expressions for $\Delta C(\xi, s)$ at $\xi = 1$, give the

following transfer function for a CSBR:

$$G(s) = \frac{\Delta C^b(s)}{\Delta C^b_{in}(s)} = \frac{K}{1 + \tilde{\tau} z^2 + \tilde{\gamma} M(z)}, \tag{6.4}$$

where

$$K = \frac{1}{1 - \tau\kappa}, \quad \tilde{\tau} = K\tau \quad \text{and} \quad \tilde{\gamma} = K\gamma.$$

The function $M(z)$ depends on the shape of the substrata:

$$M(z) = \begin{cases} z \tanh z & (plane) \\ z\dfrac{K_1(\rho z)I_1(z) - K_1(z)I_1(\rho z)}{K_1(\rho z)I_0(z) + K_0(z)I_1(\rho z)} & (cylinder) \\ -1 + z\dfrac{\rho z \sinh \delta z + \cosh \delta z}{\rho z \cosh \delta z + \sinh \delta z} & (sphere), \end{cases} \tag{6.5}$$

where $\delta = 1 - \rho$ is the non-dimensional biofilm thickness. Note that the zero order rate coefficient $\mu(\xi)$ has no effect on how changes in influent concentrations affect the effluent concentrations.

The transfer function (6.4) can also be applied to biological slabs and flocs, and the corresponding catalyst particles. For planar slabs of thickness $2L$, cylinder flocs ($\rho = 0$) and sphere flocs ($\rho = 0$), $M(z)$ remain the same for the slabs but simplify to $zI_1(z)/I_0(z)$ for cylinders and $-1 + z \coth z$ for spheres.

6.2.1 Singularities

The method of deriving rational transfer functions by Wik and Breitholtz (1998) requires that the locations of the singularities of the transfer function $G(s)$ are known. The singularities follow from setting the denominator in $G(s)$ equal to zero:

$$1 + \tilde{\tau} z^2 + \tilde{\gamma} M(z) = 0, \tag{6.6}$$

or equivalently:

$$M(z) = -\frac{\tau}{\gamma}(z^2 + \frac{1}{\tau} - \kappa). \tag{6.7}$$

In Appendix C it is shown that if $z = x + iy$ the imaginary part of $M(z)$ has the same sign as xy for all shapes considered. Since the sign of the imaginary part of the right hand side equals that of $-xy$, all possible solutions to Eq. (6.7) must be located on the real and imaginary axes.

On the real axis $M(x)$ is a positive even function for all shapes. Hence, solutions to Eq. (6.6) may exist on the real axis only if $\kappa > 1/\tau$ ($\tilde{\gamma}$ and $\tilde{\tau}$ less than zero). The solutions are centered around $x = 0$, where the positive solutions have to be less than $\sqrt{\kappa - 1/\tau}$. Hence, both the real solutions $z = x$ and the imaginary solutions

$z = iy$ to Eq. (6.7) result in singularities to $G(s)$, i.e. $\alpha = z^2 - \kappa$, located on the negative real axis. This implies that the CSBR-system is stable, i.e., bounded changes in influent concentration can never cause uncontrolled oscillations in the effluent concentration from the reactor.

Since $M(x)$ is monotonous for $x > 0$, there may be only one singularity $\alpha = x^2 - \kappa$ corresponding to a real solution x to Eq. (6.7). Below, it is shown that the remaining singularities $\alpha = -y^2 - \kappa$, corresponding to imaginary solutions iy to Eq. (6.7), are located in non-overlapping intervals of increasing size. Because the singularities are then spread out along the negative real axis with larger and larger distances between them they are *countable*, which is used in the derivation of the rational approximations of $G(s)$. Knowing the approximate locations of the singularities, they may readily be found numerically by a Newton-Raphson method, for example.

Planes

Using $\tanh iy = i \tan y$, the solutions to Eq. (6.7) on the imaginary axis are given by:

$$\tilde{\gamma} \tan y = \frac{1}{y} - \tilde{\tau} y. \tag{6.8}$$

The solutions to this equation are centered around $y = 0$. When $\tilde{\tau}$ and $\tilde{\gamma}$ are positive, the positive solutions satisfy

$$0 < y_1 < \frac{\pi}{2} < y_2 < \frac{3\pi}{2} < y_3 < \frac{5\pi}{2} < y_4 < \ \ldots \tag{6.9}$$

and when $\tilde{\tau}$ and $\tilde{\gamma}$ are negative, the positive solutions satisfy

$$\frac{\pi}{2} < y_1 < \frac{3\pi}{2} < y_2 < \frac{5\pi}{2} < y_3 < \ \ldots \tag{6.10}$$

Cylinders

Using the relations $I_n(iy) = i^n J_n(y)$, $K_n(iy) = (\pi/2) i^{n+1} (-1)^n [J_n(y) + i Y_n(y)]$, where J_n and Y_n are Bessel functions of the first and second kind, and of order n, it follows that the solutions $z = iy$ to Eq. (6.6) on the imaginary axis are given by

$$\tilde{\gamma} \frac{J_1(\rho y) Y_1(y) - Y_1(\rho y) J_1(y)}{Y_1(\rho y) J_0(y) - Y_0(y) J_1(\rho y)} = \frac{1}{y} - \tilde{\tau} y.$$

The expression on the left hand side is the quotient of two equally damped oscillatory functions of y. Hence, the solutions are restricted to the intervals between the zeros of the denominator. For large y the expression approaches $-\tilde{\gamma} \tan \delta y$, and then the singularities are located in intervals similar to those for planar coordinates.

When $\rho = 0$, the solutions are located between the zeros of J_0, which can be found in tables of Bessel functions (Råde and Westergren 1990).

Spheres

On the imaginary axis, $M(z)$ becomes

$$M(iy) = \frac{\delta y - (1 + \rho y^2)\tan \delta y}{\rho y + \tan \delta y}$$

and Eq. (6.6) can be written

$$\tan \delta y = y \frac{\delta\tilde{\gamma} + \rho - \tilde{\tau} y^2}{\tilde{\gamma} - 1 + (\rho\tilde{\gamma} + \tilde{\tau}) y^2}.$$

Similar to the case of planar biofilms, the solutions are constrained to the intervals between the singularities of $\tan \delta y$.

6.2.2 Rational Transfer Functions

The transfer function (6.4) is not suitable for most standard methods of simulation, optimization and controller design. Instead, rational functions are desired, for which there are numerous standard routines available in software, such as MATLAB and MATRIXx.

Rational approximations of $G(s)$ will be derived by first determining the exact unit impulse response (or weighting function), i.e., the inverse Laplace transform of $G(s)$, and then finding a rational $\hat{G}(s)$ that arbitrarily well approximates the exact response. The theorems and definitions used can be found in standard textbooks on analytical functions [see e.g. Fischer (1990)].

Denote the denominator of $G(s)$ by $F(s)$. The inverse Laplace transform of $G(s)$ is then

$$g(\tilde{t}) = \lim_{\sigma \to \infty} \frac{1}{2\pi i} \int_{\kappa - i\sigma}^{\kappa + i\sigma} \frac{K e^{s\tilde{t}}}{F(s)} ds.$$

Since the singularities are *countable* and located left of $s = \kappa$, we may use the *Residue Theorem* to determine the inverse Laplace transform:

$$g(\tilde{t}) = \frac{1}{2\pi i} \oint_{\Omega} \frac{K e^{s\tilde{t}}}{F(s)} ds \tag{6.11}$$

$$= K \sum_{k=1}^{\infty} \operatorname{Res} \left\{ \frac{e^{s\tilde{t}}}{F(s)} \right\}_{s=\alpha_k}, \tag{6.12}$$

where α_k are the locations of the singularities of $G(s)$, and Ω is the region left of $s = \kappa$ in the complex plane.

The denominator $F(s)$ is analytic in a neighborhood of each singularity α_k of $G(s)$. Hence, there exists a convergent Taylor expansion around each singularity:

$$F(s) = F(\alpha_k) + \left.\frac{dF}{ds}\right|_{s=\alpha_k} (s-\alpha_k) + \sum_{p=2}^{\infty} \frac{1}{p!} \left.\frac{d^p F}{ds^p}\right|_{s=\alpha_k} (s-\alpha_k)^p, \tag{6.13}$$

where $F(\alpha_k) = 0$ and

$$F'(\alpha_k) = \left.\frac{dF}{ds}\right|_{s=\alpha_k} = \tilde{\tau} + \frac{\tilde{\gamma}}{2z_k} \left.\frac{dM}{dz}\right|_{z_k=\sqrt{\alpha_k+\kappa}}.$$

Since the derivatives $F'(\alpha_k)$ are evaluated at intersection points between the rapidly changing left side of (6.7) and the square function on the right, $F'(\alpha_k)$ cannot be zero. Thus, the integrand in Eq. (6.11) has poles of order one at α_k and the residues are given by

$$\text{Res}\left\{\frac{e^{s\tilde{t}}}{F(s)}\right\}_{s=\alpha_k} = \frac{e^{\alpha_k \tilde{t}}}{F'(\alpha_k)}.$$

This gives the impulse response

$$g(\,\tilde{t}\,) = K \sum_{k=1}^{\infty} \frac{e^{\alpha_k \tilde{t}}}{F'(\alpha_k)}, \tag{6.14}$$

which is exactly the pulse response of the rational transfer function

$$\bar{G}(s) = \sum_{k=1}^{\infty} \frac{K}{F'(\alpha_k)(s-\alpha_k)}. \tag{6.15}$$

Since this transfer function must have the same stationary gain as $G(s)$, i.e. G(0), the *Final Value Theorem* implies that the sum in Eq. (6.15) is convergent for $s = 0$ (Kamen 1996). Further, the singularities α_k become largely negative with increasing k, which means that the terms represent faster and faster dynamic modes. Hence, only the first terms in the sum are significant for describing the dynamics. An arbitrarily good approximation can therefore be achieved by truncating the sum after m terms:

$$\hat{G}(s) = \sum_{k=1}^{m} \frac{K}{F'(\alpha_k)(s-\alpha_k)}. \tag{6.16}$$

Adding the stationary gain of the ignored terms to get a correct description of the steady-state behavior gives:

$$\hat{G}(s) = \sum_{k=1}^{m} \frac{K}{F'(\alpha_k)(s-\alpha_k)} + G(0) + \sum_{k=1}^{m} \frac{K}{F'(\alpha_k)\alpha_k}. \tag{6.17}$$

Due to the added direct term, this transfer function is not *strictly proper*, i.e., the degree of the numerator is not less than the degree of the denominator (Kamen 1996).

If it is required to be strictly proper *and* have a correct stationary gain then we may instead scale the expression (6.16) according to

$$\hat{G}(s) = -G(0)\left(\sum_{k=1}^{m}\frac{K}{F'(\alpha_k)\alpha_k}\right)^{-1}\sum_{k=1}^{m}\frac{K}{F'(\alpha_k)(s-\alpha_k)}. \tag{6.18}$$

Scaling back to original time is achieved by dividing s in the transfer functions by the time-scaling factor λ.

Most transfer functions derived from physical models are strictly proper and, therefore, there are methods for controller design and algorithms for system identification that are constructed for strictly proper transfer functions. In such cases expression (6.16) or (6.18) can be used. In simulations, however, the approximation (6.17) is generally to be preferred. An illustration of the differences between the two approximation methods is presented in Figure 6.1. We see that the approximation (6.17) gives a better approximation for low frequencies but is inferior at high frequencies due to the direct term.

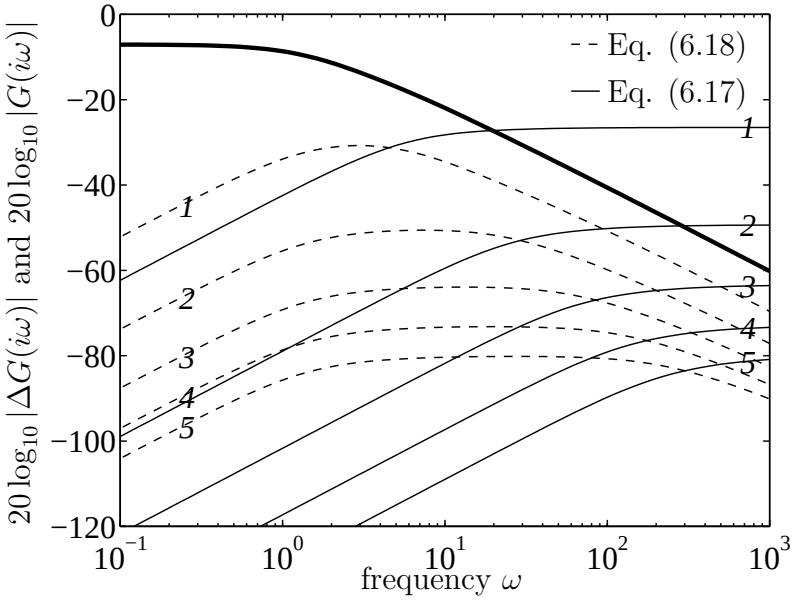

Figure 6.1 *Amplitude of $G(i\omega)$ (thick line) for planar substrata with $\tau = 1$, $\gamma = 1$ and $\kappa = 2$, and amplitudes of the approximation errors $\Delta G(i\omega) = \hat{G}(i\omega) - G(i\omega)$ for transfer functions up to order $m = 5$.*

6.2.3 Comparison with Other Methods

Several other well established methods, based on approximations of the biofilm mass balances (6.2) and (6.3), can be used to derive rational transfer functions

for the CSBR-model. These methods approximate the bulk mass balance (6.1) separately and, thus, one state variable is always used for the bulk concentration. In the proposed "residue method" the approximations are made in the frequency plane instead of in space, and it is therefore the combined behavior of both mass balances that is approximated. For low order approximations the residue method can therefore be expected to give better accuracy, particularly up to frequencies around α_{m+1}.

We choose to compare the performance of the residue method with two methods commonly used: a finite difference method and the Galerkin method using Legendre polynomials. The former one is intuitive and simple to formulate, and the Galerkin method generally gives accurate low order approximations (Finlayson 1972). Below, the applications of the three methods to a CSBR with planar substrata and $\tau = 1$, $\gamma = 1$ and $\kappa = 2$, or $\kappa = 20$, are summarized. The results of the comparisons are illustrated in Figures 6.2 and 6.3.

The Residue Method

Since $\kappa > 1/\tau$, there is one singularity corresponding to a solution to Eq. (6.7) on the real axis. Hence, solve Eq. (6.7) with $z = x > 0$ to get the singularity $\alpha_1 = x^2 - \kappa$. The remaining singularities $\alpha_k = y_{k-1}^2 - \kappa$, $k = 2 \dots m$ follow from solving Eq. (6.8) on the intervals given by (6.10). Then calculate

$$\begin{aligned} F'(\alpha_1) &= \tilde{\tau} + \frac{\tilde{\gamma}}{2x}(x + \tanh x - x \tanh^2 x) \\ F'(\alpha_k) &= \tilde{\tau} + \frac{\tilde{\gamma}}{2y_{k-1}}(y_{k-1} + \tan y_{k-1} + y_{k-1} \tan^2 y_{k-1}), \quad k = 2 \dots m \\ G(0) &= 1/(1 + \gamma\sqrt{\kappa} \tanh \sqrt{\kappa}), \end{aligned}$$

and insert these values and the values of α_k in Eq. (6.17), which gives an mth order transfer function.

The Finite Difference Method

Let $\xi_k = k\xi/m$, $k = 0, 1, \dots m$ be a discretization of the biofilm. Use symmetric central differences to approximate the second order space derivative in Eq. (6.2) and define an approximation $c_k(\tilde{t})$ of $c(\xi_k, \tilde{t})$ by

$$\frac{d}{d\tilde{t}} c_k = \frac{c_{k-1} - 2c_k + c_{k+1}}{(1/m)^2} - \kappa c_k, \quad k = 1, 2, \dots m-1,$$

$$c_1 = c_0 \quad \text{and} \quad c_m = \hat{c}^b,$$

where $\hat{c}^b$ is an approximation of the bulk concentration defined by [c.f. Eq. (6.1)]

$$\tau \frac{d}{d\tilde{t}} \hat{c}^b = c_{in}^b - \hat{c}^b - \gamma \frac{c_m - c_{m-1}}{(1/m)}.$$

The above equations can be written in the state space form

$$\begin{aligned} \frac{dx}{d\tilde{t}} &= \Phi x + \Gamma c_{in}^b \\ c^b &= \Psi x, \end{aligned}$$

where $x = [c_1 \dots c_m]^T$, $\Gamma = [0 \dots 0 \ \frac{1}{\tau}]^T$,$\Psi = [0 \dots 0 \ 1]$ and Φ is a tridiagonal matrix.

An mth order transfer function is then given by

$$\hat{G}(s) = \Psi[sI - \Phi]^{-1}\Gamma.$$

The Galerkin Method

Extend the mass balance (6.2) to $-1 < \xi < 1$. Since the solution must be symmetric around $\xi = 0$, we approximate the concentration in the biofilm with the trial function

$$\hat{c}(\xi, \tilde{t}\,) = \sum_{k=0}^{m-1} x_k(\,\tilde{t}\,) P_{2k}(\xi),$$

where P_{2k} are Legendre polynomials of order $2k$, orthogonal on the interval $[-1, 1]$ and normed such that $P_{2k}(1) = 1$. Forcing this approximation to satisfy the boundary condition $\hat{c}(1, \tilde{t}\,) = \hat{c}^b(\,\tilde{t}\,)$, setting the weighted residuals to zero and inserting the approximation into Eq. (6.1), give

$$\begin{aligned} \sum_{k=0}^{m-1} x_k &= \hat{c}^b \\ 0 &= \sum_{k=0}^{m-1} \left\{ \frac{dx_k}{dt}(P_{2n}, P_{2k}) - x_k \left((P_{2n}, \frac{d^2 P_{2k}}{d\xi^2}) - \kappa(P_{2n}, P_{2k}) \right) \right\}, \\ & \qquad\qquad n = 0, 1, \dots m-1, \\ \tau \frac{d}{d\tilde{t}} \hat{c}^b &= c_{in}^b - \hat{c}^b - \gamma \sum_{k=0}^{m-1} x_k \left. \frac{dP}{d\xi} \right|_{\xi=1}, \end{aligned}$$

where

$$(u, v) = \int_{-1}^{1} uv d\xi.$$

Use the first equation to eliminate x_{m-1} in the other two equations, for example. The result may then be written in a linear state space form, from which an mth order transfer function $\hat{G}(s)$ can be derived in the same manner as for the finite difference method. It should be noted that in this particular problem the Galerkin method equals that of the least square method, which minimizes the integral of the squared error of Eq. (6.2) when c is replaced by its approximation $\hat{c}$.

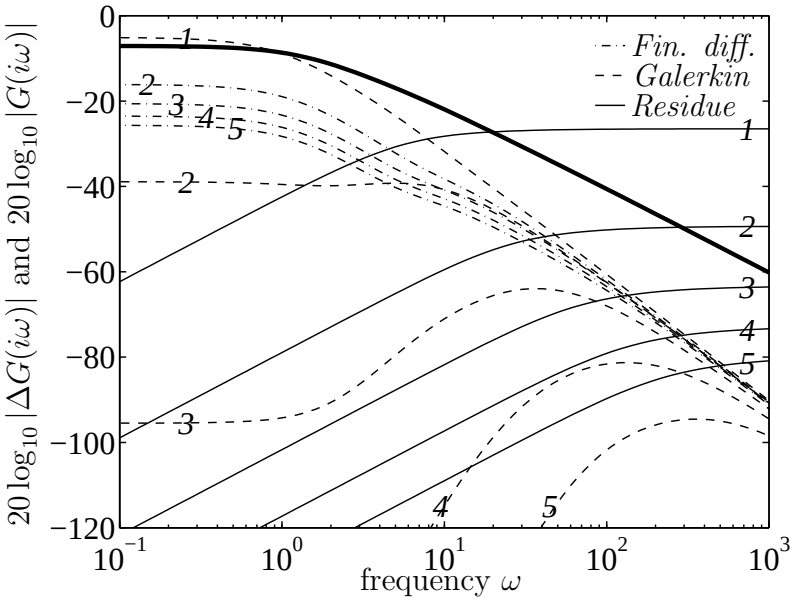

Figure 6.2 *Amplitude of $G(i\omega)$ (thick line) for planar substrata with $\tau = 1$, $\gamma = 1$ and $\kappa = 2$, and amplitudes of the approximation errors $\Delta G(i\omega) = \hat{G}(i\omega) - G(i\omega)$ for transfer function orders up to $m = 5$. Note that the lowest order of the finite difference method is $m = 2$.*

A few general features of the different approximation methods are apparent in Figures 6.2 and 6.3. The residue method gives incorrect high frequency gains due to the direct terms in Eq. (6.17). This will be avoided if the approximation (6.18) is used instead of (6.17), but at the cost of a lower accuracy for low frequencies (see Figure 6.1). Both the finite difference method and the Galerkin method have errors in the stationary gains. This stationary bias is zero when $\kappa = 0$ but increases as κ increases. For higher order approximations the Galerkin method gives the best approximations. However, for the frequencies of particular interest in controller design, i.e. where the gain of G starts to decrease, the low order approximations of the residue method are the most accurate. Even a first order transfer function may give accurate results if κ is large. This is particularly advantageous when several CSBRs are used to model a reactor since it may then be crucial to keep the order of the approximations at a minimum. As can be expected, the finite difference method gives the least accurate approximations.

6.2.4 Extension to Several Dissolved Components

An extension of the residue method to the case of several substrates is illustrated by an application to a nitrifying CSBR with planar biofilm substrata. The reaction

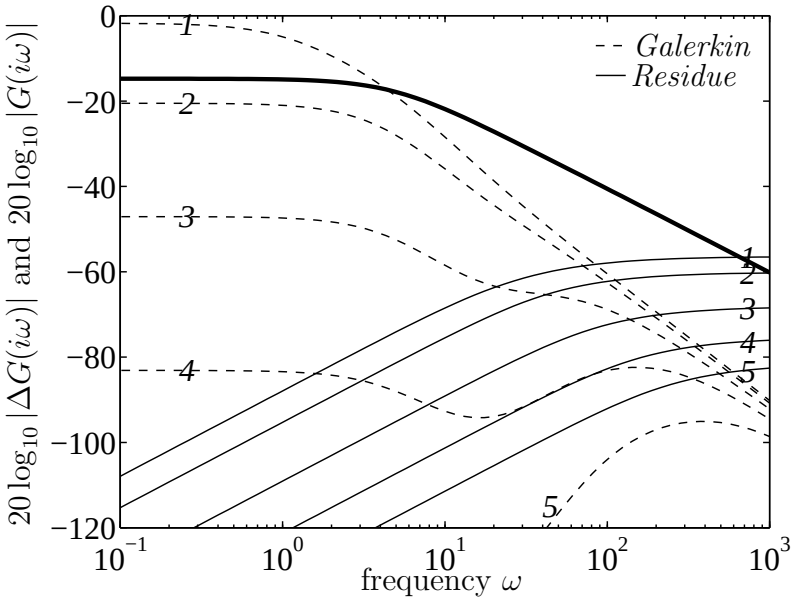

Figure 6.3 *Amplitude of $G(i\omega)$ (thick line) for planar substrata with $\tau = 1$, $\gamma = 1$ and $\kappa = 20$, and amplitudes of the approximation errors $\Delta G(i\omega) = \hat{G}(i\omega) - G(i\omega)$ for transfer function orders up to $m = 5$ determined by the residue method and by the Galerkin method.*

treated is the complete nitrification of ammonium into nitrate:

$$\mathrm{NH_4^+ + 2HCO_3^- + 2O_2 \rightarrow NO_3^- + 3H_2O + 2CO_2},$$

where only changes in ammonium and nitrate concentrations are considered.

Later on in this chapter it will be shown that ammonium may adsorb to the biofilm and that the amount of adsorbed ammonium can be assumed to be proportional to the ammonium concentration in the biofilm. Included in the model is, therefore, an adsorbed amount $k_a c_{NH_4}$ of ammonium, which changes the mass balance (3.8) for ammonium to (6.50) on page 108.

The non-dimensional mass balances over the bulk volume in a CSBR may then be written as

$$\tau \frac{d}{d\tilde{t}} c^b_{NH_4} = c^b_{NH_4,in} - c^b_{NH_4} - \gamma_1 \left[\frac{\partial}{\partial \xi} c_{NH_4} \right]_{\xi=1} \tag{6.19}$$

$$\tau \frac{d}{d\tilde{t}} c^b_{NO_3} = c^b_{NO_3,in} - c^b_{NO_3} - \gamma_2 \left[\frac{\partial}{\partial \xi} c_{NO_3} \right]_{\xi=1}, \tag{6.20}$$

where $\tilde{t} = \lambda t$, $\xi = x/L$ and

$$\tau = \frac{V}{Q}\lambda, \quad \lambda = \frac{D_{NH_4}}{L^2(\epsilon_l + k_a)}, \quad \gamma_1 = \frac{AD_{NH_4}}{QL} \quad \text{and} \quad \gamma_2 = \frac{AD_{NO_3}}{QL}.$$

Assuming a linear dependence of the intrinsic reaction rate r_v on the ammonium concentration, i.e.

$$r_{v,NH_4} = -(k_0 + k_1 c_{NH_4}), \tag{6.21}$$

the mass balances in the biofilm become

$$\frac{\partial}{\partial \tilde{t}} c_{NH_4} = \frac{\partial^2}{\partial \xi^2} c_{NH_4} - \kappa_1 c_{NH_4} - \mu_1, \tag{6.22}$$

$$\varrho \frac{\partial}{\partial \tilde{t}} c_{NO_3} = \frac{\partial^2}{\partial \xi^2} c_{NO_3} + \kappa_2 c_{NH_4} + \mu_2, \tag{6.23}$$

with boundary conditions

$$\left[\frac{\partial}{\partial \xi} c_{NH_4}\right]_{\xi=0} = 0 \quad \text{and} \quad c_{NH_4} = c^b_{NH_4} \quad \text{at} \quad \xi = 1,$$

$$\left[\frac{\partial}{\partial \xi} c_{NO_3}\right]_{\xi=0} = 0 \quad \text{and} \quad c_{NO_3} = c^b_{NO_3} \quad \text{at} \quad \xi = 1,$$

where

$$\kappa_1 = \frac{L^2}{D_{NH_4}} k_1, \qquad \mu_1 = \frac{L^2}{D_{NH_4}} k_0,$$

$$\kappa_2 = \frac{L^2}{D_{NO_3}} k_1, \qquad \mu_2 = \frac{L^2}{D_{NO_3}} k_0,$$

and

$$\varrho = \frac{D_{NH_4} \epsilon_l}{D_{NO_3}(\epsilon_l + k_a)}.$$

Laplace transformation of Eqs. (6.22), (6.23) and the boundary conditions after the stationary solutions have been subtracted gives

$$\frac{d^2}{d\xi^2} \Delta C_{NH_4} = (s + \kappa_1) \Delta C_{NH_4},$$

$$\frac{d^2}{d\xi^2} \Delta C_{NO_3} = \varrho s \Delta C_{NO_3} - \kappa_2 \Delta C_{NH_4},$$

and

$$\left[\frac{d}{d\xi} \Delta C_{NH_4}\right]_{\xi=0} = 0, \qquad \Delta C_{NH_4}(1, s) = \Delta C^b_{NH_4}(s),$$

$$\left[\frac{d}{d\xi} \Delta C_{NO_3}\right]_{\xi=0} = 0, \qquad \Delta C_{NO_3}(1, s) = \Delta C^b_{NO_3}(s),$$

where $\Delta C(s) = \mathcal{L}\left\{c(\tilde{t}) - \bar{c}(\tilde{t})\right\}$. These equations have the solutions

$$\Delta C_{NH_4} = \Delta C^b_{NH_4} \frac{\cosh \xi z_1}{\cosh z_1},$$

$$\Delta C_{NO_3} = \Delta C^b_{NO_3} \frac{\cosh \xi z_2}{\cosh z_2} + \Delta C^b_{NH_4} \frac{\kappa_2}{z_1^2 - z_2^2} \left\{ \frac{\cosh \xi z_2}{\cosh z_2} - \frac{\cosh \xi z_1}{\cosh z_1} \right\},$$

where $z_1 = \sqrt{s+\kappa_1}$ and $z_2 = \sqrt{\varrho s}$.

Subtracting the stationary solutions $\bar{c}_i^b$ from Eqs. (6.19) and (6.20), Laplace transforming the resulting equations and inserting ΔC_{NH_4} and ΔC_{NO_3}, differentiated and evaluated at $\xi = 1$, give

$$\begin{aligned}
\Delta C^b_{NH_4}(s) &= \frac{1}{\Psi_1(s)} \Delta C^b_{NH_4,in}(s) \\
\Delta C^b_{NO_3}(s) &= \frac{1}{\Psi_2(s)} \Delta C^b_{NO_3,in}(s) + \frac{\Lambda(s)}{\Psi_2(s)\Psi_1(s)} \Delta C^b_{NH_4,in}(s),
\end{aligned}$$

where

$$\begin{aligned}
\Psi_1(s) &= 1 + \tau s + \gamma_1 z_1 \tanh z_1 \\
\Psi_2(s) &= 1 + \tau s + \gamma_2 z_2 \tanh z_2 \\
\Lambda(s) &= \frac{\gamma_2 \kappa_2}{z_1^2 - z_2^2}(z_1 \tanh z_1 - z_2 \tanh z_2).
\end{aligned}$$

In transfer matrix form this can be written $\Delta C^b(s) = G(s) \Delta C^b_{in}(s)$, i.e.

$$\begin{bmatrix} \Delta C^b_{NH_4}(s) \\ \Delta C^b_{NO_3}(s) \end{bmatrix} = \begin{bmatrix} G_{11}(s) & 0 \\ G_{21}(s) & G_{22}(s) \end{bmatrix} \begin{bmatrix} \Delta C^b_{NH_4,in}(s) \\ \Delta C^b_{NO_3,in}(s) \end{bmatrix},$$

where

$$G_{11}(s) = \frac{1}{\Psi_1(s)}, \quad G_{22}(s) = \frac{1}{\Psi_2(s)} \quad \text{and} \quad G_{21}(s) = \Lambda(s) G_{11}(s) G_{22}(s).$$

The transfer functions $G_{11}(s)$ and $G_{22}(s)$ are equal to those for single-substrate systems, which have already been treated. When the reaction is of zero order ($k_1 = 0$) the transfer function matrix is diagonal, i.e. $G_{21}(s) = 0$, and the system can be seen as two single-substrate systems.

The singularities α of $\Lambda(s)$ are given by the singularities of $\tanh z_1$ and $\tanh z_2$, which are of first order and given by

$$z_j = i(l + 1/2)\pi, \quad j = 1, 2, \quad l = 0, \pm 1, \pm 2, \ldots.$$

Hence,

$$\begin{aligned}
\alpha_l &= -(l + \frac{1}{2})^2 \pi^2 - \kappa_1, \qquad l = 0, 1, 2, \ldots \\
\alpha_p &= \quad -(p + \frac{1}{2})^2 \frac{\pi^2}{\varrho}, \qquad p = 0, 1, 2, \ldots.
\end{aligned}$$

These singularities are countable, located on the negative real axis, and of first order. Hence, we may use the same methods as for single-substrate systems to determine the impulse response of $\Lambda(s)$:

$$g_\Lambda(\tilde{t}\,) = \sum_{l=1}^{\infty} \operatorname{Res}\left\{ e^{s\tilde{t}} \Lambda(s) \right\}_{s=\alpha_l} + \sum_{p=1}^{\infty} \operatorname{Res}\left\{ e^{s\tilde{t}} \Lambda(s) \right\}_{s=\alpha_p},$$

where

$$\text{Res}\left\{e^{s\tilde{t}}\Lambda(s)\right\}_{s=\alpha} = \lim_{s\to\alpha}(s-\alpha)e^{s\tilde{t}}\Lambda(s).$$

By using l'Hospitals' rule it is straightforward to show that

$$\begin{aligned}\text{Res}\left\{e^{s\tilde{t}}\Lambda(s)\right\}_{s=\alpha_l} &= \frac{2\gamma_2\kappa_2 z_1^2(\alpha_l)}{z_1^2(\alpha_l)-z_2^2(\alpha_l)}e^{\alpha_l\tilde{t}}\\ \text{Res}\left\{e^{s\tilde{t}}\Lambda(s)\right\}_{s=\alpha_p} &= \frac{2\gamma_2\kappa_2 z_2^2(\alpha_p)}{\varrho(z_1^2(\alpha_p)-z_2^2(\alpha_p))}e^{\alpha_p\tilde{t}}.\end{aligned}$$

Noting that $z_1^2 = z_2^2/\varrho + \kappa_1$, we have

$$z_1^2 - z_2^2 = z_1^2(1-\varrho) + \varrho\kappa_1 = (z_2^2(1-\varrho) + \varrho\kappa_1)/\varrho.$$

If we let $\beta_k = (k-\frac{1}{2})^2\pi^2$ and sum up the residues, we get

$$g_\Lambda(\tilde{t}) = 2\gamma_2\kappa_2\sum_{k=1}^{\infty}\frac{\beta_k}{\beta_k(1-\varrho)-\varrho\kappa_1}(e^{-(\beta_k+\kappa_1)\tilde{t}} - e^{-\beta_k\tilde{t}/\varrho}),$$

which is also the unit impulse response of

$$\bar{\Lambda}(s) = 2\gamma_2\kappa_2\sum_{k=1}^{\infty}\frac{\beta_k/\varrho}{(s+\beta_k+\kappa_1)(s+\beta_k/\varrho)}. \tag{6.24}$$

Since the time constants ϱ/β_k and $1/(\beta_k+\kappa_1)$ decrease rapidly with k, the terms in $\bar{\Lambda}$ correspond to faster and faster dynamic modes as k increases. This implies that arbitrarily close approximations can be achieved by truncating the sum. If a correct stationary gain is required, the stationary gain of the terms ignored in the truncation can be added to the truncated sum, i.e.,

$$\hat{\Lambda}(s) = 2\gamma_2\kappa_2\sum_{k=1}^{m_\Lambda}\frac{\beta_k/\varrho}{(s+\beta_k+\kappa_1)(s+\beta_k/\varrho)} + \Lambda^\circ, \tag{6.25}$$

where

$$\begin{aligned}\Lambda^\circ &= \Lambda(0) - 2\gamma_2\kappa_2\sum_{k=1}^{m_\Lambda}\frac{1}{\beta_k+\kappa_1}\\ &= \frac{\gamma_2\kappa_2}{\sqrt{\kappa_1}}\tanh\sqrt{\kappa_1} - 2\gamma_2\kappa_2\sum_{k=1}^{m_\Lambda}\frac{1}{\beta_k+\kappa_1}.\end{aligned} \tag{6.26}$$

The transfer function matrix $G(s)$ may now be approximated by

$$\hat{G}(s) = \begin{bmatrix}\hat{G}_{11}(s) & 0\\ \hat{\Lambda}(s)\hat{G}_{11}(s)\hat{G}_{22}(s) & \hat{G}_{22}(s)\end{bmatrix}, \tag{6.27}$$

where $\hat{G}_{11}(s)$ and $\hat{G}_{22}(s)$ are the approximations for single-substrate systems. The scaling back to original time is achieved by dividing s by the time-scaling factor λ.

6.3 Parameter Estimation from Pulse Responses

Determination of model parameters from residence time distributions (RTDs) is a standard procedure in chemical reactor analysis and design. Typically, a trace substance is dissolved in a small volume and added to the influent to the reactor. Assuming that the duration of the addition can be ignored, the effluent concentration of the trace substance is related to the unit impulse response according to

$$c^b_{out}(t) = \frac{m_\delta}{Q} g(t), \tag{6.28}$$

where m_δ is the mass of the added trace substance and t is the time after the addition.

Two common methods of parameter estimation from RTDs are least square fitting of simulated responses to measurement data and determination using the measured moments around the mean residence time. The latter method is usually easier to implement and also more rapid, but may give poor results if the measured concentrations do not agree well with the ones predicted by the model. In this section it will be shown how both methods apply to CSBR-systems. Particularly, the case of cascaded identical CSBRs will be discussed.

6.3.1 Methods to Simulate Pulse Responses

Simulation of impulse responses for CSBRs can be carried out by:

- Solving the PDEs describing the concentrations in the biofilm, together with the mass balances over the bulk, using a PDE-solver.
- Using approximate transfer functions, such as Eq. (6.17) and Eq. (6.18), and routines for impulse responses in software, such as MATLAB and MATRIXx.
- Using approximate transfer functions to derive explicit expressions for the corresponding impulse responses.
- Truncating the impulse response of the exact transfer function.

Estimating parameters by least square fitting of simulated responses to measurement data have to be carried out with nonlinear search methods, which implies that it is important to keep the execution time of a simulation short. Least square estimations using the first method above can, therefore, be expected to be rather slow.

If the reactor is modeled as N cascaded CSBRs (see Figure 5.4), we have

$$\Delta C^b_n(s) = G_n(s)\Delta C^b_{n-1}(s), \qquad n = 1, \ldots N,$$

where $G_n(s)$ is the transfer function for the nth CSBR. Thus, the transfer function for the entire reactor is

$$G(s) = \prod_{n=1}^{N} G_n(s).$$

If we have access to software with special routines to simulate pulse responses of transfer functions, we can determine approximate impulse responses by replacing $G_n(s)$ with $\hat{G}_n(s)$ determined with (6.16), (6.17) or (6.18), for example.

Approximations can also be directly calculated from the approximate transfer functions. If the reactor is not divided into equal CSBRs, the values of $\tilde{\tau}$ and $\tilde{\gamma}$ are different for each CSBR and, thus, the locations of the singularities α_k will also differ. Let α_{kn} be the kth singularity of $G_n(s)$. Using Eq. (6.16) the approximate transfer function in the original time-scale is then

$$\hat{G}(s) = \prod_{n=1}^{N} \sum_{k=1}^{m} \frac{\lambda_n K_n}{F'(\alpha_{kn})(s - \lambda_n \alpha_{kn})}.$$

Partial fraction decomposition (PFD) applied to the products in this expression gives

$$\hat{G}(s) = \sum_{n=1}^{N} \sum_{k=1}^{m} \frac{b_{kn}}{s - \lambda_n \alpha_{kn}}, \tag{6.29}$$

where

$$b_{kn} = \frac{\lambda_n K_n}{F'(\alpha_{kn})} \prod_{\substack{i=1 \\ i \neq n}}^{N} \sum_{l=1}^{m} \frac{K_i \lambda_i}{F'(\alpha_{li})(\lambda_n \alpha_{kn} - \lambda_i \alpha_{li})}. \tag{6.30}$$

The impulse response follows from the inverse Laplace transform of (6.29):

$$g(t) = \sum_{n=1}^{N} \sum_{k=1}^{m} b_{kn} e^{\alpha_{kn} t}.$$

If the reactor is divided into equal CSTRs, the approximate transfer function (dimensionless time) becomes

$$\hat{G}(s) = \left(\sum_{k=1}^{m} \frac{K}{F'(\alpha_k)(s - \alpha_k)} \right)^N. \tag{6.31}$$

PFD carried out on this expression gives

$$\hat{G}(s) = K^N \sum_{k=1}^{m} \sum_{n=1}^{N} \frac{b_{kn}}{(s - \alpha_k)^n}. \tag{6.32}$$

Taking the inverse Laplace transform of this expression and scaling back to the original time-scale give the impulse response

$$g(t) = K^N \sum_{k=1}^{m} \sum_{n=1}^{N} \frac{b_{kn} (\lambda t)^{n-1}}{(n-1)!} e^{\alpha_k \lambda t}. \tag{6.33}$$

The PFD-coefficients b_{kn} in Eq. (6.32) can be determined with a recursive algorithm (see Appendix D): If we let $b_{kn,N}$ denote the coefficients b_{kn} for N cascaded CSTRs, they can be determined recursively ($l = 2, 3, \ldots N$) by

$$
\begin{aligned}
b_{k1,1} &= 1/F'(\alpha_k) \\
b_{kn,l} &= \begin{cases}
\displaystyle\sum_{r=1}^{l-1}\sum_{\substack{p=1\\p\neq k}}^{m} \frac{b_{pr,(l-1)}b_{k1,1} - (-1)^r b_{kr,(l-1)}b_{p1,1}}{(\alpha_k-\alpha_p)^r}, & n = 1 \\
b_{k(n-1),(l-1)}b_{k1,1} + \displaystyle\sum_{r=n}^{l-1}\sum_{\substack{p=1\\p\neq k}}^{m} \frac{(-1)^{r-n} b_{kr,(l-1)}b_{p1,1}}{(\alpha_k-\alpha_p)^{r-n+1}}, & n = 2, 3 \ldots l-1 \\
b_{k(l-1),(l-1)}b_{k1,1}, & n = l,
\end{cases}
\end{aligned}
\tag{6.34}
$$

where the expression for $n = 2, 3 \ldots l-1$ should be used only when $l > 2$.

Another method to determine the PFD-coefficients, which is less efficient but perhaps easier to implement, is to use Nm different values θ, not equal to any α_k, and calculate the values of $\hat{G}(\theta)$ with Eq. (6.31). Eq. (6.32), with $s = \theta$, then gives a linear set of Nm equations that can be solved with respect to the coefficients b_{kn}. However, care has to be taken in the choice of the values of θ to get a well-conditioned system of equations.

In the same manner as the *Residue theorem* was applied to one CSBR (see page 73), it can be applied to the series of equal CSBRs, to get a truncated unit impulse response

$$
g(\tilde{t}\,) = K^N \sum_{k=0}^{m} \operatorname{Res}\left\{ \frac{e^{s\tilde{t}}}{F(s)^N} \right\}_{s=\alpha_k} . \tag{6.35}
$$

The order of the singularities α_k now equals the number of CSTRs and, thus, the following formula can be used to determine the residues (Fischer 1990):

$$
\operatorname{Res}\left\{ \frac{e^{s\tilde{t}}}{F(s)^N} \right\}_{s=\alpha_k} = \lim_{s\to\alpha_k} \frac{1}{(N-1)!} \left(\frac{d}{ds}\right)^{N-1} \left[(s-\alpha_k)^N \frac{e^{s\tilde{t}}}{F(s)^N} \right] .
$$

Unfortunately, the terms in this expression become quite numerous and cumbersome as N becomes large. However, if we use Eq. (6.13) to write

$$
F(s)^N = \sum_{p=0}^{\infty} f_p (s-\alpha_k)^{N+p}, \tag{6.36}
$$

the residues become reasonably simple for $N < 5$:

$$\begin{aligned}
\text{Res}\left\{\frac{e^{s\tilde{t}}}{F(s)}\right\}_{s=\alpha_k} &= \frac{e^{\alpha_k\tilde{t}}}{f_0} \\
\text{Res}\left\{\frac{e^{s\tilde{t}}}{F(s)^2}\right\}_{s=\alpha_k} &= \frac{e^{\alpha_k\tilde{t}}}{f_0^2}(f_0\tilde{t} - f_1) \\
\text{Res}\left\{\frac{e^{s\tilde{t}}}{F(s)^3}\right\}_{s=\alpha_k} &= \frac{e^{\alpha_k\tilde{t}}}{f_0^3}\left(\frac{1}{2}f_0^2\tilde{t}^2 - f_0f_1\tilde{t} + f_1^2 - f_0f_2\right) \\
\text{Res}\left\{\frac{e^{s\tilde{t}}}{F(s)^4}\right\}_{s=\alpha_k} &= \frac{e^{\alpha_k\tilde{t}}}{f_0^4}\Big(\frac{1}{6}f_0^3\tilde{t}^3 - \frac{1}{2}f_0^2f_1\tilde{t}^2 + (f_0f_1^2 - f_0^2f_2)\tilde{t} + \\
&\qquad + (2f_0f_1f_2 - f_0^2f_3 - f_1^3)\Big).
\end{aligned}$$

Note that the coefficients f_p depend on N and α_k. They may be calculated by the multinomial theorem applied to the Taylor expansion of $F(s)$, or by direct Taylor expansion of $F(s)^N$, for example. For the residues above, the coefficients are given in Appendix E.

Wik and Breitholtz (1997) have compared the three methods described here, and a Crank-Nicholson finite difference scheme, for the determination of impulse responses of cascaded equal CSBRs. The impulse response of $G(s)$, determined by (6.35) with $m = 20$, when $N = 4$, $\kappa = 0$, $\tau = 1$ and $\gamma = 1$, is shown in Figure 6.4. Considering this response as being the exact response, we can determine the errors of different approximations. In Table 6.1 the comparison is summarized. The maximum error, the dimensionless time when it occurs, the normed error, and the number of arithmetic operations (*flops*) are given. The normed error, corresponding to a mean standard deviation, is defined as

$$\|e\| = \left(\frac{1}{30}\int_0^{30} e^2(\tilde{t})d\tilde{t}\right)^{\frac{1}{2}},$$

where the error $e(\tilde{t})$ is the difference from the truncated exact response ($m = 20$). The time increments used in the evaluation of the responses were $\Delta\tilde{t} = 0.01$ for all methods.

As can be seen from Table 6.1 the method of exact truncation is the most accurate method. Even a truncation after two singularities gives ignorable errors. The method of finite differences requires a very fine discretization to give acceptable accuracy, which results in a large number of operations. It should be noted, however, that the number of operations may most likely be reduced for all methods if the routines are numerically optimized. For example, the singularities are determined with a Newton-Raphson method with poor initial guesses and a tolerance of 10^{-10} to meet, which is unnecessarily small.

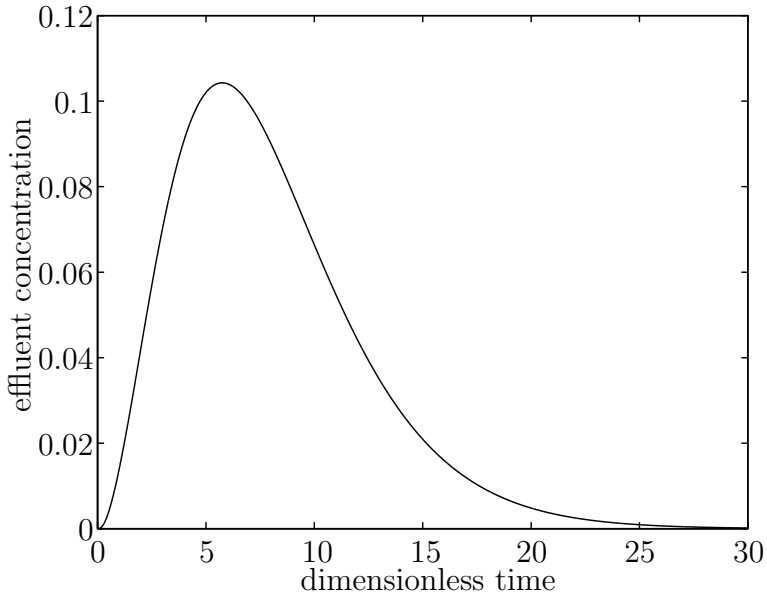

Figure 6.4 *Unit impulse response for $N = 4$, $\kappa = 0$, $\tau = 1$ and $\gamma = 1$.*

Table 6.1 *Comparison of methods to determine impulse responses*

Method		$\max\|e(\tilde{t})\|$	$\tilde{t}_{max}$	$\|e\|$	# operations
Crank-Nicholson	$m = 10$	$8.9 \cdot 10^{-3}$	3.65	$3.7 \cdot 10^{-3}$	$2.68 \cdot 10^{6}$
Crank-Nicholson	$m = 50$	$2.4 \cdot 10^{-3}$	3.18	$9.8 \cdot 10^{-4}$	$64.3 \cdot 10^{6}$
Crank-Nicholson	$m = 100$	$1.7 \cdot 10^{-3}$	2.84	$6.7 \cdot 10^{-4}$	$266 \cdot 10^{6}$
Approx. (MATLAB)	$m = 2$	$2.1 \cdot 10^{-3}$	3.79	$8.9 \cdot 10^{-4}$	$0.50 \cdot 10^{6}$
Approx. (MATLAB)	$m = 3$	$3.6 \cdot 10^{-4}$	3.74	$1.6 \cdot 10^{-4}$	$0.79 \cdot 10^{6}$
Approx. (MATLAB)	$m = 4$	$1.1 \cdot 10^{-4}$	3.72	$4.9 \cdot 10^{-5}$	$1.14 \cdot 10^{6}$
Approx. (PFD)	$m = 2$	$2.1 \cdot 10^{-3}$	3.79	$8.9 \cdot 10^{-4}$	$0.12 \cdot 10^{6}$
Approx. (PFD)	$m = 3$	$3.7 \cdot 10^{-4}$	3.75	$1.6 \cdot 10^{-4}$	$0.15 \cdot 10^{6}$
Approx. (PFD)	$m = 4$	$1.2 \cdot 10^{-4}$	3.74	$5.1 \cdot 10^{-5}$	$0.19 \cdot 10^{6}$
Approx. (PFD)	$m = 10$	$4.7 \cdot 10^{-6}$	3.74	$2.0 \cdot 10^{-6}$	$0.40 \cdot 10^{6}$
Exact truncation	$m = 2$	$1.2 \cdot 10^{-5}$	0	$2.8 \cdot 10^{-7}$	$0.18 \cdot 10^{6}$
Exact truncation	$m = 3$	$4.2 \cdot 10^{-7}$	0	$6.9 \cdot 10^{-9}$	$0.27 \cdot 10^{6}$

The accuracy and the number of operations are almost the same when MATLABs routines are used as when the PFD approach is used. However, when m and/or N are large, the MATLAB routines (*impulse* and *lsim*) sometimes fail to work, while the PFD-approach can still be used.

6.3.2 Moments of RTDs

When $\kappa = 0$, the non-dimensional transfer function of N equal CSBRs in series is

$$G(s) = \frac{\Delta C^b_{out}(s)}{\Delta C^b_{in}(s)} = \frac{1}{(1 + \tau s + \gamma\sqrt{s}\tanh\sqrt{s})^N}.$$

The qth moment can be defined as

$$\mu_q = \int_0^\infty \tilde{t}^q g(\tilde{t})d\tilde{t}, \tag{6.37}$$

where g is the unit impulse response of the system.

By the use of a few Laplace transform rules (Kamen 1996) it may readily be shown that

$$\mu_q = (-1)^q \lim_{s\to 0}\left\{\frac{d^q}{ds^q}G(s)\right\}.$$

After straightforward (but tedious) calculations the above formula can be used to determine the first three moments:

$$\begin{aligned}
\mu_1 &= N(\tau + \gamma) \\
\mu_2 &= \frac{2}{3}N\gamma + N(N+1)(\tau+\gamma)^2 \\
\mu_3 &= \frac{4}{5}N\gamma + 2N(N+1)\gamma(\tau+\gamma) + N(N+1)(N+2)(\tau+\gamma)^3.
\end{aligned}$$

Assume that an amount m_δ of trace substance has been added as a pulse to the reactor and the effluent concentration $c_{out}(t)$ has been measured. From Eqs. (6.28) and (6.37) it follows that the mean residence time is

$$T = \frac{\int_0^\infty t c^b_{out}(t)dt}{\int_0^\infty c^b_{out}(t)dt} = \frac{1}{\lambda}\mu_1,$$

where the integral in the denominator should equal m_δ/Q.

Similarly, the variance around the mean residence time can be shown to be

$$\begin{aligned}\sigma^2 &= \frac{\int_0^\infty (t-T)^2 c^b_{out}(t)dt}{\int_0^\infty c^b_{out}(t)dt} \\ &= \frac{1}{\lambda^2}(\mu_2 - \mu_1^2) \\ &= \frac{2N\gamma}{3\lambda^2} + \frac{T^2}{N},\end{aligned}$$

and the skewness

$$\begin{aligned}\varsigma^3 &= \frac{\int_0^\infty (t-T)^3 c^b_{out}(t)dt}{\int_0^\infty c^b_{out}(t)dt} \\ &= \frac{1}{\lambda^3}(\mu_3 - 3\mu_1\mu_2 + 2\mu_1^3) \\ &= \frac{2\gamma}{\lambda^3}(\lambda T + \frac{2}{5}N) + \frac{2T^3}{N^2},\end{aligned}$$

which can be seen as a measurement of the response asymmetry. It should be noted that the skewness is very sensitive to model errors and measurement errors.

In physical parameters the above moments are

$$T = \frac{V + \epsilon_l AL}{Q} \tag{6.38}$$

$$\sigma^2 = \frac{2AL^3\epsilon_l^2}{3QD} + \frac{T^2}{N} \tag{6.39}$$

$$\varsigma^3 = \frac{2AL^5\epsilon_l^3}{NQD^2}\left(\frac{D}{L^2\epsilon_l}T + \frac{2N}{5}\right) + \frac{2T^3}{N^2}. \tag{6.40}$$

If we compare these moments with those of a series of N equal CSTs having a total volume V, we will see that a hold up term equal to the void volume $\epsilon_l AL$ in the biofilm, divided by the flow, is added to the mean residence time, and a term $2AL^3\epsilon_l^2/(3QD)$ is added to the variance.

6.3.3 Dependency on Parameters

Often, reactors, such as trickling filters and biofilters, do not have a natural division into an exact number of CSBRs. A model with cascaded CSBRs is then rather a tool for describing the hydraulics and dynamics. Considering the total bulk volume V and the total area of biofilm A to be fixed, how does the division affect the pulse response? In Figure 6.5, unit impulse responses are shown for increasing numbers of CSBRs in the case of zero order reaction ($\kappa = 0$).

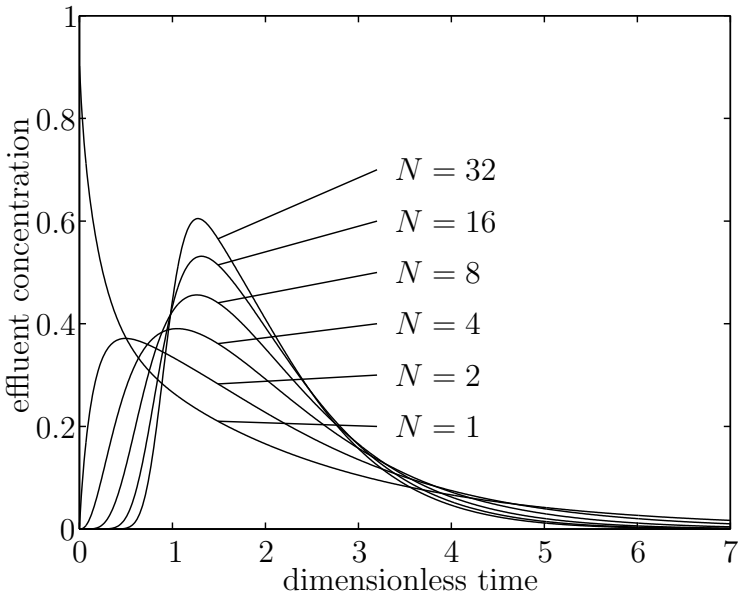

Figure 6.5 *Unit impulse responses of N cascaded CSBRs when $\kappa = 0$, $\tau = 1/N$ and $\gamma = 1/N$.*

The effects of changes in the parameters Q, D, L, V, A and ϵ_l are illustrated by simulations of a reactor where the default values give $N = 4$, $\gamma = 0.25$ and $\tau = 0.25$. The dependency of the pulse response on the parameters is studied by setting the parameters, one by one, to twice their original value (Q_o, D_o, L_o, V_o, A_o and $\epsilon_{l,o}$). The resulting responses are shown in Figures 6.6 and 6.7.

From the simulations it is evident that the values of ϵ_l, L and A have significant effects on the responses, while the diffusion coefficient only has a small effect on the impulse response. Larger values of ϵ_l, L and A give pronounced tailing and slower responses, which can be attributed to an increased hold-up of substance in the biofilm liquid volume $\epsilon_l AL$. Note that changes in these parameters affect the shape of the responses differently. Changes in A and ϵ_l reshape the entire responses, while changes in L mainly affect the tails of the responses.

The phenomena of pronounced tailing due to biofilm diffusion have been observed in experiments by, for example, Riemer *et al.* (1980) who studied submerged biofilters, Stevens *et al.* (1986) in their study of fluidized biological beds, and Suschka (1987) in his study of percolating biological filters. If the biofilm diffusion is not considered, it may give rise to incorrect estimates of parameters, hydraulics, and actual retention times.

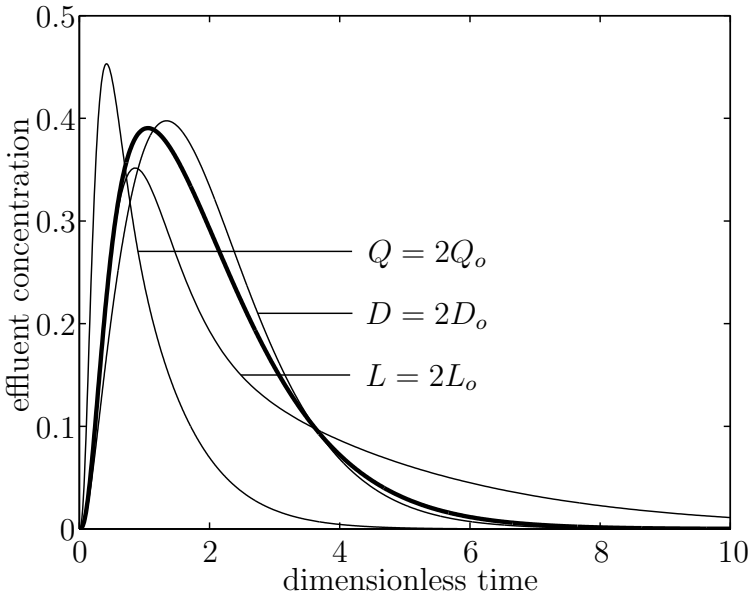

Figure 6.6 *Pulse responses when $N = 4$, $\kappa = 0$, $\tau = 0.25$, $\gamma = 0.25$ (thick line) and when Q, L or D has been changed to twice the original value.*

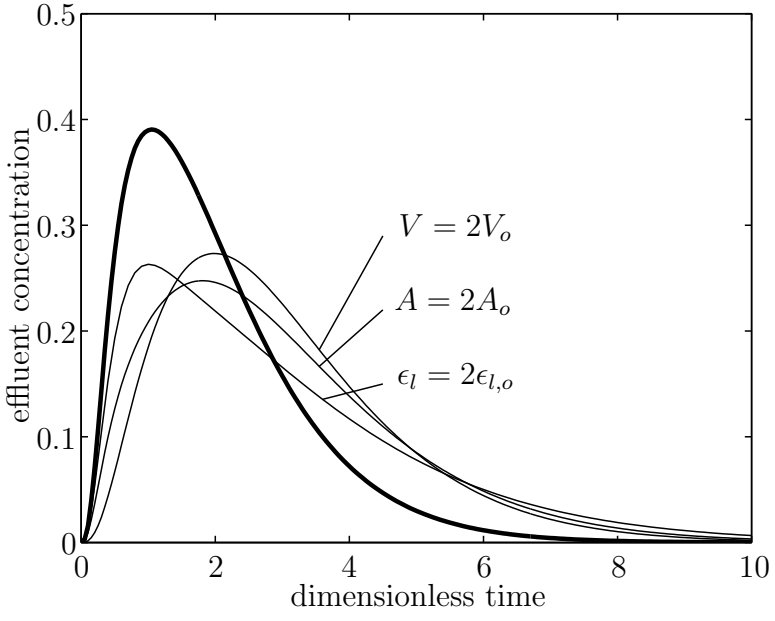

Figure 6.7 *Pulse responses when $N = 4$, $\kappa = 0$, $\tau = 0.25$, $\gamma = 0.25$ (thick line) and when ϵ_l, A or V has been changed to twice the original value.*

As for models of continuously stirred tanks in series, an increase in Q gives a faster response, and an increase in V gives a slower response. However, doubling the flow halves the mean residence time, but doubling the volume V does not double the mean residence time, which is explained by Eq. (6.38). Note that the value of the diffusion coefficient does not affect the mean residence time, but, according to Figure 6.6, an increase in the diffusion coefficient delays the response peak slightly.

Finally, the effects of the kinetic constants are studied for the case of first order kinetics. For biofilm reactors, typical values of κ range from zero to about 200. In Figure 6.8 pulse responses for values of κ in the interval $[0, 100]$ are shown. As can be seen from the figure, the heights of the pulses are very dependent on κ, particularly for small values of κ.

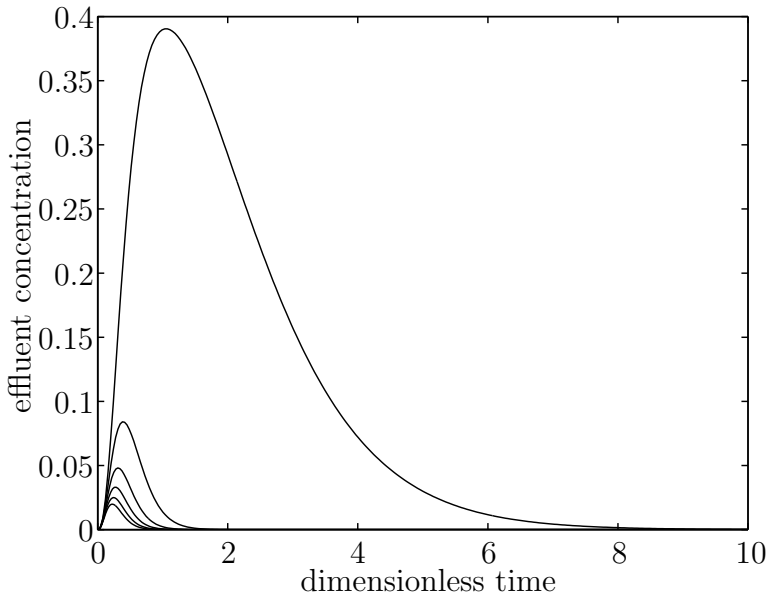

Figure 6.8 *Pulse responses when $N = 4$, $\tau = 0.25$, $\gamma = 0.25$, and $\kappa = 0$, 20, 40, 60, 80 and 100 (ordered from top to bottom).*

6.3.4 Estimation by Least Squares

Wik *et al.* (1995) carried out five pulse response experiments on the pilot-scale NTF at the Rya WWTP (described on page 56) with dissolved LiCl as trace substance, at the flows $Q = 14.5$ l/s and $Q = 7.3$ l/s.

We model the NTF as N identical CSBRs in series. The biofilm area is assumed to be the specific surface area of the media, 226 $\mathrm{m^2 m^{-3}}$, times the volume of the media, which gives $A = 9320$ $\mathrm{m^2}$. Since LiCl is not involved in any reaction, the response will be that of a zero order reaction, i.e., $\kappa = 0$. The diffusion coefficient

for Li is set to 80% of the value in water (see Appendix B) at the water temperature during the experiments (10.1°C) and the biofilm porosity is set to $\epsilon_l = 0.3$, as in the previous simulations of nitrifying biofilms.

Assuming values of the remaining unknown parameters N, L and the total bulk water volume V in the NTF, an approximate transfer function for the NTF in the original time-scale can be determined from Eq. (6.17):

$$\hat{G}(s) = \left(\sum_{k=1}^{m} \frac{1}{F'(\alpha_k)(s/\lambda - \alpha_k)} + 1 + \sum_{k=1}^{m} \frac{1}{F'(\alpha_k)\alpha_k} \right)^N , \tag{6.41}$$

where $\lambda = D_{Li}/(L^2\epsilon_l)$ is the time-scaling factor. The direct term

$$\left(1 + \sum_{k=1}^{m} \frac{1}{F'(\alpha_k)\alpha_k} \right)^N ,$$

gives a theoretical impulse at $t = 0$ having a very small area, which has to be ignored in a comparison with data.

After determination of the solutions y_k to Eq. (6.8) with a Newton-Raphson search on the intervals (6.9), the singularities $\alpha_k = -y_k^2$, the derivatives

$$F'(\alpha_k) = \tau + (\gamma/2y_k)(y_k + \tan y_k + y_k \tan^2 y_k)$$

and $\hat{G}(s)$ can be determined. Pulse responses may then efficiently be simulated using Eqs. (6.28) and (6.33) in the software MATLAB, for example, which allows for the estimation of reactor parameters by means of least square fitting to experimental data.

For the pulse response experiments, all carried out on the same day, the biofilm thickness can be assumed to be the same at both flows. The number of CSBRs is also set to be the same, while the bulk volume, which, unfortunately, was not possible to measure, most likely depends on the flow. Hence, the unknown parameters to be estimated from the experiments are N, L and the bulk volume V at the two different flows.

The best fit was achieved, successively for increasing N, by applying the nonlinear least square algorithm by Levenberg and Marquardt (MATLAB Optimization toolbox, 1996) to minimize the sum of the squared differences $e(t_i)$ between the measured effluent lithium concentrations and the responses of $\hat{G}$.

There are two simple methods to speed up the identification process. One is to use only a few singularities in the beginning, e.g. $m = 2$, and then increase m to improve the accuracy. The other one is to calculate good initial values for the least square algorithm. This can be achieved by using the mean residence time and the variance of the measured residence time distributions. Insertion of N into Eq. (6.39) gives initial values for L, which, after insertion into Eq. (6.38), gives initial values for V.

The best fit, shown in Figures 6.9 and 6.10, was found for $N = 10$ and the parameter values

$$\hat{\theta} = \begin{bmatrix} \hat{V}_1 \\ \hat{V}_2 \\ \hat{L} \end{bmatrix} = \begin{bmatrix} 2.40 \text{ m}^3 \\ 3.20 \text{ m}^3 \\ 0.64 \text{ mm} \end{bmatrix}.$$

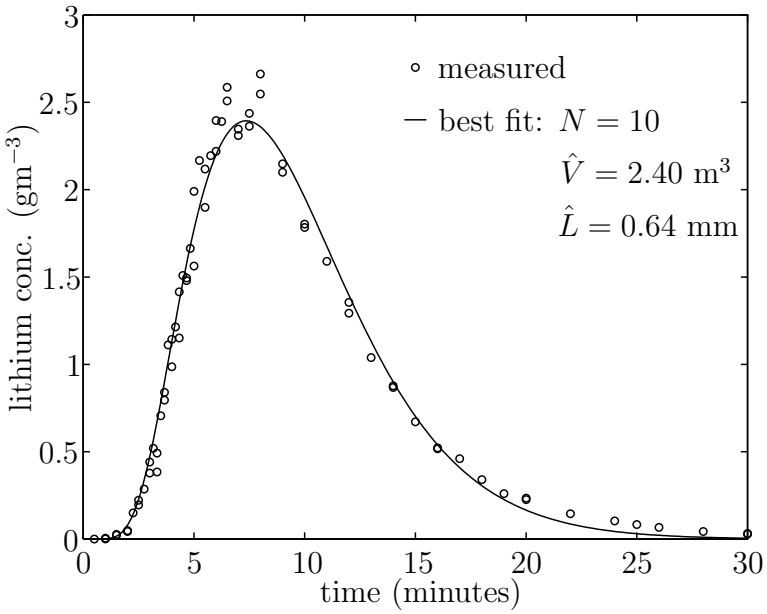

Figure 6.9 *Measured pulse response and the closest simulation for the Rya pilot plant NTF at $Q = 7.3$ l/s.*

Only four terms in the sum of Eq. (6.41) had to be used in the estimation. However, two terms would have been sufficient for a description of the dynamics, which can be seen from the transfer function (scaled to minute time-scale) determined for the flow $Q = 14.5$ l/s:

$$\hat{G}_{NTF}(s) = \left(\frac{0.1984}{1 + 1.50s} + \frac{0.7607}{1 + 0.36s} + \frac{0.0365}{1 + 0.13s} + \frac{0.0032}{1 + 0.05s} + 0.0013 \right)^{10}.$$

The third term has already a time constant of 0.13 minutes, which is less than a tenth of the first term, and a gain of less than 4% of the total gain.

Calculating the differences $e(t_k)$ and the Jacobian $(de/d\theta)$ for these values of N and $\hat{\theta}$, a covariance matrix for the identified parameters can be estimated as (Ljung, 1987, p 243):

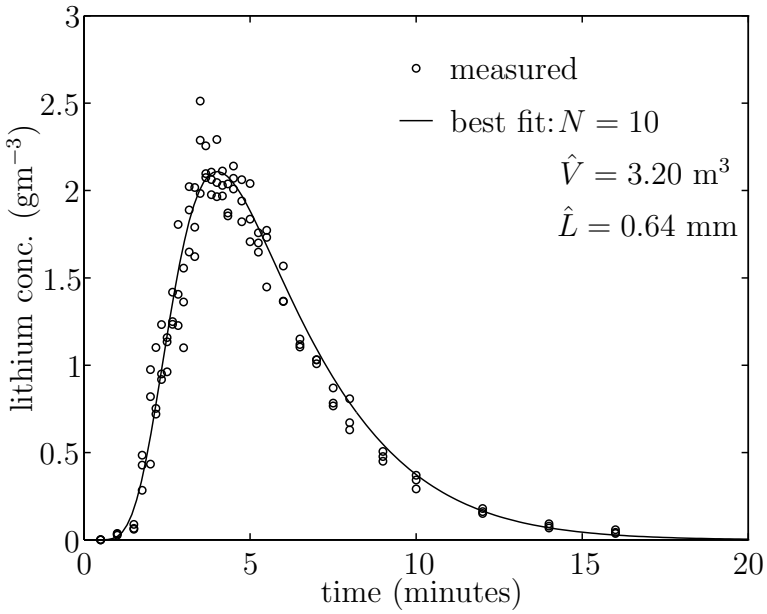

Figure 6.10 *Measured pulse response and the closest simulation for the Rya pilot plant NTF at $Q = 14.5$ l/s.*

$$\begin{aligned} \mathrm{Cov}(\hat{\theta}) &= \frac{1}{M}\sum_{t_k} e^2(t_k)\left[\sum_{t_i}\left(\frac{de(t_i)}{d\theta}\right)\left(\frac{de(t_i)}{d\theta}\right)^T\right]^{-1} \\ &= 10^{-3}\begin{bmatrix} 0.556 & 0.025 & -0.122 \\ 0.025 & 0.508 & -0.026 \\ -0.122 & -0.026 & 0.127 \end{bmatrix}, \end{aligned}$$

where $M = 175$ is the number of measurements. The small variance shows that the dependencies of the estimated values $\hat{V}_1$, $\hat{V}_2$ and $\hat{L}$ on each other are weak. In Figure 6.11 the dependence of the minimized sum of squares on N is shown.

When $N = 10$, the measured mean residence times and variances for the experiment at $Q = 7.3$ l/s, inserted into Eqs. (6.38) and (6.39), give $\hat{L} = 0.80$ mm and $\hat{V}_1 = 2.20$ m^3. The experiment at $Q = 14.5$ l/s gives $\hat{L} = 0.63$ mm and $\hat{V}_2 = 3.1$ m^3, which are close to the values estimated with the least square method.

The agreement achieved with this model, which is far better than with a model of CSTs in series applied to the same data (Wik *et al.* 1995), shows that the hold up in the biofilm should be considered in the analysis of pulse responses for this kind of reactors. Furthermore, it gives a hydraulic model closer to an expected plug flow (a larger value of N), and a larger increase in bulk volume with flow, which agrees better with the theories of liquid film flow (Levich 1962).

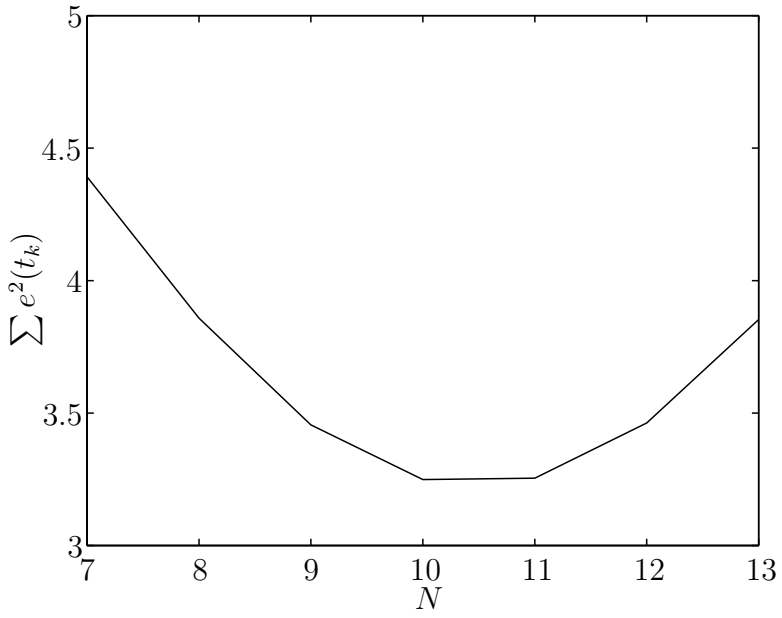

Figure 6.11 *The sum of squared errors for the best choice of parameters θ at each value of N.*

6.4 Comparisons with Experiments

A couple of experiments illustrating the fast dynamics have been carried out on the pilot plant NTF at the Rya WWTP and on two similar plants at the Sjölunda WWTP in Malmö, Sweden. In this section, data from these experiments are compared with simulations using the rational transfer functions and fairly simple nonlinear models. The data from the experiments can be found in three technical reports by Wik (1996), (1997*b*) and (1998).

6.4.1 Experiments at the Rya WWTP

Step Response Experiments

On June 15 and June 16 1995, two step response experiments were carried out on the pilot-scale NTF at Rya. The NTF-influent was water pumped from the effluent channel of the Rya WWTP in Göteborg and recirculated water from the NTF itself (see Figure 6.12). The mixed influent water was sprinkled on top of the filter media by the dual arm distributor rotating at 0.7 rpm.

A continuous ammonium meter of titration type was connected to the effluent from

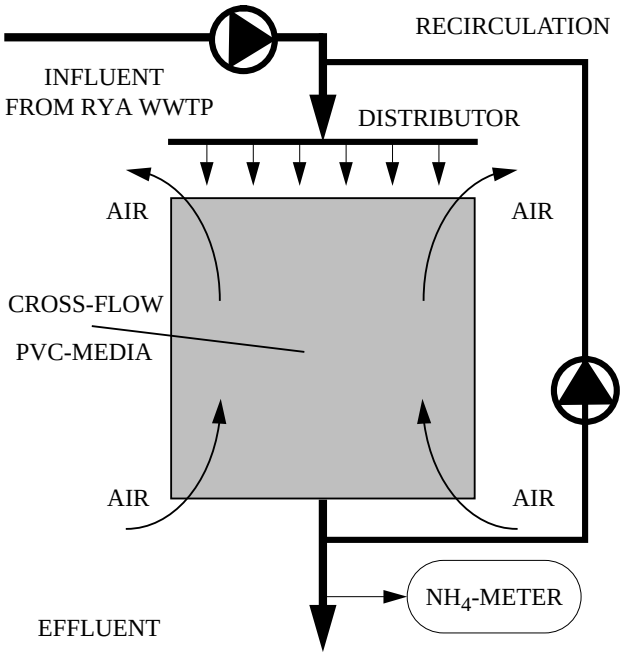

Figure 6.12 *Pilot plant setup.*

the NTF (Process-Styrning AB 1989). The meter values and the pump flows were registered as 1-minute or 6-minute average values by the computer system of the WWTP. The ammonium meter consisted of a beaker, a stirrer, a hydroxide sensor, a temperature sensor and a slope pump (see Figure 6.13). The slope pump sucked the water through a 1.8 m hose having an inner diameter of 8 mm at 10 ml/min. At the same time a small amount of 10% NaOH solution was sloped into the beaker that had a volume of 150 ml. Because of the sodium hydroxide, the ammonium entering the beaker turned into ammonia, which, due to differences in partial pressure, diffused through a membrane into an electrolyte surrounding the hydroxide sensor. The electrolyte (2.5 ml) had a high and approximately constant concentration of ammonium chloride, which means that the hydroxide sensor gave a measurement of the ammonia concentration in the electrolyte through the equilibrium relation

$$\frac{[NH_4^+][OH^-]}{[NH_3]} = K,$$

where K is a temperature dependent equilibrium constant. The temperature dependence was compensated for in the meter electronics. Before each experiment the meters were calibrated using standard solutions of 1.0 gN m^{-3} and 12 gN m^{-3}.

The step response experiments were carried out at a constant flow of 13.8 l/s and were achieved by first having recirculation over the plant and then turning off the recirculation at the same time as the flow from the effluent from the WWTP was raised. Two such experiments (a and b) were carried out one day after the other.

The ammonium concentrations were manually measured before and after each step experiment and the influent ammonium concentrations were determined by mass balances over the NTF. Effluent concentrations were recorded as 6-minute averages by the computer system. The water temperatures were 16.4°C (a) and 16.3°C (b).

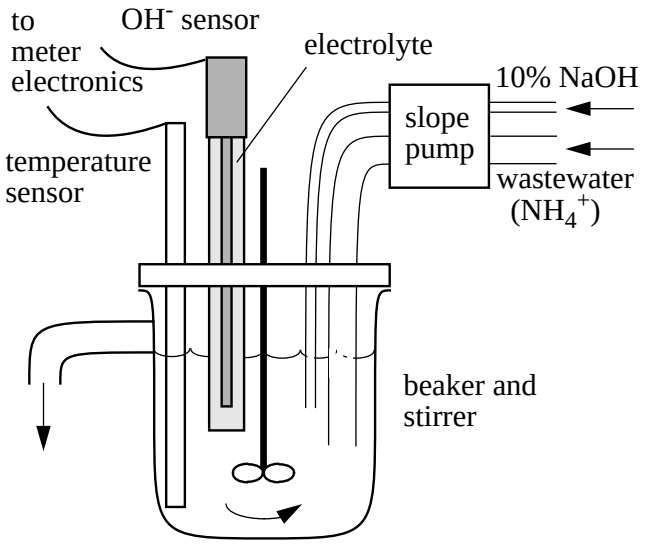

Figure 6.13 *Illustration of the continuous ammonium meter.*

Trickling Filter Model

We use the same assumptions and the same approach as we used for the pulse response experiments, i.e., the model is structured as N equal CSBRs in series. The difference is that now ammonium is nitrified in the biofilm. Only the net oxidization of ammonium into nitrate (1.1) is considered and we model only the ammonium and oxygen concentrations since the alkalinity was high enough not to be rate limiting during the experiments. We also use the simplifying assumption that the bulk is saturated with oxygen.

The rate of the oxidization depends on the concentration X_a of nitrifiers in the biofilm, which we assume is constant in the entire plant. Investigations of bacteria in biofilms generally indicate a spatial distribution of the bacteria over the depth of the film. For example, in water having a low organic content the nitrifiers will mainly be located close to the surface of the biofilm, where the ammonium and oxygen concentrations are high (see Figures 4.7 and 4.8). The location of the bacteria is closely related to where the concentrations are appropriate for each species, or in mathematical terms, where the expressions for the reaction rates are high. Only small amounts of substrates react in parts of the biofilm where the rates are low, independently of the bacterial concentration. Thus, the flux into and out of the

biofilm is quite independent of the spatial distribution as long as the variations are fairly smooth in the regions where the rates are high.

A mass balance over the bulk in the nth CSBR gives [c.f. Eqs. (5.1), (5.2) and Figure 5.4]

$$\frac{V}{N}\frac{d}{dt}c^b_{i,n} = Q(c^b_{i,n-1} - c^b_{i,n}) - \frac{AD_i}{N}\left[\frac{\partial}{\partial x}c_{i,n}\right]_{x=L}, \quad i = \mathrm{NH}_4^+, \tag{6.42}$$

where V is the total volume of bulk liquid in the reactor, A is the total biofilm area in the NTF, $c^b_{i,n}$ is the bulk concentration of substrate i, $c_{i,n}$ is the concentration of substrate i in the nth BFC, L is the biofilm thickness, D_i is the diffusion coefficient for substrate i in the biofilm (assumed to be 80% of the value in water), and x is the distance from the biofilm substratum. Based on the parameter estimations from the pulse response experiments, we use $N = 10$, $L = 0.64$ mm and linearly interpolate the volume to the flow $Q = 13.8$ l/s, which gives $V = 3.1$ m^3. Since the bulk is assumed saturated with oxygen, Eq. (6.42) only has to be used for ammonium.

Eq. (3.8) gives

$$\epsilon_l\frac{\partial c_{i,n}}{\partial t} = D_i\frac{\partial^2 c_{i,n}}{\partial x^2} - r_{v,i}, \quad 0 < x < L, \quad i = \mathrm{NH}_4^+, \mathrm{O}_2, \tag{6.43}$$

where we use $\epsilon_l = 0.3$ as in the pulse response experiments. The boundary conditions are

$$\frac{\partial}{\partial x}c_{i,n}(0,t) = 0 \quad \text{and} \quad c_{i,n}(L,t) = c^b_{i,n}(t), \tag{6.44}$$

where $c^b_{O_2,n}(t) = c^{sat}_{O_2}$.

The ammonium production rate is assumed to be described by a double Monod-expression and the stoichiometry is assumed to follow the one found by Wezernak and Gannon (1967):

$$r_{v,NH_4} = -X_a\frac{\mu_{m,ao}}{Y_a}\frac{c_{O_2}}{(0.4 + c_{O_2})}\frac{c_{NH_4}}{(1.0 + c_{NH_4})}, \tag{6.45}$$

$$r_{v,O_2} = 4.33\, r_{v,NH_4}, \tag{6.46}$$

where X_a denotes the concentration of nitrifiers, $\mu_{m,ao}$ is their maximum growth rate and Y_a is the yield coefficient. The bacterial concentrations were chosen such that the stationary effluent ammonium concentration, after the steps were applied, agreed with the measured ones, which resulted in $X_a = 1130$ gCOD/m^3 (experiment a) and $X_a = 1240$ gCOD/m^3 (experiment b).

Ammonium Meter Model

If plug flow through the hose is assumed, a mass balance over the beaker yields:

$$V_b\frac{d}{dt}c_b(t) = q_b\left\{c^b_{NH_4,out}(t-d) - c_{NH_3,b}(t)\right\} - q_m(t), \tag{6.47}$$

where V_b is the volume of the beaker, $c^b_{NH_4,out}$ is the effluent ammonium concentration from the NTF, d is the time delay when the water travels through the hose, $c_{NH_3,b}$ is the ammonia concentration in the beaker, q_b is the flow through the beaker, and q_m is the ammonia diffusing through the membrane into the electrolyte. However, q_m can be ignored relative to the nitrogen flux through the beaker.

The diffusion through the membrane is driven by the difference between the partial pressures of ammonia in the beaker and in the electrolyte. If the ammonia concentrations are assumed to be proportional to the partial pressures, according to Henry's law, a mass balance over the sensor gives:

$$V_e \frac{d}{dt} c_{NH_3,e}(t) = K_d(c_{NH_3,b}(t) - c_{NH_3,e}(t)), \tag{6.48}$$

where V_e is the volume of the electrolyte, K_d is a constant, and $c_{NH_3,e}$ is the ammonia concentration in the electrolyte, i.e., the variable that gives the registered ammonium concentration.

Laplace transformation of Eqs. (6.47) and (6.48) and elimination of $C_b(s)$, give the following second order transfer function from effluent ammonium concentration to measured ammonia concentration:

$$\frac{C_{NH_3,e}(s)}{C^b_{NH_4,out}(s)} = \frac{e^{-ds}}{(1+\tau_1 s)(1+\tau_2 s)}, \tag{6.49}$$

where the time constants are $\tau_1 = V_b/q_b = 14.4$ minutes and $\tau_2 = V_e/K_d$.

The time constant τ_2 was experimentally determined from a step response experiment, where the inlet hose of the meter was moved from the NTF-effluent to a bucket containing effluent water from the WWTP. This caused a step increase in ammonium concentration from 5 to 19 gN/m^3. By comparison between the theoretical step response of the transfer function (6.49) and the measured one (1-min values), the time constant was estimated to be $\tau_2 = 4.5$ minutes (see Figure 6.14). The drops in the registered ammonium concentration in the figure are due to air bubbles on the membrane. Note that the theoretical time delay $d = 9$ minutes, determined by dividing the volume of the hose with the flow, was also verified by the experiment.

Numerical Methods

Simulated NTF-effluent responses to steps in ammonium concentration were achieved by solving Eqs. (6.42) to (6.46) with a Crank-Nicholson finite difference scheme, where the biofilm was divided into 200 nodes, the time increments used were $\Delta t = 0.01 L^2 \epsilon_l / D_{O_2}$ and at each time step the nonlinear reaction term r_v was evaluated at the previous time step. Stationary conditions were assumed to hold before each experiment. The stationary solutions were found by first using the Crank-Nicholson scheme 1000 steps with a reduced discretization, then interpolating the solutions for

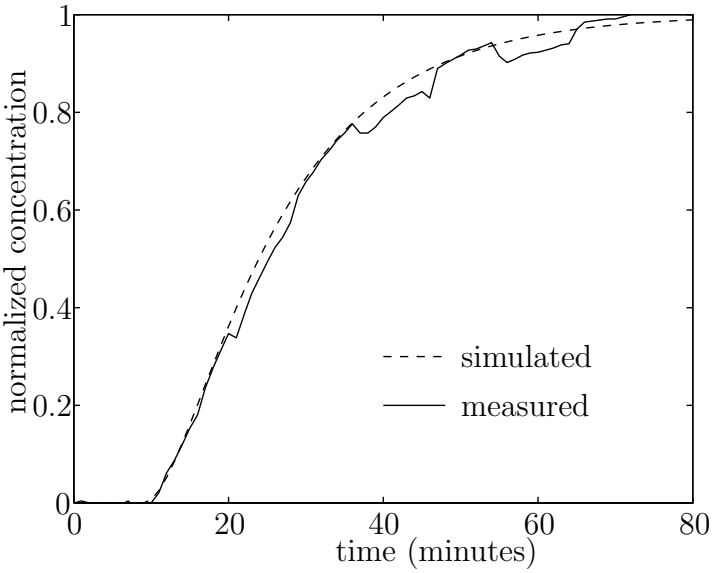

Figure 6.14 *Normalized step responses of the ammonium meter.*

the finer grid, and finally using this as initial input in a Gauss-Newton method that solves the steady-state Crank-Nicholson formulation. The simulated effluent ammonium concentrations were used as input to the ammonium meter model. Simulated responses from the ammonium meter were determined with the MATLAB-routines *c2dm* and *filter* (MATLAB Control System Toolbox, 1990), which require only the transfer function (6.49) and the sampling interval.

Results

In Figures 6.15 and 6.16 the measured and simulated concentrations are shown. In the model, the bacteria have been assumed to respond instantly to changes in substrate concentrations. Hence, the close agreement between simulations and measurements indicates a very quick response of the nitrifying bacteria. Note, however, that the transients of the effluent concentration are suppressed by the rather slow dynamics of the ammonium meter. The difference between simulated and measured concentrations prior to the steps can be explained by the meter giving zero concentrations due to the concentration being below the operating range (> 0.5 gN m^{-3}).

Variations around an operating point

An experiment, where the flow was rapidly changed around an operating point, was carried out on November 30, 1995. Both the influent and effluent ammonium

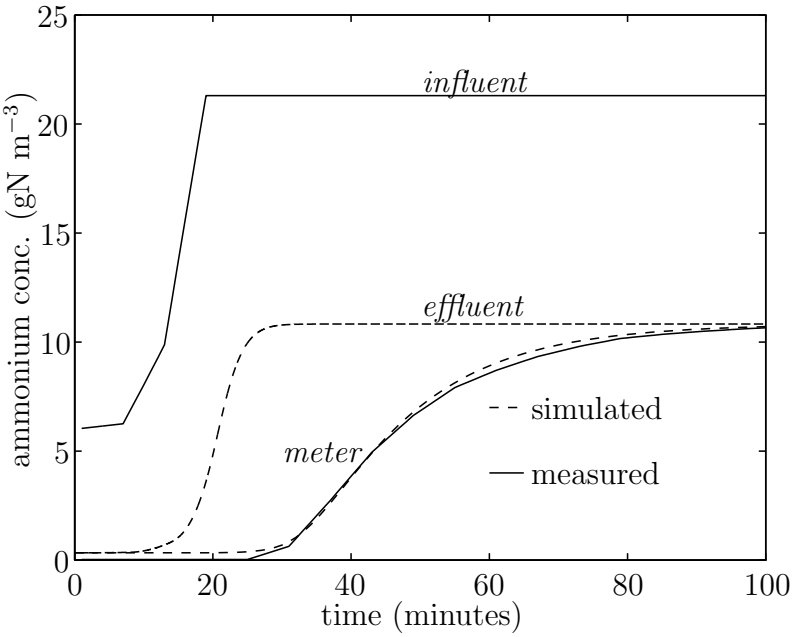

Figure 6.15 *Measured and simulated concentrations in step experiment a.*

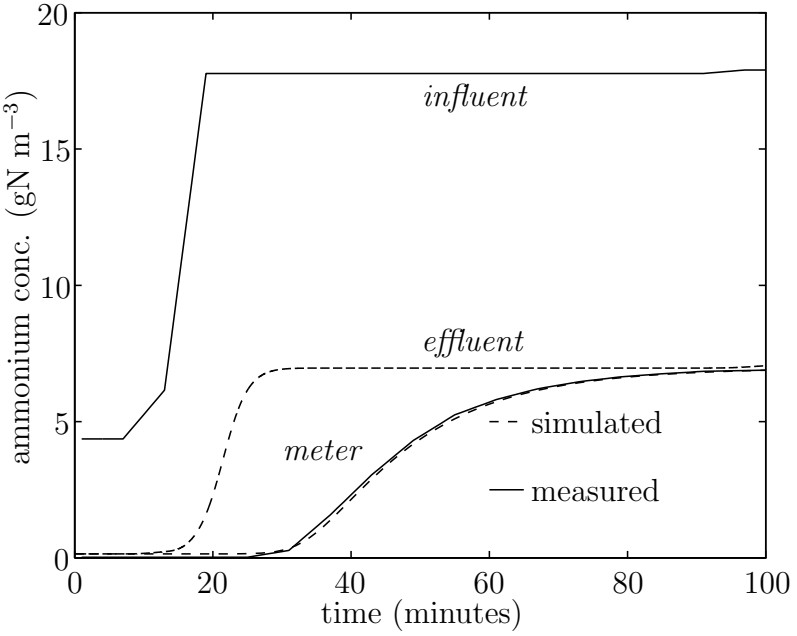

Figure 6.16 *Measured and simulated concentrations in step experiment b.*

concentrations were measured with continuous ammonium meters. No recirculation was used in the experiment. In Figure 6.17 the measured concentrations and the flow during the experiment are shown.

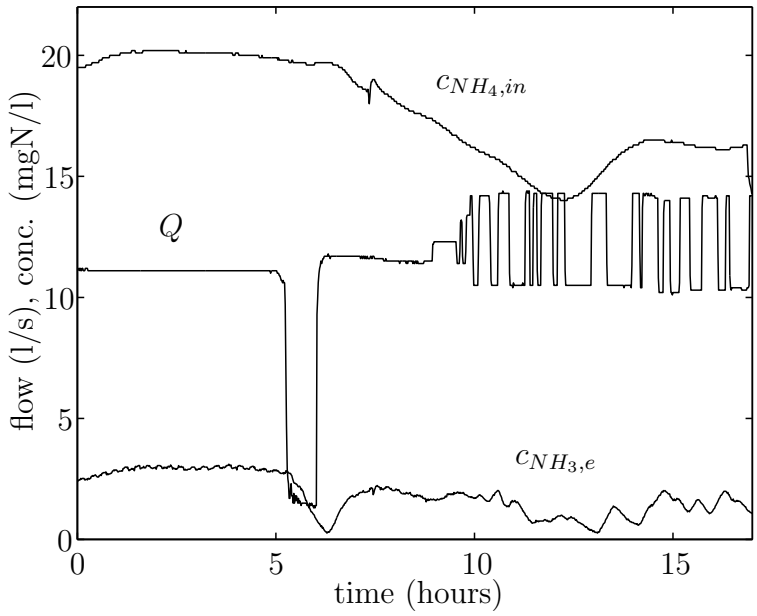

Figure 6.17 *Measured flow, influent ammonium concentration and effluent ammonium concentration.*

If the ammonium concentration is sufficiently high in an NTF, oxygen is the rate limiting substrate and the nitrification rate can be assumed to be of zero order. Assuming that the bulk is saturated with oxygen, the transition level for the ammonium bulk concentration between oxygen limitation and ammonium limitation can be estimated by Eq. (1.6):

$$c_{NH_4}^{lim} = \frac{D_{O_2}}{4.33 D_{NH_4}} c_{O_2}^{sat},$$

which is 2.7 gN m^{-3} for the average water temperature 12.2°C during the experiment.

The influent concentration varied from 15 to 20 gN m^{-3} and the effluent concentration was around 2 gN m^{-3} (see Figure 6.17). Hence, at the very lowest parts of the plant the nitrification rate depended on the ammonium concentration and in the upper parts the nitrification rate can be assumed of zero order.

A rational transfer function matrix for changes in ammonium and nitrate concentrations at this operating point can be achieved as follows: First, we use the results from the pulse responses and divide the NTF into 10 CSBRs of equal size, interpolate the bulk volume to $V = 2.95$ m^3 at the operating flow $Q_o = 12.3$ l/s, use the same values of ϵ_l and L and set the diffusion coefficients to 80% of the values

in water. Then, the rate coefficient k_1 in Eq. (6.21) is set to zero in the first nine CSBRs, because oxygen was rate limiting there, and assigned a value ($3.0 \cdot 10^4$ d^{-1}) in the last CSBR. No adsorption of ammonium had been observed in this plant. Hence, the adsorption coefficient k_a is set to zero.

For varying flow the mass balance (6.1) results in a nonlinear model. However, since the flow was varied around an operating point, a linearized mass balance can be used by introducing *equivalent influent concentrations*

$$\tilde{c}^b_{i,in}(t) = \frac{Q(t)c^b_{i,in}(t)}{Q_o}.$$

Using these concentrations as inputs in the same way as the original influent concentrations were used in Section 6.2.4, we can determine rational transfer function matrices for each CSBR from Eq. (6.27). Since the first nine CSBRs are equal, the rational transfer function matrix for the entire NTF become

$$\hat{G}_{NTF}(s) = \hat{G}^9(s)\hat{G}^*(s),$$

where $\hat{G}(s)$ is the transfer function matrix for each of the first nine CSBRs ($k_1 = 0$), and $\hat{G}^*(s)$ is the transfer function matrix for the last CSBR ($k_1 \neq 0$). Using Eq. (6.27) for the determination of $\hat{G}(s)$ and $\hat{G}^*(s)$, we get the following relation between the influent and effluent ammonium and nitrate concentrations:

$$\begin{bmatrix} \Delta C^b_{NH_4,out}(s) \\ \Delta C^b_{NO_3,out}(s) \end{bmatrix} = \begin{bmatrix} \hat{G}_{11}(s) & 0 \\ 0 & \hat{G}_{22}(s) \end{bmatrix}^9 \times \begin{bmatrix} \hat{G}^*_{11}(s) & 0 \\ \hat{\Lambda}(s)\hat{G}^*_{11}(s)\hat{G}_{22}(s) & \hat{G}_{22}(s) \end{bmatrix} \begin{bmatrix} \Delta\tilde{C}^b_{NH_4,in}(s) \\ \Delta\tilde{C}^b_{NO_3,in}(s) \end{bmatrix}.$$

By studying the time constants we find that a sufficiently close approximation of $G(s)$ can be achieved with truncations after two terms for $\hat{G}_{11}$, $\hat{G}_{22}$ and $\hat{\Lambda}$ and after only one term for $\hat{G}^*_{11}$:

$$\begin{aligned} \hat{G}_{11}(s) &= 0.017 + \frac{0.436}{1+1.078s} + \frac{0.547}{1+0.312s} \\ \hat{G}_{22}(s) &= 0.020 + \frac{0.379}{1+1.167s} + \frac{0.601}{1+0.330s} \\ \hat{G}^*_{11}(s) &= 0.0002 + \frac{0.400}{1+0.165s} \\ \hat{\Lambda}(s) &= 1.01 + \frac{0.260}{(1+0.014s)(1+0.848s)} + \frac{0.226}{(1+0.012s)(1+0.094s)}. \end{aligned}$$

Apparently, $\hat{\Lambda}(s)$ can be further reduced by ignoring the time constants 0.014 minutes and 0.012 minutes.

Unfortunately, only the ammonium concentrations were continuously measured in this experiment. A comparison between the measured ammonium concentrations and the concentrations simulated with

$$\Delta C_{e,NH_3}(s) = G_m(s)\Delta C^b_{NH_4,out}(s) = G_m(s)\hat{G}_{11}(s)^9\hat{G}^*_{11}(s)\Delta\tilde{C}^b_{NH_4,in}(s),$$

where $G_m(s)$ is the transfer function (6.49) for the ammonium meter in the effluent, is shown in Figure 6.18. The comparison shows good agreement, except during a period when the flow dropped to far less than the flow used in the derivation of the model.

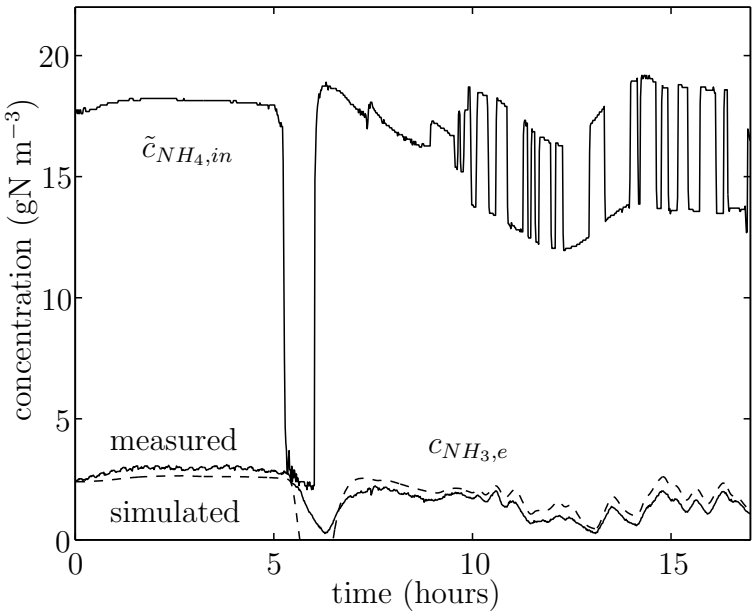

Figure 6.18 *Equivalent influent ammonium concentration, measured effluent ammonium concentration (solid) and simulated effluent ammonium concentration (dashed).*

6.4.2 Experiments at the Sjölunda WWTP

As discussed in Section 6.3.3, residence time distributions for biofilm reactors often exhibit pronounced tailing, which can make conventional and simple flow-models, such as "N-tanks in series" (Levenspiel 1972), unsuitable for describing dynamic responses. The reason for the tailing is a hold-up of substances in the biofilm. This hold-up may have, at least, two reasons:

- Diffusion of substances into and out of the biofilm.
- Adsorption of substances to the biofilm.

We have already modeled the first reason above and the close agreement between simulations and experiments indicates that adsorption is not an important phenomenon in the plant at the Rya WWTP, for example. However, the literature gives no support for this to be generally true. Due to a net negative charge on the surface of many organic matters in wastewater, there is a potential for adsorption

of positively charged ions, e.g. ammonium ions, to the biofilm. Nielsen (1996) has found that ammonium can be adsorbed to activated sludge. By treating sludge samples with excessive amounts of KCl, which ion-exchanged with the adsorbed ammonium, he estimated the adsorbed amounts to be as high as 0.4-0.5 gN/kgSS at dissolved ammonium concentrations of 15 gN m^{-3}. Unfortunately, sufficiently large biofilm samples cannot readily be taken from trickling filters to be analyzed in the same manner. Further, in a study of submerged denitrifying biofilters, Riemer *et al.* (1980) stated that, due to pronounced tailing caused by adsorption of dye to the biofilm, the dye Eosine-Y was unsuitable as a tracer for determination of RTDs.

Adsorption does not affect effluent concentrations under stationary conditions. However, changes in the amount of adsorbed substances, due to changes in operating conditions, affect transient responses. Adsorption of ammonium may, therefore, be observed by measurements of influent and effluent ammonium concentrations during step increases and step decreases in the ammonium load, for example. Such measurements are also more interesting for plant and controller designs, since they directly relate to an operational behavior of the plant.

In a number of step response experiments carried out on a pilot-scale NTF at the Sjölunda WWTP in Malmö, the influent concentrations of dissolved nitrogen were approximately constant during the experiments, while the corresponding effluent concentrations differed from those in the influent. The differences were particularly significant during transient periods of approximately five mean residence times, determined from trace substance pulse responses, after the steps were applied. The differences can be explained by denitrification at high ammonium loads, and adsorption and desorption of ammonium to the biofilm caused by changes in the ammonium bulk concentration.

An extension of the model used in the comparisons with data from the NTF at the Rya WWTP, to consider adsorption and desorption of ammonium, nitrification in two steps and denitrification, is presented. Simulations, using this model, agree with the experimental observations, which further supports the conclusions above. Apart from modeling and design aspects, adsorption of ammonium has a direct practical implication. Influent and effluent measurements to determine stationary nitrification rates should be made a longer time after changes in operating conditions than indicated by trace substance RTDs.

Material and Methods

The experiments presented are two pulse response experiments (denoted P), two responses to step increases in influent ammonium concentration (NI), one step decrease in influent ammonium concentration (ND), one step increase in flow (QI), and one experiment where KCl was added to the influent during half an hour (K). Measurements of how the bulk volume in the NTF depends on the flow were also made (denoted V). All experiments were carried out on a setup of two identical circular pilot-scale trickling filters, NTF1 and NTF2, in May 1997 and in January

Table 6.2 *Influent conditions*

Date	May 12	May 13	Jan 13	Jan 14
Experiments*	P	NI,QI	P,NI,ND	K,V
Temperature (°C)	15.5	15.5	14.8	14.8
Total N (gm^{-3})	17.3	19.8	-	16.5
COD unfiltered (gm^{-3})	51	55	-	61
COD filtered (gm^{-3})	39	48	-	56
Alkalinity (mole $HCO_3^- m^{-3}$)	4.34	5.36	5.92	6.13
pH	7.95	7.9	7.65	7.75
SS (gm^{-3})	10	13	12	15
Total P unfiltered (gm^{-3})	0.16	0.04	0.18	0.24
Total P filtered (gm^{-3})	0.04	0.05	0.10	0.08
NH_4-N (gm^{-3})	15.4	19.5	16.8	14.9
NO_2-N (gm^{-3})	0.01	0.01	0.01	0.01
NO_3-N (gm^{-3})	0.1	0.3	0.01	0.01

* P=pulse response, NI=ammonium increase, ND=ammonium decrease, QI=flow increase, K=KCl-addition, V=volume measurements

1998. The influent conditions during the experiments are presented in Table 6.2. These concentrations are representative operating conditions for the plants, which had been operating with the same filter media for several years prior to the experiments. The filter media are of a cross-flow structure with a specific surface area of 145 m^2m^{-3} and 60° angle of inclination. With filter depths of 3.6 m and inner diameters of 3.0 m the total area of biofilm was approximately 3690 m^2 in each NTF. The two plants could either be operating in parallel (normal operation), with influent water being effluent water from the Sjölunda WWTP in Malmö, or in series (see Figure 6.19). Influent water to each plant was evenly sprinkled over the NTFs by dual arm distributors rotating at 0.5 rpm. Further details about the plants have been given by Andersson *et al.* (1994).

Except for the experiment where the flow through NTF2 was increased and in the measurements of the bulk water volume, the flow pumped by P2 (see Figure 6.19) was held at 33 m^3h^{-1} during all times. The pulse response experiments were achieved by adding 60 ml of dissolved LiCl, having a concentration of approximately 60 gLi/l, with a syringe on the vacuum side of pump P2. The step decrease in influent ammonium concentration to NTF2 was achieved by changing the filters from operating in parallel to operating in series by opening valve V12 and closing valve V2 (see Figure 6.19). This procedure took less than five seconds. Conversely, by opening valve V2 and closing valve V12, step increases in influent ammonium concentration were achieved by altering the filters from operating in series to operating in parallel. The flow increase experiment was achieved by increasing the frequency of pump P2 to raise the flow from 18 m^3h^{-1} to 33 m^3h^{-1}, which are levels that the pump had

been calibrated for. This increase, which took less than a few seconds, resulted in a raise in ammonium load of the same size as the step increases in influent ammonium concentration caused. In the last experiment a solution of 220 gKCl/l was added to the vacuum side of pump P2 for 30 minutes with a slope pump, at a rate of 0.516 l/min.

In all experiments the effluent samples were collected from a sampling tap in the outlet of the NTF, and the influent samples were taken from either the influent tub to the NTFs or the effluent tub of NTF1 (when operating in series). All data presented have been compensated for transport delays, all less than 20 s, in the pipes of the system. Details about the sampling analyses have been given by Wik (1999*a*).

The measurements of the bulk water volume in NTF2 were carried out by first closing valve V31 and letting the flow stabilize through the filter for more than an hour. Then, the influent pump P2 was switched off and the effluent valve V20 was closed. By turning on pump P3 and balancing the level in the effluent tub with valve V20, the amount of water leaving the filter could be determined from the pumped flow 1.22 l/s, and the time. After approximately 10-25 minutes, depending on the flow rate when pump P2 was switched off, the effluent rapidly became very dark from snail shells and particulate matter and the flow dropped to less than a few deciliters per second. The time of this sudden (less than half a minute) change was taken as the transition from effluent water being bulk water to becoming water contained in the biofilm. One measurement of the volume in NTF1 was made in exactly the same manner.

Modeling

We model this plant in the same manner as we modeled the pilot plant at the Rya WWTP, except that we extend the model to consider denitrification, adsorption of ammonium and also model the nitrification in two steps: ammonium oxidization and nitrite oxidization as in Section 3.5. Thus, the model equations are Eqs. (6.42), (6.43) and (6.44) applied to the substrates

$$i = \mathrm{O_2},\ \mathrm{NH_4^+},\ \mathrm{HCO_3^-},\ \mathrm{NO_2^-} \text{ and } \mathrm{NO_3^-}.$$

The amount of ammonium adsorbed to the biofilm at each time is assumed to be proportional to the ammonium concentration, i.e. $k_a c_{NH_4}$. Due to the adsorption the mass balance equation (6.43) has to be adjusted for ammonium. Since the accumulation of adsorbed ammonium at each time is $k_a(\partial c_{NH_4}/\partial t)$, the mass balance becomes

$$(\epsilon_l + k_a)\frac{\partial}{\partial t}c_{j,NH_4} = D_{NH_4}\frac{\partial^2}{\partial x^2}c_{j,NH_4} + r_{v,NH_4}, \qquad 0 < x < L. \tag{6.50}$$

The stoichiometry and reaction rates are summarized in Table 6.3. These are extensions of the IAWQ model no. 1 for activated sludge (Henze *et al.* 1987) to model the

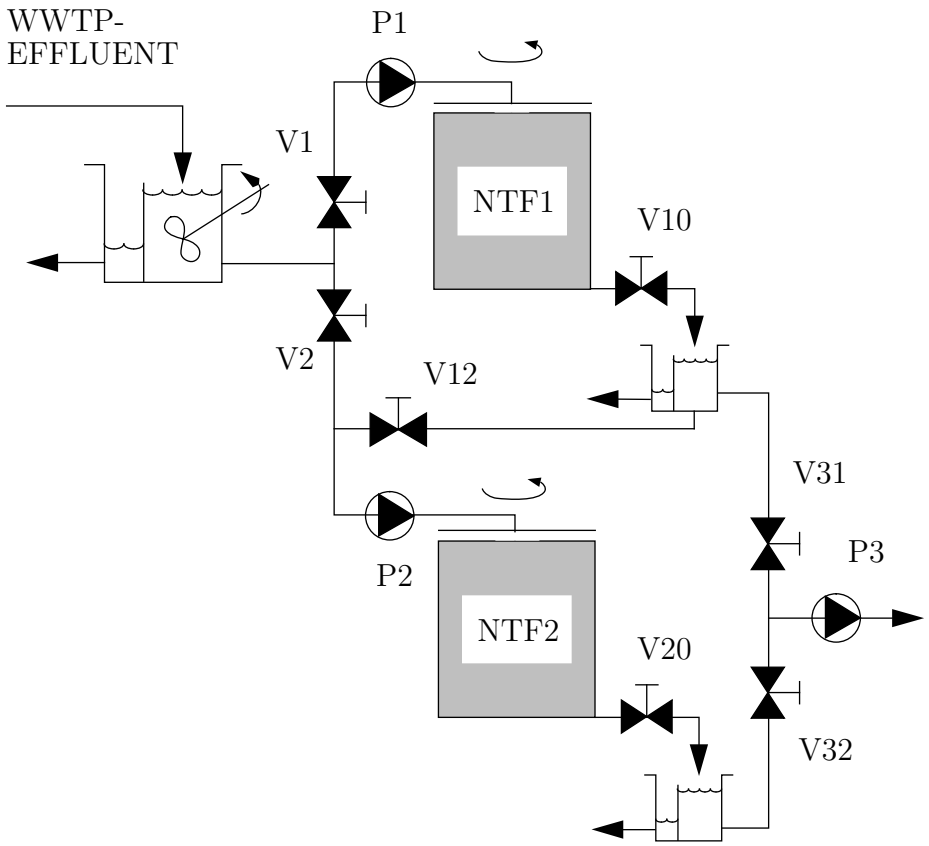

Figure 6.19 *Plant configuration.*

nitrification of ammonium into nitrate in two steps with nitrite as an intermediate product. Reduction of nitrite by heterotrophs has been modeled by Nowak *et al.* (1995), e.g., but is ignored in this model for easier calibration. The chosen values of the yield coefficients, which are given in Appendix B, give the stoichiometry by Wezernak and Gannon (1967). Given the stoichiometry, the values of μ_m, η and Y can be incorporated into the bacterial concentrations X, which makes them redundant. As pointed out by Henze *et al.* (1987) the IAWQ model is fairly insensitive to the switching coefficients K and $K_{O,h}$, which are also given in Appendix B. The same observation holds for the model presented here.

In the simulations, $X_{ao}\mu_{m,ao}$ was set to 2000 gCODd^{-1}m^{-3} and $X_{no}\mu_{m,no}$ was set to 730 gCODd^{-1}m^{-3}, which gave stationary effluent ammonium and nitrite concentrations that were close to the measured ones. When denitrification was simulated, $(1 - Y_h)X_h\mu_{m,h}\eta/Y_h$ was set to 1400 gCODd^{-1}m^{-3}. The adsorption coefficient k_a was set to 0.5. The model equations were numerically solved with an explicit Crank-Nicholson finite difference scheme, where the biofilm was discretized into 100 elements and the time steps were $\Delta t = 0.001L^2\epsilon_l/D_{O_2}$ days.

Table 6.3 *Process kinetics and stoichiometry*

	Substrate i					
Process k	Stoichiometric coefficient ν_{ki}					Process rate R_k
	O_2	NH_4^+	HCO_3^-	NO_2^-	NO_3^-	
Ammonium ox.	$\frac{3.43 - Y_{ao}}{Y_{ao}}$	$\frac{1}{Y_{ao}}$	$\frac{1}{7Y_{ao}}$	$\frac{-1}{Y_{ao}}$	0	$X_{ao}\mu_{m,ao}\frac{c_{O_2}}{K_{O_2,ao}+c_{O_2}}\frac{c_{NH_4}}{K_{NH_4}+c_{NH_4}}$
Nitrite ox.	$\frac{1.14 - Y_{no}}{Y_{no}}$	0	0	$\frac{1}{Y_{no}}$	$\frac{-1}{Y_{no}}$	$X_{no}\mu_{m,no}\frac{c_{O_2}}{K_{O_2,no}+c_{O_2}}\frac{c_{NO_2}}{K_{NO_2}+c_{NO_2}}$
Denitrification	0	0	$\frac{1 - Y_h}{14 \cdot 2.86 Y_h}$	0	$\frac{1 - Y_h}{2.86 Y_h}$	$X_h\eta\mu_{m,h}\frac{K_{O,h}}{K_{O,h}+c_{O_2}}\frac{c_{NO_3}}{K_{NO_3}+c_{NO_3}}$

$$r_{v,i} = \sum_k \nu_{ki} R_k$$

Results

In Figure 6.20 the results of the measurements of the bulk volume are presented. The measured bulk volume increases close to linearly with the flow rate in the operating region studied and the measured volume in NTF1 agrees with the volumes for NTF2.

The results of the pulse response experiment in January are shown in Figure 6.21. As expected, the response exhibits the typical tailing of biofilm reactors. Included in the figure is the closest, in the sense of least squares, simulated response when the bulk volume is set to the measured volume $V = 1.59$ m^3 at the flow $Q = 33$ m^{3}h^{-1}. The estimated value of ϵ_l is fairly close to the value 0.3 that was used for simulation of the pilot plant NTF at the Rya WWTP. The number of tanks and the biofilm thickness also agree with the values $N = 10$ and $L = 0.64$ mm that were estimated from the pulse response experiments on that plant. Included in Figure 6.21 is the closest response of a conventional "N tanks in series model", which was achieved for $N = 3$. As can be seen, this model captures neither the initial phase nor the tailing of the response. Note also that three tanks imply a flow that is far from the typical flow in trickling filters which is close to plug-flow.

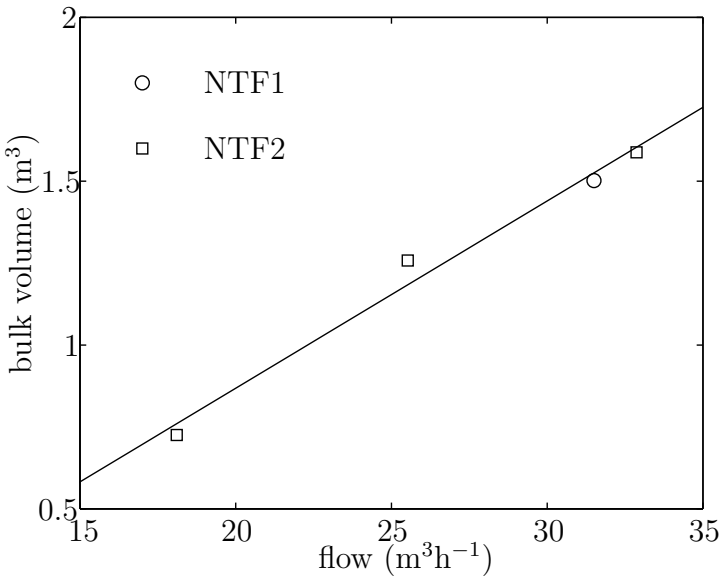

Figure 6.20 *Measured bulk water volume.*

In each of the experiments with step changes in the ammonium load, the influent total concentration of dissolved nitrogen, i.e. the sum of ammonium, nitrite and nitrate concentrations, was close to constant (see Figure 6.22). However, after the step changes the effluent concentration either increased (for the step decrease in influent ammonium concentration) or decreased. The differences between influent and effluent dissolved nitrogen concentrations are shown in Figure 6.23. The negative difference in the step decrease experiment implies that accumulated nitrogen in the

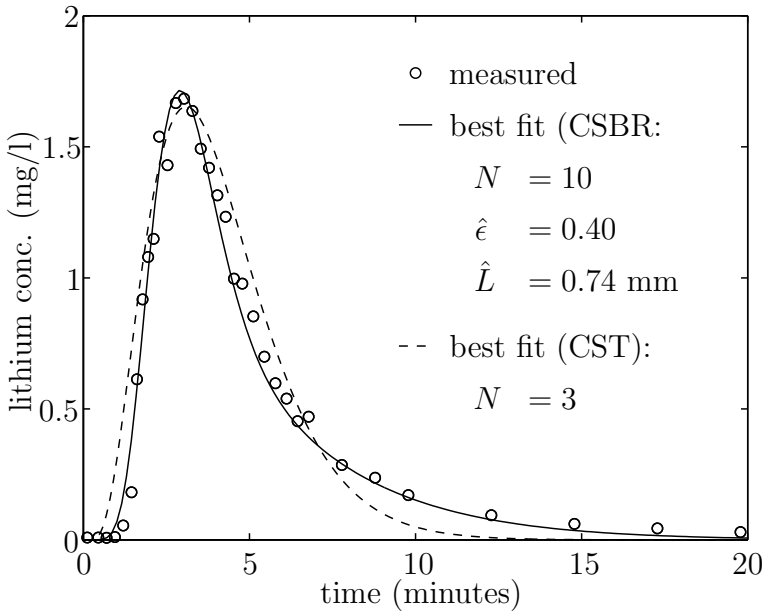

Figure 6.21 *Simulated and measured pulse responses (Jan).*

filter is released. Conversely, the positive difference in the other experiments indicate an accumulation of nitrogen in the reactor. By integration of the differences in the step experiments, and multiplication by the flow, the amounts of adsorbed ammonium can be roughly estimated to be around 10 gN. This corresponds to 2.7 mgN per square meter of biofilm, or 3.6 mgN per liter biofilm, which is far less than found by Nielsen (1996) for the sludge samples.

In Figure 6.23 it can be seen that prior to the step decrease experiment there is a loss of approximately 0.7 gN m^{-3} dissolved nitrogen in the filter. Approximately the same loss is observed in the ammonium step increase experiments when the transients settle. However, at low loads the loss of nitrogen is almost negligible. This indicates that nitrate is denitrified. The increased denitrification at higher loads can be explained by oxygen depletion in the deeper parts of the biofilm due to higher nitrification rates. Note, however, that as the transients settle in the flow-increase experiment, there is no indication of denitrification. The last drop in the difference is probably caused by a measurement error of the concentration of NO_x^- (the sum of NO_3^- and NO_2^-), but this does not explain why the effluent concentrations differ from those in the ammonium step increase experiment carried out on the same day. Poor wetting prior to the increase, which causes higher oxygen concentrations in the biofilm and, consequently, less denitrification, is a possible explanation of at least some of the difference.

In Figure 6.24 the measured influent concentrations in the step experiments in January are shown. The alkalinity and the nitrite concentrations were only measured in the step increase experiment in January. Influent nitrite concentrations assumed

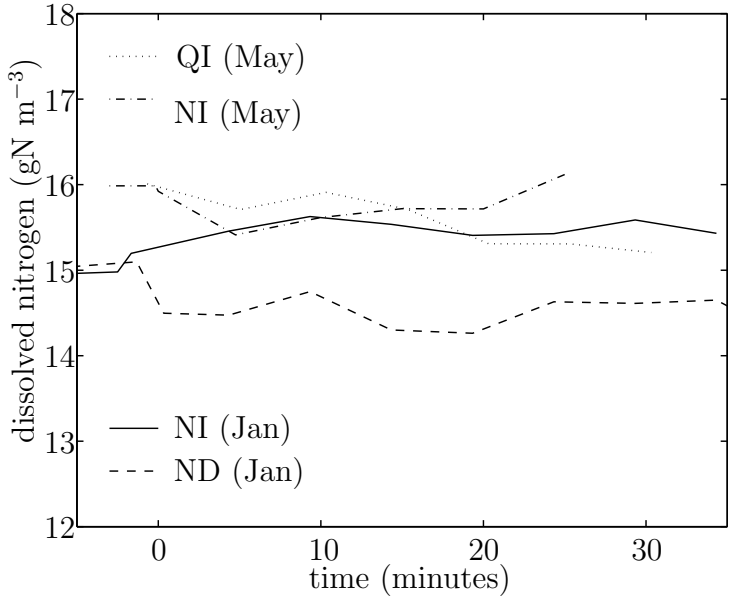

Figure 6.22 *Influent total concentrations of dissolved nitrogen.*

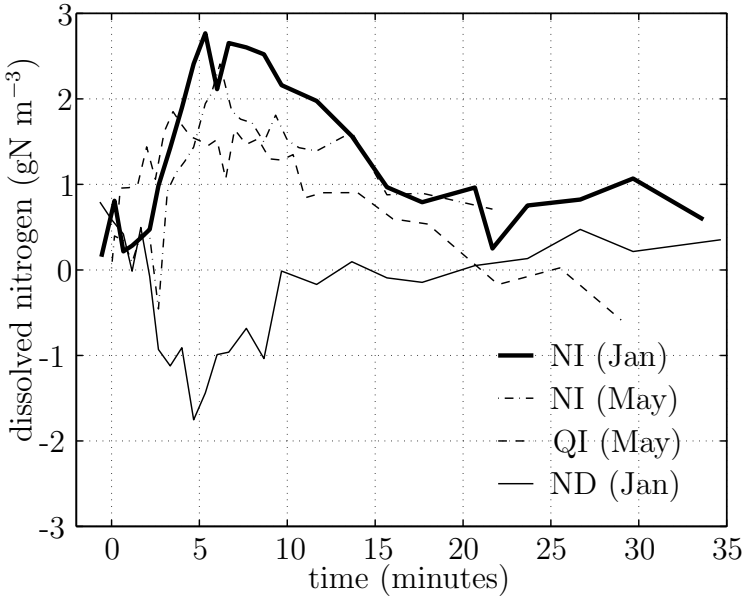

Figure 6.23 *Difference between influent and effluent total concentration of dissolved nitrogen ($NH_4^+ + NO_2^- + NO_3^-$).*

for simulation of the step decrease experiment are included in Figure 6.24b. The simulated effluent concentrations are insensitive to the influent nitrite concentration, since the amount of incoming nitrite is fairly small relative to the amounts of nitrite produced in the nitrification. The levels are set to 0.06 gN m^{-3} prior to the step and 1.3 gN m^{-3} after the step, which are the opposite influent concentrations to those in the step increase experiment carried out a few hours earlier (cf. Figure 6.24a).

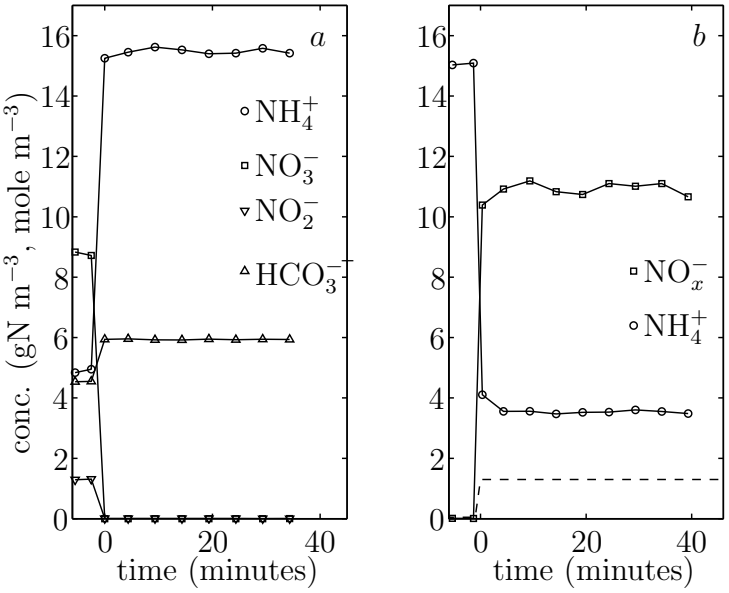

Figure 6.24 *Measured influent concentrations in the step increase experiment (a), and the step decrease experiment (b) in January. The dashed line in (b) is the nitrite concentration assumed for simulation.*

Four different kinds of simulation were carried out:

(a) Simultaneous nitrification, denitrification and adsorption according to the full model.

(b) Only nitrification and adsorption ($X_h = 0$).

(c) Only nitrification and denitrification ($k_a = 0$).

(d) Only nitrification ($X_h = 0$ and $k_a = 0$).

The influent concentrations in the simulations were linearly interpolated from the measurements presented in Figure 6.24. The bulk volume V in the model was set to the measured volume, and the values of N, ϵ_l and L used in the simulations are those that gave the RTD closest to the measured one. In Figures 6.25 and 6.26 the simulated and measured effluent concentrations are presented. Note that the

denitrification only affects the alkalinity and nitrate concentrations and that the adsorption does not affect the stationary concentrations.

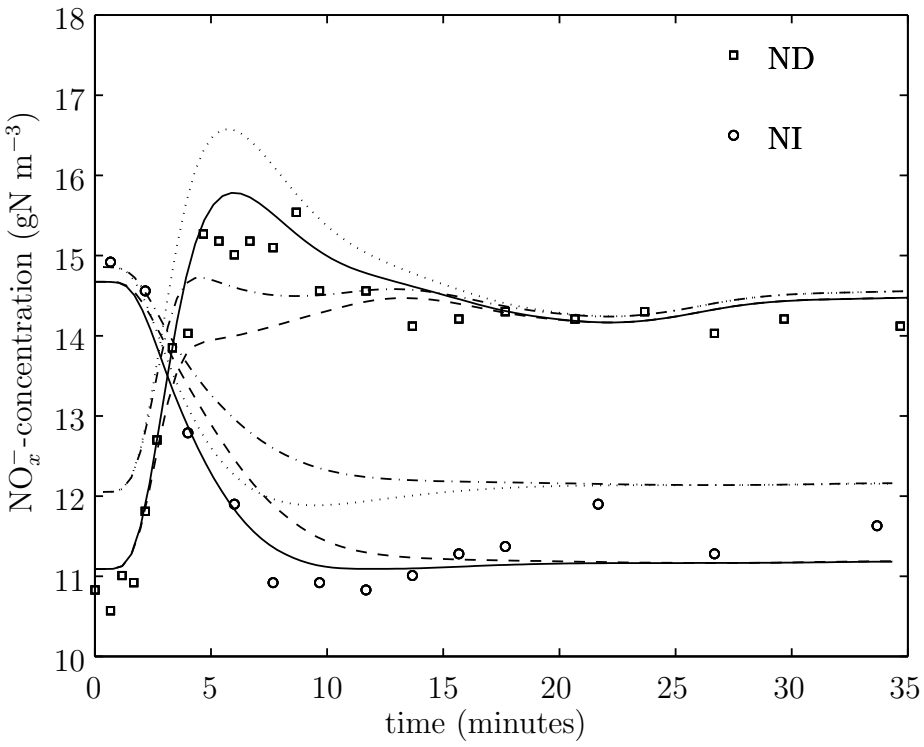

Figure 6.25 *Measured effluent concentrations of NO_x^- and concentrations simulated with the full model (solid lines), when $X_h = 0$ (dotted lines), when $k_a = 0$ (dashed lines), and when $X_h = k_a = 0$ (dot-dashed lines).*

It is evident that the full model (a) gives the closest agreement between simulated and measured concentrations in both experiments. The models with no denitrification (b and d) overestimate the effluent NO_x^- concentrations and underestimate the effluent alkalinity more than the others. The models with no adsorption (c and d) give too rapid responses in effluent ammonium concentration and not as good agreement in effluent concentrations of NO_x^- as the full model. It is noteworthy that although only small amounts of ammonium were adsorbed, the responses are quite different from what they would have been if no adsorption had occurred. Note, also, that the effluent transients in the step decrease experiment are faster than in the step increase experiment. This feature is captured by all models due to the nonlinear rate expression for the ammonium oxidization.

The reason why the model with no adsorption gives too rapid transients is that the characteristic time of Eq. (6.50) is about the same as for the RTD-model when $k_a = 0$. Hence, the response will be close to the integrated pulse response. In Fig-

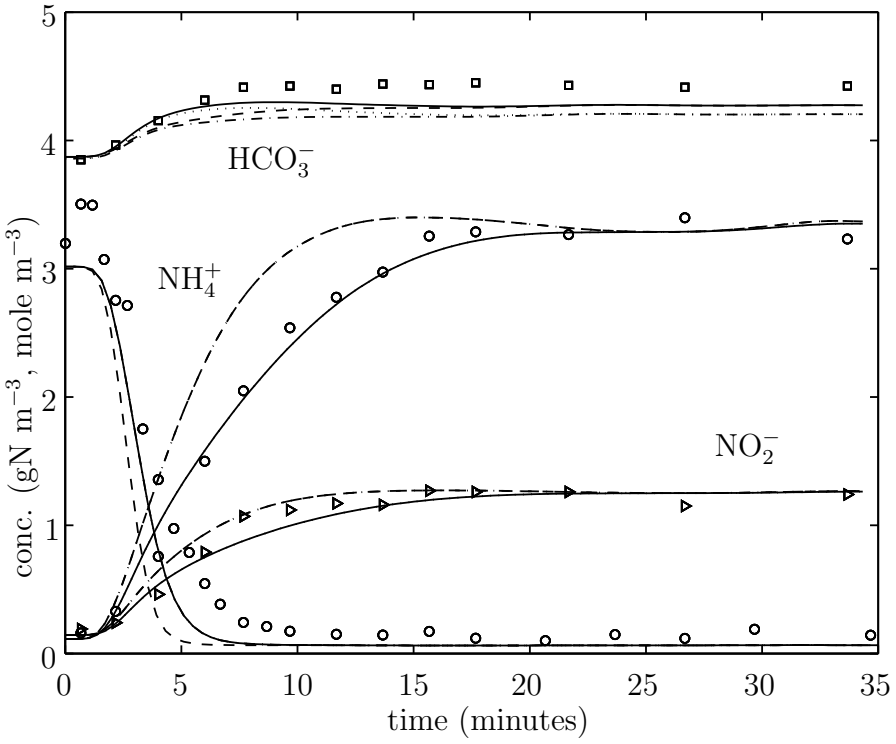

Figure 6.26 *Measured effluent concentrations and concentrations simulated with the full model (solid lines), when $X_h = 0$ (dotted lines), when $k_a = 0$ (dashed lines), and when $X_h = k_a = 0$ (dot-dashed lines).*

ure 6.27 the integrated pulse responses are compared with the effluent ammonium concentrations and effluent alkalinity in the step increase experiments. The integrated RTDs and the alkalinity agree well, but the responses in effluent ammonium concentration are considerably slower than the pulse responses. Since the alkalinity is reduced proportionally to the nitrified ammonium, the responses in effluent ammonium concentration and effluent alkalinity would follow each other closely if no adsorption occurred. However, the adsorption increases the hold-up of ammonium, which makes the response in ammonium concentration slower. This implies that influent and effluent measurements of the ammonium concentration, to determine stationary nitrification rates, should be made longer after changes in operating conditions than the RTDs indicate. The measured mean residence time is five minutes and, judging from the responses in Figure 6.27, the measurements should be made after at least six times that time.

In the experiment where KCl was added there was a tendency of increased effluent concentrations (max 0.5 gN m^{-3}) during a period after the addition started and a period of decreased concentrations (max 0.3 gN m^{-3}) after the addition stopped. These observations agree with the theory of an ion-exchange between ammonium

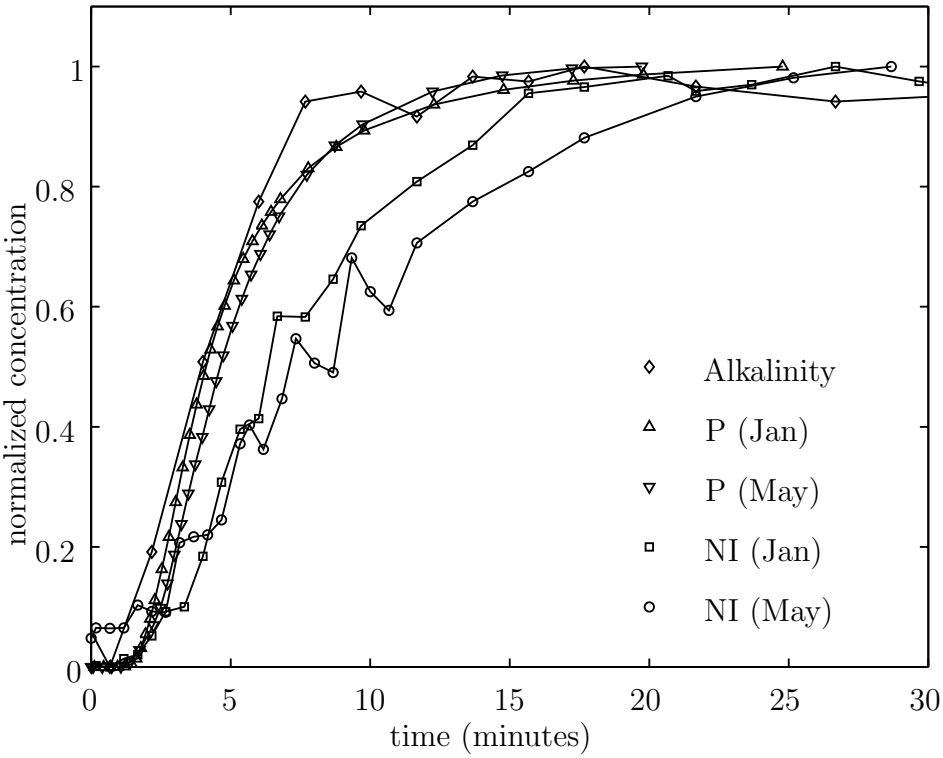

Figure 6.27 *Normalized change in effluent ammonium concentrations (NI), alkalinity and normalized integrated RTDs (P).*

and potassium ions. However, the changes are too small relative to the variance of the measurements to make any conclusions to what extent such an ion-exchange occurred.

The step experiments carried out on the pilot-scale NTF at Rya did not indicate any adsorption of ammonium. The reasons for the differences in the observations from the plant at Rya and the plant at Sjölunda should be searched for in differences between the biofilms and the water qualities. The most apparent differences in water quality between the plants are a much softer water, a lower alkalinity, a lower pH and a lower conductivity for the plant at Rya. The macro-fauna of the plant at Sjölunda has been thoroughly investigated by Andell *et al.* (1993), who found that worms of the families *Naididae* and *Enchytraeididae* were dominating the macro-fauna. Snails (*Physa fontinalis*) were occasionally numerous, which was also observed during the experiments in January. Snails were never encountered in the plant at Rya. Apparently, the plant at Rya and the plants at Sjölunda had different macro-faunas although they were of the same kind and operated with similar influent concentrations. This can be seen as an indication of different biofilm compositions as well. The nitrification rates at the Sjölunda WWTP were also higher than those at the Rya WWTP.

6.5 Conclusions and Discussion

Using standard assumptions for the biofilm, non-rational transfer functions have been derived describing the fast dynamics of continuously stirred biofilm reactors (CSBRs) when the intrinsic reaction rate is of zero or first order and the biofilm substrata are planar, cylindrical or spherical in shape. The same equations and transfer functions may also be applied to catalytic reactors with porous catalysts. A method, based on the fact that the singularities of the transfer functions are spread out along the negative real axis, has been introduced to derive rational transfer functions that approximate the non-rational ones. These approximations have several appealing properties:

- The approximation regards the bulk dynamics and the biofilm dynamics as one system, as opposed to approaches where the distributed system for the biofilm dynamics is approximated separately.
- Efficient routines for simulations, using the rational transfer function models, are available in most types of numerical software.
- Many standard methods of controller design require rational transfer functions.
- The derivation only requires Newton-Raphson searches for the values of the singularities and evaluation of a few expressions.
- Changes in physical parameters, in particular the first order rate coefficient that may depend significantly on temperature, can easily be related to changes in the transfer function.
- Since the approximation is based on truncation of a sum of first order transfer functions with decreasing time constants and decreasing gain, the order of the approximate transfer function can be chosen for a specific application in a natural way and without any recalculations.

Typically, it is possible to use only second order transfer functions for each CSBR, i.e. the mass balances over the CSBRs and the second order partial differential equations describing the concentrations in the biofilm can be replaced by second order ordinary differential equations (ODEs). Sometimes, only one singularity has to be used, which corresponds to an approximation by a first order ODE.

The models and the methods have been applied to nitrifying trickling filters, where the filter is modeled by N cascaded CSBRs. The approximate transfer function and the first principle transfer function were used to estimate reactor and biofilm parameters from residence time distributions. Using the estimated values, a transfer function matrix was derived, describing the dynamics caused by changes in influent ammonium concentration and influent flow. Simulations using this transfer function agreed fairly well with experimental data, which indicates the possible use of the transfer function approach for more realistic operating conditions.

A number of experiments, where the ammonium load into a large pilot-scale tertiary NTF was changed as steps at nearly constant concentrations of total dissolved nitrogen, have been carried out. The following experimental observations were made:

- Under stationary conditions the effluent total concentrations of dissolved nitrogen (ammonium, nitrite and nitrate) were almost equal to the corresponding influent concentrations at low ammonium loads and 0.5-1.0 gN m^{-3} lower than the influent concentration at high loads.
- After the step changes there was a period of approximately half an hour when the difference between influent and effluent concentrations of dissolved nitrogen was negative after a step decrease and positive after a step increase.
- The transients of the effluent ammonium concentration were significantly slower than could be expected from LiCl trace substance pulse response experiments.

From the experiments it is concluded that denitrification occurs in the biofilm at high loads due to oxygen depletion in the inner parts of the biofilm and that ammonium is being adsorbed to the biofilm when the load increases and desorbed at approximately the same rate when the load decreases. A rough estimate of the amount of adsorbed ammonium is 2.7 mgN per m^2 of biofilm at influent ammonium concentrations of 15 gN m^{-3}.

A physically based model, including nitrification in two steps, denitrification and ammonium adsorption and desorption, has been presented. The model was calibrated from the pulse responses, measured bulk water volume and stationary effluent concentrations of ammonium, nitrite and nitrate. Responses simulated with this model agree with the experimental data, which further supports the above conclusions. From the simulations it is evident that the effects of adsorption on the responses are considerable although the actual amounts of adsorbed ammonium are small relative to amounts that have been observed in activated sludge.

The adsorption and desorption of ammonium may affect the transient behavior of the plant to such an extent that they should be taken into account in models of the fast dynamics. Further, the resulting slower transients imply that influent and effluent measurements of ammonium, to determine stationary nitrification rates, should be made quite a long time after changes in operating conditions.

Similar experiments carried out on another nitrifying trickling filter of the same kind, which had been operating with almost the same influent concentrations, did not indicate any adsorption. The factors influencing the adsorption need to be further investigated to make a priori estimations of the fast dynamic behavior of a plant.

Chapter 7

QUASI-STEADY STATE

A plant in a quasi-steady state is defined as a plant where the transients of the dissolved components, after a change in operating conditions, have settled and where the solid components in the biofilm are in a steady state corresponding to a different operating point. With this definition of a quasi-steady state a 2^2 factorial design experiment, carried out on a pilot scale NTF during a period of two months, is analyzed. The purpose of the experiment was to see how the nitrification rate was affected by changes in flow and influent ammonium concentration at a constant ammonium load. A statistical analysis of the experiments revealed no difference in efficiency between the setup with high hydraulic load and low influent ammonium concentration, and vice versa. Model simulations agree fairly well with the experimental data, with differences in nitrification rate between the setups that are within the error margins of the experiments. From the analysis it is concluded that an increase in flow improved the mass transfer into the biofilm, probably due to increased turbulence. This was accounted for in the model by an oxygen mass transfer coefficient that increases with flow.

Assume that a plant has been operating under certain conditions for a long time. The bacterial distributions in the biofilm can then be assumed to be in a steady state. After a change of operating conditions the dissolved components will have a transient behavior that will settle after a fairly short time. The bacterial distributions, on the other hand, may be assumed to be unchanged. Mathematically, this state is determined by first solving a true steady-state for the original operating conditions, and then letting the bacterial concentrations be constant while determining the steady-state solution for the dissolved components for the new operating conditions. The resulting state is denoted a *quasi-steady state*.

Experiments, where the influent concentrations are changed and kept constant until the effluent concentrations stabilize, are often carried out on plants to evaluate their efficiency. Normally, the operating conditions before the experiments are then only known as averages of sparse samples. Model simulations of the plant being in a quasi-steady state can be a useful tool for the evaluations of such experiments.

Modeling aspects, numerical techniques and some experimental comparisons with a model of a nitrifying trickling filter are presented in this chapter. The section concerning the comparisons is mainly based on the work of Wik *et al.* (1995).

7.1 Modeling

From the definition of a plant in a quasi-steady state we may express the modeling in two steps:

1. The true steady state for the operating conditions that the solid components in the biofilm should be determined for.
2. The steady state for the dissolved components using the values of the solid components determined in step 1.

If the bulk concentrations are known, the true steady state can be determined as in Chapter 4. However, in this chapter we focus on the case when we have CSBR-models. Then, only the influent concentrations to the (first in a series of) CSBRs are typically known. As a basis for the derivation of the stationary equations the dynamic multi-species biofilm model in Chapter 3 is used.

The stationary mass balances for the dissolved components in a CSBR with planar substrata are [cf. Eqs. (3.8), (5.1) and (5.2)]:

$$Q(c_{i,in}^b - c_i^b) = AD_i \left[\frac{dc_i}{dx}\right]_{x=L} - A_g J_{g,i}, \qquad i = 1, \dots n_l \tag{7.1}$$

and

$$\frac{d}{dx}\left(D_i \frac{dc_i}{dx}\right) = -r_{v,i}, \quad 0 < x < L, \tag{7.2}$$

with the boundary conditions [cf. (3.9) and (3.10)]

$$D_i \frac{dc_i}{dx} = 0 \qquad \text{at } x = 0, \tag{7.3}$$

$$D_i \frac{dc_i}{dx} = \frac{D_i^b}{L_w}(c_i^b - c_i) \qquad \text{at } x = L. \tag{7.4}$$

By setting L_w to zero, the latter boundary condition becomes the Dirichlet boundary condition $c_i(L) = c_i^b$.

We may reformulate the boundary condition at $x = L$ by eliminating c_i^b from Eqs. (7.1) and (7.4). For non-gaseous compounds, i.e., those compounds that have $J_{g,i} = 0$, the boundary condition at $x = L$ becomes

$$D_i \frac{dc_i}{dx} = \frac{QD_i^b}{QL_w + AD_i^b}(c_{i,in}^b - c_i), \tag{7.5}$$

which is a boundary condition of the same form as (7.4), but with the bulk concentration c_i^b replaced by the influent bulk concentration c_{in}^b.

If the flux at the bulk/air interface for a gaseous compound is expressed as a function of the bulk concentration, we may proceed in the same way. For example, if the oxygen mass transfer is modeled as in Chapter 5, i.e.,

$$J_{g,O_2} = K_{L,O_2}(c_{O_2}^{sat} - c_{O_2}^b),$$

we get the boundary condition

$$D_{O_2}\frac{d}{dx}c_{O_2} = \frac{QD_{O_2}^b}{Q'L_w + AD_{O_2}^b}(c_{in,O_2}^b - c_{O_2}) + \frac{D_{O_2}^b A_g K_{L,O_2}}{Q'L_w + AD_{O_2}^b}(c_{O_2}^{sat} - c_{O_2}), \qquad (7.6)$$

where $Q' = Q + A_g K_{L,O_2}$.

Thus, the concentrations of the dissolved components are given by first solving Eq. (7.2) with boundary conditions (7.3), (7.5) and (7.6), and then using Eq. (7.1) or Eq. (7.4) to determine the bulk concentrations c_i^b from the concentrations c_i at the biofilm surface.

The distribution of solid components in the biofilm is given by Eqs. (4.2) and (4.4):

$$\frac{du}{dx} = \frac{1}{1-\epsilon_l}\sum_{j=1}^{n_s}\epsilon_j(\mu_{o,j} + \varphi_j), \qquad 0 < x < L, \qquad (7.7)$$

$$\frac{d\epsilon_j}{dx} = \frac{\epsilon_j}{u(1-\epsilon_l)}\left(\mu_{o,j}(1-\epsilon_l) - \sum_{k=1}^{n_s}\epsilon_k(\mu_{o,k} + \varphi_k)\right), \quad j = 1, \ldots n_s, \qquad (7.8)$$

where the following expressions have to hold at the substratum:

$$0 = u(0), \qquad (7.9)$$

$$0 = \epsilon_j(0,t)\left(\mu_{o,j} - \frac{1}{1-\epsilon_l}\sum_{k=1}^{n_s}\epsilon_k(\mu_{o,k} + \varphi_k)\right) \quad j = 1, \ldots n_s. \qquad (7.10)$$

As discussed in Chapter 4, the second expression above typically implies that all species in the biofilm must have the same observed specific growth rate at the biofilm substratum, i.e., $\mu_{o,j} = \mu_{o,i}$ for all species i and j existing in the biofilm. Generally, the conditions on the influent bulk concentrations for coexistence are less restrictive than the conditions on the bulk concentrations found in Chapter 4, since the reduction of the bulk concentrations over the CSBR depends on the bacteria concentrations in the biofilm. Provided the biofilm is sufficiently thick, the natural boundary condition is therefore $\mu_{o,j} = \mu_{o,i}$ for all i and j.

The stationary biofilm thickness has to satisfy [cf. Eq. (3.15)]

$$f(L, Q, \ldots) = u(L). \qquad (7.11)$$

To conclude the modeling, the first step to achieve a quasi-steady state is to solve Eqs. (7.2), (7.7) and (7.8) with boundary conditions (7.3), (7.5), (7.6), (7.9) and (7.10). In the second step Eq. (7.2), with boundary conditions (7.3), (7.5) and (7.6), is solved without changing the volume fractions determined in the first step.

7.2 Numerical Techniques

Numerically, there are several ways to solve the model equations. The true stationary solution in step 1 can be determined with a shooting and matching routine in more or less the same way as in Chapter 4:

I. Assign an initial biofilm thickness L.

II. Guess the volume fractions $\epsilon_j(0)$ at the biofilm substratum for $n_s - 1$ species.

III. Guess the concentrations, $c_i(0)$, of $n_l - n_s + 1$ substrates at the biofilm substratum.

IV. Use the boundary condition (7.10), which gives a linear dependence for all $\epsilon_j(0)$ on each other:

$$\mu_{o,j} = \frac{1}{1-\epsilon_l} \sum_{k=1}^{n_s} \epsilon_k(\mu_{o,k} + \varphi_k), \quad j = 1, \ldots n_s$$

and nonlinear dependencies for the substrate concentrations:

$$\mu_{o,j} = \mu_{o,i} \quad \text{for all } i \text{ and } j,$$

to determine the remaining volume fraction and the remaining $n_s - 1$ substrate concentrations at the substratum.

V. Set $u(0)$ to a small number (e.g. 10^{-13}) and integrate Eqs. (7.2), (7.7) and (7.8) from the substratum to the biofilm surface.

VI. Insert the resulting substrate concentrations and gradients, as well as the known concentrations, into the boundary conditions (7.5) and (7.6). Determine the residual errors and, by numerical differentiation, the gradients with respect to the variables guessed in II and III.

VII. Use, for example, a Newton method to determine improved guesses of the substrate concentrations and volume fractions at the substratum. Repeat from IV until the residuals are less than a set tolerance.

VIII. Assume that the value of $u(L)$ is correct and use Eq. (7.11) to determine a new biofilm thickness. Repeat from II, with initial guesses from the solution for the former thickness, until the change in biofilm thickness is less than the tolerance.

Sometimes the boundary condition $\mu_{o,j} = \mu_{o,i}$ in step IV is difficult to use for calculation of the substrate concentrations that are not guessed in step III. All substrate concentrations may then be guessed, and the boundary condition be treated in the

same way as the boundary conditions at the biofilm surface, i.e., the residual is determined in every step and included in the Newton search. In order to avoid finding no, or an incorrect, solution in the matching process it is important to have either initial guesses that are very close to the solution, or to have a routine that allows the user to define constraints on the variables.

In the second step only the stationary equations for the dissolved components have to be solved for a new set of influent concentrations. The equations define a second order boundary problem that is, generally, only slightly nonlinear. This problem can also be solved by shooting and matching. All substrate concentrations at $x = 0$ are then guessed and Eq. (7.2) is integrated from $x = 0$ to $x = L$, where the residual errors are determined from the boundary conditions (7.5) and (7.6). New guesses are made based on a Newton method until the requested tolerance is met. No further iterations are needed since the biofilm thickness and bacterial concentrations have already been determined in the first step.

7.3 Comparisons with Experiments

Hansson (1994) carried out a set of 2^2 factorial design experiments on the pilot scale nitrifying trickling filter, described on pages 56 to 58, at the Rya wastewater treatment plant in Göteborg. The Rya WWTP was at the time a conventional activated sludge plant with simultaneous precipitation of phosphorus to be extended for nitrogen removal. Part of the effluent from the present plant was planned to be nitrified in a trickling filter and recirculated to the activated sludge tanks for denitrification (Lyngå and Balmér 1992). This process was estimated to give a nitrogen removal of 60-70%, reducing the effluent nitrogen content to approximately 10 gN m^{-3}. However, the recirculation ratio then had to be 100-200% of the influent flow to the plant, which would give low influent ammonium concentrations to the NTF, 6-9 gN m^{-3}, whereas the hydraulic load would be high (approximately 200 md^{-1}). The low ammonium concentrations would cause the nitrification process in the trickling filters to be partially limited by the diffusion of ammonium. Hence, the low ammonium concentrations were expected to influence the nitrification rate negatively.

The repeated 2^2 factorial design experiments, independently varying the hydraulic load and ammonium concentration, were carried out in order to evaluate the short term effects of the hydraulic load and the influent ammonium concentration to the NTF. The use of a model for comparisons with the experiments made it easier to evaluate the experimental results and to draw physical conclusions.

The NTF is modeled with the same approach as in the studies of the fast dynamics, i.e., the filter is divided into N cascaded CSBRs (see Figure 5.4). Since the organic contents in the influent were very low, the competition by heterotrophs is ignored and we use the biofilm model for only autotrophic nitrifying bacteria with the rate expressions in Table 3.1. The contact area between the bulk and the air is assumed

to be the same as the biofilm area and the oxygen mass transfer coefficient given by Eq. (5.7) is used. The values $N = 10$, $\epsilon_l = 0.3$ and $L = 0.64$ mm, estimated from the residence time distributions and used in Chapter 6, are used here as well. The thickness of the liquid boundary layer, L_w, is assumed to be zero. All other parameters are given in Appendix B, except for the maximum growth rates, which were set to $\mu_{m,ao} = 0.6$ d^{-1} and $\mu_{m,no} = 0.9$ d^{-1} such that the nitrification rate for the the setup with the highest load approximately agrees with the measured ones on the average.

7.3.1 Experimental Setup

The experiments were carried out using wastewater pumped from the effluent channel of the Rya WWTP and recirculated water from the effluent of the NTF itself as influent water to the filter. Average operating conditions for the pilot plant during the experimental period (Feb.-May) are given in Table 7.1. The rotational speed of the dual arm distributor was 0.7 rpm during the experiments. Two pumps were used for mixing the two flows (see Figure 6.12). They could be set manually or automatically at flows in the range of 0-15 l/s. With a knowledge of the ammonium concentration in the two flows, the pumps could be set to feed the trickling filter with any flow and ammonium concentration up to the limits set by the pumping capacity and the ammonium concentration in the effluent wastewater of the WWTP. For these experiments, the ammonium concentration in the effluent wastewater from the WWTP was measured by the online instrument, described in Section 6.4.1, before each experiment. The effluent concentration from the NTF was estimated for the conditions of the experiment. Using the estimated concentration, the approximate flows giving the target flow and target influent ammonium concentration were then calculated from mass balances over the NTF. For the 2^2 factorial design experiments, the target setup values are given in Table 7.2. The estimated effluent ammonium concentrations were 6.0 gN m^{-3} in setup A and 0 gN m^{-3} in the others. These rough estimates resulted in a systematic error in the achieved load, which is commented further on.

Setup C represents the situation where the future trickling filter (existing today) is operated as a pure post nitrification unit and setup B corresponds to the situation where the recirculation to the anoxic zone of the activated sludge stage is approximately 100% of the influent flow to the WWTP. The ammonium load, which is defined as

$$J_{q,NH_4} = \frac{Q}{A} c^b_{NH_4,in},$$

where $A = 9320$ m^2 is the biofilm area in the reactor, is equal in setup B and setup C (1.3 gN m^{-3}d). The two values of the flow correspond to hydraulic loads of 140 md^{-1} and 270 md^{-1}. On 15 separate occasions from February to May, the trickling filter was subjected to the four different conditions of the factorial design and one repeat experiment within a few hours. Samples of the influent and effluent of the trickling filter were taken after approximately 1 h, when the fast transients should have

Table 7.1 *Average influent conditions (Feb.-May 1994)*

	Average	Min.	Max.
Q (l/s)	15.2	8.5	22.8
T (°C)	11.0	6.8	16.2
$c^b_{NH_4,in}$ (gN m^{-3})	15.6	5.11	25.8
$c^b_{NO_2,in}$ (gN m^{-3})	0.06	0.00	0.23
$c^b_{HCO_3,in}$ (mole HCO_3 m^{-3})	2.7	1.9	3.7
pH	7.3	6.6	7.6
COD (gO_2 m^{-3})	37	19	56
Suspended solids (gSS m^{-3})	14.6	8.5	50.4
Phosphates (gP m^{-3})	0.08	0.02	0.46

settled, and analyzed for ammonium, nitrate, nitrite, COD, pH, phosphorus and alkalinity.

Table 7.2 *Target setup values*

		$c^b_{NH_4,in}$ (gN m^{-3})	
		16	8
Q (l/s)	18	A	B
	9	C	D

7.3.2 Comparisons

Due to the varying status of the NTF and the rough estimations of the effluent ammonium concentration in the setups, there were difficulties in achieving identical conditions for each setup experiment. This resulted in small variations in the flows but relatively large variations in the ammonium concentrations (see Table 7.3). However, on the average the conditions agreed fairly well with the target values.

The nitrification rate in each experiment versus the ammonium load is shown in Figures 7.1 and 7.2, which demonstrates the differences between setups A, B, C and D. The tendency towards a decreasing nitrification rate with an increasing load for setup A, and also to some extent in B and C, is a consequence of the assumption regarding the effluent ammonium concentration made when determining the two pumping flows.

The experimental and simulated mean value results are given in Table 7.3. It can be seen in Table 7.3 and Figures 7.1 and 7.2 that the simulations agree fairly well with

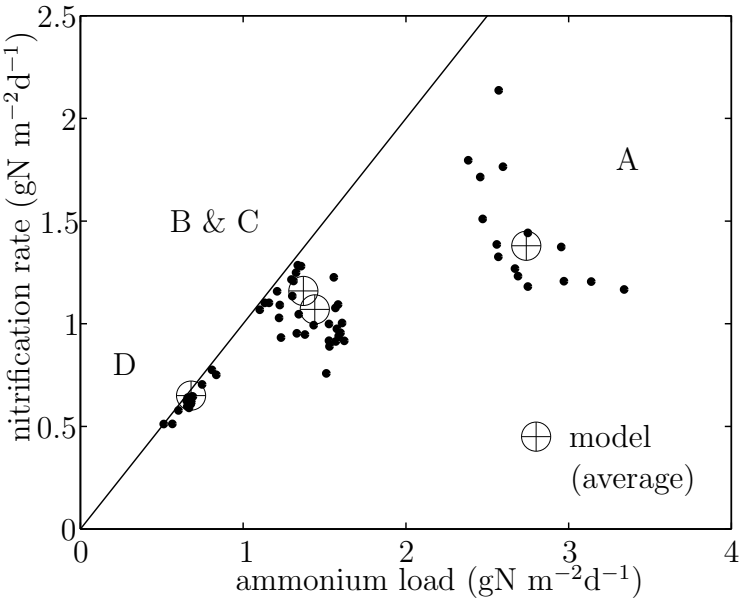

Figure 7.1 *Average simulated and measured nitrification rates versus ammonium load in all setups.*

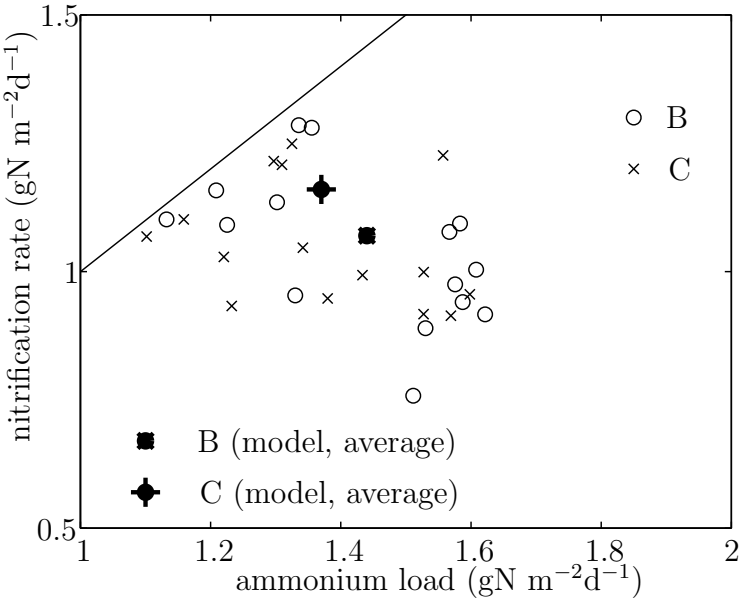

Figure 7.2 *Average simulated and measured nitrification rates versus ammonium load in setups B and C.*

the experimental data. However, one difference should be pointed out. The model predicts a higher nitrification rate in C than in B. There are two reasons for this. The first reason is that the nitrification in both setups is almost complete and, hence, ammonium is rate limiting in the lower regions of the trickling filter. This causes the nitrification rate to decrease substantially as the ammonium concentration reaches a certain value. According to the model the ammonium concentrations in the effluent are, therefore, very close for the two setups. This causes the predicted nitrification rates to be slightly higher in setup C. The second reason is that the high ammonium concentration in C increases the diffusion rate of ammonium into the biofilm, which was the reason why a decreased efficiency was expected at the higher hydraulic load. If the nitrification rate in reality is equal, or even higher in B than in C, this would mean that the conditions are improved by a higher flow. One plausible explanation could be that the turbulence in the bulk liquid increases with the flow. This would improve the oxygenation of the bulk, with an increased nitrification rate as a consequence. In the model this is only accounted for by the dependence of the oxygen mass transfer coefficient on the flow, according to Eq. (5.7). In a comparison presented by Wik *et al.* (1995) the bulk was assumed to be saturated with oxygen and, hence, no dependency on the flow was included in the model. The difference in simulated nitrification rate between setups B and C was then slightly higher (1.07 gN $m^{-2}d^{-1}$ in setup B and 1.20 gN $m^{-2}d^{-1}$ in setup C).

Table 7.3 *Average (±SD) experimental and simulated results*

Setup		A	B	C	D
Q_{in}	(l/s)	17.8±0.93	17.7±0.45	9.09±0.19	9.16±0.35
$c_{NH_4,in}$	(gN m^{-3})	16.6±1.90	8.75±1.05	16.3±1.95	7.95±1.01
$c_{NO_2,in}$	(gN m^{-3})	0.23±0.11	0.31±0.11	0.18±0.21	0.12±0.10
$c_{HCO_3,in}$	(mole $HCO_3^- m^{-3}$)	2.70±0.34	1.64±0.31	2.67±0.34	1.52±0.20
$c_{NO_3,in}$	(gN m^{-3})	5.10±2.90	12.8±3.01	5.07±2.76	14.1±4.70
$c_{NO_2,out}$	(gN m^{-3})	0.54±0.13	0.50±0.20	0.45±0.11	0.19±0.14
	model average	0.72	0.36	0.36	0.07
$c_{HCO_3,out}$	(mole $HCO_3^- m^{-3}$)	1.43±0.35	0.65±0.25	0.88±0.33	0.43±0.12
	model average	1.50	0.71	0.70	0.42
$c_{NO_3,out}$	(gN m^{-3})	13.2±3.05	19.3±3.49	17.7±3.10	21.7±6.54
	model average	13.0	19.3	18.7	21.8
$c_{NH_4,out}$	(gN m^{-3})	7.78±2.99	2.38±1.64	3.78±2.58	0.54±0.26
	model average	8.11	2.20	2.52	0.27
nitrification rate (gN $m^{-2}d^{-1}$)		1.45±0.27	1.04±0.14	1.05±0.12	0.63±0.07
	model average	1.39	1.07	1.16	0.65

If the boundary layer on the biofilm surface is not negligible, the increased turbulence should also decrease the thickness of the boundary layer. As a consequence, the concentrations at the biofilm surface should increase, as was found by Horn (1994), which in turn should also increase the nitrification rate.

In order to statistically analyze the difference in nitrification rates between setup B and C, the nitrification rate is assumed to be independent of the ammonium load in the range found for the two setups. The difference in rate within each experimental series may then be assumed to be samples from a normal distribution. Estimating the variance and using Student's t-distribution yield a 95% confidence interval for the nitrification rate in setup C minus the rate in B as 0.01±0.20. This interval covers, with large margins, the average difference found in the model simulations.

According to the theory applied in the model, the oxidation of ammonium is a straightforward nitrification of ammonium into nitrite and nitrate, while reducing the alkalinity by 2 mole HCO_3^-/14 gN-NH_4^+. This stoichiometric relation is supported by the experimental results. The average ratio between oxidized ammonium and reduced alkalinity was 7.0 (±1.5) gN/mole HCO_3^- for all experiments, and on the average all ammonium was oxidized into nitrite and nitrate, as can be seen in Figure 7.3. Accepting the theory, the measured difference in ammonium, alkalinity and nitrate plus nitrite over the NTF are three different measurements of the same process. The repeat experiments can be used to evaluate the variance in each of the three differences. Having estimated the variances, a weighted mean of the nitrification rate with minimum variance can be calculated from the three differences. Using the weighted nitrification rates, the 95% confidence interval for the rate in setup C minus the rate in setup B is reduced to -0.03±0.11, which almost covers the difference found in the simulations. However, the interval far from covers the difference found when the dependence of the oxygen mass transfer on the flow was not included in the model.

The measured effluent nitrite concentrations are shown in Figure 7.4. As can be expected, the nitrite concentration drops with decreasing effluent ammonium concentration. When ammonium becomes rate limiting in the lower regions of the trickling filter, the ammonium oxidation decreases and less nitrite is produced, but the nitrite oxidation will continue as long as there is nitrite left in the bulk water. The reasoning above and the experimental results are supported by simulations. Included in Figure 7.4 are simulated results for fixed flows of 9 l/s and 18 l/s for varying influent ammonium concentrations, which lead to varying effluent ammonium concentrations. Temperature, alkalinity and nitrite concentrations in the influent water were chosen as the average values given in Table 7.1 in the simulations. The model predicts slightly higher nitrite concentrations when the flow is low. This is due to lower oxygen concentrations caused by a lower value of the oxygen transfer coefficient K_{L,O_2} at the lower flow. In the comparison by Wik *et al.* (1995), where the bulk was assumed saturated with oxygen, the predicted nitrite concentrations were slightly higher at the higher flow.

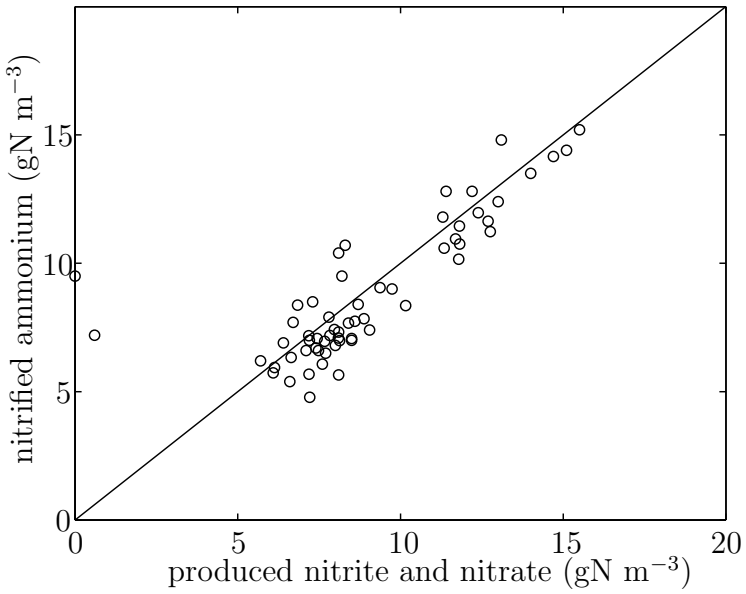

Figure 7.3 *Consumed ammonium versus produced nitrite and nitrate in the trickling filter.*

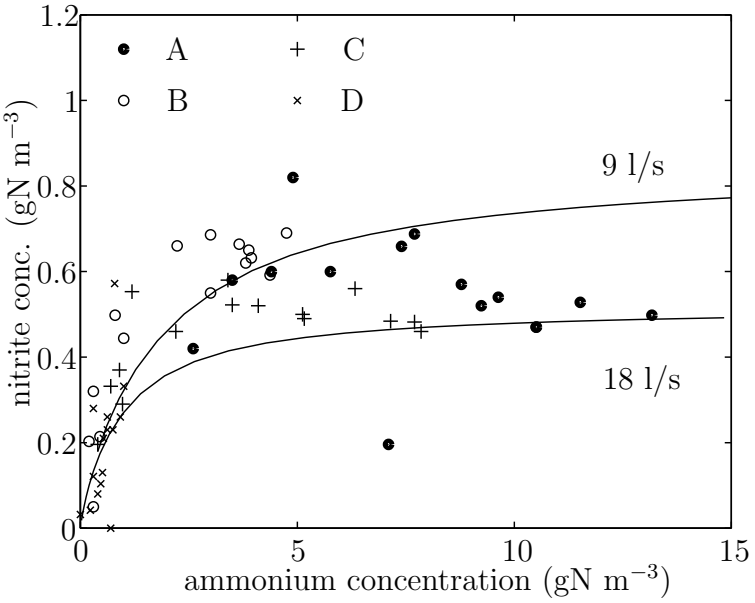

Figure 7.4 *Measured and simulated nitrite and ammonium concentrations in the effluent.*

7.4 Conclusions and Discussion

A plant in a quasi-steady state has been defined as a plant where the transients of the dissolved components, after a change in operating conditions, have settled and where the solid components in the biofilm are in a steady state corresponding to a different operating point. The application of this definition to CSBR-models results in a two step procedure: First a true steady-state has to be found, and then the volume fractions in the biofilm are kept constant while the equations for the dissolved components are solved for a steady state. A numerical procedure for simulation of a quasi-steady state, based on a solver of ordinary differential and algebraic equations, have been described.

Experiments, where the influent concentrations are changed and kept constant until the effluent concentrations stabilize, are often carried out on plants to evaluate their efficiency. In the evaluation of such experiments, modeling the plant as being in a quasi-steady state can be a useful tool in an analysis of the experiments. A 2^2 factorial design experiment carried out on a pilot scale NTF during a period of two months has been analyzed using such an approach. The analysis of the influence of the hydraulic load and influent ammonium concentration on the nitrification rate revealed no significant difference in performance between a high hydraulic load and low ammonium concentration, and vice versa, at the same ammonium load. The quasi-steady state model agreed fairly well with the measured concentrations of ammonium, nitrite, nitrate and alkalinity. However, the difference between simulated performance and experimental data indicates an improved substrate transport into the biofilm by a higher flow. A likely reason is an increased turbulence, which gives an improved oxygenation of the bulk. This can be modeled by a flow-dependent oxygen mass transfer coefficient. An increased turbulence would also reduce the thickness of a possible liquid boundary layer on the biofilm, which in such a case would improve the substrate flux into the biofilm as well.

Chapter 8

SLOW DYNAMICS

When the long term effects of the conditions for a biofilm reactor are to be studied, the dissolved components can generally be assumed to be in a steady state. Microbial processes, such as the growth and decay of the bacteria, will then govern the reactor behavior. A simulation method is described, which is based on solving the stationary equations with a finite element method and the dynamic equations with a physically based method. Simulations and data from an experiment, where an NTF had been alternatingly fed unnitrified and completely nitrified wastewater, agree fairly well. However, the differences in transient behavior indicate that for a closer agreement a biologically more sophisticated approach than the standard one has to be used in the biofilm model. An approach that includes exogenous dormancy is proposed, which can be used to model a time delay in the decay process initiated by starvation. Two different operating strategies of NTFs are studied by simulation: periodically inversing the order of two NTFs in series and varying the flow through NTFs operating in parallel. The simulations indicate that there is a potential of increasing the nitrifying capacity of filters operating at low ammonium loads with these strategies, provided the influent concentrations of organic matter are low. However, to what extent the capacity can be increased depends on the specific death rate of the nitrifiers, which needs to be further studied.

As already mentioned in Chapter 3, the origin of the dynamics in biofilm reactors can be divided into three groups:

(a) Changes in the biology.

(b) Transients of the dissolved components in the liquid phase of the biofilm.

(c) Transients in the bulk liquid.

Usually it takes days for the bacterial composition in the biofilm to change, while it only takes a few minutes for the concentrations in the biofilm to settle after changes

in the bulk concentration. The rapidity of the hydraulic modes (c) depends mainly on the bulk volume to flow ratio. Typically, the hydraulic modes are also fast. For example, in Chapter 6 we saw that the fast modes in trickling filters (modes b and c) settled in less than an hour. This natural separation of the dynamic modes implies that we only have to solve the dynamic equations for the solid components when we are simulating the slow dynamic behavior of biofilm reactors. We can solve the equations for the dissolved components in a steady state.

8.1 Model Equations

We recapitulate the equations for a CSBR with planar substrata where the dissolved components are in the steady state:

The dynamics of the solid components are given by Eqs. (3.12) to (3.15) which can be reformulated as

$$\rho_j \frac{\partial}{\partial t}\epsilon_j = -\frac{\partial}{\partial x}(u\rho_j\epsilon_j) + r_{vs,j}, \quad 0 < x < L, \quad j = 1, \ldots n_s, \tag{8.1}$$

$$u = \int_0^x \frac{1}{1-\epsilon_l} \sum_{j=1}^{n_s+1} \frac{r_{vs,j}}{\rho_j} dx'. \tag{8.2}$$

The dissolved components in the biofilm are given by

$$\frac{d}{dx}\left(D_i \frac{dc_i}{dx}\right) = -r_{v,i}, \quad 0 < x < L, \quad i = 1, \ldots n_l, \tag{8.3}$$

with the boundary conditions derived in Chapter 7, i.e.,

$$D_i \frac{dc_i}{dx} = 0 \qquad \text{at } x = 0, \tag{8.4}$$

$$D_i \frac{dc_i}{dx} = \frac{QD_i^b}{QL_w + AD_i^b}(c_{i,in}^b - c_i) \qquad \text{at } x = L, \tag{8.5}$$

$$D_i \frac{dc_i}{dx} = \frac{QD_i^b}{Q'L_w + AD_i^b}(c_{i,in}^b - c_i) + \frac{D_i^b A_g K_L}{Q'L_w + AD_i^b}(c_i^{sat} - c_i) \quad \text{at } x = L, \tag{8.6}$$

where $Q' = Q + A_g K_L$. The boundary condition (8.5) should be used for non-gaseous components and the boundary condition (8.6) can be used for gaseous components, such as oxygen.

The bulk concentrations are given by

$$c_b = c_i(L) + L_w \frac{D_i}{D_i^b}\left[\frac{dc_i}{dx}\right]_{x=L},$$

and the biofilm thickness is given by Eq. (3.15), i.e.,

$$\frac{dL}{dt} = u(L) - f(L, Q, t). \tag{8.7}$$

8.2 Numerical Techniques

In the simulations presented in this chapter, the stationary equations for dissolved components, i.e. Eqs. (8.3) to (8.6), are solved with the finite element method (FEM) using the recently developed MATLAB toolbox FEMLAB (Comsol 1998). This toolbox solves the following general system of partial differential equations:

$$\begin{cases} -\nabla \cdot (b \otimes \nabla u + \alpha \otimes u - \gamma) + \beta \otimes \nabla u + au &= f &, \quad \Omega \\ \underline{n} \cdot (b \otimes \nabla u + \alpha \otimes u - \gamma) + qu &= g - h^T \lambda &, \quad \partial\Omega \\ hu &= r &, \quad \partial\Omega, \end{cases}$$

where $\underline{n}$ denotes the normal vector. With $u = c$, $b = D$, $f = r_v$, $\alpha = \gamma = \beta = a = h = r = 0$, and q and g from Eqs. (8.4) to (8.6), the system equals the stationary equations for dissolved components in the biofilm.

The substrate production rate r_v is typically a nonlinear function of the concentrations c_i. This implies that the solution has to be found by iteration. FEMLAB uses a damped Newton algorithm with the Armijo-Goldstein line search strategy. For this problem the Jacobian used is determined by numerical differentiation.

The major advantage of using the finite element method in FEMLAB instead of the previously discussed shooting and matching routines is the robustness of the finite element method. For the systems simulated in this chapter there were no problems of convergence that could not be resolved. However, fairly good initial guesses have to be provided, especially if it is important to keep the execution time short. The choice of initial guesses is discussed at the end of this section. The disadvantage, compared with the shooting and matching FORTRAN-routine D02SAF (NAG n.d.), is that FEMLAB is about ten times slower.

Further, it is important that the function returning the rate r_v in the iteration can deal with negative concentrations, since it is not possible to include constraints on the solution vector. A simple way to deal with the negative concentrations is to return zero rates when the Newton routine calls with negative concentrations. This method did not fail in any of the simulations. The solutions by the FEM-routine were successfully verified by the use of the concentrations at the substratum given by FEMLAB. Solving Eq. (8.3) with an ODE-solver from $x = 0$ to $x = L$ with these concentrations as initial values resulted in a perfect agreement with the FEM-solution.

The equations describing the dynamics of the volume fractions are solved with a method similar to that of Kissel *et al.* (1984). The biofilm is discretized into segments of equal size. After having solved the boundary problem for the dissolved components, we determine the rate of the volume change for the solid components, i.e.,

$$r_j = \epsilon_j \mu_{o,j}, \quad j = 1, \ldots n_s, \quad \text{and} \quad r_{n_s+1} = \sum_{j=1}^{n_s} \epsilon_j \varphi_j,$$

for each biofilm segment using the substrate concentrations in the midpoints of the

biofilm segments. After the multiplication of these rates by the integration time step, and the addition of the results to the old volume fractions, the sum of the new volume fractions is no longer $1 - \epsilon_l$ in every biofilm segment. The volume fractions in each biofilm segment are therefore normalized to give the sum $1 - \epsilon_l$, and the segments are expanded, or shrunk, such that the total volume of the segments are the same as before the normalization. By interpolation, a new division of the biofilm is made and a new biofilm thickness is calculated before the next time step is taken. The procedure is described in detail in Appendix F and illustrated in Figure 8.1 for a very rough discretization into biofilm segments. In the simulations the biofilm segments have a thickness of approximately 10^{-5} m, which corresponds to a division of the biofilm into approximately 50 segments, and the time step size used is 0.1 d. In Appendix F it is shown that this method converges towards Eqs. (8.1) and (8.2) when the thickness of the biofilm segments and the time step size approach zero.

Initial guesses

For the solution of the stationary equations for dissolved components initial guesses are required both for the finite element method and for shooting and matching routines. When a simulation is running, the solution at the previous time instant can be used to find an initial guess. The problem is therefore to find a suitable initial guess for the first time step. For reactors that are modeled by cascaded CSBRs, such as trickling filters, it is only for the first CSBR that a method to find good guesses is really needed. The solution at the preceding CSBR can be used as an initial guess for the others. One way to derive initial guesses is to use the simplified stationary models in Chapter 1. Applied to a nitrifying biofilm we may proceed as follows:

(i) Set the concentration of nitrite oxidizers to zero.

(ii) Set the bulk concentration equal to the influent concentration and determine which substrate that is rate limiting with Eq. (1.6).

(iii) Set the concentration of the rate limiting substrate at the substratum to zero, and use Eq. (1.5) to determine the other substrate concentrations.

(iv) Use Eq. (1.7), or Eqs. (1.8) and (1.9), to determine the fluxes and the concentration gradients at the biofilm surface.

(v) Integrate Eq. (8.3) from the surface to the substratum. If some concentrations become negative, increase the concentrations at the substratum to become positive and integrate from the substratum to the biofilm surface until the concentrations at the bulk agree with the boundary conditions.

(vi) Use the solution as an initial guess and solve the boundary problem (8.3) to (8.6) for the case when the concentration of nitrite oxidizers is zero.

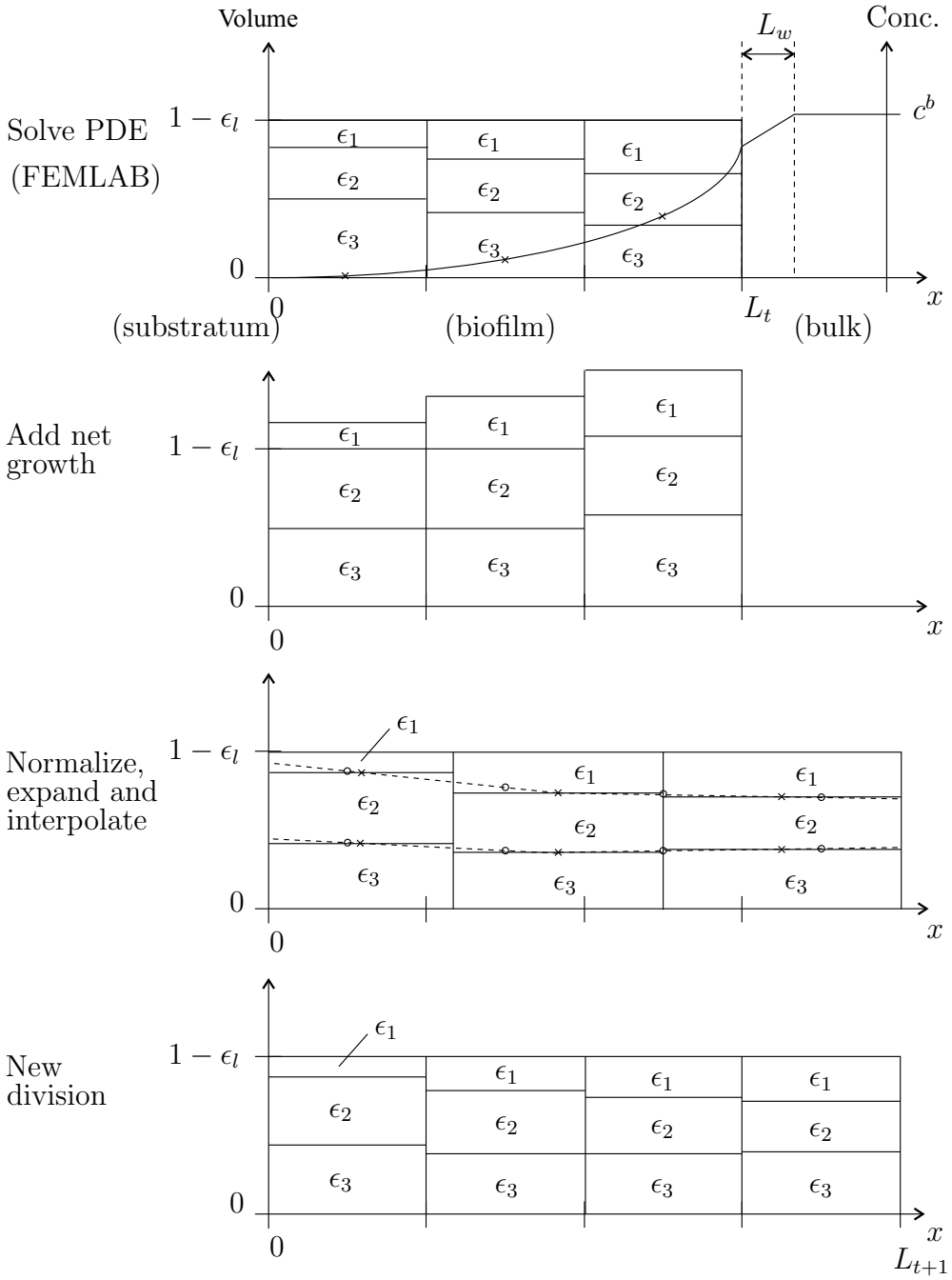

Figure 8.1 *Illustration of one time step in the solution method when the biofilm is divided into only a few segments, $n_s = 2$ and there is no erosion.*

(vii) Increase the concentration of nitrite oxidizers successively to the desired concentration, and use the solution from the former concentration as an initial guess when solving the equations.

For shooting and matching routines initial guesses are only needed for the concentrations at the substratum and the gradients at the biofilm surface, which implies that step (v) can be omitted.

8.3 Comparison with an Experiment

Boller and Gujer (1986) have carried out an experiment on a pilot scale NTF, with plastic cross-flow media, that clearly demonstrates the slow dynamic behavior. During a period of more than two months they first fed the NTF with completely nitrified tertiary wastewater for 25 days, then they fed wastewater containing ammonium for about 20 days, and finally they switched back to nitrified wastewater for 25 days. A few times in each period they dosed ammonium for a short time and determined the nitrification rate. Prior to the experiment, the NTF had been fed wastewater containing ammonium such that a stable nitrifying biofilm had developed.

In Table 8.1 the details about the trickling filter, and the experimental conditions are summarized [Boller and Gujer (1986), Markus Boller (personal communication)].

Table 8.1 *NTF data and experimental conditions*

	Parameter	Notation	Value	Unit
NTF Data	Cross sectional area	A_r	0.636	m^2
	Bed height	h	6.75	m
	Specific surface area	a	230	m^2m^{-3}
	Hydraulic load	q	4.0	mh^{-1}
	Average water temperature	T	11	°C
Before experiment	Influent ammonium	$c_{NH_4,in}$	13	gN m^{-3}
	Influent alkalinity[1]	$c_{HCO_3,in}$	4.2	mole m^{-3}
	Influent nitrite[1]	$c_{NO_2,in}$	0.2	gN m^{-3}
During experiment	Influent ammonium	$c_{NH_4,in}$	6.8	gN m^{-3}
	Influent alkalinity[2]	$c_{HCO_3,in}$	3.3	mole m^{-3}
	Influent nitrite[2]	$c_{NO_2,in}$	0.1	gN m^{-3}

[1] Deduced from (Boller and Gujer 1986) (results are insensitive to this value)
[2] Deduced from ammonium conc. and [1] (results are insensitive to this value)

The trickling filter has specifications similar to the pilot scale NTFs at the Rya WWTP and the Sjölunda WWTP which were presented in Chapters 5 and 6. Therefore, we model this plant in the same way, i.e., as 10 cascaded CSBRs and a biofilm porosity of 0.3. Further, we use the biofilm model for autotrophic nitrifying bacteria, with the rate expressions in Table 3.1 and parameter values in Appendix B. The

mass transfer resistance between the bulk and the biofilm is assumed to be negligible ($L_w = 0$). The oxygen mass transfer from the air to the bulk is modeled by Eq. (5.4) with $K_{L,O_2} = 2.4$ md^{-1}, as estimated by Boller and Gujer (1986). To achieve the measured nitrification rates the maximum growth rates are set to $\mu_{m,ao} = 0.75$ d^{-1} and $\mu_{m,no} = 1.0$ d^{-1}.

Two different models of the biofilm erosion are used:

(i) The biofilm has a constant thickness $L = 0.6$ mm.

(ii) The erosion function in Eq. (3.15) is assumed to depend only on the biofilm thickness (Wanner and Gujer 1986):

$$f(L) = 200L^2 \text{ (md}^{-1}\text{)}.$$

The value 200 m^{-1}d^{-1} in the erosion function gives an initial stationary biofilm thickness in the upper parts of the NTF that is close to 0.6 mm.

The measured and simulated nitrification rates are shown in Figures 8.2 and 8.3. We see that the nitrifying capacity decreases when no ammonium is fed to the filter and increases after ammonium is being fed again. The reason is that the concentration of nitrifiers in the biofilm decreases when no ammonium is fed, and increases when ammonium is available. The model describes roughly the same dynamic behavior. Apparently, the model with fixed biofilm thickness gives a closer agreement. The reason is that in the erosion model with variable thickness the biofilm thickness decreases rapidly as the net growth of the bacteria decreases and the time it takes to rebuild the biofilm makes the response to increased ammonium loads slower (see Figure 8.4).

It can be noted that the transient behavior after ammonium is being fed again is similar to that found by Wijffels *et al.* (1994) and Wijffels and Tramper (1989) in their investigations of nitrifiers immobilized in carrageenan gel beads.

The most apparent difference between the simulated nitrification rates and the measured ones is that the model predicts a rapid decrease in nitrifying capacity immediately after ammonium has stopped being fed, while the measurements show only a slow decrease in the beginning. The difference is less apparent after the second period without ammonium. It should be kept in mind, however, that the influent concentrations used in the simulations are average values, which may explain some of the differences. In Section 8.5 it is discussed how the observed differences can be explained from a biological reasoning that can be included in the biofilm model.

8.4 Simulations

Tertiary nitrifying trickling filters (NTFs) for treatment of municipal wastewater have only a few variables that can be manipulated during operation. The most

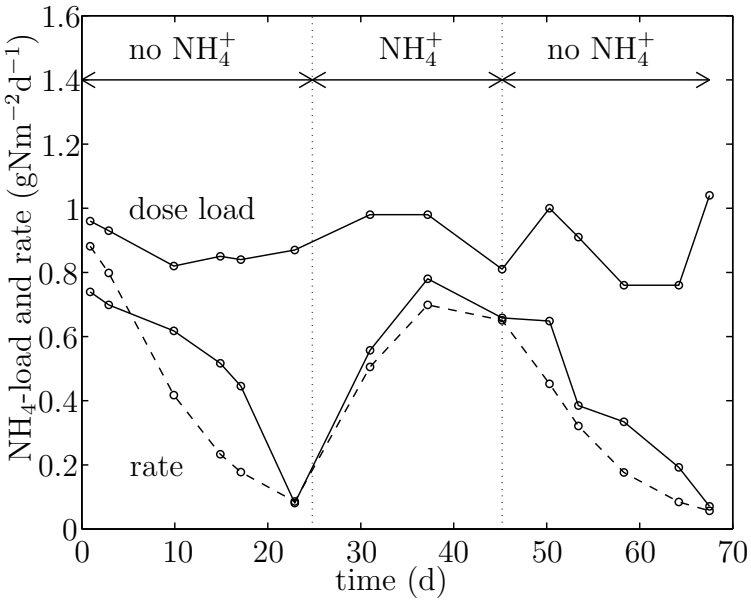

Figure 8.2 *Dose load (solid), measured nitrification rate (solid) and simulated nitrification rate (dashed) when the biofilm thickness is constant.*

important ones are the ventilation, the influent concentrations and the flow. However, the possibilities to use these variables to improve the nitrifying efficiency are limited. Natural draft often ensures sufficient aeration without the use of forced ventilation. Further, in general the flow cannot be manipulated independently of the other treatment units, and since the influent concentrations are the effluent concentrations of the preceding upstream process, neither can the concentrations readily be changed. Sometimes, though, recycled water from the sludge presses, which has a high ammonium content, can be added to the influent of the NTF. When there is a recirculation over the NTF, the flow and influent concentrations can also be manipulated by a change of the recirculation ratio and flow.

With setups of NTFs operating in series or in parallel there are a few ways that, independently of the other processes, may improve the nitrifying capacity. At low loads, the second NTF of two NTFs in series often operates at nutrient conditions that in the long run cannot support high concentrations of nitrifiers. Complete nitrification can therefore not be maintained during short periods of high loads. By inversing the order of the NTFs, a fairly high concentration of nitrifiers should be possible to achieve in both NTFs, which should improve the capacity to reduce peak influent ammonium concentrations. In the experimental study by Boller and Gujer (1986) the nitrifying capacity in the tertiary NTFs dropped considerably after 10-20 days of starvation, and it took about 10 days to regain the capacity lost during the starvation. Based on these results they suggested that the operating

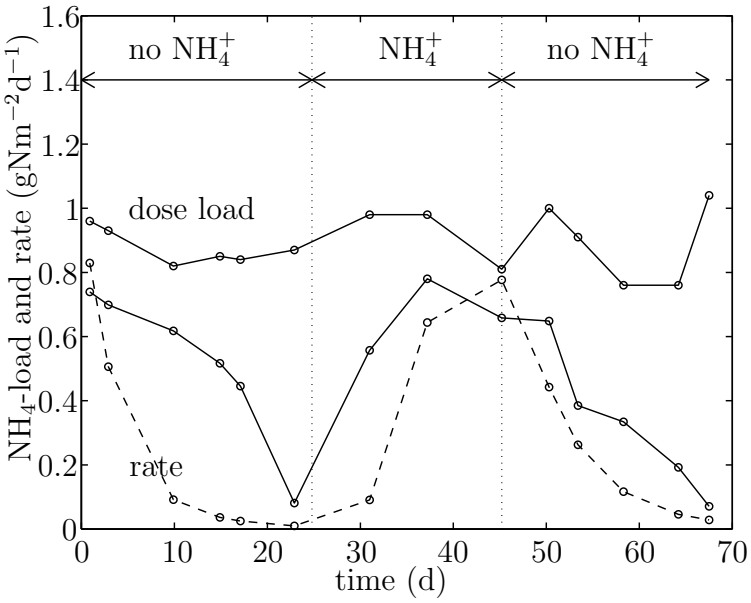

Figure 8.3 *Dose load (solid), measured nitrification rate (solid) and simulated nitrification rate (dashed) when the biofilm thickness varies.*

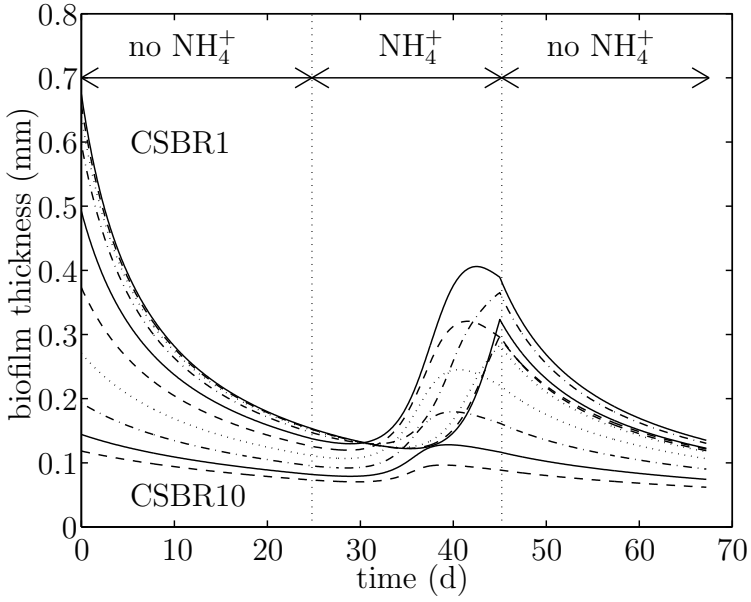

Figure 8.4 *Simulated biofilm thickness in the simulation with varying biofilm thickness.*

order of NTFs in series should be inversed within periods of 10 days. In a long term experimental study Andersson *et al.* (1994) observed an approximately 20 percent improved efficiency when they switched the operating order of two NTFs in series once a week. Judging from the time series of the measurements, though, the statistical significance of this improvement is rather low.

Nitrifiers have low growth rates, but they may regain high nitrification rates after fairly long periods of low loads. This indicates that non-stationary conditions, i.e. periods of high ammonium loads combined with periods of low ammonium loads, may be more advantageous than a constant loading. Hence, an operating strategy for NTFs in parallel, where the flow through each NTF is varied while the total flow through the NTFs is constant, may possibly improve the nitrifying capacity. For the same reason, it may be favorable to store the highly concentrated recycle water from the sludge presses and add it during short periods instead of adding it continuously to the influent.

In this chapter, we investigate by simulation: (i) switching orders of two NTFs operating in series and (ii) varying the individual flow through two NTFs operating in parallel. The possible improvements with these strategies are consequences of the slow dynamics of the growth and decay of the nitrifiers. This makes experiments showing the actual effects of the strategies on the nitrifying capacity extremely time consuming since the slow dynamics do not fully show in experiments carried out in a period of only a few days. Further, the effects of the strategies can be small without being negligible. Due to uncontrolled variations (disturbances) in water quality and plant conditions, an extensive measuring campaign must therefore be used during a long period of time in order to get reliable averages. This gives a strong motivation for studying the strategies by simulations before investigating them experimentally.

8.4.1 Switching Orders of Cascaded NTFs

In this simulation study we use the plant data for the NTFs at the Sjölunda WWTP to compare with the experimental data by Andersson *et al.* (1994). The approximate averages in their study are summarized in Table 8.2. The NTFs are modeled in the same way as in the last section, but with the plant specifications in Section 6.4.2. The biofilm porosity is set to 0.4, which was estimated from residence time distributions (see Figure 6.21). The same two kinds of erosion models as in the last section are used: either the biofilm is assumed to have a constant thickness $L = 0.74$ mm, as estimated from the residence time distributions, or the erosion function $f(L) = 100L^2$ (md^{-1}) is used, which gives an average stationary biofilm thickness of 0.74 mm in the first NTF. The oxygen mass transfer from the air to the bulk is modeled by Eqs. (5.4) and (5.7).

The influent to the first NTF is set to the values in Table 8.2. As a measurement of the nitrifying capacity, the simulated nitrification rate at twice these influent concentrations is used. The plants at the Sjölunda WWTP had very high nitrifi-

cation rates and, therefore, the maximum growth rates were set to $\mu_{m,ao} = 0.8$ d^{-1} and $\mu_{m,no} = 1.0$ d^{-1}. Further, the biofilm densities were increased from the default values in Appendix B to $\rho_{ao} = \rho_{no} = \rho_{inert} = 10$ kgCOD m^{-3}. The conditions prior to the switching are those achieved by simulating the two NTFs in series for 60 days with the influent conditions in Table 8.2 and initial conditions $\epsilon_{ao} = 0.3$, $\epsilon_{no} = 0.1$ and $L = 0.74$ mm in all CSBRs. The resulting initial concentrations of dissolved components and solid components in the biofilm are close to stationary. In Figure 8.5 the initial concentrations of the dissolved components are shown. We see that the nitrification is close to complete over the two NTFs, which implies that ammonium is rate limiting in the lowest parts of the second NTF.

Table 8.2 *Conditions in the simulation study*

Variable	Notation	Value	Unit
Influent ammonium concentration	$c_{NH_4,in}$	17	gN m^{-3}
Influent alkalinity	$c_{HCO_3,in}$	5.4	mole m^{-3}
Influent nitrite concentration	$c_{NO_2,in}$	0.001	gN m^{-3}
Influent BOD_7 *	$c_{BOD,in}$	10	gm^{-3}
Hydraulic load	q	120	md^{-1}
Water temperature	T	14	°C
Effluent ammonium concentration	$c_{NH_4,out}$	0.5	gN m^{-3}
Effluent BOD_7 *	$c_{BOD,in}$	9	gm^{-3}

* Not used in the simulations

Five different time intervals ($\Delta t_{switch} = 1$, 2, 4, 7 and 14 days) between inversing the order were simulated for both choices of erosion model. For all time intervals the switching strategies were simulated for 56 days. The results are summarized in Table 8.3 and illustrated in Figures 8.6, 8.7 and 8.8. The values in Table 8.3 are averages over the last switching period Δt_{switch} of the simulations. Note that $\Delta t_{switch} = \infty$ denotes stationary conditions (no switching), which is taken as the initial conditions. The values of the nitrifying capacity are the nitrification rates in the two NTFs when the influent concentrations to the first NTF were twice the values in Table 8.2.

In Figure 8.6 the total volumes occupied by the nitrifying species in each CSBR are shown for the case of a fixed biofilm thickness. The volumes in the case of variable biofilm thickness are almost identical to the ones in the figure even though the thickness decreased with distance from the inlet (see Figure 8.7). As expected, the two NTFs become far more uniform when the operating order is switched.

In Figure 8.8 the total nitrifying capacity, i.e. the capacity over both NTFs, are shown for the case of fixed biofilm thickness. According to the simulations, the more often the operating order is switched, the higher the nitrifying capacity. When

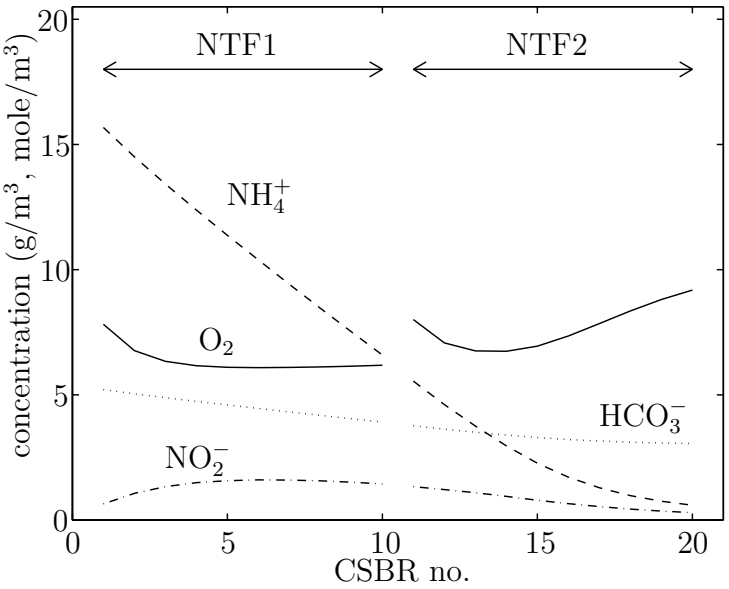

Figure 8.5 *Concentrations of dissolved components in the two NTFs at stationary conditions and constant biofilm thickness.*

the switching period decreases, it appears as if the capacity converges towards a limit that is close to the capacity when there is a switch every day. However, to simulate shorter time intervals than $\Delta t_{switch} = 1$ d the model should also consider the fast dynamics.

The increase in nitrifying capacity with decreasing switching periods was even more pronounced in the simulations with variable biofilm thickness. Switching the order less often than every four days did hardly improve the total capacity at all (see Table 8.3). Switching every day or every second day resulted in the same increase in capacity as in the case of fixed biofilm thickness. Quite surprisingly the switching improves the nitrifying capacity by only a few percent even though the biofilm is much more uniform in the two filters. The reason is that it is only close to the effluent that the ammonium concentration is sufficiently low to cause any substantial decrease in the nitrifying population.

Lowering all influent concentrations to 60 percent and 80 percent of the values in Table 8.2 will increase the parts of the second NTF where ammonium is rate limiting (cf. Figures 8.5 and 8.9). Consequently, the amount of nitrifiers will also decrease in those parts of the NTF (see Figure 8.10). At such low loads the advantage of switching is more apparent. Inversing the operating order every day then improves the nitrifying capacity by 12 percent and 25 percent compared with the capacity at stationary conditions (see Figure 8.11).

Table 8.3 *Simulation results for variable thickness*

	Δt_{switch}	d	1	2	4	7	14	∞
NTF1	Volume of *ao*	dm^3	203	207	216	225	221	209
	Volume of *no*	dm^3	77.4	77.5	77.6	78.0	74.9	68.2
	Average thickness	mm	0.66	0.66	0.66	0.66	0.65	0.74
	$c_{NH_4,out}$	gN m^{-3}	7.12	7.13	7.11	7.08	6.91	6.59
	$c_{NO_2,out}$	gN m^{-3}	1.14	1.15	1.20	1.28	1.36	1.44
	$c_{HCO_3,out}$	mole m^{-3}	3.99	3.99	3.99	3.98	3.96	3.91
	Rate	gN $m^{-2}d^{-1}$	2.27	2.27	2.27	2.28	2.32	2.39
	Capacity	gN $m^{-2}d^{-1}$	2.38	2.38	2.40	2.41	2.45	2.51
NTF2	Volume of *ao*	dm^3	191	186	176	164	156	172
	Volume of *no*	dm^3	76.6	76.3	74.9	71.9	69.4	76.7
	Average thickness	mm	0.66	0.66	0.66	0.66	0.66	0.56
	$c_{NH_4,out}$	gN m^{-3}	0.44	0.44	0.46	0.49	0.64	0.59
	$c_{NO_2,out}$	gN m^{-3}	0.30	0.30	0.30	0.31	0.35	0.30
	$c_{HCO_3,out}$	mole m^{-3}	3.03	3.03	3.04	3.04	3.06	3.06
	Rate	gN $m^{-2}d^{-1}$	1.54	1.54	1.53	1.52	1.44	1.38
	Capacity	gN $m^{-2}d^{-1}$	2.28	2.27	2.23	2.18	2.02	1.97

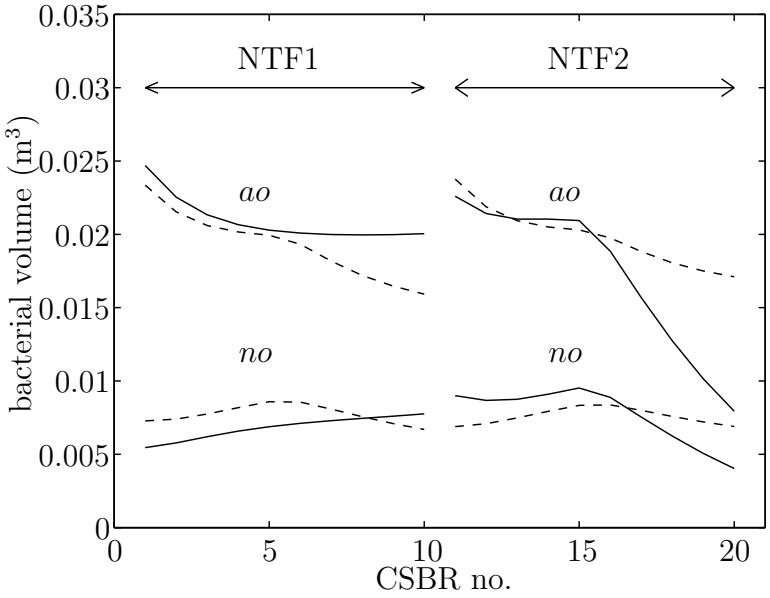

Figure 8.6 *Volume of the ammonium oxidizers (ao) and the nitrite oxidizers (no) in all CSBRs at stationary conditions (solid) and after 56 days of switching the order once every day (dashed).*

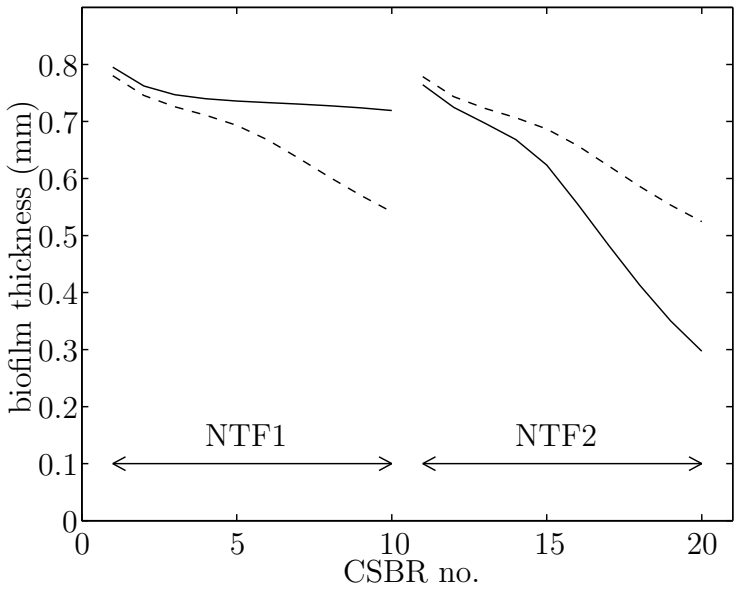

Figure 8.7 *Biofilm thickness in all CSBRs at stationary conditions (solid) and after 56 days of switching the order once every day (dashed).*

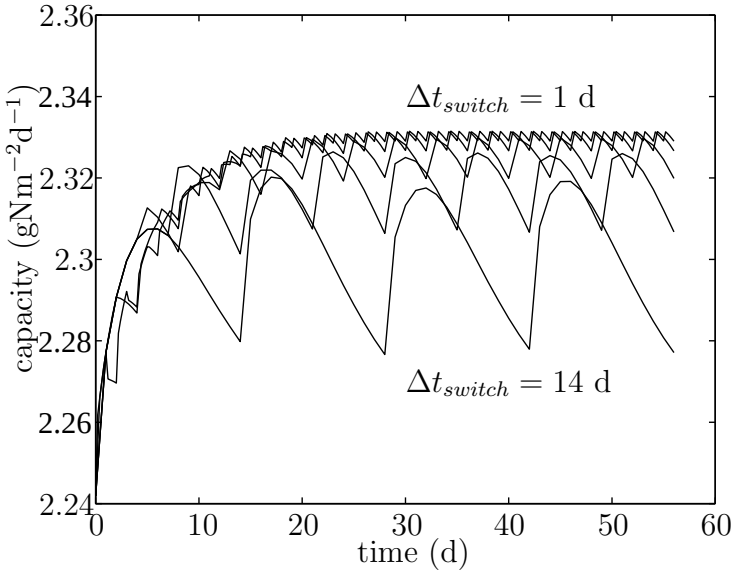

Figure 8.8 *Nitrifying capacity for fixed film thickness when switching the order with time intervals Δt_{switch} =1, 2, 4, 7 and 14 days.*

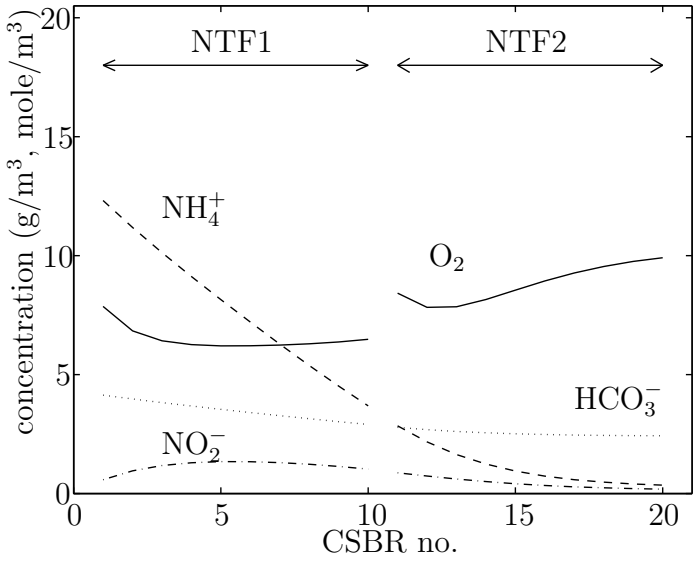

Figure 8.9 *Concentrations of dissolved components in the two NTFs at stationary conditions and constant biofilm thickness when the influent concentrations have been reduced by 20%.*

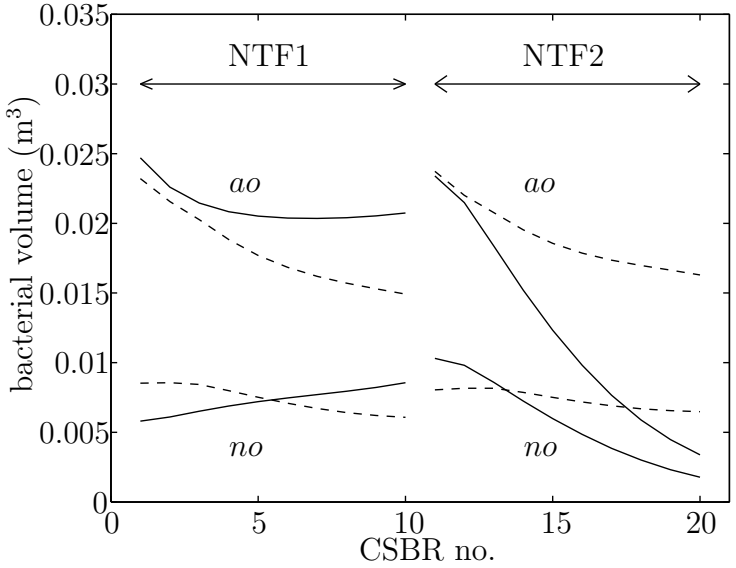

Figure 8.10 *Volume of the ammonium oxidizers (ao) and the nitrite oxidizers (no) in all CSBRs at stationary conditions (solid) and after 56 days of switching the order once every day (dashed) when the influent concentrations have been reduced by 20%.*

To see what the effects are of a competition of heterotrophs, a simulation was carried out with an influent BOD concentration of 15 gm^{-3} and a daily switching of the operating order. Only the complete oxidization of ammonium into nitrate is considered, i.e., the rate expressions in Table 4.1 are used instead of those in Table 3.1. The influent ammonium concentration and alkalinity are 80 percent of the ones in Table 8.2. Figure 8.12 shows the resulting effluent concentration of ammonium and BOD.

This time the switching strategy resulted in a 6 percent decrease in the nitrifying capacity, determined by an increase of only the ammonium concentration and the alkalinity to twice the values in Table 8.2. On the other hand, the BOD uptake rate increased slightly. There are two main reasons for this. First, the competition by the heterotrophs reduced the amount of nitrifiers such that the effluent ammonium concentration is higher. As already shown, this makes the advantage of switching less significant even without the competition by heterotrophs. Further, under stationary conditions the heterotrophs dominate only the upper parts of the first NTF before almost all organic matter has been consumed. This leaves the remaining parts of the two NTFs to the nitrifiers alone. When the order is inversed daily, the bacterial distribution becomes almost equal and uniform in the two NTFs. The heterotrophs have a higher growth rate than the nitrifiers, which makes them prone to dominate over the nitrifiers in the outer parts of the biofilm, where they consume oxygen and cause a diffusion resistance for dissolved components. When the operating order is switched, this "barrier" is distributed over the biofilm in both NTFs.

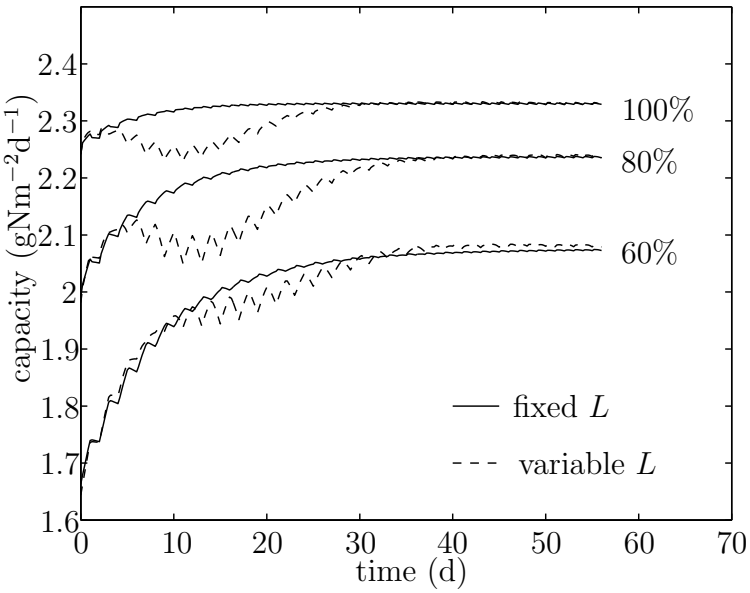

Figure 8.11 *Nitrifying capacity when switching every day and the influent concentrations are 100%, 80%, and 60% of the values in Table 8.2.*

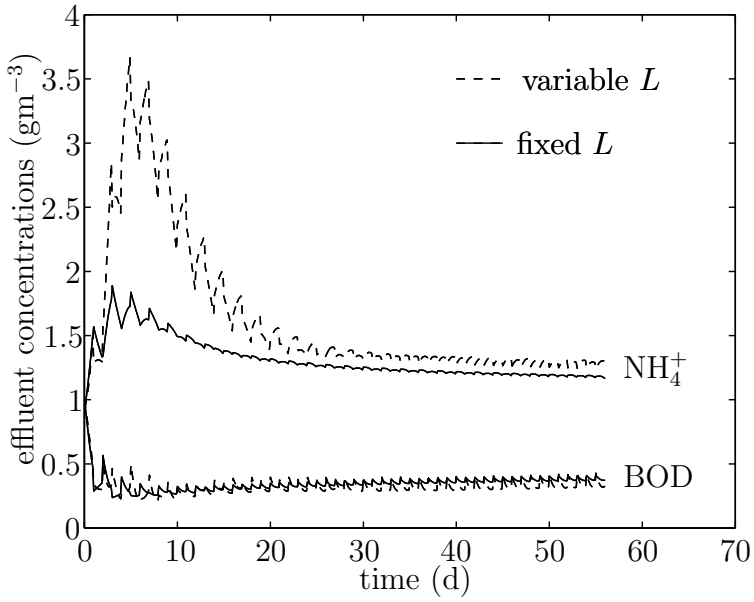

Figure 8.12 *Effluent concentrations of ammonium and BOD when the order is inversed daily. Influent concentrations of ammonium and alkalinity are 80% of the values in Table 8.2 and the influent BOD concentration is 15 gm^{-3}.*

Reducing the influent BOD to 10 gm^{-3} and the ammonium concentration and alkalinity to 60 percent of the values in Table 8.2 gives the effluent concentrations and the nitrifying capacity in Figure 8.13. This time both the effluent concentrations of ammonium and BOD are reduced. The nitrifying capacity increases by 4 percent, which is far less than the 25 percent increase when there was no competition by heterotrophs.

It should be noted that the competition by the heterotrophs, which causes the inferior results when the order is inversed, is very dependent on the Monod saturation coefficient K_{BOD}. The higher the value, the less competitive the heterotrophs are. On a COD-basis the coefficient may vary up to 180 gm^{-3} according to Henze *et al.* (1987). In these simulations the value was only 5.0 gm^{-3}. It is therefore likely that, at such low influent BOD concentrations as simulated, the competition has been overestimated. For example, in the experiment by Andersson *et al.* (1994) the BOD reduction over the NTFs was only 1 gm^{-3} (see Table 8.2), which implies that there cannot have been any significant competition by heterotrophs.

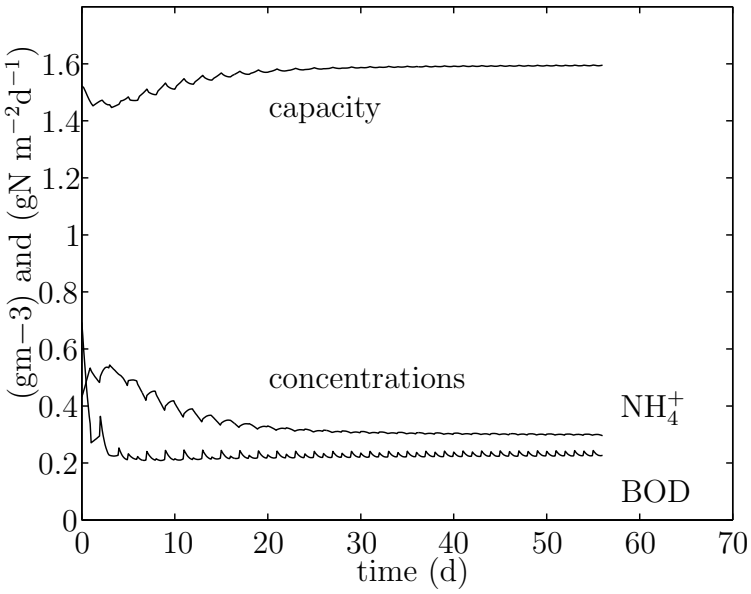

Figure 8.13 *Nitrifying capacity and effluent concentrations of ammonium and BOD when the order is inversed daily. The influent concentrations are 60% of the values in Table 8.2 and the influent BOD concentration is 10 gm^{-3}.*

8.4.2 Varying Flow through NTFs in Parallel

In this investigation we use the specifications and representative influent concentrations for the six parallel full-scale NTFs operating at the Rya WWTP today. The values are summarized in Table 8.4.

Table 8.4 *Data and representative conditions for the Rya full-scale NTFs*

	Notation	Value	Unit
Specific surface area	a	230	m^{2}m^{-3}
Bed height	h	7.2	m
Influent ammonium concentration	$c_{NH_4,in}$	10	gN m^{-3}
Influent alkalinity	$c_{HCO_3,in}$	2.5	mole m^{-3}
Influent nitrite concentration	$c_{NO_2,in}$	0.1	gN m^{-3}
Hydraulic load	q	166	md^{-1}

The operating strategy that is simulated is a variation of the flow in two NTFs operating in parallel. We only simulate one NTF, where the flow is varied ±20 percent with time intervals of one day, but averaging over the last two days when simulating for 56 days should give representative values for both the NTFs. The trickling filter is modeled in the same way as in the last section but in this case all parameter values are the ones in Appendix B at 20°C. The biofilm thickness is fixed to 0.64 mm, as estimated from the pulse response experiments carried out on the pilot plant at the Rya WWTP (see Section 6.3.4). Three different average hydraulic loads are simulated: 100%, 80% and 60% of the load in Table 8.4.

In Table 8.5 the average values of the last two simulated days (*varying*) are compared with the stationary values when the flow is not varied (*ss*). From the table we can see that the capacity increases only marginally by varying the flow. Since the effluent ammonium concentrations increase slightly, this strategy cannot be motivated on the basis of these simulations.

Table 8.5 *Simulation results of varying the flow ±20%*

Hydraulic load	md^{-1}	166		133		99.4	
		varying	*ss*	*varying*	*ss*	*varying*	*ss*
Volume* of *ao*	dm^3/m^2	152	152	129	128	101	99.5
Volume* of *no*	dm^3/m^2	59.0	59.3	50.3	50.2	39.6	39.4
$c_{NH_4,out}$	gN m^{-3}	0.71	0.53	0.52	0.38	0.41	0.29
$c_{NO_2,out}$	gN m^{-3}	0.23	0.20	0.18	0.15	0.15	0.12
$c_{HCO_3,out}$	mole m^{-3}	1.17	1.15	1.15	1.12	1.13	1.11
Rate	gN $m^{-2}d^{-1}$	0.93	0.95	0.76	0.77	0.58	0.58
Capacity	gN $m^{-2}d^{-1}$	1.32	1.31	1.12	1.10	0.87	0.86

* Per square meter of reactor

8.5 Discussion

The biofilm model in Chapter 3, which has been the basis for the models used so far in this chapter, considers three microbial transformations: growth, endogenous respiration and inactivation, or death of cells (see Figure 8.14). Early biofilm models generally considered only the bacterial growth. However, since the introduction of the multi-species biofilm models by Kissel *et al.* (1984) and Wanner and Gujer (1984) it has been common to use the three transformations mentioned or only the growth and a decay process in biofilm modeling.

There are numerous biological processes that have been ignored in this description. Naturally, dead cells do not remain inert for ever. Eventually, lysis disintegrates the cells and the residues dissolve in the surrounding liquid. Protozoa and higher

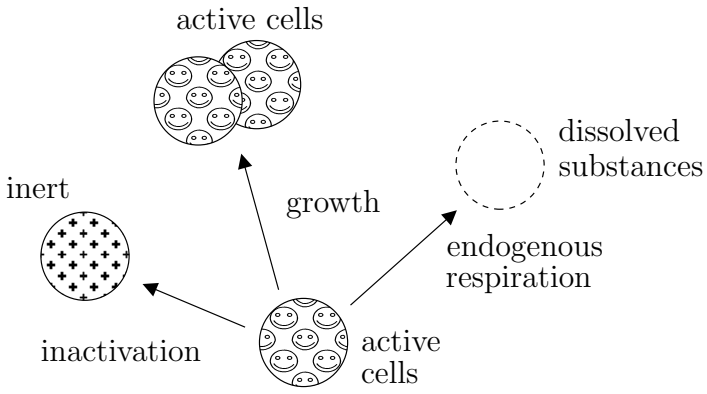

Figure 8.14 *Illustration of the microbial transformations in the biofilm model.*

organisms are grazing the biofilm and then consuming viable cells (as well as inert material), which is often not a negligible process. Controlling the amount of biofilm predators, such as worms and larvae, is frequently a problem at wastewater treatment plants using biofilm units. Endogenous respiration is typically a quite marginal process and, hence, the relatively high respiration rate coefficients sometimes used in biofilm models can be seen as an indirect model of a "constant" grazing by predators and their oxygen consumption.

The death of bacteria is a complex phenomenon. Death may result from substrate depletion, toxic substances and invasion by viruses, for example. Inability to form colonies and grow does not imply death. Cells can be merely injured and recover given the right growth conditions. Like most living species, the cells do not die instantly from starvation. Instead, they remobilize inner resources and stop growing when the growth conditions become too unfavorable. This transformation is sometimes called *exogenous dormancy*. If they starve for too long, they will eventually die but, if the conditions become appropriate before this occurs, they may quickly reactivate. In Figure 8.15 the described biological transformations are illustrated. A process that can be significant is the maintenance process, which is not a true transformation and therefore not shown in the figure. The maintenance requires energy and reflects a diversion of substrate away from growth. Consequently, the maintenance decreases the observed yield of cells from substrate.

Though not explicitly used in biofilm modeling, the concept of dormant bacteria is not new. Soil bacteriologists were aware of the possibility of exogenous dormancy even in the sixties, but it was considered controversial when Stevenson (1978) proposed it to be an important phenomenon in aquatic systems. Since then there has been intense research in the area of bacterial survival under nutrient starvation in aquatic systems. The hypothesis that it is an essential strategy for survival of many species to enter a dormant state when the growth conditions are limited is now generally accepted among microbiologists.

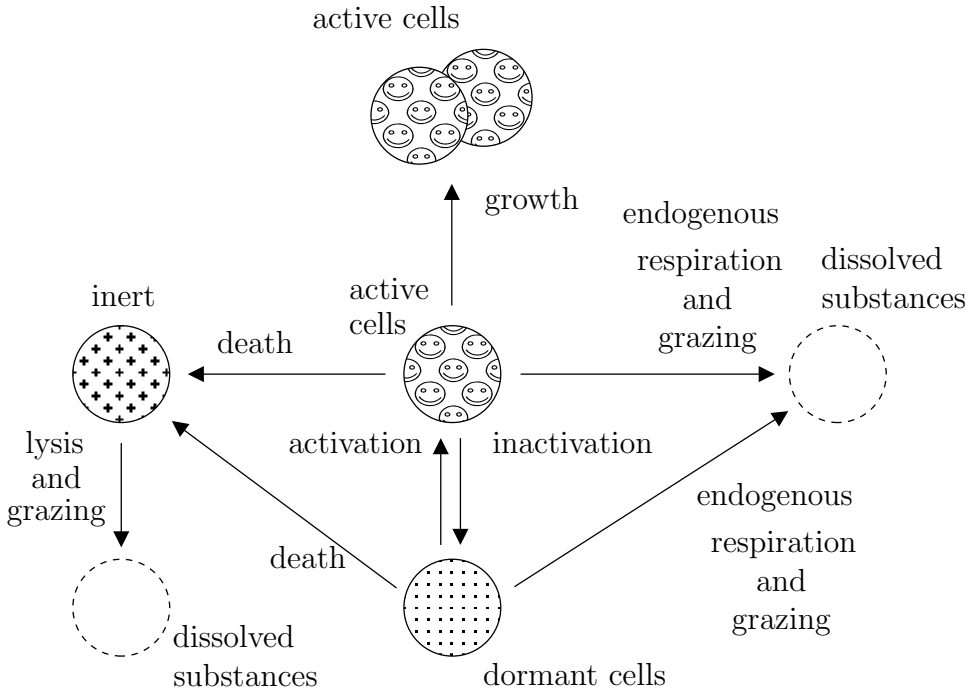

Figure 8.15 *Illustration of microbial transformations.*

Numerous studies in the area has been made on *coli* and *vibrio* species but also *Pseudomonas* and *Enterobacter* species have been studied (Nyström (1989) and references there). Some arctic *vibrio* species have been shown to survive more than one year of starvation although half of the cells were dead after 6-7 weeks (Novitsky and Morita 1977).

The late introduction of the concept *exogenous dormancy* has been blamed on the traditional experimental methods used in the investigations of bacteria, i.e., stationary conditions or batch cultures where the focus has been on describing the growth phase. The obvious drawbacks of these kinds of experiments have direct parallels to the typical experiments carried out on laboratory biofilm reactors.

The best way of including dormancy in biofilm models for biofilm reactors requires more knowledge about the starvation processes of the modeled species. However, a few ideas can be drawn from experimental studies on other bacteria:

- The inactivation, i.e. when the bacteria go from the active reproductive state into the dormant state, begins almost instantly after substrate limitation.
- In the inactivation process, the cells may shrink and increase in numbers (Amy *et al.* 1983), which gives the cells a higher area to volume ratio and, consequently, an improved ability for substrate uptake.
- When inactivated, the endogenous respiration may decrease substantially (Novit-

sky and Morita (1977), Nyström (1989) and references there).

- The activation process may occur within a few hours after the growth conditions have become appropriate (Kjelleberg *et al.* 1982, Amy *et al.* 1983, Horn and Hempel 1997*b*). If the cells have decreased in size when inactivated, they regain a larger size again.

Using the transformations in Figure 8.15 we can formulate an extension of the model in Chapter 3 that includes dormant cells. Denoting active bacteria by subscript a, dormant by d and inert by i, the net growth rates of the three different states of a species are

$$\begin{aligned} r_{vs,a} &= \rho\epsilon_a(\mu - R_{E,a} - R_I - R_{D,a}) + \rho\epsilon_d R_A && (8.8)\\ r_{vs,d} &= \rho\epsilon_a R_I + \rho\epsilon_d(-R_{D,d} - R_{E,d} - R_A) && (8.9)\\ r_{vs,i} &= \rho\epsilon_a R_{D,a} + \rho\epsilon_d R_{D,d} + \rho\epsilon_i(-R_L - R_{E,i}), && (8.10) \end{aligned}$$

where μ is the specific growth rate, R_E is the sum of the specific endogenous respiration rate and the grazing, R_I is the specific inactivation rate, R_D is the specific death rate, R_A is the specific activation rate and R_L is the specific rate of lysis. For simplicity, the density ρ (gCOD m^{-3}) has been assumed to be the same for all states.

If we compare Figures 8.14 and 8.15, we see that the "standard" modeling approach implies that the active and dormant states in Figure 8.15 are considered to be one state of viable cells. Adding $r_{vs,a}$ and $r_{vs,d}$ gives the net growth rate of the viable bacteria:

$$r_{vs,a+d} = \rho\epsilon_a\mu - \rho(\epsilon_a R_{E,a} + \epsilon_d R_{E,d}) - \rho(\epsilon_a R_{D,a} + \epsilon_d R_{D,d}). \qquad (8.11)$$

Under favorable growth conditions the amount of dormant cells is negligible, i.e. $\epsilon_d = 0$. If we assume lysis and grazing of inert material to be very slow processes, the rate expressions (8.10) and (8.11) will then be equal to those in Chapter 3.

Under poor growth conditions the situation is the opposite. If we assume the inactivation process to be fast, all bacteria will be dormant and

$$r_{vs,a+d} = -\rho\epsilon_d R_{E,d} - \rho\epsilon_d R_{D,d}.$$

Hence, if we let $\epsilon = \epsilon_a + \epsilon_d$, we can formulate a simplified expression for the net growth rate of viable bacteria:

$$r_{vs} = \rho\epsilon\mu\eta - \rho\epsilon R_{E,d}(1 - (1 - \frac{R_{E,a}}{R_{E,d}})\eta) - \rho\epsilon R_{D,d}(1 - (1 - \frac{R_{D,a}}{R_{D,d}})\eta), \qquad (8.12)$$

where η is a function that reflects the amount of active bacteria relative to the amount of dormant bacteria. When $\eta = 0$, all bacteria are dormant and when $\eta = 1$, all bacteria are active. We could, for example, use

$$\eta(\mu) = \frac{\mu^p}{\mu_I^p + \mu^p}(1 + \frac{\mu_I^p}{\mu_m^p}), \qquad (8.13)$$

where μ_I determines a "transition" level of the specific growth rate where the bacteria become active.

Though a dormant state was not explicitly mentioned, Horn and Hempel (1997*a*) modeled the death process in an autotrophic/heterotrophic biofilm in a similar way, based on the experimental findings that it was only when substrate is limited that the death process is relevant. In their model they also included maintenance and lysis of (active) heterotrophic bacteria. Unfortunately, the starvation of nitrifiers was not studied. However, in another study by Horn and Hempel (1997*b*) they investigated a nitrifying biofilm without competition by heterotrophs and also exposed the nitrifiers to about one month of starvation. The decay processes of the nitrifiers were modeled in the same way, except that in order to achieve agreement with measured oxygen profiles it was assumed that five times (!) as much oxygen was consumed in the endogenous respiration during starvation. The close agreement between the simulated results and the (sparse) measurements from the ten months experiment indicates that the long term effects of starvation can be modeled in this manner.

By measuring the oxygen concentrations in the biofilm Horn and Hempel (1997*b*) also found that it took about two hours for the concentrations to stabilize when the biofilm was exposed to ammonium after one month in pure water. This can be interpreted as the time it took for the nitrifiers to activate.

Since the specific death rate of dormant cells should reasonably be much higher than the corresponding rate for active cells, the death rate in Eq. (8.12) decreases to the death rate of the active bacteria as the growth conditions improve.

The dormant state in Figure 8.15 should imply a delay before cells become inert as found by Amy *et al.* (1983), for example. The measured response in the experiment by Boller and Gujer (1986) also exhibits such a delay when the nitrifiers are exposed to water containing no ammonium for the first time (see Figure 8.2). However, the second time the filter is fed with nitrified water, the delay is less apparent. Since the specific death rate in Eq. (8.12) increases instantly when the growth conditions become poor, the expression for the net growth rate actually predicts the opposite transient response. The death rate is proportional to the bacterial concentration and, thus, the decrease in the concentration of viable bacteria will be largest immediately after the nutrient limitation begins. In other words, there is a contradiction between the hypothesis that the bacteria enter a dormant state for survival and the reasonable assumption that dormant cells die at a higher rate than active ones. The "flaw"is that, at each time instant, the only information in the model about the past lies in the bacterial concentration itself. This may be enough to describe the behavior under favorable growth conditions and the long term effects of a constant starvation. However, when the cells enter the dormant state, the past conditions should affect the endurance of the cells during starvation. For example, it is known that the number of DNA replication sites of copiotrophic bacteria and the number of additional cells formed initially after starvation begins depend on the history of the growth conditions (Nyström 1989). Applying this reasoning to the rate expres-

sion (8.12), we see that one way to introduce this memory is in the function η where it is multiplied by the death rate. Instead of using the present specific growth rate μ as argument, we could use a function of old growth rates. A weighted mean, where the latest values have the largest weight, could be used, for example.

An exponential decrease in the dependence of old growth conditions on the death rate can be achieved by modeling the death rate of viable cells as

$$R_D = R_{D,d}(1 - (1 - \frac{R_{D,a}}{R_{D,d}})\eta(\mu_d)) \tag{8.14}$$

$$\tau \frac{d}{dt}\mu_d = \mu - \mu_d, \tag{8.15}$$

where η is the function defined by Eq. (8.13).

In Figure 8.16 it is illustrated how this model can be used to get a fairly long lag before the death rate increases when the bacteria are exposed to starvation and a rapid activation when the growth conditions become favorable. The parameters are set to $\mu_I = 0.1\mu_m$, $p = 2$ and $\tau = 1.0$ d. By increasing p we can get a steeper slope of the change in η, by increasing the time constant τ we can get longer lags and by increasing μ_I we can get less difference between the activation lag and the inactivation lag.

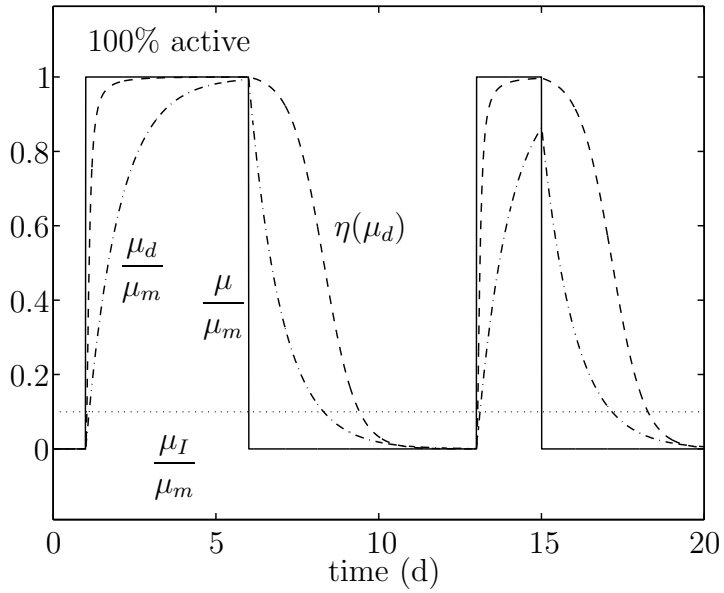

Figure 8.16 *Illustration of how a specific death rate that depends on old growth rates can be modeled ($\mu_I = 0.1\mu_m$, $p = 2$ and $\tau = 1.0$ d).*

The variable μ_d contains information about the growth history of one cell, or several cells that have had the same history. Since the cells move within the biofilm,

Eq. (8.15) has to be modified when used in the biofilm model:

$$\frac{\partial \mu_d}{\partial t} = \frac{1}{\tau}(\mu - \mu_d) - u\frac{\partial \mu_d}{\partial x}, \qquad 0 < x < L, \tag{8.16}$$

where u is the velocity of the biofilm matrix given by Eq. (8.2). We may implement this equation in the algorithm in Section 8.2 by updating μ_d every time step in each segment according to Eq. (8.15) and then interpolate in the same way as the volume fractions are interpolated.

What are the implications on the operating strategies studied in Section 8.4 of a specific death rate that increases during starvation and a delay of the kind shown in Figure 8.16?

Switching orders of cascaded NTFs

From the previous simulations we could see that the more often we inversed the order, the higher the nitrifying capacity that we achieved. The delay should imply that there will be less difference between switching very often and quite often. In other words, switching every day or every four days should give about the same nitrifying capacity if it takes a few days before the specific death rate increases when the nitrifiers become substrate limited.

An increase in specific death rate with decreasing specific growth rate implies that more nitrifiers will have higher specific death rates when the order is switched. At stationary conditions most of the nitrifiers are in the first NTF. When the operating order is inversed, a large part of these nitrifiers will be located where the specific growth rate is low and, hence, the specific death rate is high. As a result, the total amount of nitrifiers in the two NTFs will be less if the order is switched than under stationary conditions.

To see how this affects the capacity, the previous simulations at 60 percent of the influent concentrations in Table 8.2 and a daily switching are repeated with the death rates modified according to Eqs. (8.14) and (8.16). If we assume zero death rates for active bacteria, the specific death rates of viable ammonium oxidizers and nitrite oxidizers are [c.f. Eq. (3.25)]

$$R_{j,3} = k_{I,j}(1 - \eta_j(\mu_{d,j})), \qquad j = ao,\, no.$$

The coefficients $k_{I,j}$ are the same as before and the parameters $\mu_{I,j}$ and p in the function η_j are set to $\mu_{I,j} = 0.1\mu_{m,j}$ and $p = 2$. Further, the growth rates are multiplied by $\eta_j(\mu_j)$ as in Eq. (8.12).

With $\tau = 0$, i.e. $\mu_d = \mu$, the switching resulted in a deteriorated capacity by 3 percent and a 9 percent decrease in the total amount of ammonium oxidizers in the two NTFs compared with stationary operation. With $\tau = 1.0$ d^{-1}, as in Figure 8.16, the total amount of ammonium oxidizers decreased by 3 percent but the capacity was improved by 1.3 percent. However, this is far less than the 25 percent achieved in the previous simulations with a constant specific death rate.

Varying flow through NTFs in parallel

The simulations, where the flow was varied between two levels with equal time at both flows, resulted in only a small increase in capacity compared with a stationary operation at the average flow. Based on the simulations, this strategy could not be motivated since at the higher flow the effluent ammonium concentration increased more than it decreased at the lower flow.

Unlike when the operating order is switched, there is no disadvantage of an increasing death rate with substrate limitation. A re-simulation of the 20 percent daily switching of the hydraulic load in Table 8.4 with $\tau = 0$ resulted in 1.0 percent improved nitrifying capacity, which is slightly more than in the previous simulations (see Table 8.5). Furthermore, the delay has positive effects on the efficiency of the trickling filter. A resimulation with $\tau = 1.0$ d^{-1} resulted in a 3 percent improved capacity, and almost no increase in the average effluent ammonium concentration.

The possible disadvantage of this strategy is due to the increased effluent ammonium concentrations at the higher flow. A significant delay implies that short periods of increased flow can be combined with longer periods of a lower flow. The higher effluent concentrations at the higher flow will then only have a small effect on the average ammonium concentration. Optimization of the flow levels and the time periods to maximize the efficiency should result in a further improved capacity and a lower average effluent concentration. However, this requires a reliable model of the actual death rate.

8.6 Conclusions

When the long term effects of the conditions for a biofilm reactor are to be studied, the dissolved components can generally be assumed to be in a steady state. Microbial processes, such as the growth and decay of the populations in the biofilm, will then govern the reactor behavior. A method to simulate such slow dynamics has been described, and in Appendix F it has been shown that under mild conditions this algorithm converges to the original problem to be solved.

A standard modeling approach of biofilms considers the microbial transformations: growth, endogenous respiration and inactivation (death). Although this gives a more complete description than earlier models, several transformations and biological processes are ignored in such a model. An extended model has been proposed, where both exogenous dormancy of bacteria and the history of the growth conditions are considered. The approach gives a delay in the decreased efficiency of biofilm reactors subjected to unfavorable growth conditions for the bacteria. This agrees with the observations from a comparison between simulations and an experiment, where an NTF had been alternatingly fed unnitrified and completely nitrified wastewater for periods of about three weeks.

Biofilm reactors that operate at low substrate loads and can be modeled by cascaded CSBRs will have less bacteria closer to the effluent, due to substrate limitations and subsequent starvation of the bacteria there. Simulations of the slow dynamics in NTFs show that by a switching of the operating order of reactors in series and by a variation of the flow in reactors operating in parallel a more uniform distribution of the bacteria in the reactors can be achieved. This can improve the capacity to reduce peak loads as well as lower the effluent concentrations under stationary influent conditions. However, the possible advantages of the simulated operating strategies have been found to be quite sensitive to how the specific death rate of the bacteria is modeled. The standard approach with a constant inactivation rate coefficient resulted in a substantially improved efficiency when the operating order of two NTFs was inversed every day. Varying the flow by $\pm$ 20 percent every day, however, resulted in only a small increase in the capacity at the same time as the average effluent ammonium concentrations increased slightly.

Simulations with specific death rates that increase when substrate is limited resulted in a decreased efficiency when the operating order was switched daily. On the other hand, varying the flow became more advantageous. A delay of the increase in the specific death rates had positive effects on both operating strategies, particularly for the strategy of varying the flow.

Two different models of the biofilm thickness were used in the simulations: constant thickness or an erosion function that is proportional to the squared biofilm thickness. Except for differences during a transient period after commencing the strategies, the two models gave almost the same results.

Simulations of inversing the order of two NTFs indicate that, if there is a significant reduction of organic matter over the filters, the heterotrophic bacteria can take more advantage of a switching of the operating order than the autotrophs. In other words, the possible advantages of regularly inversing the operating order are less if the organic content in the influent is high. Too high concentrations of organics may actually cause a decrease of the nitrifying capacity when the operating order is switched.

Chapter 9

CONCLUSIONS

Fixed biofilms, which are matrix-enclosed populations of organisms attached to impermeable solid surfaces, are the most common form of microbial life. There are several problems associated with fixed biofilms, such as biofilm fouling in pipes and heat exchangers, corrosion by iron oxidizing bacteria, microbial colonization on invasive medical products and dental plaque. However, biofilms are also increasingly used in environmental biotechnology processes, such as the treatment of potable water and wastewater. The aim of this thesis has been to give some insight into dynamic modeling of biofilms and fixed biofilm reactors. Because of the project underlying the simulations and experiments presented, the focus has been on nitrifying trickling filters (NTFs) for treatment of tertiary wastewater. However, most of the methods used are applicable to fixed biofilm reactors in general. Some of the modeling methods are also applicable to mathematically related areas, such as the modeling of porous catalytic reactors and immobilized cells or gel beads. All models that have been presented are physically based.

A quite well-established and general dynamic multi-species model of biofilms, which takes into consideration the transportation phenomena inside the biofilm as well as bacterial processes causing the population dynamics, has been used as a basis for the development of simplified biofilm models. Mathematically, the model consists of two coupled subsystems of partial differential equations. One subsystem describes the concentrations of the dissolved components in the liquid phase of the biofilm and the other subsystem describes how the different solid phases (inert material and various species of micro-organisms) vary over the depth of the biofilm. Since the biofilm thickness varies with time, the entire system is an example of a moving boundary problem.

The main assumption in the derivation of this general biofilm model is an aggregation of the states parallel to the substratum. Its validity relies on the biofilm being fairly smooth and continuous. In the last few years experimental findings of biofilm heterogeneity show that in many cases this assumption is obsolete. However, the assumption appears to be valid for mature biofilms exposed to moderate substrate loads and shear forces, such that the biofilm growth is approximately balanced by the erosion. Since this is often the case in many biofilm reactors, the modeling

problems associated with biofilm heterogeneity may not be as severe as sometimes claimed.

A fundamental model unit in the modeling of the biofilm reactors is the continuously stirred biofilm reactor (CSBR), which is a tank with a homogeneous gas phase and bulk liquid, and a biofilm that can only vary with the distance from the substratum. These units can be combined to model a wide range of biofilm reactors in the same way as continuously stirred tank reactors are used in chemical reaction engineering and design. Specifically, it has been shown that models with cascaded CSBRs can be suitable for modeling the dynamics of NTFs.

Different operating modes of biofilm reactors can be deduced from the origin of the dynamics. Generally, the dynamic modes can be separated into slow modes and fast modes. The slow dynamics are mainly caused by changes in biology, which can take days or weeks to change. The fast dynamics on the other hand are mainly caused by the reactor hydraulics and the changes in the concentrations of the dissolved components in the biofilm. These modes typically have transients that settle in less than a few hours. Based on this division, simplified models and numerical solution methods have been presented for four different operating modes: (i) a true steady state, where both the fast and the slow dynamics are in a steady state, (ii) a quasi-steady state, where the fast and slow modes are in steady states corresponding to two different operating conditions, (iii) fast dynamics, where the biofilm composition is time invariant and (iv) slow dynamics, where only the fast modes are in a steady state.

It has been shown how direct solutions, which are solutions not achieved by relaxation, of the general multi-species biofilm model in the steady state can be determined by the use of an ordinary differential and algebraic equation solver. By using this approach to solve the steady-state problem, it has been shown how to determine the conditions under which different micro-organisms can coexist in a stationary biofilm. Generally, the thicker the biofilm, the easier it is for species to coexist. This implies that controlling the biofilm thickness can be a way of controlling the biofilm composition as well.

When we are only interested in the fast dynamic behavior of a biofilm reactor, the original biofilm model can be significantly simplified since the solid phases and the biofilm thickness can be assumed to be constant. The model equations for a CSBR can then be used to model reactors with porous catalysts as well. If the reaction rates inside the biofilm can be assumed to depend linearly on one substrate concentration, but arbitrarily on the distance from the substratum, the equations for the fast dynamics in a CSBR can be used to derive non-rational transfer functions that describe how changes in the influent concentrations affect the effluent concentrations. Low order rational transfer functions that closely approximate the non-rational ones can be determined with a derived method, named the *Residue Method*, that is based on the singularities of the non-rational transfer functions. These rational transfer functions have several appealing properties: (i) many numerical softwares have numerically efficient routines to simulate systems modeled

with such transfer functions, (ii) standard methods of controller design often require rational transfer functions, (iii) the determination of the transfer functions only requires Newton-Raphson searches on limited intervals and evaluation of a few expressions, and (iv) changes in physical parameters, in particular the first order rate coefficient, which may depend significantly on temperature, can easily be related to changes in the transfer function.

Since the *Residue Method* approximates the combined dynamics of the bulk and the biofilm, the performance of the lowest order approximations is superior to the performance of other approximation methods, for example the *Galerkin Method*, that are based on separate approximations of the mass balances in the bulk and in the biofilm. Sometimes, only first or second order transfer functions are necessary to achieve close approximations. Another advantage of the *Residue Method* is that the approximation is a truncation of a sum of first or second order transfer functions with decreasing time constants and decreasing gain. This implies that the order of an approximation can be determined on the basis of how rapid the changes in the influent concentrations are.

Trace substance pulse response experiments for the determination of residence time distributions are an example of when the reaction rate depends linearly on the concentration, since no reaction at all takes place then. For such experiments, expressions have been derived from the non-rational transfer functions that show how the mean residence time, variance and skewness of the distributions depend on the reactor and biofilm parameters, such as the diffusion coefficient, biofilm porosity, biofilm area, biofilm thickness, bulk volume and flow. These expressions show that the liquid volume in the biofilm plays a central role in the hold-up of substances in the reactor. However, the biofilm area, biofilm thickness and biofilm porosity, whose product is the liquid volume in the biofilm, shape the residence time distribution differently. This opens for the possibility of estimating these parameters from experiments using the approximate transfer functions, since it may then be crucial to to calculate the responses rapidly.

From measured residence time distributions of two different large pilot-scale NTFs at different flows the biofilm porosity, bulk volume, biofilm thickness and suitable numbers of cascaded CSBRs were estimated with low variances using non-linear least squares and simulations with the transfer functions. A separate experiment showed that the bulk volume in a cross-flow plastic media NTF increased linearly with the flow in the operating region of the plant.

For a plant where both the flow and the influent concentrations vary around an operating point, the original influent concentrations can be replaced by an "equivalent influent concentration" that is proportional to the substrate load. Applying this approach to an experiment where the flow into one of the pilot scale NTFs varied rapidly showed fairly close agreement between the measured effluent concentrations and the ones simulated with transfer functions that had been determined with the parameters estimated from the residence time distributions. This indicates the possible use of the transfer function approach for more realistic operating conditions

than a constant flow.

When the influent concentrations vary over a wide range in a short time, the transfer function approach, which is based on linearization, can be used only if the concentrations are such that the reaction rate can be assumed to be linearly dependent on the substrate concentrations in the entire operating range. This is often not the case. However, comparisons between step response experiments, where the influent ammonium concentration into two different NTFs was drastically increased or decreased, and simulations with Monod kinetics showed very good agreement. On one of the plants, very close agreement was found when only the oxidization of ammonium was modeled. The other plant, however, had responses to changes in influent ammonium load that were much slower. Based on transient and stationary differences between the influent and the effluent total concentrations of dissolved nitrogen, it was concluded that in this plant both adsorption and desorption of ammonium as well as denitrification occurred. Modeling the amount of adsorbed ammonium as proportional to the ammonium concentration, and the denitrification in the same manner as it is modeled in activated sludge processes, resulted in a close agreement between simulations and measured concentrations of ammonium, nitrite, nitrate and alkalinity. It also showed that even small amounts of adsorbed substances, such as found in these experiments, may significantly affect the transients after changes in influent conditions. For this plant it was concluded that measurements of the (quasi-stationary) nitrification rate after changes in the ammonium load should be carried out later than at least six times the mean residence time (determined from LiCl trace substance pulse response experiments) after the change.

A plant in a quasi-steady state is defined as a plant where the transients of the dissolved components, after a change in operating conditions, have settled and where the solid components in the biofilm are in a steady state corresponding to a different operating point. Experiments, where the influent conditions are changed and kept constant until the effluent concentrations stabilize, are commonly carried out on plants to evaluate their efficiency. In such experiments the biofilm can be assumed to be unchanged. Normally, the operating conditions before the experiments are then only known as averages (of sparse samples). Using the average values to determine the steady state of the biofilm, the quasi-steady state definition of a plant can be a useful tool in the evaluation of this kind of experiments.

A factorial design experiment, carried out on a pilot scale NTF during a period of two months, has been analyzed using a model of the NTF in a quasi-steady state. The experiment was carried out to see how the nitrification rate was affected by changes in flow and influent ammonium concentration at a constant ammonium load into the plant, because it was feared that a recirculation, which decreases the influent ammonium concentrations, would lower the nitrification rate. However, a statistical analysis revealed no difference between the setup with high hydraulic load and low ammonium concentration, and vice versa. Model simulations agreed fairly well with the experimental data, with differences in nitrification rate between the setups that were within the error margins of the experiments. From the analysis it was concluded that an increase in flow improved the mass transfer into the biofilm,

probably due to increased turbulence. This was accounted for in the model by an air-bulk oxygen mass transfer coefficient that increased with flow. The coefficient had been determined with a simplified model and oxygen and ammonium measurements from sampling holes in the NTF. An analysis showed that simulation results are fairly insensitive to the exact value of this coefficient.

When the long term effects of the conditions for a biofilm reactor are to be studied, the dissolved components can generally be assumed to be in a steady state. Processes, such as the growth and decay of the microbial populations in the biofilm, will then govern the reactor behavior. A method to simulate such slow dynamics has been described, and it has been shown that the algorithm converges to the original problem to be solved when the time step size and the thickness of the segments of the discretized biofilm approach zero.

A standard modeling approach of biofilms considers three microbial transformations: growth, endogenous respiration and inactivation (death). Although this gives a more complete description than earlier models, several transformations and biological processes are ignored in such a model. An extended model has been proposed, where both exogenous dormancy of bacteria and the history of the growth conditions are considered. This approach can be used to model a time delay in the decay process initiated by starvation. As a result, the decrease in capacity of biofilm reactors becomes slower immediately after they are subjected to unfavorable growth conditions. This agrees with the observations from a comparison between simulations with a constant specific death rate and an experiment, where an NTF had been alternatingly fed unnitrified and completely nitrified wastewater for periods of about three weeks.

Biofilm reactors that operate at low substrate loads and can be modeled by cascaded CSBRs will have less bacteria closer to the effluent, due to substrate limitations and subsequent starvation of the bacteria there. Simulations of the slow dynamics in NTFs show that by a switching of the operating order of reactors in series and by a variation of the flow in reactors operating in parallel a more uniform distribution of the bacteria in the reactors can be achieved. This can improve the capacity to reduce peak loads as well as lower the effluent concentrations under stationary influent conditions. However, the possible advantages of the simulated operating strategies was found to be quite sensitive to how the specific death rate of the bacteria is modeled. The standard approach with a constant inactivation rate coefficient resulted in a substantially improved efficiency when the operating order of two NTFs was inversed every day. Varying the flow by $\pm$ 20 percent every day, however, resulted in only a small increase in the capacity at the same time as the average effluent ammonium concentrations increased slightly.

Simulations with specific death rates that increase when substrate is limited resulted in a decreased efficiency when the operating order was switched daily. On the other hand, varying the flow became more advantageous. A delay of the increase in the specific death rates had positive effects on both operating strategies, particularly for the strategy of varying the flow.

Simulations of inversing the order of two NTFs indicate that, if there is a significant reduction of organic matter over the filters, the heterotrophic bacteria can take more advantage of a switching of the operating order than the autotrophs. In other words, the possible advantages of regularly inversing the operating order are less if the organic content in the influent is high. Too high concentrations of organics may actually cause a decrease of the nitrifying capacity when the operating order is switched.

Bibliography

Amy, P. S., C. Pauling and R. Y. Morita (1983). Starvation-survival processes of a marine vibrio. *Appl. Environ. Microbiol.* **45**(3), 1041–1048.

Andell, I., H. Aspegren and B. Andersson (1993). Macrofauna in nitrifying trickling filters. Technical report. VA-verket Malmö. 205 80 Malmö, Sweden.

Andersson, B., H. Aspegren, D. S. Parker and M. P. Lutz (1994). High rate nitrifying trickling filters. *Wat. Sci. Tech.* **29**(10-11), 47–52.

Arcangeli, J. P. and E. Arvin (1995). Growth of an anaerobic and an anoxic toluene-degrading biofilm - a comparative study. *Wat. Sci. Tech.* **32**(8), 125–132.

Aris, R. (1975). *The mathematical theory of diffusion and reaction in permeable catalysts*. Vol. 1. Clarendon press, Oxford.

Arvin, E. and P. Harremoës (1990). Concepts and models for biofilm reactor performance. *Wat. Sci. Tech.* **22**(1/2), 171–192.

Atkinson, B. and I. J. Davies (1974). The overall rate of substrate uptake (reaction) by microbial films. Part I - a biological rate equation. *Trans. Instn. Chem. Engrs.* **52**, 248–259.

Atkinson, B. and I. S. Daoud (1968). The analogy between micro-biological "reactions" and heterogeneous catalysis. *Trans. Instn. Chem. Engrs.* **46**, T19–T24.

Balmelle, B., K. M. Nguyen, B. Capdeville, J. C. Cornier and A. Deguin (1992). Study of factors controlling nitrite build-up in biological processes for water nitrification. *Wat. Sci. Tech.* **26**(5-6), 1017–1025.

Bishop, P. L. (1997). Biofilm structure and kinetics. *Wat. Sci. Tech.* **36**(1), 287–294.

Boller, M. and W. Gujer (1986). Nitrification in tertiary trickling filters followed by deep-bed filters. *Wat. Res.* **20**(11), 1363–1373.

Boller, M., M. Tschui and W. Gujer (1997). Effects on transient nutrient concentrations in tertiary biofilm reactors. *Wat. Sci. Tech.* **36**(1), 101–109.

Boller, M., W. Gujer and M. Tschui (1994). Parameters affecting nitrifying biofilm reactors. *Wat. Sci. Tech.* **29**(10-11), 1–11.

Bradshaw, D. J. (1995). Metabolic responses in biofilms. *Micobial Ecology in Health and Disease* **8**, 313–316.

Burrell, P. C., J. Keller and L. L. Blackall (1998). Microbiology of a nitrite-oxidizing bioreactor. *Appl. Environ. Microbiol.* **64**(5), 1878–1883.

Characklis, W. G. (1990). Kinetics of microbial transformations. In: *Biofilms* (W. G. Characklis and K. C. Marshall, Eds.). Wiley, New York. pp. 233–264.

Comsol (1998). *FEMLAB - Reference manual*. Computer Solutions Europe AB. Björnäsvägen 21, S-113 47 Stockholm, Sweden.

Costerton, J. W., Z. Lewandowski, D. E. Caldwell, D. R. Korber and H. M. Lappin-Scott (1995). Microbial biofilms. *Annu. Rev. Microbiol.* **49**, 711–745.

de Beer, D. and P. Stoodley (1995). Relation between the structure of an aerobic biofilm and transport phenomena. *Wat. Sci. Tech.* **32**(8), 11–18.

de Beer, D., P. Stoodley and Z. Lewandowski (1994*a*). Liquid flow in heterogeneous biofilms. *Biotechnol. Bioeng.* **44**, 636–641.

de Beer, D., P. Stoodley, F. Roe and Z. Lewandowski (1994*b*). Effects of biofilm structures on oxygen distribution and mass transport. *Biotechnol. Bioeng.* **43**, 1131–1138.

de Gooijer, C. D., R. H. Wijffels and J. Tramper (1991). Growth and substrate consumption of Nitrobacter agilis cells immobilized in carrageenan: Part 1. Dynamic modeling. *Biotechnol. Bioeng.* **38**, 224–231.

Debus, O., H. Baumgärtl and I. Sekulov (1994). Influence of fluid velocities on the degradation of volatile aromatic compounds in membrane-bound biofilms. *Wat. Sci. Tech.* **29**(10-11), 253–262.

Deuflhard, P. (1974). A modified Newton method for the solution of ill-conditioned systems of nonlinear equations with application to multiple shooting. *Numer. Math.* **22**, 289–315.

dos Santos, V. A. P. M., L. M. Marchal, J. Tramper and R. H. Wijffels (1996). Modeling and evaluation of an integrated nitrogen removal system with microorganisms co-immobilized in double layer gel beads. *Biotechnol. Prog.* **12**, 240–248.

Drtil, M., P. Németh and I. Bodík (1993). Kinetic constants of nitrification. *Wat. Res.* **27**(1), 35–39.

Drury, W. J., P. S. Stewart and W. G. Characklis (1993). Transport of 1-μm latex particles in Pseudomonas aeruginosa biofilms. *Biotechnol. Bioeng.* **42**, 111–117.

Edwards, C. H. and D. E. Penney (1982). *Calculus and analytic geometry*. Prentice-Hall. Englewood Cliffs, New Jersey.

Finlayson, B. A. (1972). *The Method of Weighted Residuals and Variational Principles*. Academic Press, New York.

Fischer, S. D. (1990). *Complex variables*. Mathematics series. 2nd ed.. Wadsworth & Brooks/Cole. Pacific Grove, California.

Flora, J. R. V., M. T. Suidan, P. Biswas and G. D. Sayles (1993). Modeling substrate transport into biofilms: Role of multiple ions and pH effects. *J. Environ. Eng.* **119**(5), 908–930.

Flora, J. R. V., M. T. Suidan, P. Biswas and G. D. Sayles (1995). Modeling substrate transport into biofilms: Role of multiple ions and pH effects-closure. *J. Environ. Eng.* **121**(4), 369–370.

Froment, G. F. and K. B. Bischoff (1979). *Chemical Reactor Analysis & Design.* Wiley, New York.

Fruhen, M., E. Christian, W. Gujer and O. Wanner (1991). Significance of spatial distribution of microbial species in mixed culture biofilms. *Wat. Sci. Tech.* **23**, 1365–1374.

Fu, Y. C., T. C. Zhang and P. L. Bishop (1994). Determination of effective oxygen diffusivity in biofilms grown in a completely mixed biodrum reactor. *Wat. Sci. Tech.* **29**(10-11), 455–462.

Gadani, V., P. Villon, J. Manem and B. Rittmann (1993). A new method to solve a non-steady-state multispecies biofilm model. *Bull. Math. Biol.* **55**(6), 1039–1061.

Gönenç, I. E. and P. Harremoës (1985). Nitrification in rotating disc systems - I. *Wat. Res.* **19**(9), 1119–1127.

Gujer, W. and M. Boller (1986). Design of a nitrifying tertiary trickling filter based on theoretical concepts. *Wat. Res.* **20**(11), 1353–1362.

Gujer, W. and M. Boller (1990). A mathematical model for rotating biological contactors. *Wat. Sci. Tech.* **22**(1-2), 53–73.

Gujer, W. and O. Wanner (1990). Modelling mixed population biofilms. In: *Biofilms* (W. G. Characklis and K. C. Marshall, Eds.). Wiley, New York. pp. 397–443.

Hansson, E. (1994). Nitrifikation i biobädd - dess beroende av varierande flöde och ammoniumkoncentration. Rapport 1994:2. GRYAAB. Karl IX v. 417 22 Göteborg, Sweden.

Harremoës, P. (1976). The significance of pore diffusion to filter denitrification. *J. Water Pollut. Control Fed.* **48**(2), 377–388.

Henze, M., C. P. L. Grady, W. Gujer, G. Marais and T. Matsuo (1987). A general model for single-sludge wastewater treatment systems. *Wat. Res.* **21**, 505–515.

Henze, M., P. Harremoës, J. C. Jansen and E. Arvin (1990). *Spildevandsrensning, Biologisk og kemisk.* Polyteknisk Forlag, 2800 Lyngby, Denmark.

Horn, H. (1994). Dynamic of nitrifying bacteria population in a biofilm controlled by an oxygen microelectrode. *Wat. Sci. Tech.* **29**(10-11), 69–76.

Horn, H. and D. C. Hempel (1995). Mass transfer coefficients for an autotrophic and a heterotrophic biofilm system. *Wat. Sci. Tech.* **32**(8), 199–204.

Horn, H. and D. C. Hempel (1997*a*). Growth and decay in an auto-/heterotrophic biofilm. *Wat. Res.* **31**(9), 2243–2252.

Horn, H. and D. C. Hempel (1997*b*). Substrate utilization and mass transfer in an autotrophic biofilm system: experimental results and numerical simulation. *Biotech. Bioeng.* **53**, 363–377.

Hunik, J. H., C. G. Bos, M. P. van den Hoogen, C. D. De Gooijer and J. Tramper (1994). Co-immobilized Nitrosomonas europea and Nitrobacter agilis cells: Validation of a dynamic model for simultaneous substrate conversion and growth in κ-carrageenan gel beads. *Biotechnol. Bioeng.* **43**, 1153–1163.

Hunik, J. H., M. P. van den Hoogen, W. de Boer, M. Smit and J. Tramper (1993). Quantative determination of the spatial distribution of Nitrosomonas europea and Nitrobacter agilis cells immobilized in κ-carrageenan gel beads by a specific flourescent-antibody labelling technique. *Appl. Environ. Microbiol.* **59**(6), 1951–1954.

Kamen, E. W. (1996). The Fourier, Laplace and z-transforms. In: *The Control Handbook* (W. S. Levine, Ed.). Chap. 2. CRC Press. Florida.

Kissel, J. C., P.L. McCarty and R. L. Street (1984). Numerical simulation of mixed culture biofilm. *J. Environ. Eng.* **110**(2), 393–411.

Kjelleberg, S. K., B. H. Humphrey and K. C. Marshall (1982). Effects of interfaces on small, starved marine bacteria. *Appl. Environ. Microbiol.* **43**(5), 1166–1172.

Knowles, G., A. L. Downing and M. J. Barrett (1965). Determination of kinetic constants for nitrifying bacteria in mixed culture, with the aid of an electronic computer. *J. Gen. Microbiol.* **38**, 263–278.

Kugaprasatham, S., H. Nagoka and S. Ohgaki (1992). Effect of turbulence on nitrifying biofilms at non-limiting substrate concentrations. *Wat. Res.* **26**(12), 1629–1638.

Lacampe, B., F. Hansen, P. Penillard and F. Rogalla (1993). Wastewater nutrient removal with advanced biofilm reactors. *Wat. Sci. Tech.* **27**(5-6), 263–276.

Lambert, J. D. (1991). *Numerical Methods for Ordinary Differential Systems - the Initial Value Problem*. Wiley. Chichester, UK.

Levenspiel, O. (1972). *Chemical Reaction Engineering*. 2nd ed.. Wiley & Sons, New York.

Levich, V. G. (1962). *Physiochemical Hydrodynamics*. Prentice Hall. Englewood Cliffs, New Jersey.

Lewandowski, Z., P. Stoodley, S. Altobelli and E. Fukushima (1994). Hydrodynamics and kinetics in biofilm systems - recent advances and new problems. *Wat. Sci. Tech.* **29**(10-11), 223–229.

Ljung, L. (1987). *System identification - theory for the user*. Prentice Hall. Englewood Cliffs, New Jersey.

Lobo, V. M. M. and J. L. Quaresma (1989). *Handbook of electrolyte solutions: Part B*. Physical science data 41. Elsevier, Amsterdam.

Lyngå, A. and M. Årebäck (1991). Nitrifikation i biorotor - försök utförda februari-april 1991. Rapport 1991:4. GRYAAB. Karl IX väg, 417 22 Göteborg, Sweden.

Lyngå, A. and P. Balmér (1992). Denitrification in a non-nitrifying activated sludge system. *Wat. Sci. Tech.* **26**(5-6), 1097–1104.

MathWorks (1990). *MATLAB Control System Toolbox, User's Guide*. The MathWorks Inc.. 24 Prime Park Way, Natick, MA, USA.

MathWorks (1996). *MATLAB Optimization Toolbox, User's Guide*. 2nd ed.. The MathWorks Inc.. 24 Prime Park Way, Natick, MA, USA.

Mattsson, A. and A. Rane (1993). Nitrifikation i biobädd - försök utförda december 1990 - augusti 1992. Rapport 1993:1. GRYAAB. Karl IX väg, 417 22 Göteborg, Sweden.

Motta, E. J. La (1995). Modeling substrate transport into biofilms: Role of multiple ions and pH effects-discussion. *J. Environ. Eng.* **121**(4,), 368–369.

NAG (n.d.). *D02SAF - NAG Fortran Library Routine Document, Mark 16*.

Nevalainen, I., E. Kostyal, E. L. Nurmiaho-Lassila, J. A. Puhakka and M. S. Salkinoja-Salonen (1993). Dechlorination of 2,4,6-trichlorophenol by a nitrifying biofilm. *Wat. Res.* **27**(5), 757–767.

Nielsen, P. H. (1996). Adsorption of ammonium to activated sludge. *Wat. Res.* **30**(3), 762–764.

Novitsky, J. A. and R. Y. Morita (1977). Survival of a psychrophilic marine vibrio under long-term nutrient starvation. *App. Environ. Microbiol.* **33**(3), 635–641.

Nowak, O., K. Svardal and P. Schweighofer (1995). The dynamic behaviour of nitrifying activated sludge systems influenced by inhibiting wastewater compounds. *Wat. Sci. Tech.* **31**(2), 115–124.

Nyström, T. (1989). Macromolecular synthesis and turnover during adaption to energy and nutrient starvation by a marine vibrio sp.. Phd thesis. University of Göteborg. ISBN 91-86022-47-4.

Ohashi, A., D. G. Viraj de Silva, B. Mobarry, J. A. Manem, D. A. Stahl and B. E. Rittmann (1995). Influence of substrate C/N ratio on the biofilm structure of multi-species biofilms consisting of nitrifiers and heterotrophs. *Wat. Sci. Tech.* **32**(8), 75–84.

Okabe, S., K. Hirata and Y. Watanabe (1995). Dynamic changes in spatial microbial distribution in mixed-population biofilms: experimental results and model simulation. *Wat. Sci. Tech.* **32**(8), 67–74.

Process-Styrning AB (1989). *Beskrivning: AMMONIUMMÄTARE B461.* Process-Styrning AB. Box 410, 135 24 Tyresö, Sweden.

Råde, L. and B. Westergren (1990). *BETA - Mathematics Handbook.* 2nd ed.. Studentlitteratur and Chartwell-Bratt. Lund, Sweden.

Reichert, P. (1994). *Concepts underlying a computer program for the identification and simulation of aquatic systems.* EAWAG. CH-8600 Dübendorf, Switzerland.

Riemer, M., G. Holm Kristensen and P. Harremoës (1980). Residence time distribution in submerged biofilters. *Wat. Res.* **14**(8), 949–958.

Riley, J. P. and G. Skirrow (1975). *Chemical Oceanography.* Vol. 4. 2nd ed.. Academic Press, London.

Rittmann, B. E. (1982). The effect of shear stress on biofilm loss rate. *Biotechnol. Bioeng.* **24**, 501–506.

Rittmann, B. E. (1985). The effect of load fluctuations on the effluent concentration produced by fixed-film reactors. *Wat. Sci. Tech.* **17**, 45–52.

Rittmann, B. E. (1989). Mathematical modeling of fixed film growth. In: *Dynamic Modeling and Expert Systems in Wastewater Engineering* (P. Chapman, Ed.). Chap. 2, pp. 39–57. Lewis Publishers. USA.

Rittmann, B. E. and C. W. Brunner (1984). The nonsteady-state-biofilm process for advanced organics removal. *J. Wat. Pollut. Control Fed.* **56**(7), 874–880.

Rittmann, B. E. and J. A. Manem (1992). Development and experimental evaluation of a steady-state, multispecies biofilm model. *Biotechnol. Bioeng.* **39**, 914–922.

Rittmann, B. E. and P. L. McCarty (1980). Model of steady-state-biofilm kinetics. *Biotechnol. Bioeng.* **22**, 2343–2357.

Rittmann, B. E. and V. L. Snoeyink (1984). Achieving biologically stable drinking water. *J. Am. Wat. Works Ass.* **76**(10), 106–114.

Rittmann, B. E., J. M. Regan and D. A. Stahl (1994). Nitrification as a source of soluble organic substrate in biological treatment. *Wat. Sci. Tech.* **30**(6), 1–8.

Rodrigues, A. E., L. Zuping and J. M. Loureiro (1991). Residence time distribution of inert and linearly adsorbed species in a fixed bed containing "large-pore" supports: Applications in separation engineering. *Chem. Eng. Sci.* **46**(11), 2765–2773.

Rusten, B., L. J. Hem and H. Ødegaard (1995*a*). Nitrification of municipal wastewater in moving-bed biofilm reactors. *Wat. Environ. Res.* **67**(1), 75–86.

Rusten, B., L. J. Hem and H. Ødegaard (1995*b*). Nitrogen removal from dilute wastewater in cold climate using moving-bed biofilm reactors. *Wat. Environ. Res.* **67**(1), 65–74.

Schramm, A., L. H. Larsen, N. P. Revsbech and R. I. Amann (1997). Structure and function of a nitrifying biofilm as determined by microelectrodes and flourescent oligonucleotide probes. *Wat. Sci. Tech.* **36**(1), 263–270.

Schramm, A., L. H. Latsen, N. P. Revsbech, N. B. Ramsing, R. I. Amann and K. H. Schleifer (1996). Structure and function of a nitrifying biofilm as determined by in situ hybridization and the use of microelectrodes. *Appl. Environ. Microbiol.* **62**(12), 4641–4647.

Stevens, D. K., P. M. Berthouex and T. W. Chapman (1986). The effect of tracer diffusion in biofilm on residence time distributions. *Wat. Res.* **20**(3), 369–375.

Stevenson, L. H. (1978). A case for bacterial dormancy in aquatic systems. *Microbial Ecology* **4**, 127–133.

Stoodley, P., D. de Beer and Z. Lewandowski (1994). Liquid flow in biofilm systems. *Appl. Environ. Microbiol.* **60**(8), 2711–2716.

Strang, G. (1988). *Linear algebra and its applications*. 3rd ed.. Harcourt Brace Jovanovich, Inc.. Orlando, Florida. p. 15.

Suschka, J. (1987). Hydraulic performance of percolating biological filters and consideration of oxygen transfer. *Wat. Res.* **21**(8), 865–873.

Szwerinski, H., E. Arvin and P. Harremoës (1986). pH-decrease in nitrifying biofilms. *Wat. Res.* **20**(8), 971–976.

Tschui, M., M. Boller, J. Eugster, C. Mäder and C. Stengel (1994). Tertiary nitrification in aerated pilot biofilters. *Wat. Sci. Tech.* **29**(10-11), 53–60.

van Benthum, W. A. J., M. C. M. van Loosdrecht, L. Tijhuis and J. J. Heijnen (1995). Solids retention time in heterotrophic and nitrifying biofilms in a biofilm airlift suspension reactor. *Wat. Sci. Tech.* **32**(8), 53–60.

van Loosdrecht, M. C. M., D. Eikelboom, A. Gjaltema, A. Mulder, L. Tijhuis and J. J. Heijnen (1995). Biofilm structures. *Wat. Sci. Tech.* **32**(8), 35–43.

Wagman, D. D., W.H. Evans, V. B. Parker, R.H. Schumm, I. Halow, S. M. Bailey, K. L. Churney and R. L. Nuttall (1982). The NBS tables of chemical thermodynamic properties: selected values for inorganic substances. *Journal of Physical and Chemical Reference Data*. Supplement No. 2.

Wanner, O. (1989). Modeling population dynamics. In: *Structure and Function of Biofilms* (W. G. Characklis and P. A. Wilderer, Eds.). pp. 91–110. John Wiley & Sons.

Wanner, O. (1995). New experimental findings and biofilm modelling concepts. *Wat. Sci. Tech.* **32**(8), 133–140.

Wanner, O. and P. Reichert (1996). Mathematical modeling of mixed-culture biofilms. *Biotechnol. Bioeng.* **49**, 172–184.

Wanner, O. and W. Gujer (1984). Competition in biofilms. *Wat. Sci. Tech.* **17**, 27–44.

Wanner, O. and W. Gujer (1986). A multispecies biofilm model. *Biotechnol. Bioeng.* **18**, 314–328.

Watanabe, Y., H. E. Bravo and K. Nishidome (1982). Simulation of nitrification and its dynamics in a rotating biological contactor. *Wat. Sci. Tech.* **14**, 811–832.

Wezernak, C. T. and J. J. Gannon (1967). Oxygen-nitrogen relationships in autotrophic nitrification. *Appl. Microbiol.* **15**(5), 1211–1215.

Wijffels, R. H., A. W. Schepers, M. Smit, C. D. de Gooijer and J. Tramper (1994). Effect of initial biomass concentration on the growth of immobilized Nitrosomonas europaea. *Appl. Microbiol. Biotechnol.* **42**, 153–157.

Wijffels, R. H. and J. Tramper (1989). Performance of growing Nitrosomonas europea cells immobilized in κ-carrageenan. *Appl. Microbiol. Biotechnol.* **32**, 108–112.

Wijffels, R. H. and J. Tramper (1995). Nitrification by immobilized cells. *Enzyme and Microbial Technology* **17**, 482–492.

Wijffels, R. H., C. D. de Gooijer, A. W. Schepers, E. E. Beuling, L. F. Mallee and J. Tramper (1995*a*). Dynamic modeling of immobilized Nitrosomonas europea: Implementation of diffusion limitation over expanding microcolonies. *Enzyme and Microbial Technology* **17**, 462–471.

Wijffels, R. H., G. Englund, J. H. Hunik, E. J. T. M. Leenen, Å. Bakketun, A. Günter, J. M. Obon de Castro and J. Tramper (1995*b*). Effects of diffusion limitation on immobilized nitrifying microorganisms at low temperatures. *Biotechnol. Bioeng.* **45**, 1–9.

Wik, T. (1993). Dynamisk modellering av nitrifikation i biobädd. Technical Report CTH/RT/I-93/005. Control Eng. Lab.. CTH, S-412 96 Göteborg, Sweden.

Wik, T. (1996). Experiment utförda på en nitrifierande biobädd 1995. Technical Report CTH/RT/R-96/003. Control Eng. Lab.. CTH, S-412 96 Göteborg, Sweden.

Wik, T. (1997*a*). Modelling dynamics of nitrifying trickling filters and ammonium meters. *Med. Fac. Landbouww. Univ. Gent* **62**(4b), 1641–1647.

Wik, T. (1997*b*). Nitrifikation i biobädd - puls och stegsvarsförsök utförda på Sjölundaverket i maj 1997. Technical Report CTH/RT/I-97/004. Control Eng. Lab.. CTH, 412 96 Göteborg, Sweden.

Wik, T. (1998). Nitrifikation i biobädd - adsorption av ammonium i pilotanläggningarna vid Sjölundaverket. Technical Report 1998:1. Dept. Signals and Systems, Control Eng. Lab.. CTH, 412 96 Göteborg, Sweden.

Wik, T. (1999*a*). Adsorption and denitrification in nitrifying trickling filters. *Wat. Res.* **33**(6), 1500–1508.

Wik, T. (1999*b*). Rational transfer function models for nitrifying trickling filters. *Wat. Sci. Tech.* **39**(4), 121–128.

Wik, T., A. Mattsson, E. Hansson and C. Niklasson (1995). Nitrification in a tertiary trickling filter at high hydraulic loads. *Wat. Sci. Tech.* **32**(8), 185–192.

Wik, T. and C. Breitholtz (1996). Steady-state solution of a two-species biofilm problem. *Biotechnol. Bioeng.* **50**(6), 675–686.

Wik, T. and C. Breitholtz (1997). Transfer functions for series of continuously stirred biofilm reactors. Technical Report CTH/RT/I-97/001. Control Eng. Lab.. CTH, 412 96 Göteborg, Sweden.

Wik, T. and C. Breitholtz (1998). Rational transfer function models for biofilm reactors. *AIChE J.* **44**(12), 2647–2657.

Wik, T. and C. Lindeborg (1994). Modelling the dynamics of a trickling filter for waste water treatment. In: *3rd IEEE Conf. on Control Appl.*. Glasgow, UK. pp. 1035–1040.

Williamson, K. and P. L. McCarty (1976). A model of substrate utilization by bacterial films. *J. Wat. Pollut. Control Fed.* **48**(1), 9–24.

Wimpenny, J. (1995). Biofilms: Structure and organisation. *Microbial Ecology in Health and Disease* **8**, 305–308.

Wobus, A., S. Ulrich and I. Röske (1996). Degradation of chlorophenols by biofilms on semi-permeable membranes in two types of fixed bed reactors. *Wat. Sci. Tech.* **32**(8), 205–212.

Yantarasri, T., A. Garcia III and D. Brune (1992). Thermodynamic model of nitrification kinetics. *J. Environ. Eng.* **118**(4), 568–584.

Zhang, T. C. and P. L. Bishop (1994*a*). Density, porosity and pore structure of biofilms. *Wat. Res.* **28**(11), 2267–2277.

Zhang, T. C. and P. L. Bishop (1994*b*). Structure, activity and composition of biofilms. *Wat. Sci. Tech.* **29**(7), 335–344.

Zhang, T. C., Y. C. Fu and P. L. Bishop (1994). Competition in biofilms. *Wat. Sci. Tech.* **29**(10-11), 263–270.

Appendix A

Energy Balance

When modeling aquatic biological systems energy balances are usually not considered for the determination of temperatures. Since bacteria, generally, carry out exothermic reactions, the temperature in the biological system can be assumed to rise. However, it is the energy gained in the transformation of reactants into products that the bacteria use for growth, which implies that the temperature may not be affected by the reactions.

It is fairly simple to calculate an upper limit of the temperature rise over the reactor that can be caused by the transformations. For the case of nitrifying bacteria oxidizing ammonium into nitrate in a trickling filter, the upper limit can be calculated as follows:

The oxidization of ammonium into nitrate is carried out by ammonium oxidizers and nitrite oxidizers in two steps:

$$NH_4^+ + \frac{3}{2}O_2 \rightarrow NO_2^- + H_2O + 2H^+ \tag{A.1}$$

$$NO_2^- + \frac{1}{2}O_2 \rightarrow NO_3^-. \tag{A.2}$$

The H^+ is neutralized by the bicarbonate in the waste water according to

$$2H^+ + 2HCO_3^- \rightarrow 2CO_2 + 2H_2O. \tag{A.3}$$

Note that these are ideal stoichiometric relations. The bacteria use some of the carbon, oxygen, nitrogen and hydrogen for making more complex molecules building up their biomass. This requires energy, which is gained from the reactions above.

Standard enthalpies of formation and specific heat capacities at 25^oC can be found in e.g. "The NBS tables of chemical thermodynamic properties : selected values for inorganic substances" (Wagman *et al.* 1982). In Table A.1 the relevant values are summarized. Since the concentrations of the substrates are very low, infinite dilution is assumed.

The heat of reaction is calculated as the sum of the enthalpy of each element on the left hand side of each reaction, weighted by their stoichiometric coefficients,

Table A.1 *Enthalpies and specific heat capacities of the elements*

Substance	Enthalpy of formation H^o (kJ/mole)	Spec. heat capacity c_p^o (kJ/mole K)
O_2 (ao, g)	-11.7	0.029355
H_2O (l)	-285.83	0.075291
NO_2^- (ao)	-104.6	-0.0975
NO_3^- (ao)	-205.0	-0.0866
NH_4^+ (ao)	-132.51	0.0799
H^+ (ao)	0	0
CO_2 (ao)	-413.8	0.03711
HCO_3^- (ao)	-691.99	-

g=gas; l=liquid; ao=aqueous solution.

and subtracted from the sum of those on the right hand side, also weighted by the stoichiometric coefficients. In the same manner the dependence on temperature can be calculated. In Table A.2 these values are summarized for reactions (A.1) to (A.3) above.

Table A.2 *Enthalpies and specific heat capacities of reaction*

Reaction	Heat of reaction $\Delta_f H^o$ (kJ/mole)	Spec. heat cap. of reaction Δc_p^o (kJ/mole K)
(A.1)	-240.37	-0.146
(A.2)	-94.55	-0.004
(A.3)	-15.28	-
Σ	-350.2	-

All three reactions are exothermic in their nature, i.e. the heat of reaction is negative. Hence, the maximum energy that may be used for the temperature rise can be calculated as the sum of the energy released in reaction (A.1) to (A.3).

As a numerical example we use the pilot plant nitrifying trickling filter at Rya WWTP (see Chapter 6) with an influent ammonium concentration of 20 gN m^{-3} and a flow $Q = 10$ l/s. This corresponds to an ammonium load of 0.0143 mole/s. Assuming all the ammonium is oxidized into nitrate yields an energy release of $0.0143 \cdot 350.2 = 5$ kJ/s.

If it is further assumed that all the released energy is used for heating up the water

passing through the trickling filter, the following energy balance holds at 25°C:

$$Q\rho c^o_{p,H_2O}\Delta T = 5 \text{ kJ/s}.$$

If we insert the specific heat capacity of water, $c_{p,H_2O} = 4.18$ kJ/kg, the flow and the density of water (1 kg/l), the maximum temperature rise becomes 0.12 °C. As can be seen in Table A.2, the magnitude of the specific heat capacities of the reactions is far less than the values of the heat of reaction. Thus, the value of the temperature rise will not change significantly with temperature.

The calculated temperature difference should be compared with the measured temperature differences over the trickling filter which are less than ±1 °C, where the sign depends on the temperature difference between the water and the surrounding air. Averaging over one year, the temperature is reduced by 0.1 °C over the trickling filter.

If we use the maximum growth rates in Appendix B for the nitrifying species, we can estimate the temperature dependence of the rate of reaction to be approximately 10 %/°C. Since the nitrification rate is approximately proportional to the square root of the rate of reaction, differences in temperature between the surrounding air and the water affect the nitrification rate by less than 4 % (per ^{o}C) and the heat released by the nitrification affects the nitrification rate by less than 0.4 %.

Hence, it can be concluded that an energy balance considering the energy released by the nitrification is not necessary. It is also doubtful if there is any point in including an energy balance between the water and the air in the model.

Appendix B

Parameters

Table B.1 *Parameters depending on the temperature T (°C)*

Parameter	Value	Unit	Ref.
	Diffusion coefficients (80% of the values in water)		
D_{O_2}	$(682 + 29.8T - 0.0343T^2 + 0.0160T^3) \cdot 10^{-7}$	m^2d^{-1}	1
D_{NH_4}	$(730 + 12.8T + 0.606T^2 - 0.00533T^3) \cdot 10^{-7}$	m^2d^{-1}	1
D_{HCO_3}	$(450 + 7.16T + 0.446T^2 - 0.00533T^3) \cdot 10^{-7}$	m^2d^{-1}	1
D_{NO_2}	$(610 + 12.8T + 0.606T^2 - 0.00533T^3) \cdot 10^{-7}$	m^2d^{-1}	4
D_{NO_3}	$(610 + 12.8T + 0.606T^2 - 0.00533T^3) \cdot 10^{-7}$	m^2d^{-1}	4
D_{Li}	$(400 + 14.9T + 0.143T^2) \cdot 10^{-7}$	m^2d^{-1}	5
D_{BOD}	$830 \cdot 10^{-7}$ (20°C)	m^2d^{-1}	
	Growth rates		
$\mu_{m,ao}$	$10^{0.0413T-0.944}$	d^{-1}	3
$\mu_{m,no}$	$10^{0.0255T-0.492}$	d^{-1}	3
$\mu_{m,h}$	4.5 (20°C)	d^{-1}	2
	Others		
$c_{O_2}^{sat}$	$14.53 - 0.411T + 9.6 \cdot 10^{-3}T^2 - 1.2 \cdot 10^{-4}T^3$	gO_2m^{-3}	6

References

1. Gujer and Boller (1986)
2. Henze *et al.* (1987)
3. Knowles *et al.* (1965)
4. Kissel *et al.* (1984)
5. Lobo and Quaresma (1989)
6. Riley and Skirrow (1975)

Table B.2 *Constant parameters*

Parameter	Value	Unit	Comment
Y_a	0.15	gCOD/gN	
Y_{ao}	0.15	gCOD/gN	Chapter 4
Y_{ao}	0.11	gCOD/gN	
Y_{no}	0.04	gCOD/gN	
Y_h	0.40	gCOD/gBOD	
b_{ao}	0.03	d^{-1}	
b_{no}	0.03	d^{-1}	
b_h	0.3	d^{-1}	
k_a	0.5		
$k_{I,ao}$	0.1	d^{-1}	
$k_{I,no}$	0.1	d^{-1}	
$k_{I,h}$	0.1	d^{-1}	
$K_{O_2,ao}$	0.4	gO_2m^{-3}	
$K_{O_2,no}$	0.4	gO_2m^{-3}	
$K_{O_2,h}$	0.4	gO_2m^{-3}	
K_{O_2}	0.4	gO_2m^{-3}	
K_{NH_4}	1.0	gN m^{-3}	
K_{HCO_3}	0.3	mole HCO_3m^{-3}	
K_{NO_2}	0.8	gN m^{-3}	
	1.0	gN m^{-3}	Chapter 6
K_{NO_3}	0.1	gN m^{-3}	
K_{BOD}	5.0	gBOD m^{-3}	
$K_{O,h}$	0.1	gO_2m^{-3}	
ρ	3600	gCOD m^{-3}	

The values summarized in Table B.2 are typical values used in models of biofilms and activated sludge processes in wastewater treatment [c.f. Arvin and Harremoës (1990), Drtil *et al.* (1993), Henze *et al.* (1987), Gönenç and Harremoës (1985), Gujer and Boller (1986), Horn and Hempel (1997*a*), Knowles *et al.* (1965), Kissel *et al.* (1984), Rittmann and Snoeyink (1984), and Wanner and Reichert (1996)]. The reported values, and in particular the values of the saturation coefficients K, vary quite a lot. However, the models used in this thesis are generally insensitive to the actual values of the saturation coefficients.

Appendix C

Sign Investigations

Planes

If we write the complex variable z as $x + iy$ and use the fact that (Råde and Westergren 1990)

$$\tanh z = \frac{\sinh 2x}{\cosh 2x + \cos 2y} + i\frac{\sin 2y}{\cosh 2x + \cos 2y},$$

the imaginary part of $M(z)$ in Eq. (6.5) becomes

$$\mathrm{Im}\{M(z)\} = \frac{x \sin 2y + y \sinh 2x}{\cosh 2x + \cos 2y},$$

which has the same sign as xy.

On the real axis we have $M(x) = x \tanh x$, which is a positive even function in x.

Cylinders

To show that the imaginary part of $M(z)$ in Eq. (6.5) has the same sign as xy for cylinders is not as straightforward as for planes and spheres. From physical insight we know that $M(z)$ approaches $M(z)$ for planes as ρ approaches one and, hence, the sign of $\mathrm{Im}\{M(z)\}$ must, in this case, equal that of xy. Using, e.g., the fact that both $I_0(z)$ and $zI_1(z)$ are infinite sums of z^2, it is readily shown that the imaginary part of $M(z)$ is an odd function in both x and y and, hence, the sign of $\mathrm{Im}\{M(z)\}$ equals that of xy for all x and y if the first quadrant is mapped onto the upper half-plane. With this background and from numerous numerical calculations, we conclude that so is the case for all values of ρ.

On the real axis we have

$$M(x) = x\frac{K_1(\rho x)I_1(x) - K_1(x)I_1(\rho x)}{K_1(\rho x)I_0(x) + K_0(x)I_1(\rho x)}.$$

The modified Bessel functions I_0 and K_0 are positive even functions in x, while I_1 and K_1 are odd functions with the same sign as their arguments. Further, since $\rho < 1$, we have $I_1(x) > I_1(\rho x)$ and $K_1(\rho x) > K_1(x)$. Hence, $M(x)$ is a positive even function in x.

Spheres

Setting $\delta z = x + iy$ gives (Råde and Westergren 1990)

$$\begin{aligned} \cosh \delta z &= \cosh x \cos y + i \sinh x \sin y \\ \sinh \delta z &= \sinh x \cos y + i \cosh x \sin y. \end{aligned}$$

Denoting the denominator of the quotient in $M(z)$ in Eq. (6.5) by $D(z)$, it is straightforward to show, using these expressions and rules for trigonometric and hyperbolic functions, that

$$|D|^2 \mathrm{Im}\{M(z)\} = Im_1 + (\rho/\delta)^2(x^2 + y^2)Im_2 + (\rho/\delta)xyIm_3,$$

where

$$\begin{aligned} Im_1 &= \frac{1}{2}(y \sinh 2x - x \sin 2y) \\ Im_2 &= \frac{1}{2}(y \sinh 2x + x \sin 2y) \\ Im_3 &= 2(1 + \sinh^2 x - \cos^2 y). \end{aligned}$$

Im_1 and Im_2 have the same sign as xy, $Im_3 \geq 0$, and $D(z)$ has no singularities in any of the quadrants. Hence $\mathrm{Im}\{M(z)\}$ has the same sign as xy.

On the real axis $M(z)$ can be written as

$$M(x) = \frac{\delta x - \tanh \delta x + \rho x^2 \tanh \delta x}{\rho x + \tanh \delta x},$$

which is a quotient of odd functions and thus a positive even function in x.

Appendix D

Determination of PFD-Coefficients

In this section it is shown how the coefficients b_{kn} in Eq. (6.32) can be determined. There are several possibilities to calculate these PFD-coefficients. Two methods are discussed here. First, we derive the numerically more efficient method, which is the recursive algorithm on page 85.

We begin by proving the following identity:

$$\frac{1}{(s-\alpha_k)^r(s-\alpha_p)} = \sum_{q=1}^{r} \frac{(-1)^{r-q}}{(\alpha_k-\alpha_p)^{r-q+1}(s-\alpha_k)^q} + \frac{1}{(\alpha_p-\alpha_k)^r(s-\alpha_p)}, \qquad \text{(D.1)}$$

where it is assumed that $\alpha_k \neq \alpha_p$ when $k \neq p$.

According to the law of partial fraction decomposition (PFD) there exist unique constants A_q and B such that

$$\frac{1}{(s-\alpha_k)^r(s-\alpha_p)} = \sum_{q=1}^{r} \frac{A_q}{(s-\alpha_k)^q} + \frac{B}{s-\alpha_p}. \qquad \text{(D.2)}$$

If we multiply Eq. (D.2) by $(s-\alpha_p)$ and let $s=\alpha_p$, we get

$$B = \frac{1}{(\alpha_p-\alpha_k)^r}.$$

Multiplication of Eq. (D.2) by $(s-\alpha_k)^r$ gives

$$\frac{1}{s-\alpha_p} = \sum_{q=1}^{r} A_q(s-\alpha_k)^{r-q} + B\frac{(s-\alpha_k)^r}{s-\alpha_p}.$$

Repeated differentiation $p = 0, 1, \ldots$ times gives

$$\begin{aligned} \frac{d^p}{ds^p}\left(\frac{1}{s-\alpha_p}\right) &= \frac{p!(-1)^p}{(s-\alpha_p)^{p+1}} \\ &= \sum_{q=1}^{r-p} A_q \frac{(r-q)!}{(r-q-p)!}(s-\alpha_k)^{r-q-p} + \\ &\quad + B\frac{d^p}{ds^p}\left(\frac{(s-\alpha_k)^r}{s-\alpha_p}\right). \end{aligned} \qquad \text{(D.3)}$$

By successive differentiation it is readily verified that

$$\frac{d^p}{ds^p}\left(\frac{(s-\alpha_k)^r}{s-\alpha_p}\right) = \frac{r!}{(r-p)!}\frac{(s-\alpha_k)^{r-p}}{s-\alpha_p} + \mathcal{O}[(s-\alpha_k)^{r-p+1}],$$

where $\mathcal{O}[(s-\alpha_k)^{r-p+1}]$ denotes a function where all terms are powers of at least $(s-\alpha_k)^{r-p+1}$. Thus, the last term in Eq. (D.3) goes to zero as $s \to \alpha_k$ for all $p < r$. This implies that by letting $s = \alpha_k$ in Eq. (D.3), we get

$$\frac{p!(-1)^p}{(\alpha_k-\alpha_p)^{p+1}} = A_{r-p}p!, \quad p = 0, 1, \ldots r-1$$

and by a change of variable $q = r - p$, we get

$$A_q = \frac{(-1)^{r-q}}{(\alpha_k-\alpha_p)^{r-q+1}}, \quad q = 1, 2, \ldots r.$$

Insertion of the coefficients A_q and B into Eq. (D.2) gives the proposed expression (D.1), which holds for all s and integers r if $\alpha_k \neq \alpha_p$.

According to the laws of partial fraction decomposition, there exist unique constants b_{kn} in Eq. (6.32) for all N. If we let $b_{kn,N}$ denote the coefficients for N cascaded CSBRs, the coefficient $b_{k1,1}$ follows directly from the definition of the approximate transfer function for one single CSBR. Using Eq. (6.32) for the transfer function for $l-1$ cascaded CSBRs, the transfer function for l cascaded CSBRs can be written as the product of that transfer function with the one for a single CSBR:

$$\begin{aligned}
\hat{G}(s) &= K^{l-1}\left(\sum_{k=1}^{m}\sum_{r=1}^{l-1}\frac{b_{kr,(l-1)}}{(s-\alpha_k)^r}\right)K\left(\sum_{p=1}^{m}\frac{b_{p1,1}}{s-\alpha_p}\right) \\
&= K^l\sum_{r=1}^{l-1}\sum_{k=1}^{m}\sum_{p=1}^{m}\frac{b_{kr,(l-1)}b_{p1,1}}{(s-\alpha_k)^r(s-\alpha_p)} \\
&= K^l\sum_{r=1}^{l-1}\sum_{k=1}^{m}\left(\frac{b_{kr,(l-1)}b_{k1,1}}{(s-\alpha_k)^{r+1}} + \sum_{p\neq k}^{m}\frac{b_{kr,(l-1)}b_{p1,1}}{(s-\alpha_k)^r(s-\alpha_p)}\right).
\end{aligned}$$

Setting $K = 1$ for the sake of simplicity and using Eq. (D.1) give

$$\begin{aligned}
\hat{G}(s) &= \sum_{r=1}^{l-1}\sum_{k=1}^{m}\frac{b_{kr,(l-1)}b_{k1,1}}{(s-\alpha_k)^{r+1}} + \\
&\quad \sum_{r=1}^{l-1}\sum_{k=1}^{m}\sum_{p\neq k}^{m}\left(\sum_{q=1}^{r}\frac{(-1)^{r-q}b_{kr,(l-1)}b_{p1,1}}{(\alpha_k-\alpha_p)^{r-q+1}(s-\alpha_k)^q} + \frac{b_{kr,(l-1)}b_{p1,1}}{(\alpha_p-\alpha_k)^r(s-\alpha_p)}\right).
\end{aligned} \tag{D.4}$$

Sorting this expression in increasing orders of the poles, we get the first term by setting $q = 1$ in the last sum:

$$\sum_{r=1}^{l-1}\left(\sum_{k=1}^{m}\sum_{p\neq k}^{m}\frac{(-1)^{r-1}b_{kr,(l-1)}b_{p1,1}}{(\alpha_k-\alpha_p)^r(s-\alpha_k)} + \sum_{k=1}^{m}\sum_{p\neq k}^{m}\frac{b_{kr,(l-1)}b_{p1,1}}{(\alpha_p-\alpha_k)^r(s-\alpha_p)}\right).$$

Since the last sum contains all elements except the "diagonal elements" $k = p$, the indices k and p in that sum can be interchanged. Thus, by extracting the kth element we get

$$b_{k1,l} = \sum_{r=1}^{l-1} \sum_{p \neq k}^{m} \frac{(-1)^{r-1} b_{kr,(l-1)} b_{p1,1} + b_{pr,(l-1)} b_{k1,1}}{(\alpha_k - \alpha_p)^r},$$

which is equivalent to the expression for $n = 1$ in Eq. (6.34).

The terms in Eq. (D.4), having the highest order (l) of the poles, are only contained in the first sum. Thus, setting $r = l - 1$ in that sum gives the coefficients $b_{kl,l}$ as defined by Eq. (6.34).

The remaining coefficients, corresponding to poles of order $n = 2, \ldots l - 1$, follow from setting $r = n - 1$ in the first sum and $q = n$ in the second sum of Eq. (D.4), noting that only terms for $r \geq n$ contribute, and then extract the kth element:

$$b_{kn,l} = b_{k(n-1),(l-1)} b_{k1,1} + \sum_{r=n}^{l-1} \sum_{p \neq k}^{m} \frac{(-1)^{r-n} b_{kr,(l-1)} b_{p1,1}}{(\alpha_k - \alpha_p)^{r-n+1}}.$$

When PFD is carried out on small systems, such as when N and m are small, the coefficients are often found by polynomial identification. The polynomial identification gives a set of linear equations in the Nm coefficients. A probably simpler method is to use Nm different values θ_{ij}, which do not equal any α_k, and calculate the values of $\hat{G}(\theta)$ with Eq. (6.31). Eq. (6.32), with $s = \theta$, then gives a linear set of Nm equations:

$$\begin{bmatrix} \hat{G}(\theta_{11}) \\ \vdots \\ \hat{G}(\theta_{1N}) \\ \vdots \\ \hat{G}(\theta_{kn}) \\ \vdots \\ \hat{G}(\theta_{mN}) \end{bmatrix} =$$

$$\begin{bmatrix} \frac{1}{(\theta_{11}-\alpha_1)} & \cdots & \frac{1}{(\theta_{11}-\alpha_1)^N} & \cdots & \frac{1}{(\theta_{11}-\alpha_k)^n} & \cdots & \frac{1}{(\theta_{11}-\alpha_m)^N} \\ \vdots & & \vdots & & \vdots & & \vdots \\ \frac{1}{(\theta_{1N}-\alpha_1)} & \cdots & \frac{1}{(\theta_{1N}-\alpha_1)^N} & \cdots & \frac{1}{(\theta_{1N}-\alpha_k)^n} & \cdots & \frac{1}{(\theta_{1N}-\alpha_m)^N} \\ \vdots & & \vdots & & \vdots & & \vdots \\ \frac{1}{(\theta_{kn}-\alpha_1)} & \cdots & \frac{1}{(\theta_{kn}-\alpha_1)^N} & \cdots & \frac{1}{(\theta_{kn}-\alpha_k)^n} & \cdots & \frac{1}{(\theta_{kn}-\alpha_m)^N} \\ \vdots & & \vdots & & \vdots & & \vdots \\ \frac{1}{(\theta_{mN}-\alpha_1)} & \cdots & \frac{1}{(\theta_{mN}-\alpha_1)^N} & \cdots & \frac{1}{(\theta_{mN}-\alpha_k)^n} & \cdots & \frac{1}{(\theta_{mN}-\alpha_m)^N} \end{bmatrix} \begin{bmatrix} b_{11} \\ \vdots \\ b_{1N} \\ \vdots \\ b_{kn} \\ \vdots \\ b_{mN} \end{bmatrix}$$

To get numerically accurate solutions bad condition numbers of the Nm by Nm matrix must be avoided by a suitable choice of the values of θ_{ij}.

Both these methods require a solution of Nm linear equations, which, in practice, requires N^3m^3 arithmetic operations (Strang 1988). By calculating the operations in the recursive algorithm, it is easily verified that the required number of operations is in the order Nm^2. Hence, the recursive algorithm requires far less operations.

Appendix E

Taylor Expansion Coefficients

In Table E.1 below the Taylor coefficients for $F(s)^N$ for an expansion around the singularities α_k are given as functions of the Taylor coefficients d_n for $F(s)$.

Table E.1 *Taylor coefficients for* $F(s)^N$

N	f_0	f_1	f_2	f_3
1	d_1	$-$	$-$	$-$
2	d_1^2	$2d_1d_2$	$-$	$-$
3	d_1^3	$3d_1^2d_2$	$3(d_1^2d_3+d_1d_2^2)$	$-$
4	d_1^4	$4d_1^3d_2$	$4d_1^3d_3+6d_1^2d_2^2$	$4(d_1d_2^3+3d_1^2d_2d_3+d_1^3d_4)$

In the case of a planar substratum and negative $\tilde{\tau}$ and $\tilde{\gamma}$ it is easy to show, by straightforward differentiation and insertion of $\sqrt{\alpha_1+\kappa}=x$, that the coefficients are

$$
\begin{aligned}
d_1 &= \tilde{\tau}+\frac{\tilde{\gamma}}{2x}\left\{\tanh x+x-x\tanh^2 x\right\}\\
d_2 &= \frac{\tilde{\gamma}}{8x^3}\left\{2x^2\tanh^3 x-x\tanh^2 x-(1+2x^2)\tanh x+x\right\}\\
d_3 &= \frac{\tilde{\gamma}}{48x^5}\left\{-6\,x^3\tanh^4 x+(3x+8x^3)\tanh^2 x+3\tanh x-3x-2x^3\right\}\\
d_4 &= \frac{\tilde{\gamma}}{384x^7}\left\{24x^4\tanh^5 x+12x^3\tanh^4 x-(40x^4+6x^2)\tanh^3 x-\right.\\
&\quad \left.(15x+16x^3)\tanh^2 x+(6x^2-15+16x^4)\tanh x+4x^3+15x\right\}.
\end{aligned}
$$

By insertion of $\sqrt{\alpha_k+\kappa}=iy_{k-1}$, the remaining coefficients, or all coefficients when

$\tilde{\tau}$ and $\tilde{\gamma}$ are positive, become

$$
\begin{aligned}
d_1 &= \tilde{\tau} + \frac{\tilde{\gamma}}{2y_k}\left\{y_k + \tan y_k + y_k \tan^2 y_k\right\} \\
d_2 &= \frac{\tilde{\gamma}}{8y_k^3}\left\{-y_k + (1-2y_k^2)\tan y_k - y_k \tan^2 y_k - 2y_k^2 \tan^3 y_k\right\} \\
d_3 &= \frac{\tilde{\gamma}}{48y_k^5}\left\{2y_k^3 - 3y_k + 3\tan y_k + (8y_k^3 - 3y_k)\tan^2 y_k + 6y_k^3 \tan^4 y_k\right\} \\
d_4 &= \frac{\tilde{\gamma}}{384y^7}\left\{4y_k^3 - 15y_k + (15 + 6y_k^2 - 16y_k^4)\tan y_k + (16y_k^3 - 15y_k)\tan^2 y_k + \right. \\
&\quad \left. (6y_k^2 - 40y_k^4)\tan^3 y_k + 12y_k^3 \tan^4 y_k - 24y_k^4 \tan^5 y_k\right\}.
\end{aligned}
$$

Appendix F

Convergence

The numerical solution of the subsystem for dissolved components is not treated here. Due to the natural separation into fast and slow modes, the subsystem for dissolved components can be solved in the steady state when the dynamics of the solid components are studied. As discussed in Section 8.2, the stationary solution can be determined accurately with a finite element method, for example. Here, we only focus on describing an algorithm to solve the moving boundary problem for the solid components and to show that the algorithm converges to the original model equations when the time step size and the sizes of the biofilm segments in the discretization approach zero.

With the simplifying assumptions that the biofilm porosity is constant, and that the densities of the solid phases are constant, the equations for the solid components in the biofilm model for planar substrata in Chapter 3 are

$$\begin{aligned}
\rho_j \frac{\partial \epsilon_j}{\partial t} &= -\frac{\partial J_{s,j}}{\partial x} + \epsilon_j \rho_j \mu_{o,j}(c) \qquad j = 1, 2, \ldots n_s, \qquad 0 \le x \le L, \\
J_{s,j} &= u \rho_j \epsilon_j, \\
u &= \frac{1}{1-\epsilon_l} \int_0^x \sum_{j=1}^{n_s} \epsilon_j(x')(\mu_{o,j}(c(x')) + \varphi_j) dx', \\
\frac{dL}{dt} &= u(L) - f(L,t),
\end{aligned}$$

where c is a vector of all substrate concentrations in the biofilm.

Although not a true boundary condition, Eq. (4.6) has to hold at the biofilm substratum, i.e.,

$$\frac{\partial \epsilon_j}{\partial t} = -\epsilon_j \left[\frac{1}{1-\epsilon_l} \sum_{k=1}^{n_s} \epsilon_k (\mu_{o,k} + \varphi_k) \right] + \epsilon_j \mu_{o,j}.$$

Each ϵ_j denotes the proportion of the biofilm that is occupied by species j. Because of inactivation, some of each species is transformed into inert material. If an additional volume fraction ϵ_{n_s+1} for inert material is considered, the following equations

hold for that volume fraction:

$$\rho_{n_s+1}\frac{\partial \epsilon_{n_s+1}}{\partial t} = -\frac{\partial J_{s,n_s+1}}{\partial x} + \rho_{n_s+1}\sum_{j=1}^{n_s}\epsilon_j\varphi_j, \qquad 0 \le x \le L,$$

and

$$J_{s,n_s+1} = u\rho_{n_s+1}\epsilon_{n_s+1}, \qquad 0 \le x \le L.$$

At the substratum ($x = 0$) we have

$$\frac{\partial}{\partial t}\epsilon_{n_s+1} = -\epsilon_{n_s+1}\left[\frac{1}{1-\epsilon_l}\sum_{k=1}^{n_s}\epsilon_j(\mu_{o,j}+\varphi_j)\right] + \sum_{j=1}^{n_s}\epsilon_j\varphi_j.$$

Since we have

$$\sum_{j=1}^{n_s}\epsilon_j + \epsilon_{n_s+1} = 1-\epsilon_l,$$

the equations for inert material represent redundant information. However, they will be used in the physically based numerical method to determine the volume fractions.

If the following notation is introduced:

$$\begin{aligned} r_j(\epsilon, c) &= \epsilon_j\mu_{o,j}(c), \quad j = 1, \dots n_s \\ r_{n_s+1}(\epsilon, c) &= \sum_{j=1}^{n_s}\epsilon_j\varphi_j, \end{aligned}$$

all the equations for the solid components can be written as

$$\frac{\partial \epsilon_j}{\partial t} = -\frac{\partial}{\partial x}(u\epsilon_j) + r_j(\epsilon, c) \qquad j = 1, 2, \dots n_s+1, \qquad 0 \le x \le L, \tag{F.1}$$

$$u = \frac{1}{1-\epsilon_l}\int_0^x \sum_{j=1}^{n_s+1} r_j(\epsilon, c)dx', \qquad 0 \le x \le L, \tag{F.2}$$

and

$$\frac{dL}{dt} = u(L) - f(L, t). \tag{F.3}$$

At the substratum ($x = 0$) we have

$$\frac{d\epsilon_j}{dt} = -\epsilon_j\frac{1}{1-\epsilon_l}\sum_{k=1}^{n_s+1} r_k(\epsilon, c) + r_j(\epsilon, c), \tag{F.4}$$

$$u = 0. \tag{F.5}$$

Furthermore, we have $\sum_{j=1}^{n_s+1}\epsilon_j = 1-\epsilon_l$.

Numerical Algorithm

For each advance Δt in time, the following steps are carried out (see Figure 8.1):

1. The biofilm at time t ($0 \le x \le L_t$) is divided into $N_t - 1$ segments of size $\Delta x = h$ such that $(N_t - 1)h < L_t \le N_t h$. An additional segment of size δh, where $0 < \delta \le 1$, is introduced such that $(N_t - 1)h + \delta h = L_t$. In each biofilm segment the volume fractions ($E_{j,k,t}$, $j = 1, \ldots n_s + 1$, $k = 1, 2, 3, \ldots$) are constant.

2. The substrate concentrations $C_{k,t}$ in the middle of each segment, i.e.,

$$x_k = \begin{cases} h(k - 1/2) & k = 1, \ldots, N_t - 1 \\ (N_t - 1)h + \delta h/2 & k = N_t, \end{cases}$$

   are used for calculation of the growth of each volume fraction:

$$\Delta E_{j,k,t} = r_j(E_{k,t}, C_{k,t})\Delta t, \qquad j = 1, \ldots n_s + 1, \quad k = 1, \ldots N_t.$$

3. The volume fractions are normalized such that the proportions after the growth are

$$\bar{E}_{j,k,t+1} = \frac{E_{j,k,t} + \Delta E_{j,k,t}}{\sum_{i=1}^{n_s+1}(E_{i,k,t} + \Delta E_{i,k,t})}(1 - \epsilon_l).$$

4. After the volume fractions have been normalized the biofilm segments shrink or expand. The new distances from the middle of each biofilm segment to the substratum then become

$$\bar{x}_k = \begin{cases} \dfrac{h/2}{1-\epsilon_l} \displaystyle\sum_{j=1}^{n_s+1}(E_{j,1,t} + \Delta E_{j,1,t}), & k = 1 \\ \dfrac{h}{1-\epsilon_l}\left(\displaystyle\sum_{i=1}^{k-1}\sum_{j=1}^{n_s+1}(E_{j,i,t} + \Delta E_{j,i,t}) + \frac{1}{2}\sum_{j=1}^{n_s+1}(E_{j,k,t} + \Delta E_{j,k,t})\right), & \\ & k = 1, \ldots, N_t - 1 \\ \dfrac{1}{1-\epsilon_l}\left(h\displaystyle\sum_{i=1}^{N_t-1}\sum_{j=1}^{n_s+1}(E_{j,i,t} + \Delta E_{j,i,t}) + \frac{\delta h}{2}\sum_{j=1}^{n_s+1}(E_{j,N_t,t} + \Delta E_{j,N_t,t})\right), & \\ & k = N_t. \end{cases}$$

5. The updated volume fractions for the inner parts of the film ($E_{j,k,t+1}$, $k \ne 1$, $k \ne N_t$) at time $t + \Delta t$ are determined by linear interpolation of the updated volume fractions $\bar{E}_{j,k,t+1}$ and their distances $\bar{x}_k$ from the substratum. Two different situations around each x_k may occur:

   (a) The expansion between $x = 0$ and $x = x_k$ is positive, i.e. $\bar{x}_k \ge x_k$.

   (b) The expansion between $x = 0$ and $x = x_k$ is negative, i.e. $\bar{x}_k \le x_k$.

Provided the time step Δt is sufficiently small, i.e. $\bar{x}_k \leq x_{k+1}$, the updated volume fractions for case (a) are given by

$$E_{j,k,t+1} = \bar{E}_{j,k,t+1} + (\bar{E}_{j,k-1,t+1} - \bar{E}_{j,k,t+1})\frac{\bar{x}_k - x_k}{\bar{x}_k - \bar{x}_{k-1}}, \tag{F.6}$$

and if (b) holds, they are given by

$$E_{j,k,t+1} = \bar{E}_{j,k,t+1} + (\bar{E}_{j,k+1,t+1} - \bar{E}_{j,k,t+1})\frac{x_k - \bar{x}_k}{\bar{x}_{k+1} - \bar{x}_k}. \tag{F.7}$$

If the linear interpolation is expanded inside $\bar{x}_1$ when the expansion is positive, the same expression holds for both positive and negative expansions in the innermost biofilm segment:

$$E_{j,1,t+1} = \bar{E}_{j,1,t+1} + (\bar{E}_{j,2,t+1} - \bar{E}_{j,1,t+1})\frac{x_1 - \bar{x}_1}{\bar{x}_2 - \bar{x}_1}. \tag{F.8}$$

In the same way we extend the interpolation outside $\bar{x}_{N_t}$ for the last biofilm segment when the expansion is negative, which gives

$$E_{j,N_t,t+1} = \bar{E}_{j,N_t,t+1} + (\bar{E}_{j,N_t,t+1} - \bar{E}_{j,N_t-1,t+1})\frac{x_{N_t} - \bar{x}_{N_t}}{\bar{x}_{N_t} - \bar{x}_{N_t-1}} \tag{F.9}$$

for both positive and negative expansions.

6. The updated biofilm thickness is determined by

$$L_{t+1} = L_t + \frac{h}{1-\epsilon_l}\sum_{k=1}^{N_t-1}\sum_{j=1}^{n_s+1}\Delta E_{j,k,t} + \frac{\delta h}{1-\epsilon_l}\sum_{j=1}^{n_s+1}\Delta E_{j,N_t,t} - f(L_t,t)\Delta t.$$

Convergence

Introduce the notation

$$\begin{aligned} U_{k,t} &= \frac{h}{1-\epsilon_l}\sum_{i=1}^{k-1}\sum_{j=1}^{n_s+1}\Delta E_{j,i,t}, \\ U'_{k,t} &= \frac{1}{1-\epsilon_l}\sum_{j=1}^{n_s+1}\Delta E_{j,k,t}. \end{aligned}$$

We begin by investigating the equations for $k \neq 1$, $k \neq N_t$ and a positive expansion (a). Using

$$\sum_{j=1}^{n_s+1} E_{j,k,t} = 1 - \epsilon_l,$$

Eq. (F.6) and the expressions for $\bar{E}_{j,k,t+1}$, $\bar{x}_k$ and x_k we can now express the updated volume fractions as

$$\begin{aligned} E_{j,k,t+1} &= \frac{E_{j,k,t}+\Delta E_{j,k,t}}{1+U'_{k,t}} + \\ &\left(\frac{E_{j,k-1,t}+\Delta E_{j,k-1,t}}{1+U'_{k-1,t}} - \frac{E_{j,k,t}+\Delta E_{j,k,t}}{1+U'_{k,t}}\right)\frac{\frac{1}{h}U_{k,t}+\frac{1}{2}U'_{k,t}}{1+\frac{1}{2}(U'_{k-1,t}+U'_{k,t})}. \end{aligned}$$

Since

$$U'_{k,t} = \frac{1}{1-\epsilon_l}\left(\sum_{j=1}^{n_s+1} r_j(E_{k,t},C_{k,t})\right)\Delta t,$$

where r_j is bounded if the solution C_k for the dissolved components is bounded, we make a Taylor expansion of $1/(1+U'_{k,t})$. If Δt is small, this gives

$$\frac{1}{1+U'_{k,t}} = 1 - U'_{k,t} + \mathcal{O}(\Delta t^2) = 1 + \mathcal{O}(\Delta t),$$

where $\mathcal{O}(\,\cdot\,)$ denotes the Ordo function.

Using $U'_{k,t} = \mathcal{O}(\Delta t)$ we write the volume fractions as

$$\begin{aligned} E_{j,k,t+1} &= E_{j,k,t} - E_{j,k,t}U'_{k,t} + \Delta E_{j,k,t} + E_{j,k,t}\mathcal{O}(\Delta t^2) + \Delta E_{j,k,t}\mathcal{O}(\Delta t) + \\ &(E_{j,k-1,t}+\Delta E_{j,k-1,t} - E_{j,k,t} - \Delta E_{j,k,t})(\frac{1}{h}U_{k,t}+\frac{1}{2}U'_{k,t})(1+\mathcal{O}(\Delta t))^2. \end{aligned}$$

If we use

$$\Delta E_{j,k,t} = r_j(E_{k,t},C_{k,t})\Delta t = \mathcal{O}(\Delta t),$$

we can rewrite this as

$$\frac{E_{j,k,t+1}-E_{j,k,t}}{\Delta t} = r_j(E_{k,t},C_{k,t}) - E_{j,k,t}\frac{1}{1-\epsilon_l}\sum_{j=1}^{n_s+1} r_j(E_{k,t},C_{k,t}) -$$

$$\frac{E_{j,k,t}-E_{j,k-1,t}}{h}\frac{h}{1-\epsilon_l}\left(\sum_{i=1}^{k-1}\sum_{j=1}^{n_s+1} r_j(E_{i,t},C_{i,t}) + \frac{1}{2}\sum_{j=1}^{n_s+1} r_j(E_{k,t},C_{k,t})\right) + \mathcal{O}(\Delta t).$$

Using the same procedure on the expression (F.7) for negative expansions gives

$$\begin{aligned} E_{j,k,t+1} &= \frac{E_{j,k,t}+\Delta E_{j,k,t}}{1+U'_{k,t}} - \\ &\left(\frac{E_{j,k+1,t}+\Delta E_{j,k+1,t}}{1+U'_{k+1,t}} - \frac{E_{j,k,t}+\Delta E_{j,k,t}}{1+U'_{k,t}}\right)\frac{\frac{1}{h}U_{k,t}+\frac{1}{2}U'_{k,t}}{1+\frac{1}{2}(U'_{k,t}+U'_{k+1,t})} \\ &= E_{j,k,t} - E_{j,k,t}U'_{k,t} + \Delta E_{j,k,t} + E_{j,k,t}\mathcal{O}(\Delta t^2) + \Delta E_{j,k,t}\mathcal{O}(\Delta t) - \\ &(E_{j,k+1,t}+\Delta E_{j,k+1,t} - E_{j,k,t} - \Delta E_{j,k,t})(\frac{1}{h}U_{k,t}+\frac{1}{2}U'_{k,t})(1+\mathcal{O}(\Delta t))^2, \end{aligned}$$

which can be rearranged to

$$\frac{E_{j,k,t+1}-E_{j,k,t}}{\Delta t} = r_j(E_{k,t},C_{k,t}) - E_{j,k,t}\frac{1}{1-\epsilon_l}\sum_{j=1}^{n_s+1} r_j(E_{k,t},C_{k,t}) -$$

$$\frac{E_{j,k+1,t}-E_{j,k,t}}{h}\frac{h}{1-\epsilon_l}\left(\sum_{i=1}^{k-1}\sum_{j=1}^{n_s+1} r_j(E_{i,t},C_{i,t}) + \frac{1}{2}\sum_{j=1}^{n_s+1} r_j(E_{k,t},C_{k,t})\right) + \mathcal{O}(\Delta t).$$

For the first biofilm segment we get in the same way from expression (F.8):

$$\begin{aligned} E_{j,1,t+1} &= \frac{E_{j,1,t}+\Delta E_{j,1,t}}{1+U'_{1,t}} - \\ &\quad \left(\frac{E_{j,2,t}+\Delta E_{j,2,t}}{1+U'_{2,t}} - \frac{E_{j,1,t}+\Delta E_{j,1,t}}{1+U'_{1,t}}\right)\frac{\frac{1}{2}U'_{1,t}}{1+U'_{1,t}} \\ &= E_{j,1,t} - E_{j,1,t}U'_{1,t} + \Delta E_{j,1,t} + E_{j,1,t}\mathcal{O}(\Delta t^2) + \Delta E_{j,1,t}\mathcal{O}(\Delta t) - \\ &\quad (E_{j,2,t}+\Delta E_{j,2,t} - E_{j,1,t} - \Delta E_{j,1,t})(\frac{1}{2}U'_{1,t})(1+\mathcal{O}(\Delta t))^2, \end{aligned}$$

which gives

$$\begin{aligned} \frac{E_{j,1,t+1}-E_{j,1,t}}{\Delta t} &= r_j(E_{1,t},C_{1,t}) - E_{j,1,t}\frac{1}{1-\epsilon_l}\sum_{j=1}^{n_s+1} r_j(E_{1,t},C_{1,t}) - \\ &\quad \frac{E_{j,2,t}-E_{j,1,t}}{h}\frac{h/2}{1-\epsilon_l}\sum_{j=1}^{n_s+1} r_j(E_{1,t},C_{1,t}) + \mathcal{O}(\Delta t). \end{aligned}$$

For the last biofilm segment (where we use $N = N_t$ to save space) we get from (F.9):

$$\begin{aligned} E_{j,N,t+1} &= \frac{E_{j,N,t}+\Delta E_{j,N,t}}{1+U'_{N,t}} - \\ &\quad \left(\frac{E_{j,N,t}+\Delta E_{j,N,t}}{1+U'_{N,t}} - \frac{E_{j,N-1,t}+\Delta E_{j,N-1,t}}{1+U'_{N-1,t}}\right)\frac{\frac{1}{h}U_{N,t}+\frac{\delta}{2}U'_{N,t}}{\frac{1+\delta}{2}+\frac{1}{2}U'_{N-1,t}+\frac{\delta}{2}U'_{N,t}} \\ &= E_{j,N,t} - E_{j,N,t}U'_{N,t} + \Delta E_{j,N,t} + E_{j,N,t}\mathcal{O}(\Delta t^2) + \Delta E_{j,N,t}\mathcal{O}(\Delta t) - \\ &\quad (E_{j,N,t}+\Delta E_{j,N,t} - E_{j,N-1,t} - \Delta E_{j,N-1,t}) \times \\ &\quad \left(\frac{2}{1+\delta}\right)(\frac{1}{h}U_{N,t}+\frac{\delta}{2}U'_{N,t})(1+\mathcal{O}(\Delta t))^2, \end{aligned}$$

which can be rearranged to

$$\begin{aligned} \frac{E_{j,N,t+1}-E_{j,N,t}}{\Delta t} &= r_j(E_{N,t},C_{N,t}) - E_{j,N,t}\frac{1}{1-\epsilon_l}\sum_{j=1}^{n_s+1} r_j(E_{N,t},C_{N,t}) - \frac{E_{j,N,t}-E_{j,N-1,t}}{\frac{h+\delta h}{2}} \times \\ &\quad \frac{h}{1-\epsilon_l}\left(\sum_{i=1}^{N-1}\sum_{j=1}^{n_s+1} r_j(E_{i,t},C_{i,t}) + \frac{\delta}{2}\sum_{j=1}^{n_s+1} r_j(E_{N,t},C_{N,t})\right) + \mathcal{O}(\Delta t). \end{aligned}$$

If we assume that left and right derivatives are equal and that

$$\begin{aligned}
\frac{E_{j,k,t+1}-E_{j,k,t}}{\Delta t} &\rightarrow \frac{\partial}{\partial t}\epsilon_j(x_k,t)\\
r_j(E_{k,t},C_{k,t}) &\rightarrow r_j(\epsilon(x_k,t),c(x_k,t))\\
\frac{E_{j,k,t}-E_{j,k-1,t}}{\Delta x} &\rightarrow \frac{\partial}{\partial x}\epsilon_j(x_k^-,t)\\
\frac{E_{j,k+1,t}-E_{j,k,t}}{\Delta x} &\rightarrow \frac{\partial}{\partial x}\epsilon_j(x_k^+,t)\\
\frac{L_{t+1}-L_t}{\Delta t} &\rightarrow \frac{d}{dt}L(t)\\
\frac{1}{1-\epsilon_l}\sum_{j=1}^{n_s+1} r_j(E_{k,t},C_{k,t}) &\rightarrow \frac{1}{1-\epsilon_l}\sum_{j=1}^{n_s+1} r_j(\epsilon(x_k,t),c(x_k,t))\\
&= \frac{d}{dx}u(x_k)
\end{aligned}$$

$$\begin{aligned}
\frac{\Delta x/2}{1-\epsilon_l}\sum_{j=1}^{n_s+1} r_j(E_{1,t},C_{1,t}) &\rightarrow \frac{1}{1-\epsilon_l}\int_0^{x_1}\sum_{j=1}^{n_s+1} r_j(\epsilon,c)dx'\\
&= u(x_1)\\
\frac{\Delta x}{1-\epsilon_l}\left(\sum_{i=1}^{k-1}\sum_{j=1}^{n_s+1} r_j(E_{i,t},C_{i,t})+\frac{1}{2}\sum_{j=1}^{n_s+1} r_j(E_{k,t},C_{k,t})\right) &\rightarrow \frac{1}{1-\epsilon_l}\int_0^{x_k}\sum_{j=1}^{n_s+1} r_j(\epsilon,c)dx'\\
&= u(x_k)\\
\frac{\Delta x}{1-\epsilon_l}\left(\sum_{i=1}^{N-1}\sum_{j=1}^{n_s+1} r_j(E_{i,t},C_{i,t})+\frac{\delta}{2}\sum_{j=1}^{n_s+1} r_j(E_{N,t},C_{N,t})\right) &\rightarrow \frac{1}{1-\epsilon_l}\int_0^{x_{N_t}}\sum_{j=1}^{n_s+1} r_j(\epsilon,c)dx'\\
&= u(x_{N_t})
\end{aligned}$$

when $\Delta t \rightarrow 0$ and $\Delta x \rightarrow 0$, we get

$$\begin{aligned}
\frac{\partial}{\partial t}\epsilon_j(x_k,t) &= -\epsilon_j(x_k,t)\frac{d}{dx}u(x_k)-u(x_k)\frac{\partial}{\partial x}\epsilon_j(x_k,t)+r_j(\epsilon(x_k,t),c(x_k,t))\\
u(x_k) &= \frac{1}{1-\epsilon_l}\int_0^{x_k}\sum_{j=1}^{n_s+1} r_j(\epsilon,c)dx'\\
\frac{d}{dt}L(t) &= u(x_{N_t})-f(L(t),t).
\end{aligned}$$

Since $x_1=\Delta x/2\rightarrow 0$, $L_t-x_{N_t}<\Delta x/2\rightarrow 0$, r_j is bounded and $\partial\epsilon_j/\partial x$ is bounded, we get

$$\begin{aligned}
u(0) &= 0\\
\frac{\partial}{\partial t}\epsilon_j(0,t) &= -\epsilon_j(0,t)\frac{1}{1-\epsilon_l}\sum_{i=1}^{n_s+1} r_i(\epsilon(0,t),c(0,t))+r_j(\epsilon(0,t),c(0,t)).
\end{aligned}$$

Thus, the equations used in the algorithm converge to Eqs. (F.1) to (F.5).